Shock and Vibration

Intelligent Diagnosis, Prognosis, and Control of Machinery based on Sound and Vibration Signals

Lead Guest Editor: Pak Kin Wong
Guest Editors: Chaoshun Li, Zi-Qiang Lang, Zhi-Xin Yang, Wenxian Yang, and Xian-Bo Wang

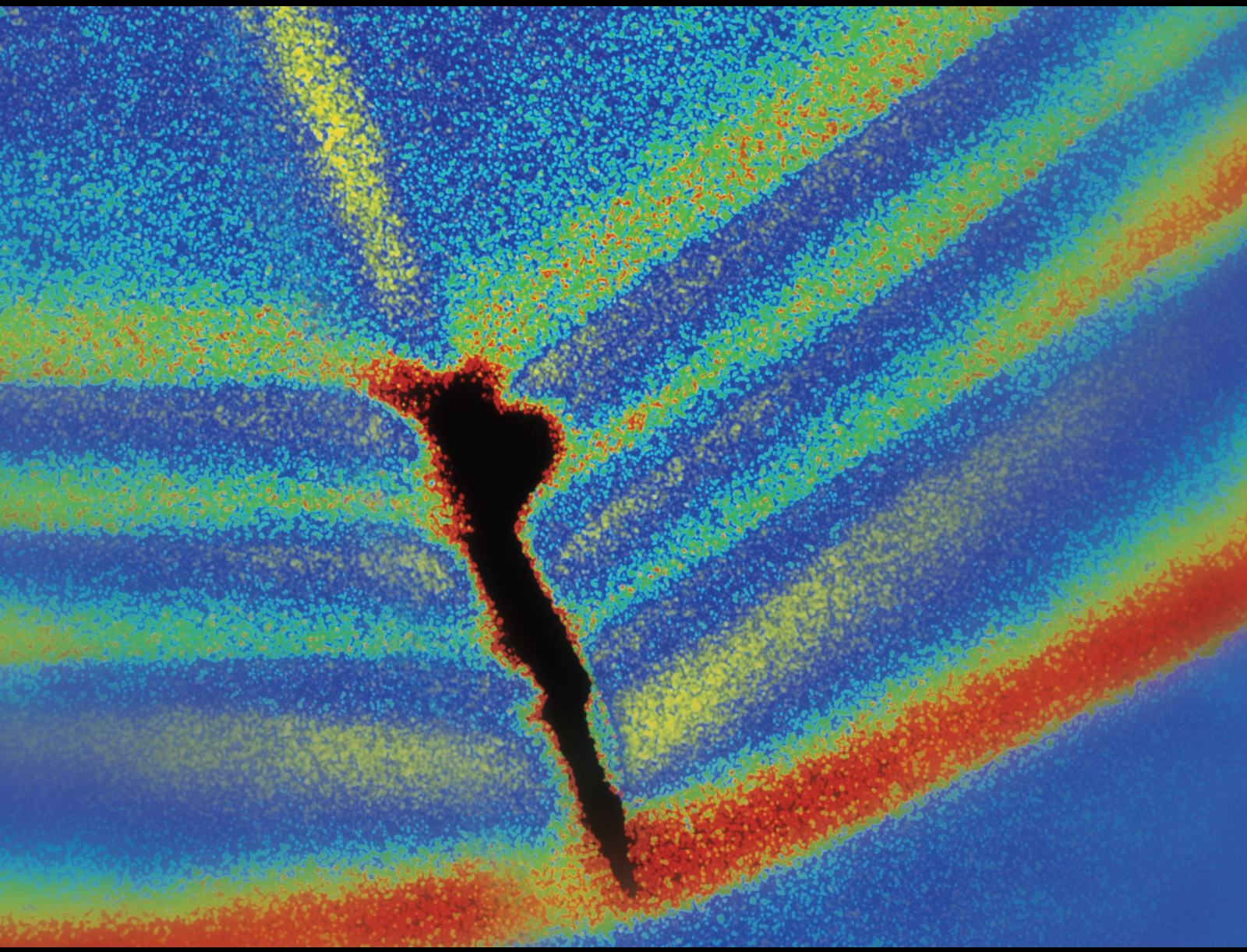

Intelligent Diagnosis, Prognosis, and Control of Machinery based on Sound and Vibration Signals

Shock and Vibration

Intelligent Diagnosis, Prognosis, and Control of Machinery based on Sound and Vibration Signals

Lead Guest Editor: Pak Kin Wong
Guest Editors: Chaoshun Li, Zi-Qiang Lang, Zhi-Xin Yang, Wenxian Yang, and Xian-Bo Wang

Chief Editor

Associate Editors

Academic Editors

Contents

Hindawi
Shock and Vibration
Volume 2022, Article ID 9010419, 16 pages
https://doi.org/10.1155/2022/9010419

Research Article

An Improved Recursive ARIMA Method with Recurrent Process for Remaining Useful Life Estimation of Bearings

Zeyu Luo,[1] **Xian-Bo Wang**,[1,2] **and Zhi-Xin Yang**[1]

[1]*State Key Laboratory of Internet of Things for Smart City, University of Macau, Macau SAR 999078, China*
[2]*College of Electrical Engineering, Henan University of Technology, Zhengzhou 450001, China*

Correspondence should be addressed to Zhi-Xin Yang; zxyang@um.edu.mo

Received 13 July 2021; Revised 18 January 2022; Accepted 26 January 2022; Published 21 February 2022

Academic Editor: Alba Sofi

A typical way to predict the remaining useful life (RUL) of bearings is to predict certain health indicators (HIs) according to the historical HI series and forecast the end of life (EOL). The autoregressive neural network (ARNN) is an early idea to combine the artificial neural network (ANN) and the autoregressive (AR) model for forecasting, but the model is limited to linear terms. To overcome the limitation, this paper proposes an improved autoregressive integrated moving average with the recurrent process (ARIMA-R) method. The proposed method adds moving average (MA) components to the framework of ARNN, adding the long-range dependence and nonlinear factors. To deal with the recursive characteristics of the MA term, a process of MA component estimating is constructed based on the expectation-maximum method. In the concrete realization of the method, the rotation tree (RTF) is introduced in place of ANN to improve the prediction performance. The experiment on FEMTO datasets reveals that the proposed ARIMA-R method outperforms the ARNN method in terms of predictive performance evaluation indicators.

1. Introduction

Bearings are critical parts of most rotating machines. They carry the resolves of shafts, but also bear the largest pressure. 44% of failure of some rotating machines are due to the malfunction of bearings, which cause force focusing on other fragile parts and then lead to systematic failure [1–4]. A difficulty in the maintenance is that the replacement of bearings needs disassembly of all related parts and requires planned maintenance based on their health condition. The necessity of prediction of the degradation process, therefore, arises that if the degradation can be predicted somehow, maintenance can be arranged to examine the least parts and repair most potential faults. Therefore, the estimation of the time before failure, that is, the remaining useful life (RUL) of bearings, is an important part of rotating machines' prognostics and health management (PHM) [5–7].

In the prediction of RUL, because of the nonlinearity and condense noise mixed within, certain forms of health indicators (HIs) are proposed to simplify the prediction. HIs are generally quantities that can be calculated according to life data, and they are designed to be more predictable than RULs and keep consistency with RULs. That is, the time HIs reach a given threshold corresponds to the time RULs are depleted, and the end of life (EoL) of the measuring equipment is met [8].

Although the end of life (EoL) of the equipment can be judged by the failure criterion, the service life itself is not a physical quantity that can be directly observed. It needs to be achieved through indirect methods (i.e., the state observation signal is processed to obtain indicators that reflect the degradation state and then the health indicators (HIs) are used to determine the EoL location with HI degradation trend prediction).

Generally, degradation prediction methods of bearings can be classified as physical model-based and data-driven-based approaches. Physical model-based approaches describe the whole system with a comprehensive mathematical model, indicating the characteristics and failure patterns of the system, especially the occurrence and growth of cracks, and the modes and energy of vibration [9–11]. Alternatively, data-driven methods dynamically build a model for the

observed machine based on the signals acquired, with a certain prior knowledge that usually comes from previous data collected. Compared with the model-driven methods, the digital model based on the data-driven monitoring method is not accurate, but from the perspective of feasibility, the observation data required by these methods are easy to be obtained, are more versatile, and can provide satisfactory prediction requirements [12–17].

It is a very popular path to build a hybrid model combining the ML-based models with time series analysis (TSA) [18–20]. Methods based on TSA deem the degradation of the equipment like a process continuous in time. The autoregressive (AR) model and its successive models are widely used time series models in prognostics. In this family of models, the past signal is linearly mapped to the current signal, and the current signal is the linear polynomial summing up the historical signals and other random factors. The moving average (MA) models are combined with the AR model to introduce long-range dependence missed from the AR model, which becomes the ARMA model [21]. Derived from this combination, the differential process is further added to it, giving rise to the autoregressive integrated moving average (ARIMA). Researchers solve forecasting tasks with all types of ARIMA models since the time they are invented [22–24]. The long-range dependence expressed in the MA terms of these models is critical in the prognostics of bearings [25]. In addition, Qiu et al. [26] compared the methods of predicting HIs and suggested that an ARMA model achieves well balances in computing complexity and performance.

Nevertheless, the traditional ARMA model solving procedure needs to repeatedly fit a variety of AR and ARMA models of different orders, which are lengthy and difficult for large data. So, it is appealing to combine ARIMA with ANN to simplify the solving. Autoregressive neural network (ARNN) is an early combination of ML and TSA [27]. The ARNN model directly uses historical observation data as the input of the neural network to solve the next observation, but different from the original model, the outputs are not necessarily obtained by a linear combination of inputs. It mends AR with nonlinear trait and black box solving of parameters and confines the input features of ANN to reduce overfit and difficulties on training. Because of the nonlinear trait of ARNN, it is also called nonlinear autoregressive neural network (NARNN) [28–31].

ARNN is based on the AR model, so the long-term coefficients described by the MA part of the ARMA model will be neglected. As [25] suggests, such leakages will lead to inaccurate prediction of HIs. Because ARMA describes more complicated models and the ARIMA is more universal than ARMA, it is natural to expect that a machine learning method combines with the ARMA or ARIMA model.

The main obstacle of such a combination of machine learning algorithms and the ARMA or ARIMA model is that the MA parts are basically the error terms between real and predicted observation, so it refers to the model result, which is still unknown when solving the model. Thus, the family of ARMA models is hard to be modeled by the ANN and other similar ML structures [32–34]. In the application of time series models to HI or RUL prediction, researchers mainly combine the ARMA family and ML methods as two independent parts, such as combining ARMA and SVM [35] and particle filter (PF) [23]. Even the ARNN has been used for such simply combination [36], or adding complexity from exogenous input to it [37]. In this type of combination, parameters and outputs of ARMA models are calculated by the traditional method and the outputs are added to predictions of other models to obtain the final result.

The contribution of this work lies in the following two aspects: first, this paper proposes an ARIMA-R method as the implementation framework of approximating the ARIMA model with ML, which is realized with the moving average approximation by recurrent means. Second, a test in series generated from an ARIMA model is carried out to examine the proposed ARIMA-R method, and the result shows that the method can estimate the next observation in such series with high accuracy.

The rest of this paper is organized as follows: Section 3 describes the ARIMA model and proposes the ARIMA-R method on its basis; Section 4 expresses the verification on the ability of the ARIMA-R model in describing generated ARIMA series and then uses the method to estimate bearing HIs through the public FEMTO dataset, with analysis of the parameter settings of the method; Section 5 concludes the whole study.

2. Methodology

2.1. ARIMA and ARNN. The ARIMA model originates from the AR model and MA model [21]. These models belong to the same type, depicting the autocorrelation of series data, which is the correlation between the data and its "lagged" copy. If autocorrelation exists, those data of the past will influence the future in some ways, usually described by functional relationships. Autocorrelation is common in times series analysis since most time series data reflects the inherited causality of the observation subject.

Assuming the autocorrelation in series is linear, the AR model and MA model can be obtained. In the AR model, the result is related to its previous observation and expressed by the linear combination of historical observations. Different from the AR model, the output in the MA model is explained by the errors of historical predictions. The prediction errors, implying the relationship between output and its trend or expectation, include accumulative historical effects and long-range dependency, as well as the influences of random history.

The combination of AR model and MA model is the ARMA model, while its improvement by applying differencing to both inputs and outputs results in the ARIMA model. The ARMA model includes short-term autoregressive and long-term moving average, which can better describe time series. However, ARMA inherits the strict requirements of the AR and MA models for the sequence to ensure the existence of autocorrelation. The sequence subject to the ARMA model is required to have weak stationarity, that is, zero mean and constant variance. The ARIMA model weakens this requirement by introducing the difference of

the sequence. It only needs the sequence to have differencing stationarity; in other words, it can become a stationary sequence after a finite number of differences.

For convenience, we denote the lag operator L with $L^d x_t = x_{t-d}$. Then, given a time series observation $X = x_1, x_2, \ldots, x_t$, the ARIMA model describes the series as

$$\begin{aligned} y_t &= (1-L)^d x_t \left(1 - \phi_1 L - \cdots - \phi_p L^p\right), \\ y_t &= c + \left(1 + \theta_1 L + \cdots + \theta_q L^q\right)\varepsilon_t, \end{aligned} \tag{1}$$

where c is the base value of X; $\varepsilon_s = \hat{y}_s - y_s$ is the historical prediction error (assumed to be white noise when $s = t$); p is the order of AR terms $(1 - \phi_1 L - \cdots - \phi_p L^p) y_t$, q of MA terms $(1 + \theta_1 L + \cdots + \theta_q L^q)\varepsilon_t$, and d of differencing orders; ϕ and θ are the parameters of the AR and MA (q) model, respectively. To emphasize the order parameters, the model may be written as follows: ARIMA (p, d, q).

This description takes the series as the d order sum of linear combination by multiple predictors in terms of AR, MA, and random noise. The orders of AR, MA, and the sum determine the specific form of ARIMA model, while the parameters of each term are to be solved to provide the prediction. With the variety of orders, the ARIMA model can generate time series ranging from white noise and random walk to complicated drift with the quadratic trend.

The simplicity of ARIMA model requires certain features of the subject data. The critical requirement is the autocorrelation of the series, so the autocorrelation function (ACF) and partial autocorrelation function (PACF) need to be calculated from the data to determine which order of AR and MA terms are available in the prediction.

A reliable procedure has been described by Box and Jenkins [38] to build the ARIMA model, including the following three steps: (1) model identification and determination of the orders p, d, and q, (2) parameter estimation of AR and MA terms, and (3) prediction checking and performance evaluation.

Proposed by [27], the ARNN attempts to use ML methods to solve AR models. The output variable (i.e., target) (p) can be expressed as follows:

$$\hat{y}_t = h\left(c, y_{t-1}, \ldots, y_{t-p}\right), \tag{2}$$

where $h(\cdot)$ is the nonlinear transformation obtained by the neural network.

Because the neural network can produce nonlinear features by introducing activation functions with strong nonlinear features, the application of activation functions with weak nonlinear characteristic in ARNN can achieve an effect that is almost equivalent to the AR model. However, this method is not expanded to the ARMA model because simply using the input data cannot directly obtain the prediction error features.

2.2. Rotation Forest. Rotation forest is an ensemble ML method, which integrates weak learners to gain accurate results. It is originally proposed only for classification purposes in [39], but the regression version was implemented later in [40].

In the field of ML, ensemble methods mainly include bagging (which is to train the classifiers with partial sample) and boosting (which is used to chain the weak classifiers for reinforcement). On the basis of bagging, the rotation forest constructs different features by rotating the features in feature space, thereby generating diversity on the classifiers. Different from bagging, although bootstrapping is used in the rotation forest method, instances are not discarded during classification, and all information about features is retained. The procedure of rotation forest can be depicted as follows.

Let $X = [x_1, x_2, \ldots, x_N]^T$ be a dataset with N instances, where each x_i instance includes m features in m-dimensional feature space F^m, $x_i = [Fx_{ii,1}, Fx_{i,2}, \ldots, Fx_{i,m}]^T \in F^m$. Therefore, X is an $N \times m$ matrix. Let $Y = [y_1, y_2, \ldots, y_N]^T$ be the regression target with respect to X.

Rotation forest generates l decision trees, D_1, D_2, D_l, to form a rotation tree.

The training set for an individual DT is processed with the following steps:

Step 1: randomly divide the feature set F into k subset $F_1, F_2, \ldots, F_k$. Assume each subset contains $q = m/k$ features.

Step 2: for each subset F_j, let X_j be the training set with only features in F_j and a bootstrap subset of X_j is drawn and used to form a new training set denoted by X'_j.

Step 3: principal component analysis (PCA) is applied to each X'_j and gives weight matrix C_j.

Step 4: all k matrices, C_1 to C_k, is used to construct a rotation matrix R in the form of diagonal block matrix that C_1 to C_k is put to the main diagonal blocks, and set all other blocks to zero as shown in equation (3). The columns of R, which are divided from feature F, are then rearranged according to F, denoted as R'.

$$R = \begin{vmatrix} C_1 & \{0\} & \ldots & \{0\} \\ \{0\} & C_2 & \ldots & \{0\} \\ \ldots & \ldots & \ldots & \ldots \\ \{0\} & \{0\} & \ldots & C_k \end{vmatrix}. \tag{3}$$

Step 5: the training set for a DT is given by $T = XR\prime$. DT is then trained by T and Y.

All l trees estimate the regression target with y^i. The average of all y^i is taken as the output of the rotation tree as in

$$\hat{y} = \sum_i \widehat{y^i}. \tag{4}$$

For the entire training set X_t, randomly generate a subset F_j of all features F_t for K times. For each subset F_j, the features in the intersection of F_j and X are selected to create the corresponding subset X_j. A random replacement

sampling is performed in X_j to produce the bootstrap sample X_j'. With K bootstrap sample $X'j$, PCA is used on $X'j$ to obtain the component matrix C_j, and all C_j rearrange internally to form a block diagonal matrix R as the rotation matrix. A rotation regression tree D is trained based on the sample X, Y and matrix R:

$$D = f\colon T \longrightarrow Y = f\colon XR' \longrightarrow Y. \tag{5}$$

To further increase the number of ensemble samples, repeat the above process L times to obtain L rotating trees and then use all rotating trees to form a rotation forest. The average prediction of all trees is the output of the rotation forest.

3. ARIMA-R

3.1. Flowchart and Basics of Proposed ARIMA-R. Compared with the AR model, the solution of the ARIMA model is more difficult and complicated. To determine the three order parameters of p, d, and q, it is necessary to enumerate different differential order d and search for the proper combination of p and q. Given a tentative d, the inputs and outputs are differenced to d order for successive calculation. The autocorrelation function (ACF) is calculated with respect to all possible lags and then another tentative middleware; the AR model is fit by the differential data for the partial autocorrelation function (PACF) or directly maximum likelihood estimation (MLE). The tentative p and q are determined by the result of ACF and PACF; then, the still tentative ARIMA model is finally solved only for evaluating the criterion such as Akaike information criterion (AIC). After testing multiple combinations of parameters, the order parameters are finally determined.

As shown in Figure 1, to simplify the solving of ARIMA model, a framework called ARIMA-R is constructed based on the ARNN method. The framework takes series data as input and provides its prediction as output.

Given a time series S and its observation X, where the time series is discrete and X contains observations until time $t-1$, $X = \{x_{t-1}, x_{t-2}, \ldots, x_1\}$, the prediction target is the observation x_t at time t. According to the ARIMA model, given orders p, d, and q, the target x_t can be expressed as follows:

$$\begin{aligned}\left(1 - \phi_1 L - \cdots - \phi_p L^p\right)(1-L)^d x_t &= c \\ &+ \left(1 + \theta_1 L + \cdots + \theta_q L^q\right)\varepsilon_t, \\ \varepsilon_\tau &= (1-L)^d \widehat{x}_\tau - (1-L)^d x_\tau,\end{aligned} \tag{6}$$

where $\phi_1, \phi_2, \ldots, \phi_p$ are the coefficients of AR terms, $\theta_1, \theta_2, \ldots, \theta_q$ are the coefficients of MA terms, ε_τ is the prediction error at time point τ, when $\tau = t$, ε_τ meets the Gaussian distribution, L is the lag operator, and c is the constant. For convenience, assume $y_t = (1-L)^d x_t$ as the observation, and the prediction error can be written as $\varepsilon_\tau = \widehat{y}_\tau - y_\tau$.

For calculation of ε_τ, we introduce the recurrent moving average (RMA) terms $(1 + \theta_1 L + \cdots + \theta_q L^q)\varepsilon_t^{(n)}$, where $\varepsilon^{(n)} = \widehat{y}^{(n-1)} - y$ is the nth generation error of prediction and real history.

For recurrent prediction, the model is depicted as follows:

$$\begin{aligned}&\left(1 - \phi_1 L - \cdots - \phi_p L^p\right)\widehat{y}_t^{(n)} \\ &\quad = c + \left(1 + \theta_1 L + \cdots + \theta_q L^q\right)\varepsilon_t^{(n)} \\ &\quad = c + \left(1 + \theta_1 L + \cdots + \theta_q L^q\right)\widehat{y}^{(n-1)} - \left(1 + \theta_1 L + \cdots + \theta_q L^q\right)y.\end{aligned} \tag{7}$$

The input term $F_t^{(n)}$ of ARIMA-R can be described as follows:

$$F_t^{(n)} = \left\{c, Ly_t, L^2 y_t, \ldots, L^p y_t, \varepsilon_t^{(n)}, L\varepsilon_t^{(n)}, \ldots, L^q \varepsilon_t^{(n)}\right\}. \tag{8}$$

Using the rotation forest based on regression tree, the prediction output of this generation can be given as follows:

$$\widehat{Y}^{(n)} = \widehat{y}_1^{(n)}, \widehat{y}_2^{(n)}, \ldots, \widehat{y}_t^{(n)} \text{where } \widehat{y}_t^{(n)} = \frac{1}{L}\sum_{i=1}^{L} D_i\left(F_t^{(n)}\right), \tag{9}$$

where L is the number of rotation trees (e.g., the magnitude of ensemble) and D_i is the single regression tree found by rotation forest algorithm.

After each iteration, if the parameters of MA terms converge or the maximum iteration generation R is reached, the recursion ends. In the end, calculate x_t from $\widehat{Y}^{(n)}$ referring to the reverse of $y_t = (1-L)^d x_t$. The first prediction $\widehat{y}^{(0)}$ needs to be estimated by other means. Considering that the evolution of regression tree may fall into local maxima, a more accurate estimate of y should be selected for the preliminary prediction value. The most universal way is to set it as equal to the last historical data x_{t-1}, which can be regarded as a coarse solution of AR(1) model. Given the condition of stationary including zero-mean sequence, an estimation of always 0 is also acceptable.

3.2. Order Determination in Proposed ARIMA-R. The main purpose of order determination is to estimate the polynomial form when building the model. Too few model variables cannot give a model that can describe the data well; too many variables are avoided in traditional modeling based on the principle of reducing assumptions, but in ML because the solution is approximate, too many feature variables are likely to cause overfitting. In the method, we choose to use an integrated algorithm based on regression decision tree-rotating tree algorithm to alleviate this problem when solving the model.

The regression tree algorithm uses features to divide the output space, and it applies the information entropy to divide the input feature space. If some features do not produce meaningful division, the pruning algorithm will be used to remove the judging branch of the feature. This study applies the bagging strategy to generate samples with diverse characteristics through random sampling. A shallow weak decision tree is generated for each sample, and the final regression result is generated. Since the weak decision tree naturally tends to be underfitting, plus that there are pruning

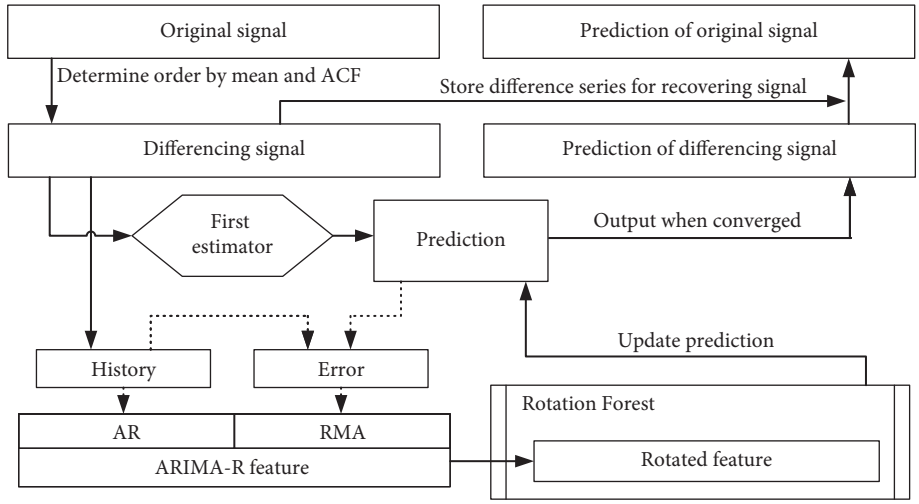

Figure 1: Flowchart of ARIMA-R.

algorithms to further reduce the decision branches, the integrated decision tree algorithm can effectively alleviate the overfitting problem caused by too many features.

3.3. Discussion about MA Terms. As shown in (1), it is easy to see that the different process in the model only uses the different observation data and the prediction error of the different data as input and the difference of the prediction result as the output. In other words, this process equally affects historical data as input and prediction results as output. Therefore, the actual problem to be predicted after d-order differential process is the same in form as the ARMA model. In this way, it is also possible to study the ARIMA model in the same way as the ARMA model.

When trying to use ML methods such as neural networks to model the ARMA model, the MA term in the ARMA model, that is, the random error term, is difficult to deal with. This term represents the error between the past predicted results and the actual results. Before modeling this term, one must first obtain all the predicted outputs before this input when training each input. This also means that a model for each data point needs to be trained step by step, instead of training a model for all data at once. In addition, in this case, there will be no consistency between models for each sequential data point and it is possible that a model only for this moment may be trained, and it has no predictive ability for data in other time periods [18, 41].

According to the definition of the MA term, the MA term is the error between the predicted result and the actual result, so the ARMA model can be rewritten as follows:

$$\begin{aligned}&\left(\left(1-\phi_1 L-\cdots-\phi_p L^p\right)+\left(1+\theta_1 L+\cdots+\theta_q L^q\right)\right)y_t\\&\quad=c+\left(1+\theta_1 L+\cdots+\theta_q L^q\right)\widehat{y}_t.\end{aligned}\tag{10}$$

As shown in (10), there are p groups of parameters for AR terms and q parameters for MA terms to be solved in the building of the model. It can be seen that the ARMA model is actually a linear model about q items of historical prediction results and $h = \max\{p, q\}$ items of historical observation data. The long-range dependence of the MA item is also because if the historical observation term is expanded each time the MA term is expanded, the previous h items of historical data will be added to the model. This also explains why the MA term should not be directly assumed as a series of uniformly distributed random variables. Although the historical prediction $\widehat{y}$ is an estimate of historical data y, it is generally assumed that the estimated error $y - \widehat{y}$ is a normal distribution with a fixed variance of zero means, but in fact, if the error is directly assumed to come from a zero-mean normal distribution, or if it is assumed to be zero, it will lose earlier observations and cause greater losses.

According to the above conclusions, the ARMA model can be established and solved by ML methods. However, the problem of how to calculate the predicted results before giving the model parameters and solving the model is still to be solved. Traditionally, the parameters are solved by calculating their maximum likelihood estimation (MLE) or least-squares estimation (LSE). However, considering that what we really need is the single-step estimation of time series prediction, it is also reasonable to calculate the result by training an artificial neuron network (ANN) or other regressors. However, in the ARNN model, MA term is excluded, so there is no solution in ARNN implementation.

This work introduces the idea of expectation maximization (EM) algorithm to carry out the iterative process [42]. The EM algorithm can calculate the MLE when the parameters are incomplete. For the statistical model of the observation data X and the unknown data Z, the parameter Θ needs to be estimated. Each iteration of the EM algorithm consists of the following two steps:

(1) Step E is to calculate the expected value of Z based on the existing model data X and the parameter th and use the expected value to replace the true value of the missing data and calculate the MLE of the parameter th

Input: $X = x_1, x_2, \ldots, x_{t-1}$
(1) $d \longleftarrow 0$
(2) **repeat**
(3) Y: $(1 - L)^d X$
(4) $D_d = Y$
(5) Calculate ACF of y
(6) $d \longleftarrow d + 1$
(7) **until** $E(y) - 0 <$ eps and ACF converge \(\triangleright\) the limit eps depends on practical situation.
(8) First guess:
(9) **for** training and testing set do
(10) Calculate Y_0 by $Y_0 = L^1 Y$ \(\triangleright\) other prediction methods also work.
(11) : **end for**
(12) : $k = 1$
(13) **repeat**
(14) **for** training and testing set do
(15) Calculate **RMA**
(16) $e\langle k\rangle = y - y\langle k - 1\rangle$
(17) Construct feature
(18) $F^{(k)}$: $F_t^{(k)} = \left\{y_{t-1}, \ldots, y_{t-p}, e_{t-1} \ldots e_{t-q}\right\}$
(19) **end for**
(20) Train the Rotation Forest in training set
(21) **for** training set do
(22) $y = D^{(k)}(F^{(k)})$
(23) **end for**
(24) Calculate $y\langle k\rangle$
(25) **for** training and testing set do
(26) $y = D^{(k)}(F^{(k)})$
(27) **end for**
(28) Calculate changes
(29) $s = \mathrm{MSE}(y^{(k)}, y^{(k)})$
(30) **until** $k > k_max$ or $s < eps$
(31) Construct $F<k>$
(32) **for** j from 1 to k do
(33) Calculate $e^{(k)}, F^{(k)}, y^{(k)}$
(34) **end for**
(35) $x_t = D(F^{(k)}) + D_1 + \cdots + D_{d-1}$
Output: estimated output x_t

Algorithm 1: ARIMA-R.

(2) Step M is to use the MLE of the parameter Θ given in Step E to find the parameter Θ when the MLE is minimized

After each iteration, update the parameter Θ and check whether it has converged. If it converges, the estimation is ended. In the EM method, the missing data Z is the expected value calculated based on other data, and the initial value of the parameter Θ is a random value.

On the one hand, the data to be estimated in step E are historical forecast data $\hat{y}$, and the expected value of $\hat{y}$ is consistent with the historical data y, which will cause the MA item to always be zero. On the other hand, if the estimated value of $\hat{y}$ is related to earlier historical data, it will speed up the convergence of the prediction model. In addition, if the parameter values of the ARMA model are initialized randomly, it is likely that the calculation result completely deviates from the true value, leading to overfitting or falling into local optimal problems. Therefore, the choice here is to use an AR(1) model to predict y and use this prediction result as the historical prediction data $\hat{y}$ and then directly solve the model parameters. Since the ARMA model describes a zero-mean sequence with stationarity, it is feasible to use zero as the prediction result.

Step M is obtained by solving and optimizing the MLE in the EM algorithm. In the method proposed here, the rotating forest can be used directly to obtain the model parameters, so only the model parameters need to be saved for the next iteration.

Only for single-step prediction, the proposed framework is useful, while on the multiple-step prediction, there is a limit to the ARIMA-R method. Since the ARIMA model is modeling the next value of observation, such a model is not fit to direct regression of future value. The only method is to predict the future step by step. In the calculation of prediction, the future errors are assumed to be zero and the future observations are replaced with the prediction before. Such treatment means that, on prediction, an ARIMA (p, d, q) model is degraded to an ARIMA $(p, d, 0)$ model. This means that the proposed ARIMA-R model must

similarly reduce to the ARIMA $(p, d, 0)$ model. Therefore, it turns out that, on multiple-step prediction of enough length, the recursive order r should be 1 or 0. In such a situation, this model is indiscriminate from the normal ARNN model.

3.4. Analysis of Computational Complexity. To analyse the computational complexity of ARIMA-R, we adopt the big O notation to describe the relation between operation quantities and input sizes. A complexity $O(p(N))$ means that when the input size N approaches infinite, the time of operation is infinite with the same order as $p(N)$.

For a signal series with length N, given orders p and q, our method needs r times of iteration in which a rotation forest is trained, where r is a small constant. Each time a rotation forest is trained, L trees are calculated. Every rotation tree needs K times of PCA and to train a decision tree based on the rearranged PCA results. In this process, L and K are predetermined parameters. Therefore, the algorithm needs to calculate $K \times L$ times of PCA and train L decision trees, in addition to L times of extra matrix multiplication. Reference [43] shows that the complexity of PCA with d-dimension vectors is $O(d^2N + d^3)$; reference [44] indicates that training a balanced regression tree on d-dimension data requires $O(dN\ logN)$ times of multiplication. We also know that a matrix multiplication between an m-by-n matrix and an n-by-p matrix is $O(\text{mnp})$. Summing up the results, the complexity is

$$O\Big((p+q)^2N + (p+q)^3 + (p+q)N\ \log\ N + (p+q)^2N\Big), \tag{11}$$

which is rewritten as

$$O\Big(s^2N + s^3 + sN\ \log\ N\Big) = O(N\ \log\ N), \tag{12}$$

where $s = p + q$ is relatively small.

Then, we come to ARIMA. As indicated by [45], the computational complexity of ARIMA itself is $O((N-p)p^2 + (N-p)q^2)$, which is better than the proposed ARIMA-R with fixed p and q. Nonetheless, the computing burden lies on the order determination part. Following the Box–Jenkins method (if assume p_max and q_max), given fixed differential parameter i, $p_max q_max$ times of searches are necessary to determine the proper order parameters p and q for ARIMA. For each parameter combination, ACF and PACF to certain orders, such as p_max order, should be calculated to obtain the AIC and determine parameters. Reference [46] suggested that if we use the common Levinson–Durbin method to solve ACF and PACF, the complexity of ACF is $O(N^2)$ and that of PACF is $O(q^2N^2)$. Because the total times of ACF and PACF solving in the Box–Jenkins method are $p_{\max}q_{\max}$, the complexity in this part is $O(p_{\max}q_{\max}q^2N^2) = O(N^2)$. In total, the complexity of ARIMA is

$$O\Big((N-p)p^2 + (N-p)q^2 + p_{\max}q_{\max}q^2N^2\Big) = O\Big(N^2\Big). \tag{13}$$

It is worth noting that the ACF and PACF solving is also needed in ARIMA-R, while the total times are reduced to $p_{\max}$. With the common operations eliminated, traditional ARIMA with the Levinson–Durbin method still needs $p_{\max}(q_{\max} - 1)$ times of searches, so the result keeps unchanging.

The above analysis suggests that the proposed ARIMA-R algorithm reduced the computing burden in order determination, in the cost of complexity increasing in parameter approximation. Overall, the computational complexity of ARIMA-R is reduced.

4. Experimental Verification in Prognostics of Bearings

Three experiments are conducted to verify the ability of the proposed ARIMA-R method: an experiment with simulated data, a single-step forecast experiment based on bearing remaining useful life datasets, and a long-term prediction experiment.

To compare the prediction errors of ARNN and that of ARIMA-R for each sample, four indicators, mean square error (MSE), mean absolute error (MAE), coefficient of determination (R^2), and mean absolute percentage error (MAPE), are introduced. Among the indicators, MSE, MAE, and MAPE are better if they are closer to 0, which means the prediction result is closer to the predicting target. R^2 indicates the proportion of the target that can be explained by the prediction, so the value of R^2 should close to 1. Mathematical expressions of these indicators are shown as

$$\text{MSE} = \frac{1}{n}\sum_{i=1}^{n}\left(y_i - \widehat{y}_i\right)^2, \tag{14}$$

$$\text{MAE} = \frac{1}{n}\sum_{i=1}^{n}\left|y_i - \widehat{y}_i\right|, \tag{15}$$

$$\begin{aligned} R^2 &= 1 - \frac{\sum_{i=1}^{n}\left(y_i - \widehat{y}_i\right)^2}{\sum_{i=1}^{n}\left(y_i - \overline{y}\right)^2} \\ &= 1 - \frac{\text{MSE}}{\text{Var}}, \end{aligned} \tag{16}$$

$$\begin{aligned} \text{MAPE} &= \frac{|y - \widehat{y}|}{|y|} \\ &= \frac{1}{n}\sum_{i=1}^{n}\frac{\left|y_i - \widehat{y}_i\right|}{|y|}. \end{aligned} \tag{17}$$

4.1. Verification with Simulated Data. To verify the prognostic capacity of the proposed ARIMA-R method, this paper selects the following parameters to establish a curve that meets the ARIMA model, as shown in Table 1.

Since the MA term actually uses random noise to replace the unknown past data when generating the ARIMA curve in simulation, other forms of the curve may also be generated with the same parameters and starting point. ARNN and ARIMA-R were used to build a model to solve the first 100 data points of the curve and then used to make a single-step prediction for the last 100 data points. The results are

Table 1: Parameters to simulate ARIMA data.

Term	Order	Order	AR param.	MA param.
AR	2	1	0.5	0.65
MA	4	2	−0.75	−0.5
Diff.	2	3		−0.2
		4		−0.1

shown in Figure 2. This experiment is a single-step prediction, that is, for each time point t, the data up to time point $t-1$ is used to predict the observation result. The x-axis in the figure is the order of observation samples, and the y-axis is the actual HI value and the difference value of HI, respectively. Figure 2(a) shows that the 1–100 observations are used as training data and the 101–200 data are used as test data. Figure 2(b) shows the different prediction results of the test data part. It can be clearly seen that the prediction of the ARIMA-R method is more accurate than that of the ARNN method.

However, it should be emphasized that such high performance comes from that the data are purely generated by the ARIMA model and in single-step prediction. For long-term prediction, random factors will dominate the result. The long-term result in Figure 3 indicates that the prediction error blooms gradually after about 15 iterations of long-term prediction.

4.2. Experiment Setup and Procedure for Single-Step Forecast. In the prognostic experiment, vibration signals of bearings at the run-to-fail situation are used. The bearing dataset is provided by FEMTO Institute, published on the NASA Prognostics Center of Excellence (PCoE) [47]. Two orthogonally installed accelerometers in horizontal and vertical directions on the housing of bearing collect vibration signals in the form of acceleration, as shown in Figure 4. For both signal channels, the sampling frequencies of signals are 25.6 kHz, while the data are collected every 10 seconds for 1 second. For all conditions and bearings, the data acquisition is begun at the normal state of bearings and ended when the bearings fail. The detail of the platform and the experiments can be obtained in [47]. The dataset includes 17 subsets under three different conditions, as shown in Table 2.

The root mean square (RMS) of the vibration signals is calculated and provided as the HI prediction target. Each set of data is a series of observation samples arranged in time order, so the time series analysis is used for processing the signals. The bearing 1_4 data are taken as an example in Figure 5. The RMS data are a flat small value at the beginning, namely, platform period, and in the middle of the wearing period, abnormal values that far exceed the average value of the platform period frequently appear; finally, in the final stage, the RMS value increases abnormally, until the bearing fails completely.

The division of stages is carried out according to the position of the node where the trend of the data changes suddenly. Since the ARIMA model is a model based on sequence prediction, it is not suitable for predicting the data when sudden changes occur. So, it is better not to make cross-stage predictions. Here, the data of the failure stage are mainly selected as the prediction object for method verification. In the process of model training using ML algorithms, the data need to be divided into a training set and a validation set. Under the assumption that the samples of the two datasets follow the same model, the training set is used to determine the model parameters and then the validation set is used to verify the performance of the model. Generally speaking, the training set and the validation set are randomly selected regardless of the order of the data, but the ARIMA model is a time series model; thus, training the model with future data will result in inaccurate performance in the past data in the validation set. Therefore, a certain length of data is selected as the training set from the beginning of the overall sequence, and the subsequent sequence is used as the verification set.

In this experiment, after selecting the training data, the key parameters can be determined through data research, mainly to determine the order of the ARIMA model, including AR order p, MA order q, and differencing order d. As mentioned in the problem of order determination in Section 2.2, the ARIMA-R method does not require precise order determination, but it is still necessary to carry out the difference and calculate the ACF to determine the differencing order d and determine the reference values of p and q.

The data are generally divided into a training set and a validation set for training the model and a test set for testing the performance of the model. However, a special division is required here. The data are first divided into normal phase data and abnormal phase data according to the trend, and then the abnormal data are used to train the model [48]. The reason is that the data of different phases cannot be regarded as in the same distribution, so it cannot be learnt by the same model. In this study, bearing datasets 1_4, 1_6, and 3_3 are used as the training target for prediction, where first 1/3 of data are selected as the training samples, and the rest are for testing. The data of these bearings in the abnormal state are shown in Figure 6.

The ACF and PACF of RMS itself and its difference are represented in Figure 7, from dataset 1–7. This dataset is not used in the prediction, and the ACF/PACF results are taken as reference in order determination. In order to be processed using the ARIMA-R model, the sequence used for model prediction needs to be a sequence of approximately zero mean after differencing, so the ACF function of the sequence is calculated first, and the PACF function is calculated based on the AR (15) model, whose orders are determined by the result of ACF function. According to the lags that the ACF/PACF value is above the significance line, the orders of model are determined as shown in the ARIMA-R part of Table 3.

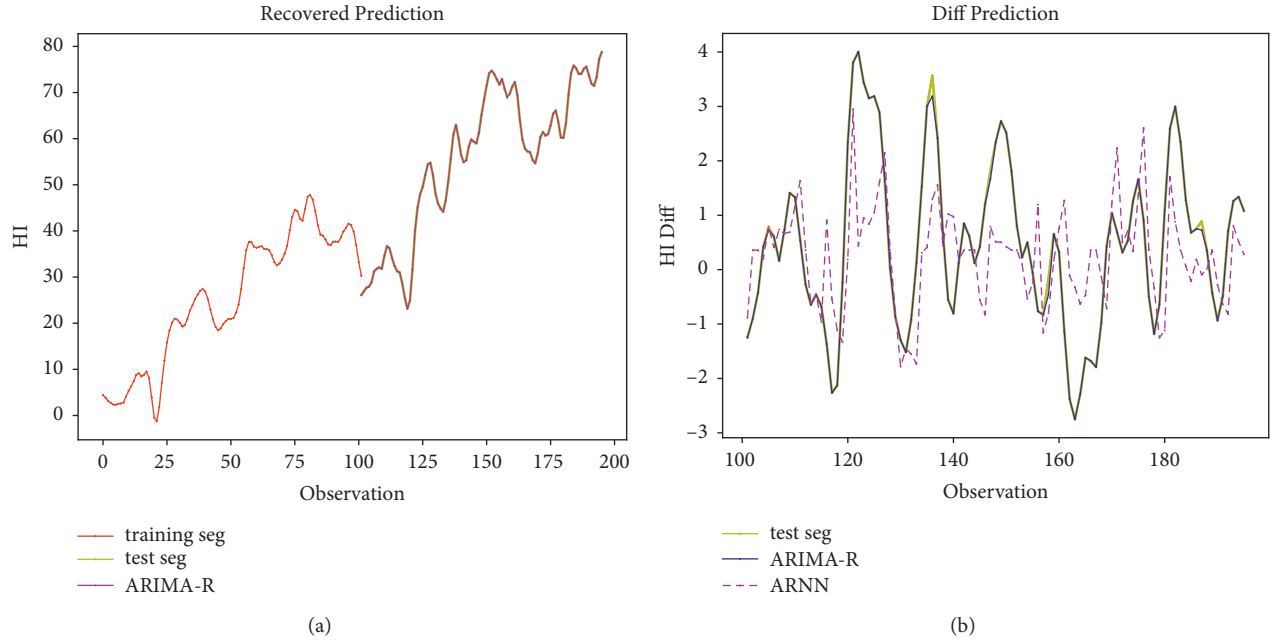

Figure 2: The single-step prediction result of the generated data. (a) The prediction result after the difference is restored. (b) The prediction result of the differenced data.

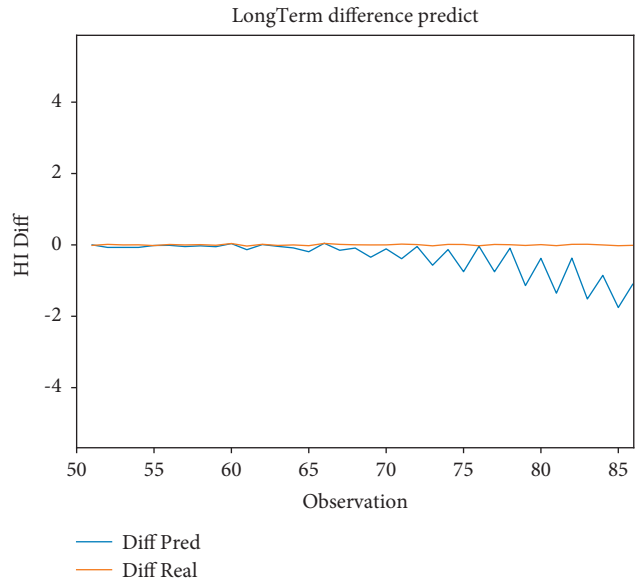

Figure 3: A part of long-term prediction by ARIMA-R.

After determining the order of the ARIMA-R model, the ML algorithm be used to train the model, so the data must be divided first. The ML algorithm inside the model is selected to be Rotation Forest Regressor (RTF), and the parameter settings of the two models are shown in Table 3. In addition, as the reference for RMA, the Lag 1 observation, that is, the last one, is used in calculating RMA for the first estimate of this observation. Since the maximum value of the three parameters d, p, and q is 20, the model can be regarded as a single-step forecast using 20 historical data.

The prediction directly given by RTF or other algorithms is the d-order difference of the observed data. The actual predicted value can be obtained by adding the predicted difference value to the sum of the observed value and difference of this observation.

Taking the data of prediction in bearing 1–4 as an example, the prediction results are shown in Figure 8(b), and the prediction result obtained after accumulating the observation value and the difference value is shown in Figure 8(a). In Figure 8(b), the comparison is the prediction result of ARNN method. Except for the first 50 data where due to sudden

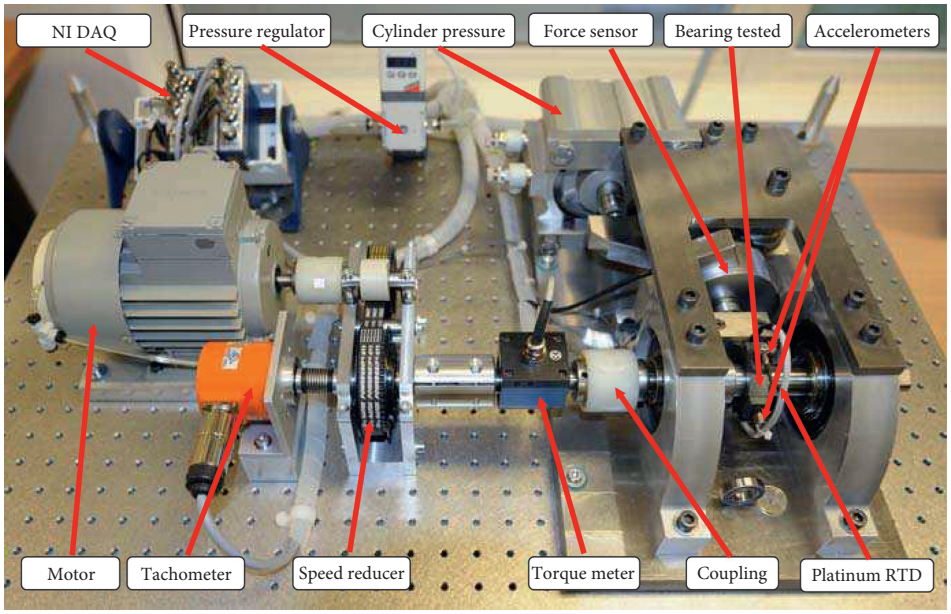

Figure 4: The experimental platform PRONOSTIA. In the accelerated degradation experiment of bearings carried out on the PRONOSTIA platform, the data collected from two mutually orthogonal acceleration sensors are transmitted to the computer through DAQ equipment. In order to accelerate the aging of the bearing, radial force is exerted on the bearing [47].

Table 2: FEMTO datasets.

Operation cond.	Condition1	Condition2	Condition3
Datasets	Bearing1_1	Bearing2_1	
	Bearing1_2	Bearing2_2	
	Bearing1_3	Bearing2_3	Bearing3_1
	Bearing1_4	Bearing2_4	Bearing3_2
	Bearing1_5	Bearing2_5	Bearing3_3
	Bearing1_6	Bearing2_6	
	Bearing1_7	Bearing2_7	

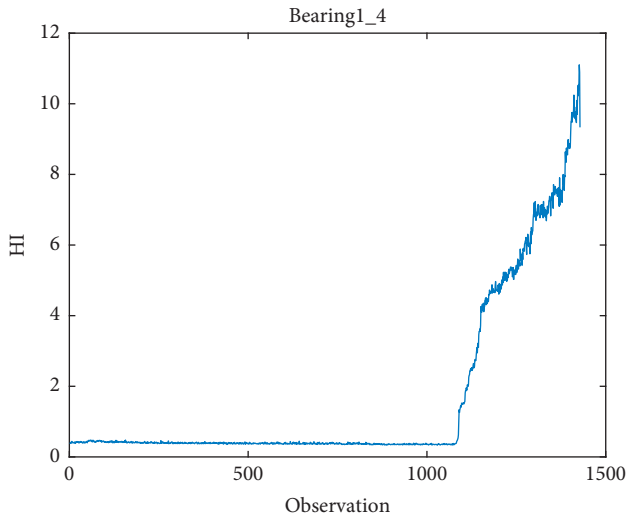

Figure 5: RMS of bearing 1_4.

changes in data and lack of historical data, the predictions of both methods are identically zero, the ARIMA-R method has certain advantages over the ARNN method. Because it is a single-step forecast, it can be seen that the forecast results are in good agreement with the actual data, but if the model is extended to multistep, serious errors will surely occur.

4.3. Experiment Performance and Analysis. The single-step prediction results of the ARIMA-R model for several test samples are shown in Table 4. Comparing the performance of the two methods in the table, it can be seen that the overall performance of the ARIMA-R method is better than that of ARNN, but there is no significant advantage. This is because the data used for testing have obvious noise, which affects the learning of the model. The performance of the ARNN algorithm in different data is unstable. This is because the number of samples is insufficient, resulting in overfitting.

The combination of the ARIMA-R model and various ensemble tree algorithms can be used to train the prediction model, and the comparison of the results is shown in Table 5. The table demonstrates the results replacing RTF in ARIMA-R with different ensemble ML algorithms. Like previous experiment, the result comes from single-step prediction on the bearing dataset, and the result from the ARNN algorithm is provided as a reference.

The algorithms chosen to combine with include Gradient Boosting Tree (GBT), AdaBoost Tree (ABT), and Random Forest (RF), in addition to ANN. The result suggests that the RTF algorithm has some advantages over the others in the framework of ARIMA-R, but is not always better. This is as expected because these ensemble trees have similar learning capabilities, and that is similar to the ability of ANN.

4.4. Long-Term Prediction. A long-term prediction by ARIMA-R is conducted on the FEMTO data, aiming to further examine the performance of the proposed method.

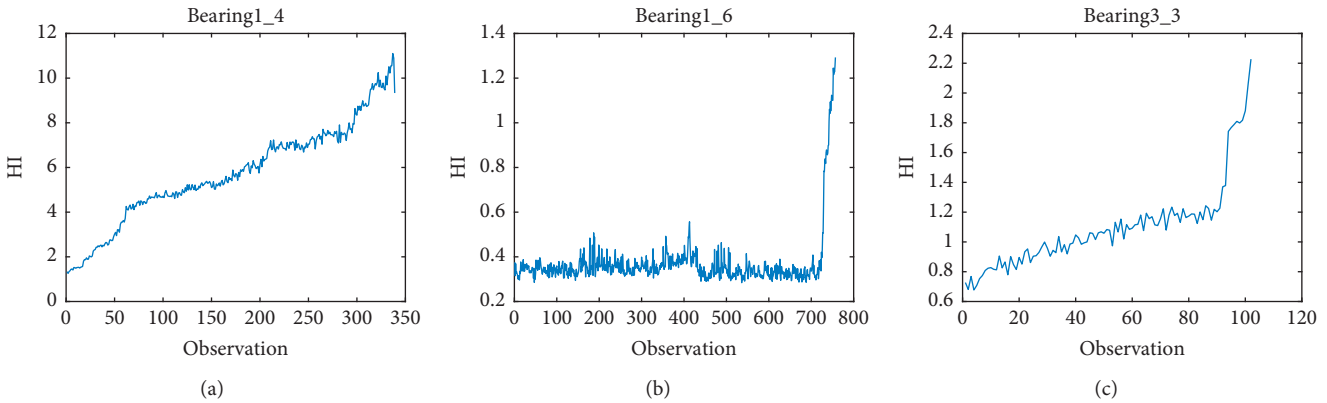

Figure 6: RMS in abnormal state. (a) Bearing 1_4. (b) Bearing 1_6. (c) Bearing 3_3.

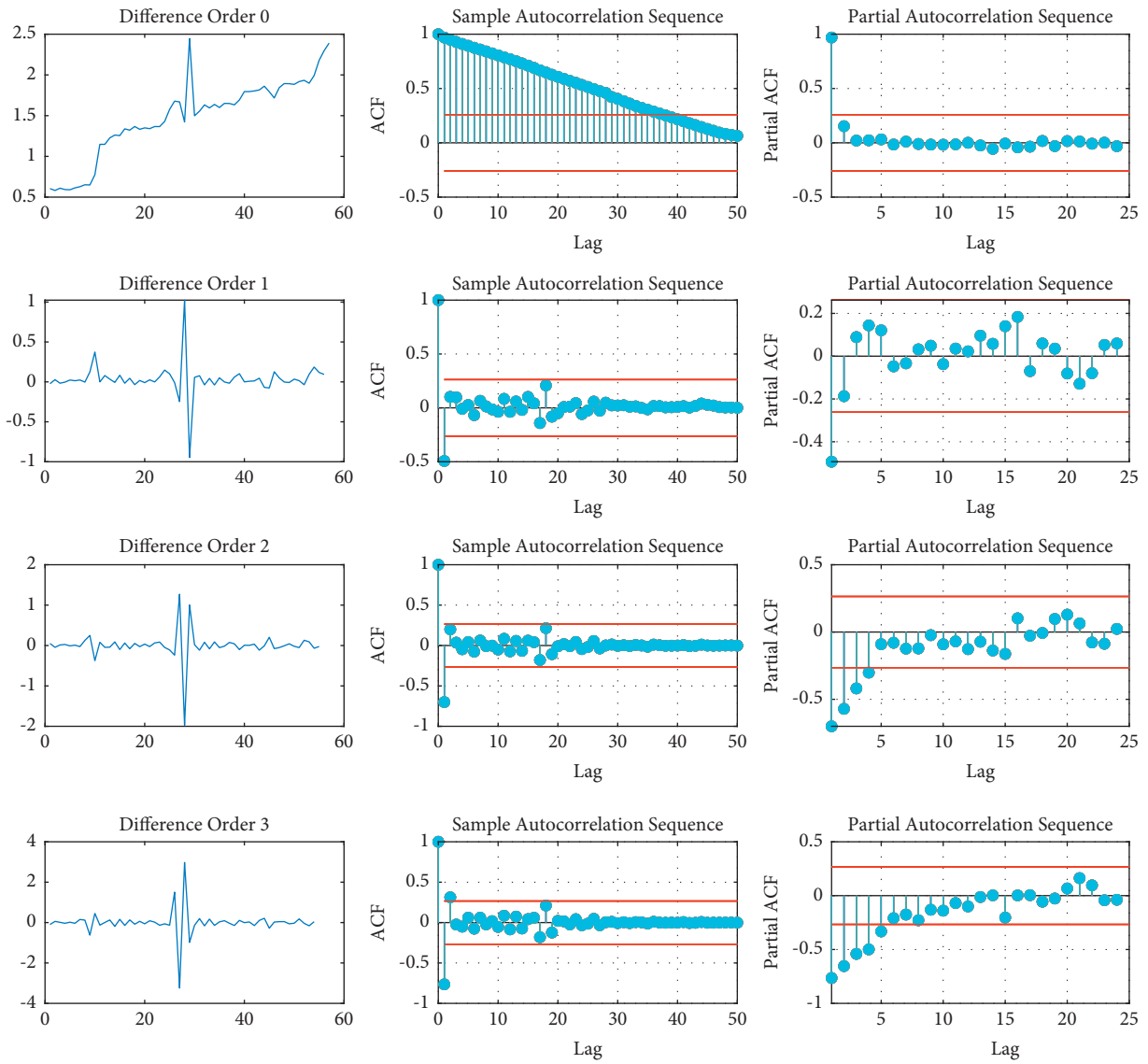

Figure 7: ACF analysis of bearing 1_7. From up to down: the 0,1,2,3 order difference of RMS.

Table 3: Parameters of ARIMA-R and algorithm associated.

ARIMA-R		Random forest and rotation forest		AdaBoost and Gradient Boost		ARNN	
p	20	Estimators	800	Estimators	200	Hidden layer	(10, 30)
q	20			Max depth	10	Activation	ReLU
d	2			Learning rate	0.2	Solver	Adam
r	2					Learning rate	Adaptive

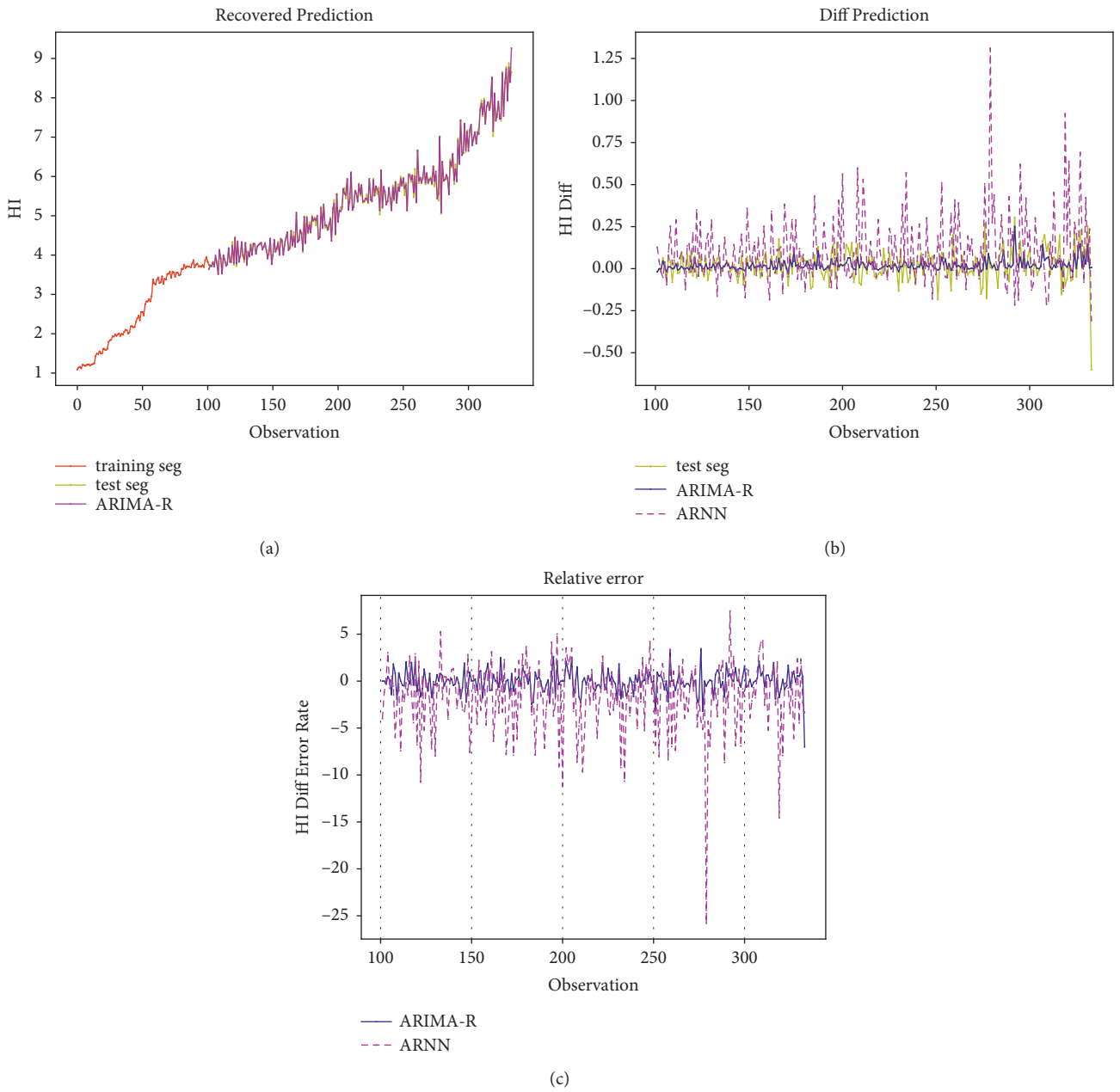

Figure 8: Single-step prediction of ARIMA-R and ARNN. (a) RMS. (b) Difference. (c) Error rate (%) of difference.

A rule similar to IEEE PHM 2012 Data Challenge is adopted. The data from bearing 1_3 to 1_7, 2_3 to 2_7, and 3_3 are taken as test data, in which only the given length of data is available, and the RUL at the end of test data is to be predicted.

As implied before, the proposed method is not fit to predict a long sequence directly. To compensate for this, a 2-order linear regression model based on ordinary least-squares (OLS), provided by scikit-learn [49], is used for initial prediction. The rotation forest regressor then modifies

Table 4: Single-step prediction of ARIMA-R and ARNN.

Algorithm	R	1_6		1_4		3_3	
		MSE	MAE	MSE	MAE	MSE	MAE
ARNN		3.58	53.30	**3.58**	53.30	2.57	45.08
ARIMA	1	1.60	30.15	3.91	55.23	**1.32**	**23.49**
ARIMA	2	**1.54**	**26.04**	5.21	**46.48**	2.57	30.91

Table 5: RMA method comparison.

Data	Algorithm		MSE	MAE	R^2	MAPE
1_4	ARNN	GBT	5.39	55.16	0.968	6.13
		ABT	8.95	72.25	0.990	1.70
		RF	3.91	55.23	0.991	1.57
	ARIMA-R	NN	4.84	64.57	0.993	1.37
		RTF	**3.58**	53.30	0.977	2.45
			5.21	**46.48**	**0.997**	**0.84**
1_6	ARNN	GBT	5.34	55.76	0.960	6.26
		ABT	2.01	30.68	0.977	4.79
		RF	1.60	30.15	0.985	3.63
	ARIMA-R	NN	1.60	31.69	0.986	3.64
		RTF	4.01	47.67	0.976	5.35
			1.54	**26.04**	**0.991**	**2.76**
3_3	ARNN	GBT	15.55	96.15	0.914	5.60
		ABT	4.55	48.25	0.975	2.58
		RF	4.15	43.91	0.977	2.29
	ARIMA-R	NN	4.00	41.64	0.978	2.17
		RTF	10.74	74.34	0.941	3.98
			2.57	**30.91**	**0.986**	**1.63**

Table 6: Prediction performance score comparison on the FEMTO dataset.

Dataset	Predicted RUL(s)	Authentic RUL(s)	Relative error (%)					
			A [51]	B [52]	C [53]	D [54]	E [50]	ARIMA-R
Bearing1_3	3973	5730	43.28	37	−1.04	−0.35	1.05	30.66
Bearing1_4	247	339	67.55	80	−20.94	5.6	20.35	27.14
Bearing1_5	1403	1610	−22.98	9	−278.26	100	11.18	12.85
Bearing1_6	1459	1460	21.23	−5	19.18	28.08	34.93	**0.05**
Bearing1_7	7338	7570	17.83	−2	−7.13	−19.55	29.19	**3.07**
Bearing2_3	4361	7530	37.84	64	10.49	−20.19	57.24	42.08
Bearing2_4	1302	1390	−19.42	10	51.8	8.63	−1.44	6.37
Bearing2_5	333	3090	54.37	−440	28.8	23.3	−0.65	89.23
Bearing2_6	822	1290	−13.95	49	−20.93	58.91	−42.64	36.30
Bearing2_7	349	580	−55.17	−317	44.83	5.17	8.62	39.86
Bearing3_3	589	820	3.66	90	−3.66	40.24	−1.22	28.17
Score	-	-	0.263	0.307	0.355	0.429	**0.569**	0.479

the prediction thereafter. The modification part is similar to the recurrent process in the proposed method. The prediction result is evaluated by the criterion introduced by [47], as depicted in the following equation:

$$\text{score} = \frac{1}{n}\sum_{i=1}^{n} e^{\ln(0.5)C_i\varepsilon_i}, \tag{18}$$

where ϵ_i is the ith relative error of predicted RUL in percentage and C_i is the coefficient that depends on ϵ_i:

$$C_i = \begin{cases} \dfrac{-1}{5}, & \epsilon_i \le 0, \\ \dfrac{1}{20}, & \epsilon_i > 0. \end{cases} \tag{19}$$

The result and criterion score are compared with results from previous research studies [50–54], as shown in Table 6. In the table, predicted RULs, authentic RULs of all test datasets, and relative errors in percentage are presented. The

score (18)of each group of predictions is shown at the bottom of the table.

We can see from the score that the proposed method has an advantage on method A-D, especially for data from bearing1_6 and bearing1_7. That is because, at the end of these datasets, the trend of sequence conforms with the weak stationarity requirement of ARIMA, e.g., the order stationarity. With such stationarity, ARIMA constructed from history observation can reflect the future closer. On the other side, bearing datasets 2_4 and 3_3 illustrate a clear situation transition during the final stage of degradation, and the predictions are far from the true RULs.

In fact, the basic assumption of ARIMA model includes certain types of stationarity on the series. Moreover, sufficient information on the history series is required to obtain a more accurate forecast. In the situation that the monitoring bearings are seriously damaged, neither stationarity nor information is sufficient. Thus, the prediction result is not only because of the predicting ability of the model itself but also due to the nonlinear component introduced by the machine learning method when the rotation forest is used to solve the model parameters.

According to the results, further analysis of the combination between the time series model represented by ARIMA and the machine learning algorithm will be important in the research hereafter.

5. Conclusion

An implementation method of approximating the ARIMA model with ML estimation is proposed in this paper, named ARIMA-R. The advantage of this method is that it does not need to calculate and predict the entire history of the training samples step by step to obtain the MA term of ARIMA model, so it is suitable for general nonrecursive ML methods. This method also adds feature terms to the ARNN model corresponding to moving average terms, improving the ability to describe RUL indicators. At the same time, the idea of using an ensemble regression tree algorithm, rotation forest, instead of ANN to find parameters is proposed to improve the predictive ability when the quantity of data is small. This modification is fit to the data accessibility in bearing HI prediction. The proposed ARIMA-R method combines ARIMA time series prediction model and ensemble regression trees and is used to predict bearing health indicators. The experimental results show that its prediction outperforms the ARNN algorithm. This method constructs the RMA quantity in an iterative way to replace the MA term in the ARIMA algorithm, which is the prediction error term. At the same time, it is proposed to use an ensemble tree instead of ANN in ARNN to improve the fitting ability of small sample training. Through this method, the major benefit is that the ARIMA model can be implemented more completely in the nonrecursive ML algorithm. Therefore, the ARIMA model and similar models such as ARMA, SARIMA, and FARIMA can be used to improve accuracy and efficiency of large-scale data fitting using ML. The further work can be included at the following three aspects. First, more samples can be used to verify the performance of the proposed method. Second, how to combine this method with other ML algorithms and life prediction frameworks is worth exploring. Third, it is meaningful that in-depth research of the relationship between preliminary estimation and the prediction results of the iterative model needs to be studied.

Data Availability

The datasets generated during and/or analysed during the current study are available in the NASA Prognostics Data Repository. URL: https://ti.arc.nasa.gov/tech/dash/groups/pcoe/prognostic-data-repository/#femto.

Conflicts of Interest

The authors declare that they have no conflicts of interest.

Acknowledgments

This work was funded in part by the Science and Technology Development Fund, Macau SAR (Nos. 0018/2 019/AKP, 0008/2 019/AGJ, FDCT/194/2 017/A3, and SKL-IOTSC-2018-2020), the University of Macau (Grant nos. MYRG2018-00 248-FST and MYRG2019-0137-FST), the Science Foundation of Henan University of Technology (Grant no. 2019BS004), the Cultivation Programme for Young Backbone Teachers in Henan University of Technology (Grant no. 21 420 171), the Natural Science Project of Henan Province (Grant no. 202 102 210 136), and the Key Laboratory of Grain Information Processing and Control, Ministry of Education, Henan University of Technology (Grant no. KFJJ-2016-110).

References

[1] M. Cerrada, R.-V. Sánchez, C. Li et al., "A review on data-driven fault severity assessment in rolling bearings," *Mechanical Systems and Signal Processing*, vol. 99, pp. 169–196, Jan. 2018.

[2] X.-B. Wang, Z.-X. Yang, and X.-A. Yan, "Novel particle swarm optimization-based variational mode decomposition method for the fault diagnosis of complex rotating machinery," *IEEE*, vol. 23, no. 1, pp. 68–79, 2017.

[3] Z.-X. Yang, X. Wang, and P. K. Wong, "Single and simultaneous fault diagnosis with application to a multistage gearbox: a versatile dual-elm network approach," *IEEE Transactions on Industrial Informatics*, vol. 14, no. 12, pp. 5245–5255, 2018.

[4] X.-B. Wang, L. Luo, L. Tang, and Z.-X. Yang, "Automatic representation and detection of fault bearings in in-wheel motors under variable load conditions," *Advanced Engineering Informatics*, vol. 49, Article ID 101321, 2021.

[5] Z.-X. Yang and P.-B. Zhang, ""Elm meets rae-elm: a hybrid intelligent model for multiple fault diagnosis and remaining useful life predication of rotating machinery," in *Proceedings of the 2016 International Joint Conference on Neural Networks (IJCNN)*, pp. 2321–2328, IEEE, Vancover, Canada, July 2016.

[6] J. Zhong, Z. Yang, and S. Wong, "Machine condition monitoring and fault diagnosis based on support vector machine," in *Proceedings of the 2010 IEEE International Conference on*

Industrial Engineering and Engineering Management, pp. 2228–2233, IEEE, Xiamen, China, October 2010.

[7] Y. Jiang, C. Li, Z. Yang, Y. Zhao, and X. Wang, "Remaining useful life estimation combining two-step maximal information coefficient and temporal convolutional network with attention mechanism," *IEEE Access*, vol. 9, pp. 16323–16336, 2021.

[8] G. Prakash, X.-X. Yuan, B. Hazra, and D. Mizutani, "Toward a big data-based approach: a review on degradation models for prognosis of critical infrastructure," *Journal of Nondestructive Evaluation, Diagnostics and Prognostics of Engineering Systems*, vol. 4, 2021.

[9] M. R. M. Akramin, M. S. Marizi, M. N. M. Husnain, and M. Shamil Shaari, "Analysis of surface crack using various crack growth models," *Journal of Physics: Conference Series*, vol. 1529, no. 4, Article ID 042074, 2020.

[10] T. E. Tallian and J. I. McCool, "An engineering model of spalling fatigue failure in rolling contact," *Wear*, vol. 17, no. 5-6, pp. 447–461, 1971.

[11] J. Liu, R. Pang, S. Ding, and X. Li, "Vibration analysis of a planetary gear with the flexible ring and planet bearing fault," *Measurement*, vol. 165, Article ID 108100, 2020.

[12] Y. Lei, N. Li, L. Guo, N. Li, T. Yan, and J. Lin, "Machinery health prognostics: a systematic review from data acquisition to RUL prediction," *Mechanical Systems and Signal Processing*, vol. 104, pp. 799–834, 2018.

[13] P. Liang, C. Deng, J. Wu, Z. Yang, J. Zhu, and Z. Zhang, "Single and simultaneous fault diagnosis of gearbox via a semi-supervised and high-accuracy adversarial learning framework," *Knowledge-Based Systems*, vol. 198, Article ID 105895, 2020.

[14] Z.-X. Yang, X.-B. Wang, and J.-H. Zhong, "Representational learning for fault diagnosis of wind turbine equipment: a multi-layered extreme learning machines approach," *Energies*, vol. 9, no. 6, p. 379, 2016.

[15] J.-H. Zhong, P. Wong, and Z.-X. Yang, "Simultaneous-fault diagnosis of gearboxes using probabilistic committee machine," *Sensors*, vol. 16, no. 2, p. 185, 2016.

[16] Z. Yang, P. K. Wong, C. M. Vong, J. Zhong, and J. Liang, "Simultaneous-fault diagnosis of gas turbine generator systems using a pairwise-coupled probabilistic classifier," *Mathematical Problems in Engineering*, vol. 2013, 2013.

[17] Z. Yang, W. I. Hoi, and J. Zhong, "Gearbox fault diagnosis based on artificial neural network and genetic algorithms," in *Proceedings of the 2011 International Conference on System Science and Engineering*, pp. 37–42, IEEE, Noida, India, December 2011.

[18] A. Tealab, "Time series forecasting using artificial neural networks methodologies: a systematic review," *Future Computing and Informatics Journal*, vol. 3, no. 2, pp. 334–340, 2018.

[19] P. Liang, C. Deng, J. Wu, G. Li, Z. Yang, and Y. Wang, "Intelligent fault diagnosis via semisupervised generative adversarial nets and wavelet transform," *IEEE Transactions on Instrumentation and Measurement*, vol. 69, no. 7, pp. 4659–4671, 2019.

[20] P. Liang, C. Deng, J. Wu, Z. Yang, J. Zhu, and Z. Zhang, "Compound fault diagnosis of gearboxes via multi-label convolutional neural network and wavelet transform," *Computers in Industry*, vol. 113, Article ID 103132, 2019.

[21] R. Hyndman and G. Athanasopoulos, *Arima Models," in Forecasting: Principles and Practice*, OTexts, Melbourne, Australia, 2nd edition, 2018.

[22] Y.-S. Lee and L.-I. Tong, "Forecasting time series using a methodology based on autoregressive integrated moving average and genetic programming," *Knowledge-Based Systems*, vol. 24, no. 1, pp. 66–72, Feb. 2011.

[23] Q. Li and S. Liang, "Degradation trend prediction for rotating machinery using long-range dependence and particle filter approach," *Algorithms*, vol. 11, no. 7, p. 89, 2018.

[24] A. Jimenez-Cortadi, F. Boto, I. Irigoien, B. Sierra, and G. Rodriguez, "Time series forecasting in turning processes using ARIMA model," in *Intelligent Distributed Computing XII*, J. Del Ser, E. Osaba, M. N. Bilbao, J. J. Sanchez-Medina, M. Vecchio, and X.-S. Yang, Eds., Springer International Publishing, New York, NY, USA, 2018.

[25] Q. Li, S. Liang, J. Yang, and B. Li, "Long range dependence prognostics for bearing vibration intensity chaotic time series," *Entropy*, vol. 18, no. 1, p. 23, 2016.

[26] G. Qiu, Y. Gu, and J. Chen, "Selective health indicator for bearings ensemble remaining useful life prediction with genetic algorithm and Weibull proportional hazards model," *Measurement*, vol. 150, Article ID 107097, 2020.

[27] J. T. Connor, R. D. Martin, and L. E. Atlas, "Recurrent neural networks and robust time series prediction," *IEEE Transactions on Neural Networks*, vol. 5, no. 2, pp. 240–254, 1994.

[28] R. Taherdangkoo, A. Tatomir, M. Taherdangkoo, P. Qiu, and M. Sauter, "Nonlinear autoregressive neural networks to predict hydraulic fracturing fluid leakage into shallow groundwater," *Water*, vol. 12, no. 3, p. 841, 2020.

[29] F. Pereira, F. Bezerra, S. Junior et al., "Nonlinear autoregressive neural network models for prediction of transformer oil-dissolved gas concentrations," *Energies*, vol. 11, no. 7, p. 1691, 2018.

[30] A. Fentis, L. Bahatti, M. Tabaa, and M. Mestari, "Short-term nonlinear autoregressive photovoltaic power forecasting using statistical learning approaches and in-situ observations," *International Journal of Energy and Environmental Engineering*, vol. 10, no. 2, pp. 189–206, 2019.

[31] L. Ruiz, M. Cuéllar, M. Calvo-Flores, and M. Jiménez, "An application of non-linear autoregressive neural networks to predict energy consumption in public buildings," *Energies*, vol. 9, no. 9, p. 684, 2016.

[32] M. R. Cogollo and J. D. Velasquez, "Are neural networks able to forecast nonlinear time series with moving average components?" *IEEE Latin America Transactions*, vol. 13, no. 7, pp. 2292–2300, 2015.

[33] A. N. Burgess and A.-P. N. Refenes, "Modelling non-linear moving average processes using neural networks with error feedback: an application to implied volatility forecasting," *Signal Processing*, vol. 74, no. 1, pp. 89–99, 1999.

[34] W. Waheeb, R. Ghazali, and H. Shah, ""Nonlinear autoregressive moving-average (NARMA) time series forecasting using neural networks," in *Proceedings of the 2019 International Conference on Computer and Information Sciences (ICCIS)*, pp. 1–5, Sakaka, Saudi Arabia, April 2019.

[35] C. Ordóñez, F. Sánchez Lasheras, J. Roca-Pardiñas, and F. J. d. C. Juez, "A hybrid ARIMA-SVM model for the study of the remaining useful life of aircraft engines," *Journal of Computational and Applied Mathematics*, vol. 346, pp. 184–191, 2019.

[36] I. Rojas, O. Valenzuela, F. Rojas et al., "Soft-computing techniques and ARMA model for time series prediction," *Neurocomputing*, vol. 71, no. 4-6, pp. 519–537, 2008.

[37] H. T. Pham, V. T. Tran, and B.-S. Yang, "A hybrid of nonlinear autoregressive model with exogenous input and autoregressive moving average model for long-term machine

state forecasting," *Expert Systems with Applications*, vol. 37, no. 4, pp. 3310–3317, 2010.

[38] G. E. P. Box, G. M. Jenkins, G. C. Reinsel, and G. M. Ljung, *Time Series Analysis: Forecasting and Control*, Wiley, Hoboken, NJ, USA, 5th edition, 2015.

[39] J. J. Rodriguez, L. I. Kuncheva, and C. J. Alonso, "Rotation forest: a new classifier ensemble method," *IEEE Transactions on Pattern Analysis and Machine Intelligence*, vol. 28, no. 10, pp. 1619–1630, 2006.

[40] C. Pardo, J. F. Diez-Pastor, C. García-Osorio, and J. J. Rodríguez, "Rotation forests for regression," *Applied Mathematics and Computation*, vol. 219, no. 19, pp. 9914–9924, 2013.

[41] A. Tealab, H. Hefny, and A. Badr, "Forecasting of nonlinear time series using ANN," *Future Computing and Informatics Journal*, vol. 2, no. 1, pp. 39–47, 2017.

[42] A. P. Dempster, N. M. Laird, and D. B. Rubin, "Maximum likelihood from incomplete data via theEMAlgorithm," *Journal of the Royal Statistical Society: Series B*, vol. 39, no. 1, pp. 1–22, 1977.

[43] I. T. Jolliffe and J. Cadima, "Principal component analysis: a review and recent developments," *Philosophical Transactions of the Royal Society A: Mathematical, Physical & Engineering Sciences*, vol. 374, no. 2065, Article ID 20150202, 2016.

[44] J. Franklin, "The elements of statistical learning: data mining, inference and prediction," *The Mathematical Intelligencer*, vol. 27, no. 2, pp. 83–85, 2005.

[45] V. B. Gavirangaswamy, G. Gupta, A. Gupta, and R. Agrawal, "Assessment of arima-based prediction techniques for road-traffic volume," in *Proceedings of the fifth international conference on management of emergent digital EcoSystems*, pp. 246–251, Neumünster Abbey, Luxembourg, October 2013.

[46] A. W. Bojanczyk, R. P. Brent, F. R. De Hoog, and D. R. Sweet, "On the stability of the bareiss and related toeplitz factorization algorithms," *SIAM Journal on Matrix Analysis and Applications*, vol. 16, no. 1, pp. 40–57, 1995.

[47] P. Nectoux, R. Gouriveau, K. Medjaher et al., ""PRONOSTIA: an experimental platform for bearings accelerated degradation tests," in *Proceedings of the IEEE International Conference on Prognostics and Health Management, PHM'12.*, pp. 1–8, IEEE Catalog Number: CPF12PHM-CDR, Denver, CO, USA, 2012.

[48] G. Aydemir and B. Acar, "Anomaly monitoring improves remaining useful life estimation of industrial machinery," *Journal of Manufacturing Systems*, vol. 56, pp. 463–469, 2020.

[49] F. Pedregosa, G. Varoquaux, A. Gramfort et al., "Scikit-learn: machine learning in Python," *Journal of Machine Learning Research*, vol. 12, pp. 2825–2830, 2011.

[50] Y. Yoo and J.-G. Baek, "A novel image feature for the remaining useful lifetime prediction of bearings based on continuous wavelet transform and convolutional neural network," *Applied Sciences*, vol. 8, no. 7, p. 1102, 2018.

[51] L. Guo, N. Li, F. Jia, Y. Lei, and J. Lin, "A recurrent neural network based health indicator for remaining useful life prediction of bearings," *Neurocomputing*, vol. 240, pp. 98–109, 2017.

[52] E. Sutrisno, H. Oh, A. S. S. Vasan, and M. Pecht, "Estimation of remaining useful life of ball bearings using data driven methodologies," in *Proceedings of the 2012 ieee conference on prognostics and health management*, pp. 1–7, IEEE, Hyatt Regency Minneapoli, September 2012.

[53] S. Hong, Z. Zhou, E. Zio, and K. Hong, "Condition assessment for the performance degradation of bearing based on a combinatorial feature extraction method," *Digital Signal Processing*, vol. 27, pp. 159–166, 2014.

[54] Y. Lei, N. Li, S. Gontarz, J. Lin, S. Radkowski, and J. Dybala, "A model-based method for remaining useful life prediction of machinery," *IEEE Transactions on Reliability*, vol. 65, no. 3, pp. 1314–1326, 2016.

Hindawi
Shock and Vibration
Volume 2022, Article ID 9970106, 14 pages
https://doi.org/10.1155/2022/9970106

Research Article

Application of Multichannel Active Vibration Control in a Multistage Gear Transmission System

Feng Zhang,[1] **Weihao Sun**,[1] **Chao Liu**,[2] **Hongchao Xiao**,[1] **and Yong Zhang**[1]

[1]*College of Mechanical Engineering and Automation, Huaqiao University, Xiamen, Fujian 361021, China*
[2]*State Key Laboratory of Ultra-Precision Machining Technology, Department of Industrial and Systems Engineering, The Hong Kong Polytechnic University, Hong Kong, China*

Correspondence should be addressed to Feng Zhang; zhangfeng@hqu.edu.cn

Received 12 March 2021; Revised 7 November 2021; Accepted 15 January 2022; Published 10 February 2022

Academic Editor: Xian-Bo Wang

Gears are the most important parts of rotating machinery and power transmission devices. When gears are engaged in meshing transmission, vibration will occur due to factors such as gear machining errors, meshing rigidity, and meshing impact. The traditional FxLMS algorithm, as a common active vibration algorithm, has been widely studied and applied in gear transmission system active vibration control in recent years. However, it is difficult to achieve good performance in convergence speed and convergence precision at the same time. This paper proposes a variable-step-size multichannel FxLMS algorithm based on the sampling function, which accelerates the convergence speed in the initial stage of iteration, improves the convergence accuracy in the steady-state adaptive stage, and makes the modified algorithm more robust. Simulations verify the effectiveness of the algorithm. An experimental platform for active vibration control of the secondary gear transmission system is built. A piezoelectric actuator is installed on an additional gear shaft to form an active structure and equipped with a signal acquisition system and a control system; the proposed variable-step-size multichannel FxLMS algorithm is experimentally verified. The experimental results show that the proposed multichannel variable-step-size FxLMS algorithm has more accurate convergence accuracy than the traditional FxLMS algorithm, and the convergence accuracy can be increased up to 123%.

1. Introduction

As a general-purpose part, gear is an important transmission device in various mechanical equipment systems and plays a very key role in equipment in machinery, transportation, chemical, aviation, aerospace, shipbuilding, and other industries. In actual applications, the gears inevitably have manufacturing and installation errors, and the gear teeth will deform under the action of the load. These errors and deformations destroy the meshing relationship of the gear transmission and make the position of the gear me\shing deviate from its theoretical position so that the instantaneous transmission ratio changes, causing the collision and impact between the teeth and forming the gear meshing. Internal excitation results in vibration and noise [1–4].

The vibration of the gear system will not only produce noise and lead to the instability of the transmission system, but also accelerate the fatigue damage of the transmission system and cause its failure and serious consequences [5]. For example, one of the main excitation sources of the helicopter body is the vibration from the transmission system [6]. Excessive vibration levels will cause discomfort to the crew, cause fatigue, affect work efficiency, and reduce the precision and reliability of precision instruments and weapon aiming systems, or even fail to work normally. Besides, vibration and noise will cause fatigue damage and damage to some components, which directly affects the flight reliability of the helicopter [7–9]. The problem of vibration and noise of a helicopter is more prominent than that of other aircraft. If part of the vibration and noise can be eliminated during the operation of the helicopter, it has important practical significance to ensure the flight safety of the helicopter and improve the ride comfort [10, 11].

For the study of the vibration of the gear transmission system, in 1967, British scholar H. Optiz published an article on the dynamic performance of spur gear and the helical gear. According to the mechanism of gear vibration and noise, it is concluded that the vibration of gearbox and noise is a function of gear transmission error and precision, and some valuable analysis curves are given. Since the mid-1970s, the research objects of many scholars are mainly flexible rotors under high speed, such as rotors on high-speed high-precision machine tools and centrifugal units, which are usually under supercritical speed. How to restrain the rotor vibration, prevent the overall instability, and ensure the safe operation of the rotor has become a key problem. In the aspect of active control actuator, electromagnetic bearing and electromagnetic damper are studied more. As early as 1980, Haberman and Brunet [12] studied the stiffness characteristics of electromagnetic bearing and proposed the "bathtub" shaped complex stiffness curve. Since then, most researchers have analyzed the supporting characteristics of the electromagnetic bearing system based on this. Zhang and Zhang [13] reviewed in detail the research progress of unbalanced control technology of electromagnetic bearing. Maslen et al. [14] made a comprehensive review and summary of the existing unbalanced vibration control methods and the latest research results in the field of electromagnetic bearing. Huang and Lin [15] used a fuzzy control method to conduct theoretical and experimental research on unbalanced vibration control of conical electromagnetic bearing. Jiang and Zmood [16] designed a controller based on H∞ for self-excitation and external interference. Electromagnetic dampers have the advantages of noncontact, no mechanical friction and wear, no lubrication, long service life, and controllable stiffness and damping. Kasarda et al. [17] applied the electromagnetic damper to the active control of subsynchronous resonance of high-speed single-disk rotor system, which reduced the resonance amplitude by 93%. Nonami et al. applied the electromagnetic damper to the vibration control of the flexible rotor shaft. The control signal of the damper was provided by the analog controller, which effectively reduced the resonance peak of the flexible rotor shaft. Elbuken et al. [18] applied the electromagnetic damper to the vibration control of the rotating suspension and effectively reduced the vibration of the rotating suspension by exerting control force on the rotating suspension through the electromagnetic damper. Using the idea of finite element model and considering the influence of meshing error, Guan et al. [19, 20] established the coupled vibration model of the gear transmission system with bending and torsion and deduced the transmission function of the vibration from the gear excitation to the gearbox body, which laid a foundation for the vibration control of the rear gear transmission system. According to the criteria of modal control force and energy consumption, Guan evaluated four different ways of actuator installation in gearbox vibration active control system. The results show that the actuator is connected by extra bearings on the shaft in the best way and is more convenient to install. In the research of gear vibration, many scholars [21–23] also adopt this actuator installation method.

Montague et al. [24] as early as the active control method used in gear vibration control in 1994, they adopt the method of feedforward control needed for the inhibition of gear vibration control was deduced, by manual adjustment of phase shift amplifier in the experiment to adjust the voltage signal of driving voltage actuator, experimental results show that the meshing frequency is 4500 Hz, with 75% of vibration attenuation. Subsequently, Sutton et al. [7] clamped the three magnetostrictive actuators on the support and controlled the vibration of the gear of the helicopter transmission in the frequency range of 250–1250 Hz to minimize the vibration kinetic energy of the supporting rod. Rebbechi et al. [25] adopt the feedforward controller to adjust the phase and amplitude of the control force to realize the vibration control of the gearbox box body. The experiment shows that the vibration at the meshing fundamental frequency, double frequency, and triple frequency of the gearbox and the radiation noise at the meshing fundamental frequency is greatly reduced. Chen and Brennan's [26] simple gear mesh model has set up the control needed to control the size of the torsional vibration being deduced, based on the nonlinear system design of the adaptive controller to control the harmonic frequency. The experiment showed that stiffness modulation factor is proportional to the load on the gear,and the torsional vibration damping is about 7 dB at meshing frequencies of 150–350 Hz. Guan et al. [27] proposed a direct hybrid adaptive control method based on the Lyapunov stability theorem to simultaneously adjust feedback gain and feedforward gain to control gear vibration, and the results showed that this method was not sensitive to gear meshing frequency error. Li et al. [28, 29] installed the actuator on the gear shaft with additional support bearings, combined with the phase-locked loop for frequency estimation of reference signals, and used the filtered LMS algorithm to control the gear vibration. After that, many scholars have improved the filtering LMS algorithm and applied it to active vibration control and achieved good control results [30–39]. Wu and Lin [40] used a digital processor (DSP) to combine three different control algorithms to form a hybrid controller to control the vibration of the gearbox, but it was too complex to be applied in practice. Li et al. [29], based on frequency estimation technology, presented an improved filtering LMS algorithm that is used to control the vibration of the gearbox. To avoid out-of-band overadjustment, an integrated adaptive linear enhancer is also used.

Most of the above researches on vibration control of gearbox adopt a single gear transmission system, so single-input and single-output control methods are adopted. In this paper, a two-stage gearbox is taken as the controlled object, and there is two gear meshing excitation in the system. To achieve global vibration suppression of the system, multiple sensors are needed to capture the dynamic vibration of the structure and multiple actuators to suppress the energy generated by excitation [41–43]. Therefore, this paper will adopt a multichannel control method [44, 45] to control the vibration of the two-stage gear transmission system actively. As a common model, the traditional FxLMS algorithm has been widely studied and applied in vibration control in

recent years, but it is difficult to achieve good performance in convergence speed and convergence accuracy. To solve the problems existing in traditional FxLMS algorithms, a multichannel FxLMS algorithm with variable step size is proposed in this paper. The algorithm accelerates the convergence speed in the initial stage of convergence, improves the convergence accuracy in the steady-state adaptive stage, and makes the system have certain robustness [46].

Traditional vibration control methods such as modal control, pole assignment, and optimal control are based on the precise model of controlled structure, but the gear transmission system is a vibration system with serious uncertainty and difficult to accurately model. It is difficult to design a steady feedback system to achieve the desired control performance by using traditional control methods. However, the adaptive control method is less dependent on prior knowledge and does not depend on specific models, so it is an ideal choice to apply the adaptive control method to the active control of gear vibration.

2. Establishment of the Two-Stage Transmission Gearbox Model

UG software can get different specifications of parts by modifying the parameters. It only needs to input some basic parameters of gears, such as tooth number, modulus, pressure angle, and tooth surface width. UG software can automatically generate the required gear model. This method can also be used for gear shaft and bearing, which greatly improves design efficiency. The main parameters of the gears in the gearbox are calculated by the formula derivation [47]. The basic data of gears are shown in Table 1.

The shaft is designed according to the size of the gear. The main radial size of the shaft is shown in Figure 1. Among them, (a) is the high-speed shaft and low-speed shaft; (b) is the intermediate shaft. The size of the box is determined according to the size of the shaft and the size of the gear. The internal size of the box is 282 mm × 135 mm × 270 mm. Use UG to generate a three-dimensional model according to the designed size, and the established three-dimensional model is shown in Figure 2. The motor is an adjustable speed motor, which can adjust the speed of the gearbox in a large range. The load is a magnetic powder brake; on the one hand, it can adjust the load, allowing a more comprehensive analysis of the dynamic characteristics of gear load. On the other hand, it could make gear mesh closer by applying a load. Due to gear wear and insufficient precision, there will be gaps between the gear components. Under low or light load conditions, the gear meshing may swing back and forth, which will have a certain impact on the acquired signal. This effect can be reduced by applying a load.

The details of the active control structure inside the gearbox are shown in Figure 3. The active control structure is composed of an actuator bracket, a piezoelectric actuator, an antiload bar, and a support bearing. The bottom of the bracket is bolted to the wall of the box, and one end of the actuator is clamped with the top sleeve. The other end of the actuator is connected with the antiload bar, and the antiload bar is fixed on the support bearing. The antiload bar is a slender shaft with a certain degree of flexibility for overload protection. Besides, to improve the control accuracy, the direction of the control force output of the piezoelectric ceramic actuator is parallel to the direction of the meshing line of the gear.

The 3D model of the two-stage gearbox was imported into ADAMS, and the virtual prototype model was constructed by adding constraints. The functional expression of contact force is

$$\mathrm{MAX}\left\{0, K\left(q_0 - q\right)^e - C \times \frac{dq}{dt} \times \mathrm{STEP}\left(q, q_0 - d, 1, q_0, 0\right)\right\}, \tag{1}$$

where K is the stiffness coefficient, q_0 is the reference collision distance of two contact objects, q is the actual collision distance of two contact objects, e is the index in the rigidity, C is the damping rate, and d is the distance that the damping rate reaches the maximum.

The gear is made of no. 45 steel, and the bearing is made of type 6003 deep groove ball bearing. For the contact collision between the gears, the contact collision parameters between the bearing ball and the inner and outer rings are set as shown in Table 2.

Add the constraints of each component, set the speed on the input shaft, and apply load on the output shaft, and the virtual prototype of the two-stage gear transmission system can be obtained, as shown in Figure 4.

To verify the usability of the virtual prototype and provide a theoretical basis for vibration active control joint simulation, dynamic simulation in ADAMS, first set the multistage gearbox virtual prototype input speed to 2540 rpm and the load to 1 N·m. At this time, the meshing fundamental frequency of low-speed shaft gear is 500 Hz, and that of high-speed shaft gear is 804 Hz. The simulation time is set as 0.5 s, and the simulation step length is 0.0001 for simulation verification. Figures 5(a)–5(d) show the vibration acceleration of the low-speed axis and the high-speed axis in the time domain and frequency domain, respectively.

3. Description of the Improved FxLMS Algorithm

3.1. Traditional FxLMS Algorithm. The online identification method of secondary channels is an additional random noise method first proposed by Eriksson and Allie [48], as shown in Figure 6. $P(n)$ is the transfer function from the primary source to the control point. $S(n)$ is a transfer function of the secondary path from the actuator to the control point and is a very complex electro-acoustic coupling system, which is mainly composed of D/A conversion, loudspeaker, secondary acoustic channel, and A/D conversion. $X(n)$ is the reference signal. $E(n)$ refers to the residual vibration response signal detected by the error sensor at the control point.

Random noise $v(n)$ is used as the input of the secondary channel adaptive online identification filter $S'(n)$. When the identification filter converges, $S'(n)$ can uniquely converge to $S(n)$. In the adaptive control process, $S'(n)$ can be used as an

Table 1: Gears at all levels.

Part name	Tooth number	Tooth surface width (mm)	Modulus (mm)	Pressure angle (°)
High-speed shaft gear	19	25	2.0	20
Low-speed shaft gear	35	25	2.0	20
Middle shaft big gear	37	20	2.0	20
Middle shaft small gear	23	30	2.0	20

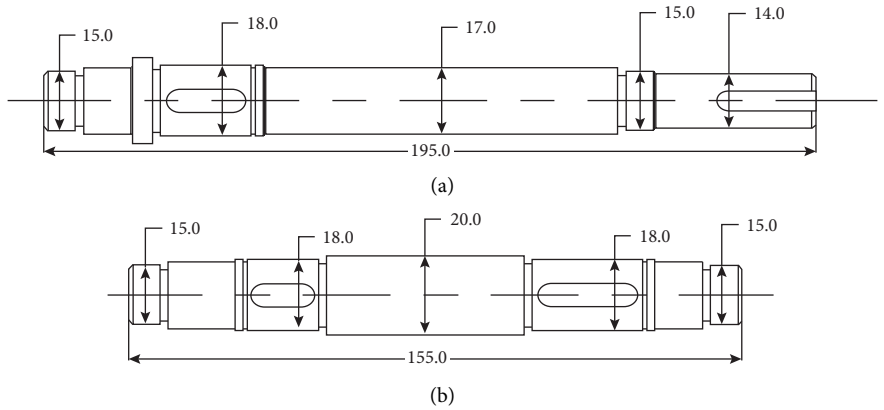

Figure 1: Dimension drawing of the shaft.

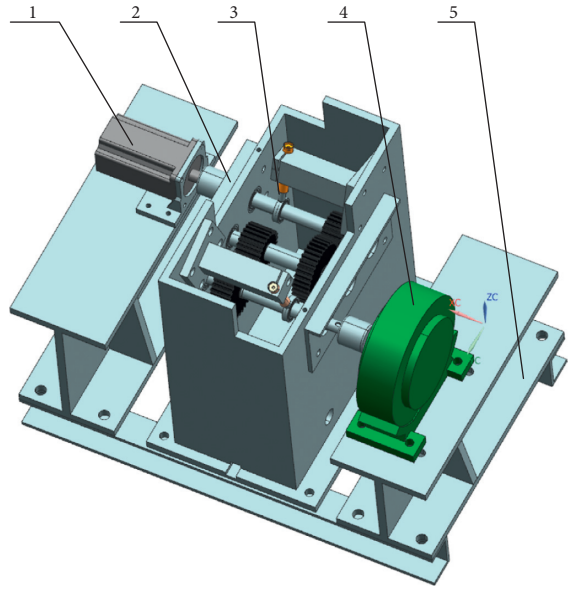

Figure 2: Gear transmission system with a built-in piezoelectric actuator. 1: motor, 2: gear box, 3: active control structure, 4: magnetic powder brake, and 5: base.

estimated transfer function of the secondary channel $S(n)$. However, this method will add random noise to the input of the actuator $y(n)$ and cause additional vibration of the control point through the secondary channel, and the vibration cannot be eliminated in the whole identification process of the secondary channel.

The calculation process of the algorithm is as follows:

$$\begin{aligned} \mathbf{e}(n) &= \mathbf{d}(n) + \mathbf{v}'(n) + y'(n), \\ \mathbf{e}_s &= \mathbf{e}(n) - \mathbf{v}(n) \times \mathbf{s}'(n). \end{aligned} \tag{2}$$

According to the LMS algorithm, the weight iteration of online identification of secondary channels can be expressed as

$$\mathbf{s}'(n+1) = \mathbf{s}'(n) + \mu_s \mathbf{v}(n)\mathbf{e}'(n), \tag{3}$$

where μ_s is the step size of filter $S'(n)$, and

$$\begin{aligned} \mathbf{s}'(n) &= [s_0, s_1, \ldots, s_{M-1}] \\ \mathbf{v}(n) &= [v(n), v(n-1), \ldots v(n-M+1)]^{\mathrm{T}}, \end{aligned} \tag{4}$$

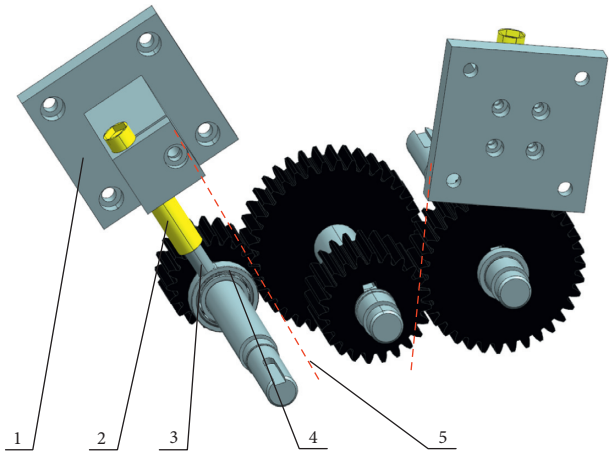

Figure 3: Internal details of active control structure. 1: actuator support, 2: piezoelectric actuator, 3: antiload rod, 4: support bearing, and 5: meshing line.

Table 2: Gears at all levels.

Part name	Gear	Ball bearing
Stiffness coefficient K	9.16×10^5 N/mm$^{3/2}$	1.644×10^5 N/mm$^{3/2}$
Stiffness force index e	1.5	1.5
Damping ratio C	30 N·S^{-1}/mm	30 N·S^{-1}/mm
The damping rate reaches the maximum distance	0.1 mm	0.05 mm
Coefficient of dynamic friction	0.05	0.0036
Coefficient of static friction	0.08	0.05

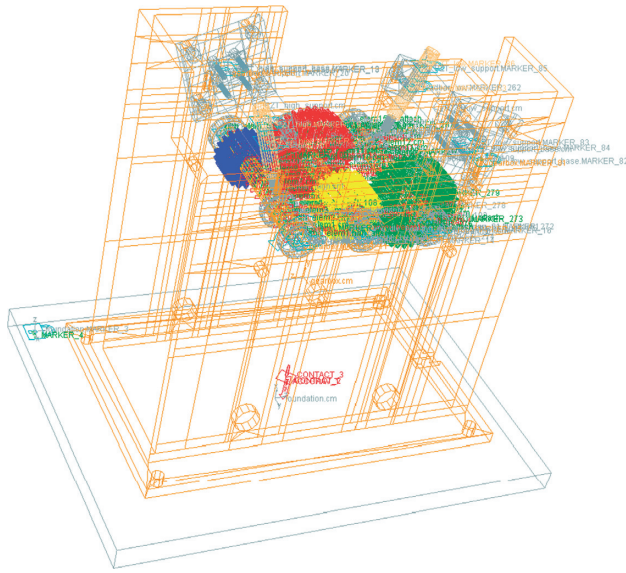

Figure 4: Overall diagram of the ADAMS virtual prototype.

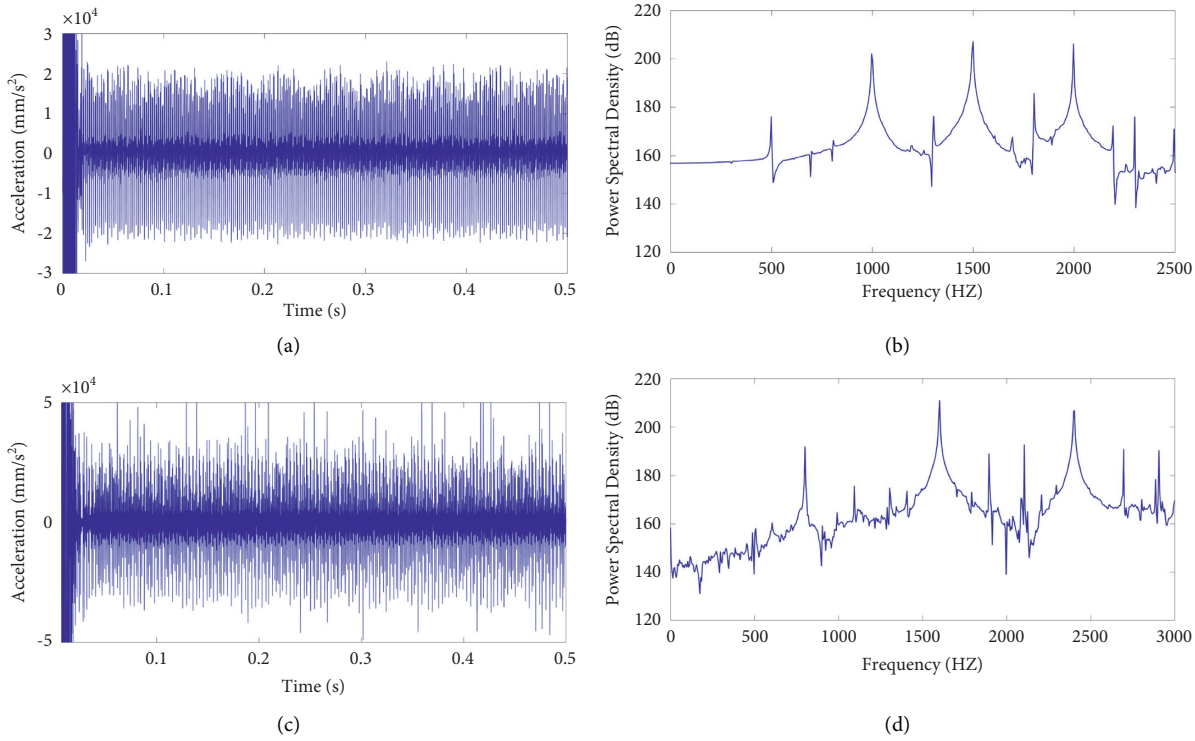

Figure 5: Diagram of vibration acceleration in the time domain and frequency domain. (a) Time domain and (b) frequency domain of the low-speed shaft gear. (c) Time domain and (d) frequency domain of the high-speed shaft gear.

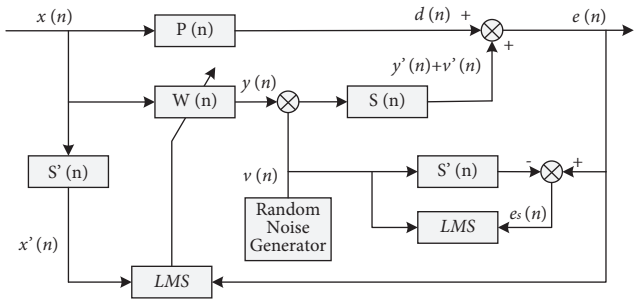

Figure 6: Eriksson's secondary channel flow diagram.

where M is the length of filter $S'(n)$.

At this time, the weight update of the FxLMS algorithm is expressed by the following formula:

$$\begin{aligned}\mathbf{w}(n+1) &= \mathbf{w}(n) + \mu \mathbf{x}'(n)\mathbf{e}(n)\\ \mathbf{w}(n) &= [w_0, w_1, \ldots w_{N-1}]^{\mathrm{T}}\\ \mathbf{x}'(n) &= [x'(n), x'(n-1), \ldots, x'(n-N+1)],\end{aligned} \tag{5}$$

where μ is the step size of the FxLMS algorithm and N is the length of the weight $W(n)$ of the FxLMS algorithm.

The traditional FxLMS algorithm updates iteratively with a fixed step size. When the step size factor is larger, the convergence rate is faster in the early stage, but in the steady-state adaptive stage, the step size is too large, and the oscillation occurs, resulting in a large error. On the contrary, when the step size factor is small, the steady-state error is small, but the convergence rate in the early stage will decrease greatly. Moreover, the traditional FxLMS algorithm mainly studies the single-channel problem. With the increasing degree of mechanical complexity, it is difficult to meet the control requirements of a single channel.

3.2. Improved Multichannel Variable-Step-Size FxLMS Algorithm. To solve the problem of the traditional fixed step size algorithm, many kinds of research have been made on the variable-step-size LMS algorithm. In this paper, three classical variable-step-size LMS are compared. Based on the variable-step-size LMS algorithm based on the sampling function, a certain change is made to the form of the variable-step-size LMS algorithm. In the case of little impact on the convergence rate, the steady-state error is smaller, and it has a better anti-interference ability.

The mechanism of variable-step-size LMS algorithm is a function model between step size factor and error. Three typical function models are as follows.

Step factor $\mu(n)$ is the Sigmoid function of error $e(n)$, as shown in the following equation:

$$\mu(n) = \alpha\left\{\frac{1}{1+e^{(-\beta|e(n)|)}} - 0.5\right\}. \tag{6}$$

Step factor $\mu(n)$ is the tongue function of error $e(n)$, as shown in the following equation:

$$\mu(n) = \alpha\left\{1 - \frac{1}{\beta e^2(n)+1}\right\}. \tag{7}$$

Step factor $\mu(n)$ is the sampling function of error $e(n)$, as shown in the following equation:

$$\mu(n) = \alpha\left\{1 - \frac{\sin(\beta \times e(n))}{\beta \times e(n)}\right\}, \tag{8}$$

where α and β take the same parameters as 4 and 8, respectively, to obtain the nonlinear curve of step factor and error signal of the above algorithm.

From Figure 7, we can see that compared with the sigmoid function and tongue function, the LMS algorithm based on the sampling function has a larger step size in the early stage, so its convergence rate is relatively fast. In the steady-state adaptive stage, the steady-state error is small because of the smaller $\mathrm{d}\mu/\mathrm{d}e(n)$ value. On this basis, the function is further improved.

$$\mu(n) = \alpha\left\{1 - \frac{\sin(\beta \times e(n) \times e(n-1))}{\beta \times e(n) \times e(n-1)}\right\}, \tag{9}$$

where the values of α and β are still 4 and 8; the curves are compared in Figure 8.

It can be seen from Figure 8 that the improved LMS algorithm based on sampling function does not reduce the step size significantly in the early stage but significantly reduces the step size in the steady-state adaptive stage, which will lead to a decrease in the convergence rate, but significantly improves the convergence accuracy. Moreover, the autocorrelation value $e(n) \times e(n-1)$ of the error signal is used to adjust the step factor in the functional relation between the step factor and the error so that the step factor has the anti-interference ability.

The iterative formula of the improved LMS adaptive algorithm based on the variable step size of the sampling function is as follows:

$$\begin{aligned} e(n) &= d(n) - X^T(n)W(n), \\ W(n+1) &= W(n) + 2\mu(n)e(n)X(n), \\ \mu(\mathrm{n}) &= \alpha\left\{1 - \frac{\sin(\beta \times e(n) \times e(n-1))}{\beta \times e(n) \times e(n-1)}\right\}. \end{aligned} \tag{10}$$

From (10), we can get

$$d(n) = X^T(n)W(n) + e(n). \tag{11}$$

According to the principle of adaptive filtering, the above equation can be rewritten as

$$d(n) = X^T(n)W^*(n) + v(n), \tag{12}$$

where $W^*(n)$ is the optimal weight coefficient of the filter, and the mean value of $v(n)$ is 0, which is unrelated to the input signal.

Substitute (12) into equation (10) to get

$$\begin{aligned} e(n) &= v(n) + X^T(n)W^*(n) - X^T(n)W(n) \\ &= v(n) + X^T(n)\left(W^*(n) - W(n)\right) \\ &= v(n) + X^T(n)\Delta W(n), \end{aligned} \tag{13}$$

where $\Delta W(n)$ is the weight coefficient deviation.

So, we get

$$\begin{aligned} e(n)e(n-1) = {} & v(n)v(n-1) + v(n)X^T(n-1)\Delta W(n-1) \\ & + X^T(n)\Delta W(n)v(n-1) \\ & + X^T(n)\Delta W(n)X^T(n-1)\Delta W(n-1). \end{aligned} \tag{14}$$

According to the fact that $v(n)$ is a Gaussian white noise signal, its correlation is poor, that is, $E[v(n)v(n-1)] = 0$, and is not related to the input signal $X(n)$, the following can be obtained:

$$E[e(n)e(n-1)] = E\left[X^T(n)\Delta W(n)X^T(n-1)\Delta W(n-1)\right]. \tag{15}$$

From equation (15), we can see that in the function of step factor and error signal obtained by the improved LMS adaptive algorithm based on variable step size of sampling function, the influence of noise signal is eliminated, so the algorithm is not affected by noise signal and has a strong anti-interference ability.

The improved LMS algorithm is applied to the multichannel active vibration control system. The improved FxLMS algorithm is the multichannel variable step size FxLMS algorithm. The schematic diagram of the active control structure is shown in Figure 9, where $x(n)$ represents the reference signal, S represents the secondary channel between all actuators and sensors, W represents the channel variable step FxLMS algorithm controller in the multichannel vibration control system, and V represents the white noise output to the secondary channel. Suppose the system has J active controllers, K sensors, the reference signal is written as $x(n)$, and the FxLMS controller W is written as

$$W = \left[w_1, w_2, \ldots, w_j\right]^T, \tag{16}$$

where w_j is the weight vector of the jth controller, which is to write the ownership value coefficient in the FxLMS algorithm as a weight vector.

The multichannel active vibration control system has $J \times K$ secondary channels; secondary channel S can be written as

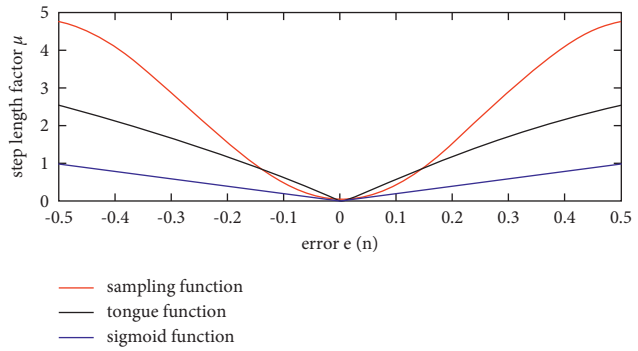

Figure 7: Step factor and error signal curve contrast diagram.

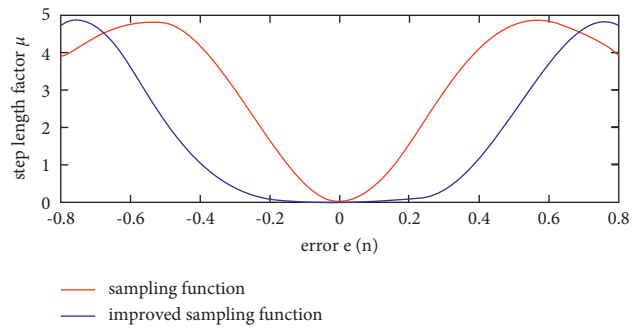

Figure 8: Comparison diagram of sample function curve and improved sample function curve.

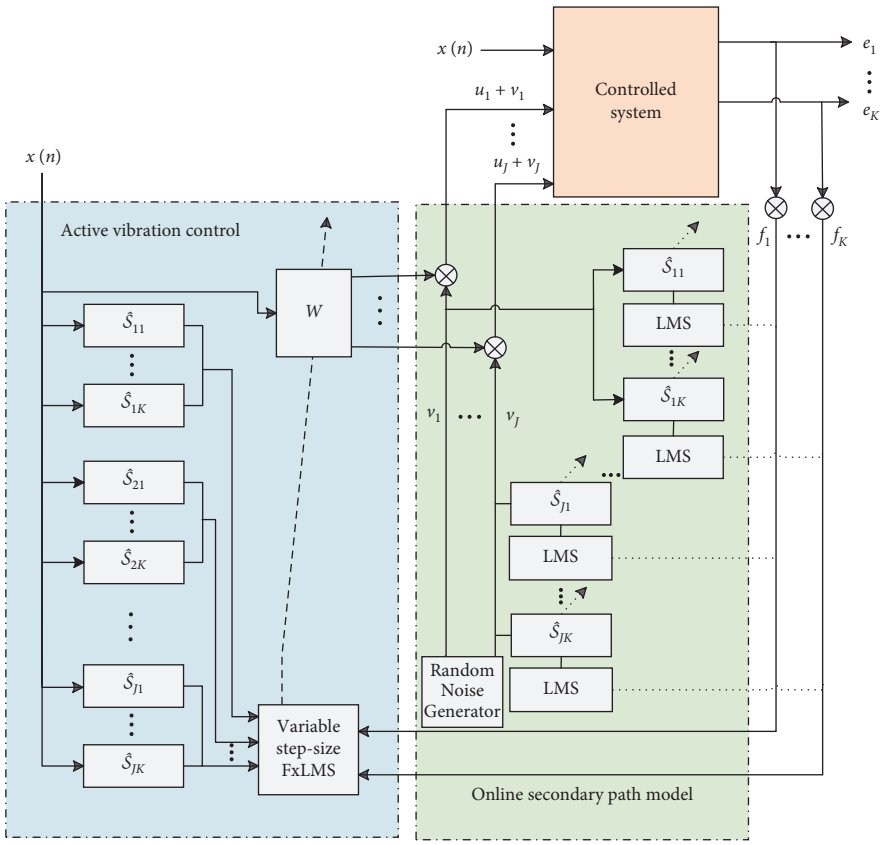

Figure 9: Multichannel variable-step-size FxLMS algorithm active vibration control structure.

$$S(n) = \begin{bmatrix} s_{11}(n) & \cdots & s_{1K}(n) \\ \vdots & \ddots & \vdots \\ s_{J1}(n) & \cdots & s_{JK}(n) \end{bmatrix}, \quad (17)$$

where $s_{JK}(n)$ represents the secondary channel between the jth active actuator and the kth sensor. $s'_{JK}(n)$ represents the filter coefficient identified using the secondary channel between the jth active actuator and the kth sensor.

4. The Cosimulation

Combined with the multichannel FxLMS algorithm structure in Figure 10 and the active control structure of the two-stage gearbox in Figure 2, the active vibration control system of the gearbox is designed as shown in Figure 10 below. The vibration caused by excitation and the gear pair is the control target. $S_1(z)$ and $S_2(z)$, respectively, represent two secondary channels. To eliminate the influence of secondary channels, corresponding models $\widehat{S}_1(z)$ and $\widehat{S}_2(z)$ are introduced into the control system to filter the input signals of the controller. In adaptive active vibration control, the selection of reference signals has a great influence on the control effect. To obtain the reference signals with high correlation with the vibration of the gear system, the frequency estimation of the vibration signals collected in real time is carried out through the second-order IIR adaptive notch filter [49] to obtain the meshing frequency of the gear pair and then synthesize the reference signals online.

Through simulation, the effectiveness of the improved FxLMS algorithm in the application of two-gearbox vibration active control is verified. In Simulink to build vibration active control system, its core is the improved FxLMS adaptive filter, due to the multiple-input multiple-output filter, the Level-2 function improved FxLMS algorithm, the adaptive trap of reference signal synthesizer using the same Level-2 function to carry on the design, use of FIR filter structure simulation of the secondary channel, connect the controller, the reference signal synthesizer, and the secondary channel model, and get the vibration active control system. The virtual prototype model of the gear transmission system in ADAMS was imported into Simulink as a mechanical module, which was connected with the control system to obtain the active vibration control cosimulation model of gear transmission integrated with the mechanical system and the control system, as shown in Figure 11.

The input speed of the gearbox is 2540 rpm. The meshing frequency of the high-speed shaft gear pair is 800 Hz and the meshing frequency of the low-speed shaft gear pair is 500 Hz. The load is 1 N·m. Set the simulation parameters as follows: the adaptive filter order as the controller is set to 80, the step size factor of the algorithm adopts the variable-step-length factor based on the sampling function, and the sampling frequency is selected as 10 kHz. Joint simulation is carried out, and the simulation results are shown in Figure 12.

Figures 12(a) and 12(c) show that compared with the traditional FxLMS algorithm, the improved FxLMS algorithm has a faster convergence rate and a smaller steady-state error. In Figure 12(a), the FxLMS control system reaches stability after about 0.15 s, while the improved FxLMS control system reaches stability after about 0.07 s. In Figure 12(c), the FxLMS control system reaches stability after about 0.12 s, while the improved FxLMS control system reaches stability after about 0.08 s. Moreover, it can be seen from Figures 12(a) and 12(c) that the improved FxLMS control system has a smaller vibration acceleration after stabilization is achieved.

Figures 12(b) and 12(d) show that the suppression of vibration by the active vibration control system is mainly at the 2nd and 3rd harmonics. In Figure 12(b), the vibration reduction of the FxLMS control system at the 2nd harmonic 1000 Hz and the 3rd harmonic 1500 Hz is 10 dB and 14 dB, respectively. The vibration reduction of the improved FxLMS control system at 1000 Hz and 1500 Hz is 23 dB and 31 dB, respectively. In Figure 12(d), the vibration reduction of the FxLMS control system at 1608 Hz and 2412 Hz of the second- and third-order harmonics is 17 dB and 28 dB, respectively. The vibration reduction of the improved FxLMS control system at 1608 Hz and 2412 Hz is 24 dB and 37 dB, respectively. It is further proved that compared with the traditional FxLMS algorithm, the improved FxLMS algorithm has a smaller steady-state error.

5. Design and Verification of Experiments

The experimental platform of the active vibration control system of the gearbox system can be divided into three parts, namely, the gear transmission system, the vibration measurement processing system, and the active control system. The established platform is shown in Figure 13.

The gear transmission system consists of a DC motor, motor governor, coupling, gear transmission part, and magnetic powder brake. The gear transmission part is composed of two pairs of meshing gears, the modulus is 2, the pressure angle is 20°, the number of teeth of high-speed shaft meshing gear is 19 and 37, respectively, and the number of teeth of low-speed shaft meshing gear is 23 and 35. Adjustable speed motor speed range is of 0–1800 rpm. The two couplings are, respectively, connected with the motor and the high-speed shaft, the magnetic powder brake, and the low-speed shaft. Magnetic powder brake can provide 0–15 N·m torque.

The vibration measurement processing systemis used to detect the vibration signal of the gearbox and the error signalinput to the controller. The acceleration sensor is used to collect the signalof the casing, and the collected signal is displayed in real time with theanalysis software DASP-V11 and is input to the controller as a calculatederror signal to calculate and output the control signal.

The active control system includes a controller, a piezoelectric actuator, a piezoelectric actuator power supply, and an actuator clamp. For the control system, this paper selects the Speedgoat real-time simulation system as the control system of active vibration control and establishes a semiphysical simulation control platform. The Speedgoat real-time simulation system provides a MATLAB/Simulink driver module that converts the algorithm control system

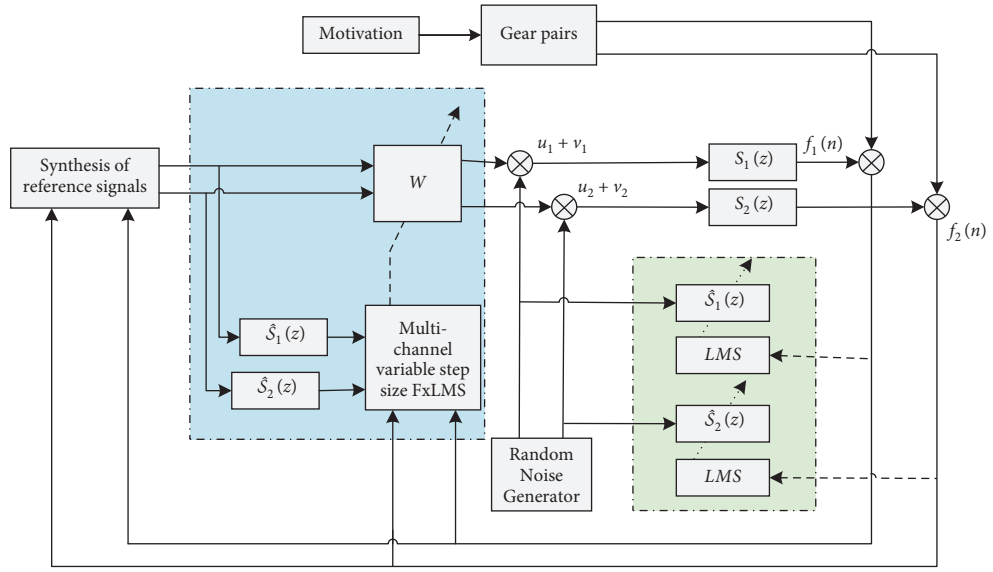

Figure 10: Multiharmonic vibration active control of the two-stage gear transmission system.

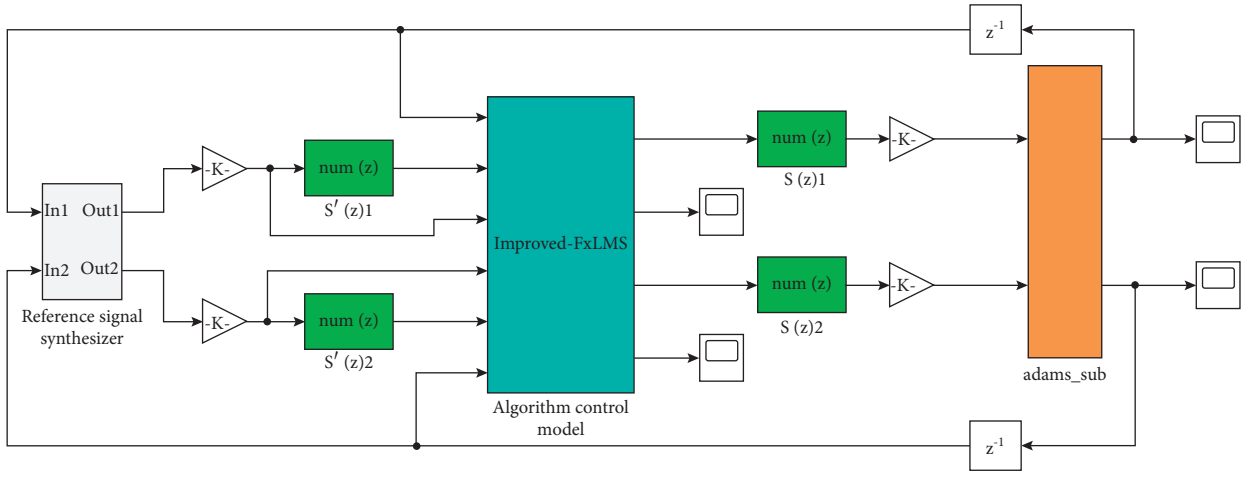

Figure 11: Active vibration control joint simulation system of the gearbox.

established on Simulink into the required C code and transmits the generated object code to the processor, which calculates the voltage signal of the piezoelectric actuator and controls the piezoelectric actuator.

To verify the effectiveness of the proposed multichannel active vibration control structure for the vibration control of the gear transmission system, the proposed active control algorithm was programmed, compiled, and downloaded to the real-time target machine as the controller of the active control system on the MATLAB/Simulink platform, and the multichannel variable-step-size FxLMS algorithm was adopted in this paper. To ensure the effectiveness of the control system, the sampling time of the controller is set to 0.0001 s. The motor speed was adjusted to 1200 rpm, the load was adjusted to 1 NM, and the active vibration control was started. The vibration signals of the gearbox body were collected through the acceleration sensor, as shown in Figure 14. The vibration signals before and after the control were Fourier transformed to obtain the vibration frequency domain control diagram, which was compared with the traditional FxLMS algorithm, as shown in Figure 15. The meshing fundamental frequencies of the low-speed shaft and high-speed shaft are 236 Hz and 380 Hz, respectively.

It can be seen from the time-domain diagram of vibration control in Figure 14 that the vibration attenuation begins at 8 s when the control begins, and the convergence is completed at the 12th second, and the vibration attenuation reaches 70% before the control. As can be seen from the local enlargement of Figure 15, the control effect is obvious at the basic frequency and multiple frequencies of gear meshing. The specific meshing frequency data is shown in Table 3 below. It can be seen from Table 3 that the decay of the meshing frequency of the low-speed shaft is about 3-4 dB, and that of the high-speed shaft is 3–5.5 dB. According to the data in Table 3, it can be calculated that the convergence accuracy has increased by 23%–82%.

When the speed is adjusted to 1530 rpm, the meshing fundamental frequency of the low-speed shaft and high-

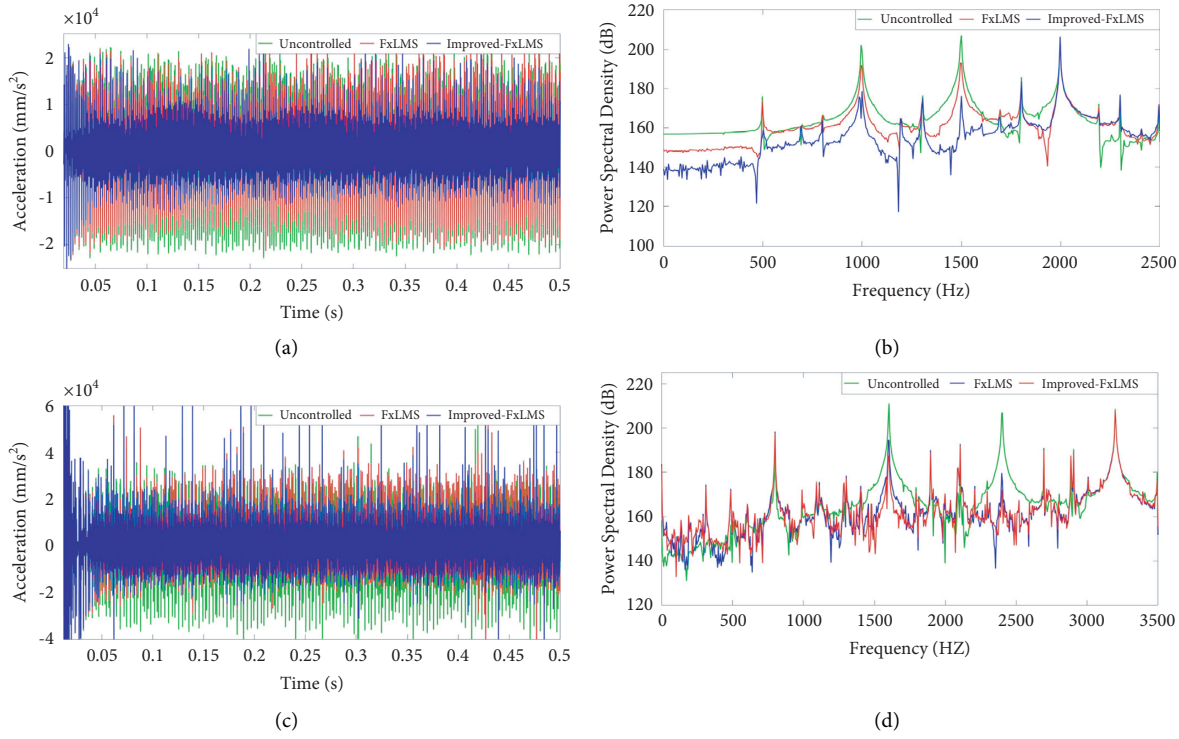

Figure 12: Simulation results of active vibration control. (a) Low-speed shaft time domain, (b) low-speed frequency time domain, (c) high-speed shaft time domain, and (d) high-speed frequency time domain.

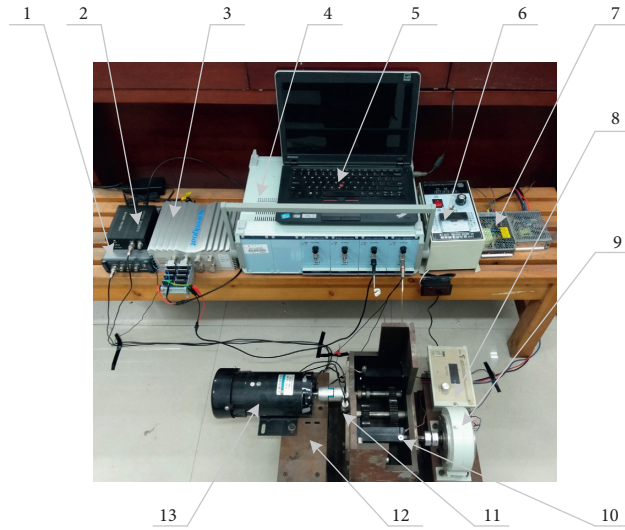

Figure 13: Active control test platform for the vibration of the gear transmission system. 1: signal collector, 2: signal conditioner, 3: controller, 4: power amplifier, 5: PC, 6: motor, 7: power, 8: torque adjuster, 9: magnetic powder, 10: piezoelectric actuator, 11: acceleration sensor, 12: multistage gear transmission system, and 13: adjustable speed motor.

speed shaft is 301 Hz and 485 Hz, respectively. The vibration generated by the gear transmission system is controlled, and the control frequency domain curve is shown in Figure 16. It can be seen from the figure that the attenuation at low-speed shaft meshing frequency is 4.5-5 dB, and the vibration attenuation at high-speed shaft meshing frequency is about 8-9 dB. The specific meshing frequency data is shown in Table 4. According to the data in Table 4, it can be calculated that the convergence accuracy has increased by 36%–123%.

Based on the active vibration control results of the gear under two rotating speeds, we can know that the proposed multichannel variable-step-size FxLMS algorithm has an effective suppression effect on the vibration at the high harmonic in the gear transmission system, and the vibration attenuation range is 3–9 dB. It can be seen that the attenuation of the meshing frequency of the high-speed shaft is higher than that of the low-speed shaft. Compared with the traditional FxLMS algorithm, the proposed multichannel

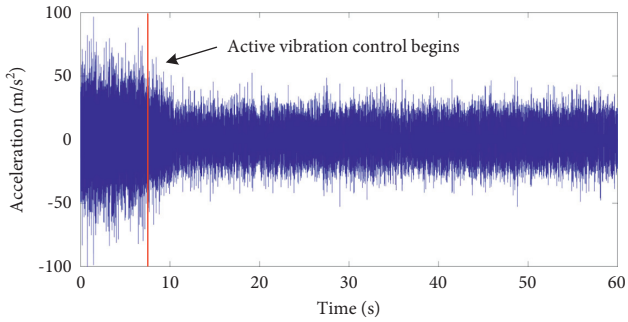

Figure 14: Time-domain control of vibration at 1200 rpm.

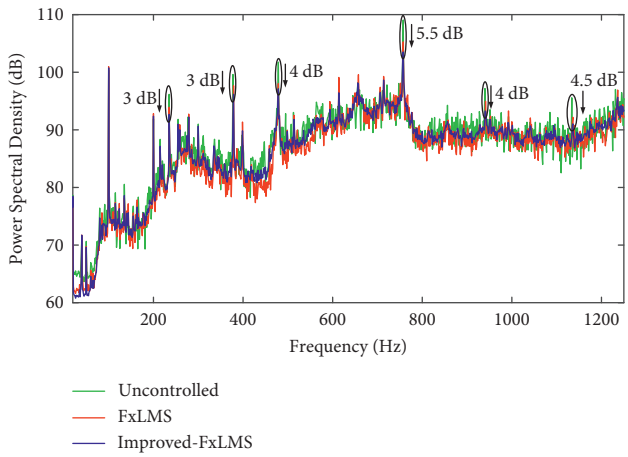

Figure 15: Vibration frequency domain control diagram at 1200 rpm.

Table 3: Active vibration control of the gear system at 1200 r/min and 1 N m.

Frequency/Hz	Power spectral density (dB)		
	Uncontrolled	FxLMS	Improved FxLMS
236	96.17	93.92	92.68
380	99.60	97.66	96.28
473	101.75	98.00	97.12
760	109.07	105.27	103.51
940	97.17	94.96	93.14
1140	95.57	92.18	91.04

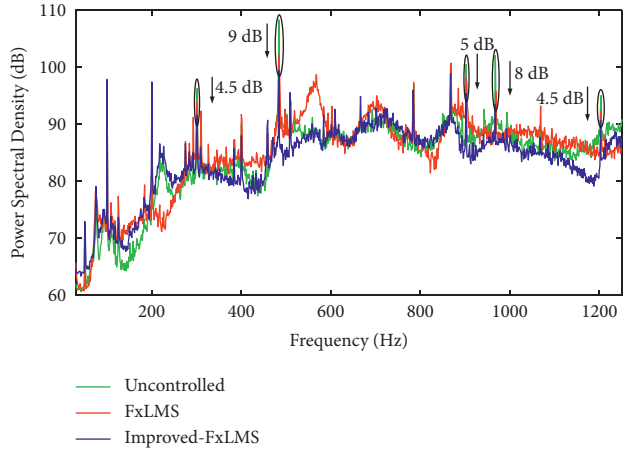

Figure 16: Vibration frequency domain control diagram at 1530 rpm.

Table 4: Active vibration control of the gear system at 1530 r/min and 1 N m.

Frequency (Hz)	Power spectral density (dB)		
	Uncontrolled	FxLMS	Improved FxLMS
301	96.27	93.82	91.54
485	108.32	102.11	99.42
902	100.46	98.20	95.42
970	102.03	95.77	93.48
1203	95.03	92.32	90.65

variable-step-size FxLMS algorithm has a better control effect. The control accuracy can be increased up to 123%.

6. Conclusion

In this paper, a novel active vibration control platform based on a piezoelectric actuator is constructed, which is composed of hardware and software such as a two-stage transmission device, control system, signal acquisition, and processing system. The multichannel variable-step-size FxLMS algorithm is used as the controller to control the vibration of the gearbox. Experimental results show that the multichannel variable-step-size FxLMS algorithm is effective for vibration control of the gear system, and its control effect is better than the traditional FxLMS control, which can reduce the vibration by 3–9 dB at the target. The control accuracy is improved by 23%–123%.

Data Availability

The data used to support the findings of this study are available from the corresponding author upon request.

Conflicts of Interest

The authors declare that they have no conflicts of interest regarding the publication of this paper.

Acknowledgments

This work was supported by China National Natural Science Funds (51405169) and the Fundamental Research Funds for the Central Universities (no. ZQN-704).

References

[1] J. Zhou, "Study on the influence of speed and load on the vibration and noise of reducer," *Vibration and Shock*, vol. 32, no. 8, pp. 193–198, 2013.

[2] M. Slim Abbes, S. Bouaziz, F. Chaari, M. Maatar, and M. Haddar, "An acoustic-structural interaction modelling for the evaluation of a gearbox-radiated noise," *International Journal of Mechanical Sciences*, vol. 50, no. 3, pp. 569–577, 2008.

[3] A. Farshidianfar and A. Saghafi, "Global bifurcation and chaos analysis in nonlinear vibration of spur gear systems," *Nonlinear Dynamics*, vol. 75, no. 4, pp. 783–806, 2014.

[4] L. L. Zhang, R. P. Zhu, G. H. Jin, L. F. Jia, and J. S. Shen, "Vibration and noise analysis of internal excitations of single pair of gears," *Journal of Vibration Engineering*, vol. 27, no. 6, pp. 915–919, 2014.

[5] J. Wang, H. Xiao, Y. Lv, T. Wang, and Z. Xu, "Detrended fluctuation analysis and hough transform based self-adaptation double-scale feature extraction of gear vibration signals," *Shock and Vibration*, vol. 2016, no. 4, 9 pages, Article ID 3409897, 2016.

[6] R. Liu, "Study on vibration fault of gear," *Journal of China Safety Science*, vol. 15, no. 2, pp. 16–18, 2005.

[7] T. J. Sutton, S. J. Elliott, M. J. Brennan, K. H. Heron, and D. A. C. Jessop, "Active isolation OF multiple structural waves ON a helicopter gearbox support strut," *Journal of Sound and Vibration*, vol. 205, no. 1, pp. 81–101, 1997.

[8] R. Maier, M. Pucher, W. Gembler, and H. Schweitzer, "Helicopter interior Noise Reduction by Active Vibration Isolation with Smart Gearbox Struts," in *Proceedings of the INTER-NOISE and NOISE-CON Congress and Conference Proceedings*, Lauderdale, FL, USA, January 1999.

[9] I. Pelinescu and B. Balachandran, "Analytical and Experimental Investigations into Active Control of Wave Transmission through Gearbox Struts," *Smart Structures and Materials*, vol. 3985, 2000.

[10] L. Bouillaut and M. Sidahmed, "Cyclostationary approach and bilinear approach: comparison, applications to early diagnosis for helicopter gearbox and classification method based on hocs," *Mechanical Systems and Signal Processing*, vol. 15, no. 5, pp. 923–943, 2001.

[11] S. V. Neriya, R. B. Bhat, and T. S. Sankar, "On the dynamic response of a helical geared system subjected to a static transmission error in the form of deterministic and filtered white noise inputs," *Journal of Vibration and Acoustics*, vol. 110, no. 4, pp. 501–506, 1988.

[12] H. Habermann and B. Brunet, "An active magnetic bearing system," *Tribology International*, vol. 13, 1980.

[13] K. Zhang and X. Zhang, "A review of unbalance control technology of active magnetic bearings," *Chinese Journal of Construction Machinery*, vol. 21, no. 8, pp. 897–903, 2010.

[14] E. H. Maslen, G. Schweitzer, H. Bleuler, M. Cole, and P. Keogh, *Magnetic Bearings—Theory, Design and Application to Rotating Machinery*, Springer, New York, NY, USA, 2009.

[15] S.-J. Huang and L.-C. Lin, "Fuzzy dynamic output feedback control with adaptive rotor imbalance compensation for magnetic bearing systems," *IEEE Transactions on Systems, Man and Cybernetics, Part B (Cybernetics)*, vol. 34, no. 4, pp. 1854–1864, 2004.

[16] Y. Jiang and R. B. H. Zmood, "Infinity control of magnetic bearings to ensure both system and external periodic disturbance robustness," in *Proceedings of the 3rd International Symposium on Magnetic Suspension Technology*, Washington, D.C, USA, December 1996.

[17] M. E. F. Kasarda, H. Mendoza, R. G. Kirk, and A. Wicks, "Reduction of subsynchronous vibrations in a single-disk rotor using an active magnetic damper," *Mechanics Research Communications*, vol. 31, no. 6, pp. 689–695, 2004.

[18] C. Elbuken, M. B. Khamesee, and M. Yavuz, "Eddy current damping for magnetic levitation: downscaling from macro- to micro-levitation," *Journal of Physics D: Applied Physics*, vol. 39, no. 18, pp. 3932–3938, 2006.

[19] Y. H. Guan, M. Li, T. C. Lim, and W. S. Shepard, "Comparative analysis of actuator concepts for active gear pair vibration control," *Journal of Sound and Vibration*, vol. 269, no. 1-2, pp. 273–294, 2004.

[20] Y. Guan, M. Li, T. C. Lim, and W. Shepard, "Comparison of actuator designs for active vibration control of a gear pair

system," in *Proceedings of the SPIE - The International Society for Optical Engineering*, vol. 4693, no. 7, pp. 529–532, San Jose, CA, USA, January 2002.

[21] Y. N. Li, F. Zhang, Q. Z. Ding, and L. Wang, "The active control method and experimental study of gear meshing vibration," *Journal of Vibration Engineering*, vol. 27, no. 2, pp. 61–67, 2014.

[22] F. Zhang, H. Y. Li, and H. Wang, *The Multi - Stage Gear Vibration Control Is Based on Adaptive Fuzzy PID Control*, Journal of Huaqiao University, no. 5, Xiamen, China, 2017.

[23] Y. N. Li, F. Zhang, L. Wang, and Q. Z. Ding, "Active control of gear meshing vibration identified on line in secondary channel," *Journal of Vibration and Shock*, vol. 32, no. 16, pp. 7–12, 2013.

[24] G. T. Montague, A. F. Kascak, A. Palazzolo, D. Manchala, and E. Thomas, "Feed-forward control of gear mesh vibration using piezoelectric actuators," *Shock and Vibration*, vol. 1, no. 5, 1994.

[25] B. Rebbechi, C. Howard, and C. Hansen, "Active control of gearbox vibration," *Proceedings of Active*, pp. 295–304, 1999.

[26] M. H. Chen and M. J. Brennan, "Active control of gear vibration using specially configured sensors and actuators," *Smart Materials and Structures*, vol. 9, no. 3, pp. 342–350, 2000.

[27] Y. H. Guan, W. S. Shepard, and T. C. Lim, "Direct hybrid adaptive control of gear pair vibration," *Journal of Dynamic Systems, Measurement, and Control*, vol. 125, no. 4, pp. 585–594, 2003.

[28] M. F. Li, T. C. Lim, and W. S. Shepard, "Modeling active vibration control of a geared rotor system," *Smart Materials and Structures*, vol. 13, no. 13, p. 449, 2004.

[29] M. F. Li, T. C. Lim, and W. S. S. Jr, "Experimental active vibration control of gear mesh harmonics in a power recirculation gearbox system using a piezoelectric stack actuator," *Smart Materials and Structures*, vol. 14, no. 14, p. 917, 2005.

[30] X. Qiu and C. H. Hansen, "A study of time-domain FXLMS algorithms with control output constraint," *Journal of the Acoustical Society of America*, vol. 109, no. 6, pp. 2815–2823, 2001.

[31] M. T. Akhtar and W. Mitsuhashi, "Improving performance of FxLMS algorithm for active noise control of impulsive noise," *Journal of Sound and Vibration*, vol. 327, no. 3-5, pp. 647–656, 2009.

[32] I. Tabatabaei Ardekani and W. H. Abdulla, "Theoretical convergence analysis of FxLMS algorithm," *Signal Processing*, vol. 90, no. 12, pp. 3046–3055, 2010.

[33] I. T. A. H. Abdulla, "Theoretical Convergence Analysis of FxLMS Algorithm," *Signal Processing*, vol. 90, 2010.

[34] B. Huang, Y. Xiao, J. Sun, and G. Wei, "A variable step-size FXLMS algorithm for narrowband Active noise control," *IEEE Transactions on Audio Speech and Language Processing*, vol. 21, no. 2, pp. 301–312, 2013.

[35] X. Mu, J. Ko, and J. Rheem, "Modified FxLMS algorithm for active noise control and its real-time implementation," *Journal of the Institute of Electronics and Information Engineers*, vol. 50, no. 9, pp. 172–176, 2013.

[36] T. Wang and W.-S. Gan, "Stochastic analysis of FXLMS-based internal model control feedback active noise control systems," *Signal Processing*, vol. 101, no. AUG, pp. 121–133, 2014.

[37] M. T. Akhtar and W. Mitsuhashi, "A modified normalized FxLMS algorithm for active control of impulsive noise," in *Proceedings of the European Signal Processing Conference*, Aalborg, Denmark, August 2015.

[38] K. Gomathi, S. Venkatachalam, and S. Kumari, "Variable step size for improving convergence of FxLMS algorithm," *Procedia Technology*, vol. 25, pp. 420–426, 2016.

[39] L. Wu, X. Qiu, and Y. Guo, "A generalized leaky FxLMS algorithm for tuning the waterbed effect of feedback active noise control systems," *Mechanical Systems and Signal Processing*, vol. 106, pp. 13–23, 2018.

[40] J. D. Wu and J. H. Lin, "Implementation of an active vibration controller for gear-set shaft using -analysis," *Journal of Sound and Vibration*, vol. 281, no. 3, pp. 1037–1055, 2005.

[41] V. Balamurugan and S. Narayanan, "Active vibration control of smart shells using distributed piezoelectric sensors and actuators," *Smart Materials and Structures*, vol. 10, no. 2, pp. 173–180, 2001.

[42] S. Prakash, T. G. Renjith Kumar, S. Raja, D. Dwarakanathan, H. Subramani, and C. Karthikeyan, "Active vibration control of a full scale aircraft wing using a reconfigurable controller," *Journal of Sound and Vibration*, vol. 361, no. 3, pp. 32–49, 2016.

[43] K. Mazur, S. Wrona, and M. Pawelczyk, "Design and implementation of multichannel global active structural acoustic control for a device casing," *Mechanical Systems and Signal Processing*, vol. 98, pp. 877–889, 2018.

[44] Y. Pu, H. Zhou, and Z. Meng, "Multi-channel adaptive active vibration control of piezoelectric smart plate with online secondary path modelling using PZT patches," *Mechanical Systems and Signal Processing*, vol. 120, pp. 166–179, 2019.

[45] Y. J. Chu, S. C. Chan, C. M. Mak, and M. Wu, "A Diffusion Fxlms Algorithm For Multi-Channel Active Noise Control And Variable Spatial Smoothing," in *Proceedings of the IEEE International Conference on Acoustics, Speech and Signal Processing*, Toronto, ON, Canada, June 2021.

[46] T. Pepin, N. J. Pignier, and J. Rabault, "Deep reinforcement learning applied to active noise control," *A Smart, Adaptive, Variable Step Size FxLMS Algorithm Design*, vol. 95, 2021.

[47] G. Li, W. Liu, and X. Su, "The sun and planetary gear design of a 1.5-MW wind turbine," *Journal of Vibration Engineering & Technologies*, vol. 6, 2018.

[48] L. J. Eriksson and M. C. Allie, "Use of random noise for on-line transducer modeling in an adaptive active attenuation system," *Journal of the Acoustical Society of America*, vol. 85, no. 2, pp. 797–802, 1986.

[49] R. Punchalard, "Mean square error analysis of unbiased modified plain gradient algorithm for second-order adaptive IIR notch filter," *Signal Processing*, vol. 92, no. 11, pp. 2815–2820, 2012.

Hindawi
Shock and Vibration
Volume 2021, Article ID 6627740, 12 pages
https://doi.org/10.1155/2021/6627740

Research Article

Multiclass Incremental Learning for Fault Diagnosis in Induction Motors Using Fine-Tuning with a Memory of Exemplars and Nearest Centroid Classifier

Magdiel Jiménez-Guarneros, Jonas Grande-Barreto, and Jose de Jesus Rangel-Magdaleno

National Institute for Astrophysics, Optics and Electronics, San Andrés Cholula, Mexico

Correspondence should be addressed to Jose de Jesus Rangel-Magdaleno; jrangel@inaoep.mx

Received 12 July 2021; Revised 23 September 2021; Accepted 13 October 2021; Published 27 October 2021

Academic Editor: Wenxian Yang

Early detection of fault events through electromechanical systems operation is one of the most attractive and critical data challenges in modern industry. Although these electromechanical systems tend to experiment with typical faults, a common event is that unexpected and unknown faults can be presented during operation. However, current models for automatic detection can learn new faults at the cost of forgetting concepts previously learned. This article presents a multiclass incremental learning (MCIL) framework based on 1D convolutional neural network (CNN) for fault detection in induction motors. The presented framework tackles the forgetting problem by storing a representative exemplar set from past data (known faults) in memory. Then, the 1D CNN is fine-tuned over the selected exemplar set and data from new faults. Test samples are classified using nearest centroid classifier (NCC) in the feature space from 1D CNN. The proposed framework was evaluated and validated over two public datasets for fault detection in induction motors (IMs): asynchronous motor common fault (AMCF) and Case Western Reserve University (CWRU). Experimental results reveal the proposed framework as an effective solution to incorporate and detect new induction motor faults to already known, with a high accuracy performance across different incremental phases.

1. Introduction

IMs support most of the production process in the modern industry's daily life due to their straightforward construction, reliability, and relatively low cost. However, IMs operate for long uninterrupted working periods, are exposed to the elements, and minimum preventive maintenance. These operative conditions raise unexpected faults that can show up at any time, causing lower productivity and economic losses. Thus, early motor failure detection and correction are challenging problems that catch many researchers' attention.

From a general overview, motor fault analysis methods split into signal processing and artificial intelligence approaches [1]. The first ones have been focused on analyzing diverse physical magnitudes to find features that help identify abnormal behavior in the motor's performance [2, 3]. For example, rotor vibrations [4], bearing faults [5], and broken rotor bar [2]. Meanwhile, artificial intelligence-based methods have been integrated to provide automatic fault detection using a data-driven approach. These methods base their performance on extracted features from raw signals to be used as inputs. In past years, deep learning (DL) architectures, such as autoencoders (AE) [6], convolutional neural network (CNN) [5, 7, 8], and capsule networks (CapsNet) [1], have been used in fault diagnosis due to their potential applicability for the automatic feature extraction, reported in several cases new state-of-the-art results. In the literature, most works combine DL architectures with different handcraft features and feature extractors (e.g., Fourier and Wavelet transform) [8]. Recently, some authors [9–12] have shown some promising advances to eliminate the

requirement of the handcraft features, where CNN architectures have demonstrated high effectiveness. Despite this progress, classification models have been focused on detecting a set of known patterns that characterize typical faults on equipment from manufacturers. However, modifications in the operative conditions can generate patterns from new failures that differ from those detected by the current model. This issue forces existing methods to learn a new model considering unknown failure conditions.

To overcome the practical challenge mentioned above, multiclass incremental learning (MCIL) arises a promising solution by updating the current model on new data instead of training once on a whole dataset. Indeed, MCIL aims to learn new classes from previous ones, although none or a few samples of old classes are retained. Unlike the conventional classification setting, in MCIL, samples from different classes come in different time phases, whereas incremental classifiers aim to achieve a competitive performance overall seen classes [13]. Motivated by this, only a few works have been reported by traditional approaches to address multiclass incremental learning. For example, Saucedo-Dorantes et al. [14] trained a self-organizing map (SOM) every time that a new detection occurs. However, this model does not retain samples from previous classes, and the complexity of the model increases when new faults are incorporated. Incremental model transfer learning (IMTL) [15] follows a domain adaptation approach to allow a classification model to detect new faults but requires all samples from past faults during the subsequent incremental phases to achieve high performance. Overall, these works are still limited because they depend on an engineered data representation. In this direction, deep learning approaches have certain advantages by learning task-specific features and classifiers from raw signals. However, deep learning models can suffer from catastrophic forgetting [16] when they are trained incrementally, i.e., the tendency of a neural network to underfit past classes when new ones are learned.

This study presents an MCIL framework based on an 1D CNN for fault detection in IMs. To tackle the catastrophic forgetting problem, the presented framework employs a memory containing representative exemplars from past data and updates a 1D CNN model across incremental states, using a fine-tuning procedure [16]. The representative exemplars from past (known) faults are selected using the Herding method [17]. Next, nearest centroid classifier (NCC) is used to classify test samples in each incremental phase. By doing this, the proposed framework maintains a constant model complexity while new classes appear each time. We evaluated and validated the presented model over two different study cases: (1) motor common faults diagnosis and (2) bearing fault diagnostics. Experimental results show that the proposed MCIL framework effectively incorporates new faults on an 1D CNN, achieving a high accuracy performance across different incremental phases.

2. Convolutional Neural Network

Convolutional neural network (CNN) is a biologically inspired artificial neural network that processes data with a known grid-like topology [18]. CNN alternates convolution and pooling layers, followed by a fully connected layer to extract features and generate the desired output. Due to the inherent one-dimensional signals obtained from a vibration analysis in IMs, it has been preferable to deal with these signals using one-dimensional models [9, 11]. Thus, we first describe 1D convolution operators, which are used in the presented work. Then, we describe the complement layers that integrate a convolutional network.

In its standard approach, CNN performs a set of convolutions between an input signal and some finite impulse response (FIR) filters. The convolution operation ($*$) is described as a weighted average of an input signal $\mathbf{x}_i$:

$$\begin{aligned} s_i &= \mathbf{k}_i * x_i \\ &= \sum_{j=0}^{L-1} \mathbf{k}_{i-j} \cdot x_j, \end{aligned} \tag{1}$$

where s_i is called i-th feature map and $\mathbf{k}$ denotes a weighting factor, called filter or kernel, with length L. The kernels are built to identify spatial features on the input data. The output from a convolutional layer defines the next layer's activation value. Then, the output $s_i^{(l)}$ of a convolutional layer (l) at i-th feature map is defined as follows:

$$s_i^{(l)} = \sigma\left(\sum_{j=1}^{L} \mathbf{K}_{i,j}^{(l)} * \mathbf{x}_j^{(l-1)} + \mathbf{b}_i^{(l)}\right), \tag{2}$$

where $\mathbf{K}_{i,j}^{(l)}$ denotes each local weighting factor of the kernel, $\mathbf{x}_j^{(l-1)}$ represents the j-th feature map at the layer $l-1$, L is the number of filters applied over $\mathbf{x}_j^{(l-1)}$, $\mathbf{b}_i^{(l)}$ is the bias, and σ is the activation function.

Most of the time, raw data contain noise and undesirable spectral shapes that affect the feature extraction process [19]. Motivated from this issue, the SincNet layer [9, 20], an extension of the standard convolution, applies a set of temporal convolutions between a raw signal and digital filters to boost the first convolutional layer output.

2.1. Sinc Convolution. Instead of learning the filters from the data, as the conventional CNN, the SincNet [9, 20] performs the convolution operation with a preset function g that requires only a reduced set of learnable parameters Θ_s, as defined in the following equation:

$$\mathbf{y}[n] = \mathbf{x}[n] * g[n, \Theta_s], \tag{3}$$

where g is a filter bank for band-pass filter in the frequency domain; it takes advantage of the Sinc function to convert to time domain through the inverse Fourier transform [19]. The use of rectangular filters represents a practical selection to define g. The magnitude Φ of a generic band-pass filter can be described as the difference between two low-pass filters.

$$\Phi[f, f_L, f_H] = \text{rect}\left(\frac{f}{2f_H}\right) - \text{rect}\left(\frac{f}{2f_L}\right), \tag{4}$$

where $\Theta_s = \{f_L, f_H\}$ the set of the trainable parameters; f_L and f_H represent low and high cutoff frequencies,

respectively, of the band-pass filter learned by the Sinc filters. $\text{rect}(\cdot)$ describes the rectangular function at the instant t as follows:

$$\text{rect}(t) = \begin{cases} 1, & |t| \leq 0.5, \\ 0, & \text{otherwise.} \end{cases} \tag{5}$$

Using the inverse Fourier transform, the reference function g becomes

$$g[n, f_L, f_H] = 2f_H \cdot \text{sinc}(2\pi f_H n) - 2f_L \cdot \text{sinc}(2\pi f_L n), \tag{6}$$

where the Sinc function is defined as $\text{sinc}(\mathbf{x}) = \sin(\mathbf{x})/\mathbf{x}$. Finally, to achieve an approximation of the ideal band-pass filter, a winnowing procedure is applied. This procedure multiplies the truncated function g with a window function ω [21], intending to smooth out the abrupt discontinuities at the ends of g:

$$g_\omega[n, f_L, f_H] = g[n, f_L, f_H] \cdot \omega[n, f_L, f_H]. \tag{7}$$

Therefore, the succeeding layers learn the filter gain of each actual layer.

2.2. Pooling Layers. These layers perform a downsampling to reduce the spatial size of features, encouraging the input data's invariance to spatial translations. In particular, a max-pooling layer reporting the j-th maximum element within a rectangular frame for each feature map. Meanwhile, a global average pooling (GAP) layer replaces the fully connected layers in a CNN model [22], averaging the feature maps from previous convolutional layers. GAP aims to force correspondences between learned feature maps and classes in the previous convolutional layers.

3. MCIL Methodology

Let $\mathcal{X}$ and $\mathcal{Y}$ denote a feature and a label space, respectively. Let $\mathbf{D} = (\mathbf{X}, \mathbf{Y}) = \{(\mathbf{x}_j, \mathbf{y}_j)\}_{j=1}^{N}$ be a labeled dataset with N samples, where $(\mathbf{X}, \mathbf{Y}) \in \mathcal{X} \times \mathcal{Y}$. In a classification problem, a task $\mathcal{T}$ consists in learning a labeling function G, such that $G: \mathcal{X} \longrightarrow \mathcal{Y}$. Notice that G represents a deep neural network with parameters Θ, so that $\mathbf{Y} = G(\mathbf{X}; \Theta)$. Likewise, G can be expressed as a composition of two functions, $G = G_y \circ G_f$, where $G_f: \mathcal{X} \longrightarrow \mathcal{Z}$ is a feature extractor and $G_y: \mathcal{Z} \longrightarrow \mathcal{Y}$ feature labeling with parameters Θ_f and Θ_y, respectively; here, $\mathcal{Z}$ is a latent feature space. The feature extractor G_f takes $\mathbf{X}$ and produces a latent feature dataset $\mathbf{Z}$. Then, G_y receives $\mathbf{Z}$ as input and produces label classifications $\mathbf{Y}$, i.e., $\mathbf{Y} = G_y(G_f(\mathbf{X}; \Theta_f); \Theta_y)$.

We focus on multiclass incremental learning (MCIL) where the model complexity is maintained constant during N incremental states, while a reduced number of samples is retained from past classes [13, 23]. We assume $N + 1$ phases, that is, N incremental phases and one initial phase S_0. A model G_0 is learned on a dataset $\mathbf{D}_0$ during the phase S_0. Due to this, we assume a memory limitation, all samples from $\mathbf{D}_0$ cannot be stored, so that exemplars $\mathbf{E}_0$ are selected and stored as a replacement of $\mathbf{D}_0$ with $|\mathbf{E}_0| \ll |\mathbf{D}_0|$. In the i-th incremental phase, dataset $\mathbf{D}_i$ from C_i classes is streamed, whereas exemplars $E_{0:\,i-1}$ from phases 0 to $i-1$ are stored in memory. The aim of MCIL is to learn a model G using exemplars $E_{0:\,i-1}$ and data set $\mathbf{D}_i$.

Figure 1 shows the flowchart of the MCIL methodology for fault detection in IMs. In the initial phase, a model G, that is 1D CNN, is trained via cross-entropy loss $\mathscr{L}_{\text{ce}}$ on the dataset $\mathbf{D}_0$, containing signals from different motor conditions. Next, exemplars $\mathbf{E}_0$ are selected using Herding method [17] over $\mathbf{D}_0$ in feature space, $\mathbf{Z}_0 = G_f(\mathbf{D}_0)$. The nearest centroid classifier (NCC) is used to classify test samples in the current phase using $\mathbf{E}_0$ as training set. In the i-th incremental phase, the output layer from the CNN is extended with randomly initialized weights for each new class. Then, the 1D CNN is fine-tuned over $\mathbf{D}_i$ and $\mathbf{E}_{0:\,i-1}$ using cross-entropy loss $\mathscr{L}_{ce}$; notice that imbalance data are produced in $\mathbf{D}_i \cup \mathbf{E}_{0:\,i-1}$ because $\mathbf{E}_{0:\,i-1}$ contains a reduced set of exemplars from past classes. This procedure updates all parameters Θ of 1D CNN. The resulting trained model G in phase i is used to extract features from $\mathbf{D}_i$ and $\mathbf{E}_{0:\,i-1}$. Herding method is used to select the exemplar set $\mathbf{E}_i$ over $\mathbf{D}_i$ in feature space. Then, NCC uses $\mathbf{E}_{0:\,i}$ as training set in feature space to classify test samples. This procedure is repeated over the different incremental phases.

3.1. CNN Architecture. The 1D CNN architecture is shown in Figure 2. 1D time-domain signals are used as inputs to the 1D CNN. One Sinc layer [9, 20] and two standard convolution layers were incorporated into the feature extractor. Conv $a \times b - c$ denotes the convolution layer of c filters with a size a and a stride b. For the lower layers, large size filters were employed to deal with high frequencies present in data. We added max-pooling layers to reduce the spatial feature dimensions. Likewise, a global average pooling layer is used to reduce the spatial dimensions of the learned features. The output layer is extended for each new class with a random initial value. The softmax activation function is used at the output layer to perform motor fault classification.

3.2. Exemplar Set Selection. The exemplar set $\mathbf{E}_i$ is adjusted in each incremental phase i using the Herding method [17], as shown in Algorithm 1. The exemplar selection is required when training data are available. Feature representation from dataset $\mathbf{D}_i$ is obtained using the feature extractor G_f (line 2). Each sample is normalized employing the L2 norm (line 3). Notice that m exemplars are selected and stored iteratively for each class (lines 5–7). One sample is added to the exemplar set in each iteration, prioritizing that sample that makes the average feature vector better approximate the mean vector.

3.3. Nearest Centroid Classifier. Nearest centroid classifier (NCC) [24] is a nearest-neighbor classifier, which is used to address the bias produced on new classes by training CNN over imbalanced data. The procedure followed by NCC is described in Algorithm 2. First, feature representations from exemplars $E_{0:\,i}$ are obtained using the feature extractor G_f

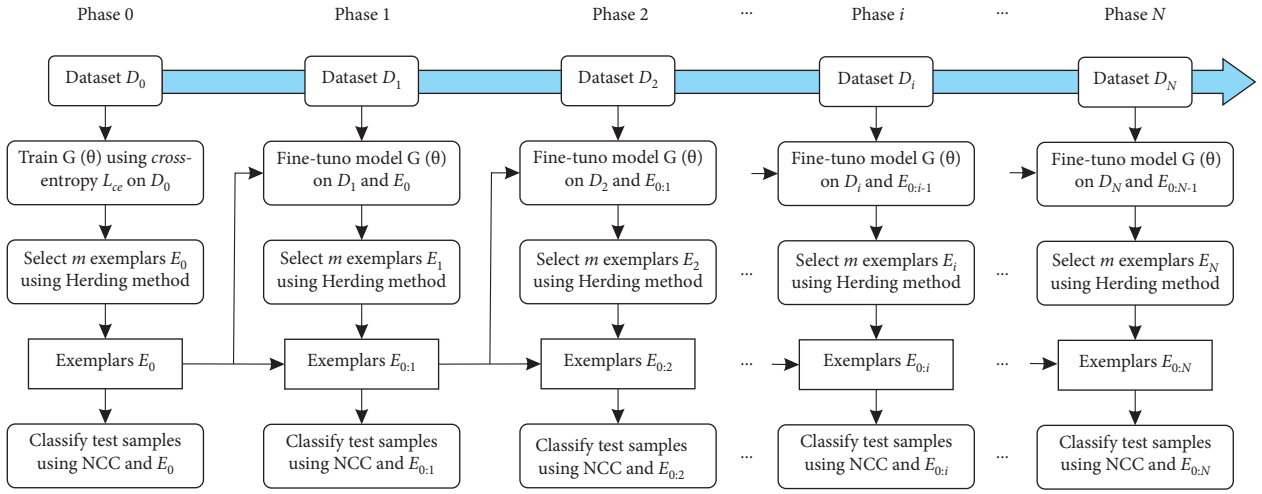

Figure 1: Flowchart of the presented methodology in order to train an incremental classifier for the fault detection in IMs.

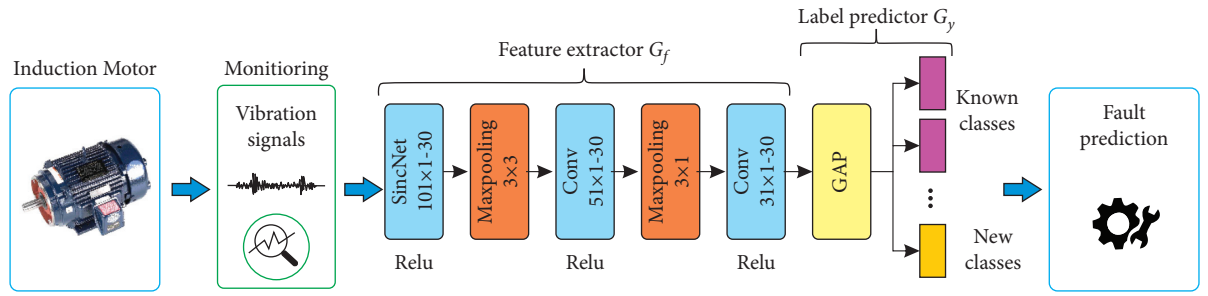

Figure 2: Architecture of the 1D CNN model.

Inputs: $X_c = \{x_1, \ldots, x_{n_c}\}$: dataset of class c; m: number of exemplars to select; G_f: feature extractor
Output: **E**: exemplar set
(1) Initialize **E** to the empty set {}
(2) $\mathbf{Z}_c \leftarrow G_f(\mathbf{X}_c)$ \(▷\) Get feature representations
(3) $\widehat{\mathbf{Z}}_c \leftarrow \mathbf{Z}_c / \|\mathbf{Z}_c\|_2$ \(▷\) L2 norm
(4) $\overline{z} \leftarrow 1/n_c \sum_{\widehat{z}} \in \widehat{Z}_c \widehat{z}$ \(▷\) Get mean feature vector
(5) **for** $k = 1, \ldots, m$ **do**
(6) $\mathbf{p}_k \leftarrow \arg\min_{\widehat{z}} \in \widehat{Z}_c \| \overline{z} - (1/k)[G_f(\widehat{z}) + \sum_{j=1}^{k-1} G_f(\mathbf{p}_j)] \|_2$
(7) **end for**
(8) $\mathbf{E} \leftarrow \{\mathbf{p}_1, \ldots, \mathbf{p}_m\}$

Algorithm 1: Herding method.

(line 1). The centroid is computed as the point from which the sum of the distances of all exemplars that belong to that particular class are minimized (lines 2–4). NCC assigns the label of the most similar class centroid to the test sample $\mathbf{x}_t$ (line 5) as follows:

$$\mathbf{y}^* = \arg\min_{c \in 1,\ldots,C} d\left(\overline{p}_c, G_f(\mathbf{x}_t)\right), \tag{8}$$

where $\overline{p}_c$ is the centroid vector for the class c, obtained from exemplars $\mathbf{E}_{0:i}$; meanwhile, d is the Euclidean distance.

Inputs: $\mathbf{E}_{0:\,i} = \{\mathbf{p}_1, \ldots, \mathbf{p}_t\}$: exemplar set from phase 0 to i; G_f: feature extractor; $\mathbf{x}_t$: sample to be classified
Output: $\mathbf{y}^*$: one hot vector of the class label; C: number of classes
(1) $\widehat{Z} \leftarrow G_f(\mathbf{E}_{0:\,i})$ \(▷\) Get feature representations
(2) **for** $c = 1, \ldots, C$ **do**
(3) $\overline{p}_c \leftarrow \arg\min_{\mathbf{p}_1 \in \widehat{Z}_c} \sum_{\mathbf{p}_2 \in \widehat{Z}_c} d(\mathbf{p}_1, \mathbf{p}_2)$
(4) **end for**
(5) $\mathbf{y}^* \leftarrow \arg\min_{c \in 1,\ldots,C} \|\overline{p}_c - G_f(\mathbf{x}_t)\|_2$ \(▷\) nearest prototype

Algorithm 2: Nearest centroid classifier.

4. Experimental Setup

This section first describes data from the different cases of study used in multiclass incremental learning for motor fault diagnosis. Next, the experimental protocol is described. Finally, we present the implementation details of the MCIL model.

4.1. Cases of Study. Our experiments were conducted on two cases of study based on vibration analysis: (1) motor common fault diagnosis and (2) bearing fault diagnosis. For this, we used two public benchmark datasets: asynchronous motor common fault (AMCF) [1] and Case Western Reserve University (CWRU) [25]. Tables 1 and 2 present the description of the data acquisition and studied faults for the AMCF and CWRU datasets, respectively. The AMCF dataset is composed of 8,000 samples from 8 motor conditions (1,000 per class), where each sample contains 1,024 points. For the CWRU dataset, experiments were performed under 1 hp workload. This dataset contains three types of fault locations in bearing (balls, inner race, and outrace), showing fault diameters of 0.007, 0.014, and 0.021 inches. CWRU contains 10,000 samples from 10 different motor conditions (1,000 per class), including health bearings.

4.2. Experimental Protocol. For each dataset, we evaluated the proposed MCIL model starting from a pretrained CNN over initial data of motor faults; meanwhile, the rest of the data coming in different phases are used to train CNN in a class-incremental way. First, we fix the number of stored exemplars to the smallest memory size allowed, and after, the number of incremental phases is varied. Next, we fix the number of incremental phases to 6 and 8 for AMCF and CWRU, while the number of exemplars per fault is varied considering $m = 5$ and $m = 10$. In each incremental phase, faults are given in a fixed random order; 80% of the data samples in each class are used for training, and the remaining 20% for testing, performing a stratified sampling. The final model in each incremental phase is used to classify classes observed so far. Experiments were repeated five times using different random initial weights, different partitions of data, and a different fault order. We calculate the average accuracy and standard deviation only for incremental states, which are of interest for MCIL. Our comparison includes the results of CNN employing all previous data available (Full) and those using a fine-tuning procedure with a random selection of exemplars (FT + R).

4.3. Implementation Details and Model Parameter Selection. Table 3 presents the details of the 1D CNN model. We used filters with a large (101), medium (51), and small (11) size to learn features from raw signals. In addition, max-pooling layers were used with a size and stride of 3 to reduce spatial feature dimensions. The 1D CNN model employs a total of 56,281 trainable parameters. The 1D CNN model was implemented in Pytorch 1.7.0, whereas NCC was obtained from scikit-learn library (https://scikit-learn.org/stable/). Experiments were performed using a PC Intel(R) Core (TM) i7 with a graphic card GTX 1080 Nvidia on Ubuntu 20.04 LTS.

In our experiments, the 1D CNN model was trained by Adam algorithm [26] during 40 and 30 epochs for the AMCF and CWRU datasets, respectively. For both datasets, the initial learning rate was set to 0.0001 at the initial phase, whereas it was set to 0.001 for incremental phases. In addition, a learning decay of 0.1 was applied at 30 and 20 epochs. Likewise, a batch size of 30 was selected from {10, 30, 50} for both datasets. This hyperparameter setting was selected after comparing different configurations across 6 and 8 incremental phases on AMCF and CWRU; 5 exemplars from each past class (known faults) were stored in memory. For model parameter selection, we used coordinate descent [27], which changes only one hyperparameter at a time, aiming the best configuration. Fine-tuning and Herding selection (FT + H) were used for CNN retraining and exemplar selection in each incremental phase. Experimental results, as shown in Table 4, indicate that the batch size has a lower negative impact compared with learning rate. For both datasets, the 1D CNN model achieves its highest average accuracy when the learning rate is 0.001 and the batch size is 10 and 30. This last value of batch size was selected because it requires a lower number of iterations for data processing during training. Finally, as shown in Figure 3, the 1D CNN model stabilizes its training above 20 and 15 epochs on AMCF and CWRU for the different incremental phases. Using 40 and 30 epochs during training, we ensure a stabilization of the 1D CNN model.

5. Results

5.1. Case 1: Motor Common Fault Diagnostics. Table 5 shows the average accuracy and standard deviation (SD) on AMCF

Table 1: Description of the AMCF dataset.

Data acquisitions	
Motor	4 hp YE2-100L2-4
Sensor type	CT1020 L accelerometer
Signal description	Vibration signals were collected using an acquisition card PCI-1716 with a sampling frequency of 250 kS/s, high-resolution of 16 bits, and 16 SE/8 DI channels
Fault description	
Type of fault	The damages of the motors are as follows: short circuit of 2 turns (SC2T), short circuit of 4 turns (SC4T), short circuit of 4 turns (SC8T), air-gap eccentricity (AE), rotor bar broken (RBB), bearing cage broken (BCB), and bearing abrasion fault (BAF)

Table 2: Description of the CWRU dataset.

Data acquisitions	
Motor	2 hp reliance electric
Sensor type	Accelerometers
Signal description	Vibration signals were collected using a 16-channel DAT recorder. Digital data was collected at 12k samples/second
Fault description	
Bearing	6205-2RS JEM SKF, deep groove ball bearing
Fault location	Balls, inner race, and out race
Fault diameters	0.007, 0.014, and 0.021 inch

Table 3: Implementation details of the 1D CNN model.

Block	Layer name	Hyperparameters	Number of trainable parameters
Input	Sample input	—	
SincNet	SincNet	Filters = 30, size = 101, stride = 1	60
	Activation function	ReLU	—
	Max-pooling	Size = 3, stride = 3	—
Conv1	Convolution 1D	Filters = 30, size = 51, stride = 1	45,930
	Activation function	ReLU	—
	Max-pooling	Size = 3, stride = 3	—
Conv2	Convolution 1D	Filters = 30, size = 11, stride = 1	9,930
	Activation function	ReLU	—
GAP	Global average pooling	—	—
Output	Fully connected	C units	361
	Activation function	Softmax	—

Table 4: Accuracy results of 1D CNN on AMCF and CWRU datasets, using different batch sizes and learning rates.

	Batch size			Learning rate		
AMCF	10	30	50	0.01	0.001	0.0001
1D CNN (FT + H)	**94.97** ± 3.40	94.24 ± 3.96	91.20 ± 07.06	80.05 ± 08.33	**94.24** ± 03.96	58.67 ± 14.14
CWRU						
1D CNN (FT + H)	98.77 ± 0.83	**98.78** ± 0.83	98.68 ± 01.09	66.42 ± 09.66	**98.78** ± 00.83	87.58 ± 06.10

Best results are boldfaced for each setting.

using a different number of incremental phases and exemplars. We observed that the most challenging scenario is presented when one exemplar per fault is retained across different incremental phases. Inversely, we can see that the most straightforward scenario is presented when a greater number of exemplars per fault is stored ($m = 5$ and $m = 10$). Notice that the performance of FT + R (fine-tuning with a random selection) dropped when $m = 1$ and the number of incremental phases decreased. In this scenario, the proposed MCIL framework (FT + NCC + H) obtained average accuracies beyond 94%, outperforming to FT + R at least 20 percentage points (pp). Moreover, we can see that FT + NCC + H achieved average accuracies of 98.32% and 98.85% over 6 incremental phases and a number of exemplars m equal to 5 and 10, outperforming to FT + R by 5.07 and 3.79 pp.

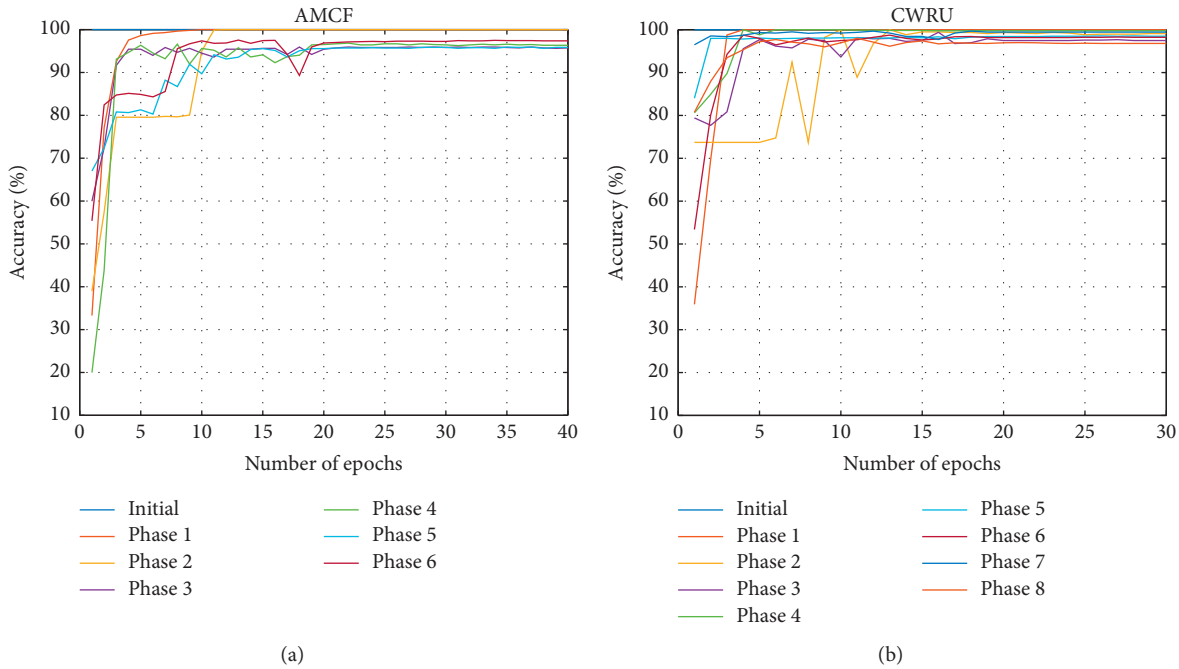

Figure 3: Accuracy performance of 1D CNN (FT + H) across different epochs. We show the accuracy performance for the different incremental phases.

Table 5: Accuracies and standard deviations (SD) over AMCF using a different number of incremental phases and exemplars.

	$m = 1$			Phases = 6	
	1 phase	3 phases	6 phases	$m = 5$	$m = 10$
FT + R	55.40 ± 03.85	68.96 ± 14.63	75.66 ± 08.37	93.25 ± 03.67	95.06 ± 03.53
FT + NCC + H	**96.70** ± 02.33	**94.73** ± 02.03	**96.22** ± 02.26	**98.32** ± 00.91	**98.85** ± 00.63
Full			99.38 ± 00.31		

Best results are boldfaced for each setting.

5.2. Case 2: Bearing Fault Diagnostics. Table 6 shows the average accuracies and standard deviations (SD) on CWRU using a different number of incremental phases and exemplars. The most challenging scenario is presented when $m = 1$, where the performance of FT + R dropped when the number of phases increased. In this scenario, FT + NCC + H achieved average accuracies beyond 93%, outperforming FT + R at least 6.27 pp. On the other hand, we observed that FT + NCC + H outperformed FT + R by only 0.48 and 0.39 pp across 8 incremental phases, while the number of exemplars is 5 and 10.

5.3. Ablation Studies

5.3.1. Effect of Each Component. We analyzed the impact of each component to determine its contribution over the final accuracy on AMCF and CWRU. Figure 4 shows the accuracy performance on AMCF and CWRU during 6 and 8 incremental phases, although one exemplar is retained in memory. Notice that accuracy results of FT without memory also were included. For both datasets, we observed that FT reduces its accuracy performance over incremental phases if memory is not available, suggesting the presence of the catastrophic forgetting problem. We can see that fine-tuning results significantly improved when memory is incorporated (FT + H), storing representative samples from past faults. Finally, notice that NCC also had a positive impact on the final accuracy (FT + NCC + H) by reducing the bias generated by incorporating new faults.

5.3.2. Effect of the Number of Exemplars. Figure 5 shows the impact on accuracy performance by varying the number of exemplars per fault. We observed that FT + R improved its results when the number of stored exemplars increased, while FT + NCC + H obtained results above 96% starting from 1 exemplar per class. We can see that FT + NCC + H achieved a competitive performance (98.32% vs. 99.38%) than training on full data, storing at least 5 exemplars per fault, while FT + R became competitive by using more than 20 exemplars.

Regarding the CWRU results, we can see that the worst performance is obtained when the number of stored exemplars per class is 1. Moreover, FT + R and FT + NCC + H

Table 6: Average accuracy and standard deviation (SD) for MCIL methods over CWRU, using a different number of incremental phases of exemplars.

	$m = 1$			Phases = 8	
	1 phase	4 phases	8 phases	$m = 5$	$m = 10$
FT + R	91.65 ± 03.40	83.90 ± 03.44	81.22 ± 04.22	98.65 ± 01.00	98.86 ± 00.96
FT + NCC + H	**97.92** ± 01.18	**94.77** ± 00.88	**93.36** ± 01.96	**99.13** ± 00.54	**99.25** ± 00.39
Full			100.0 ± 0.00		

Best results are boldfaced for each setting.

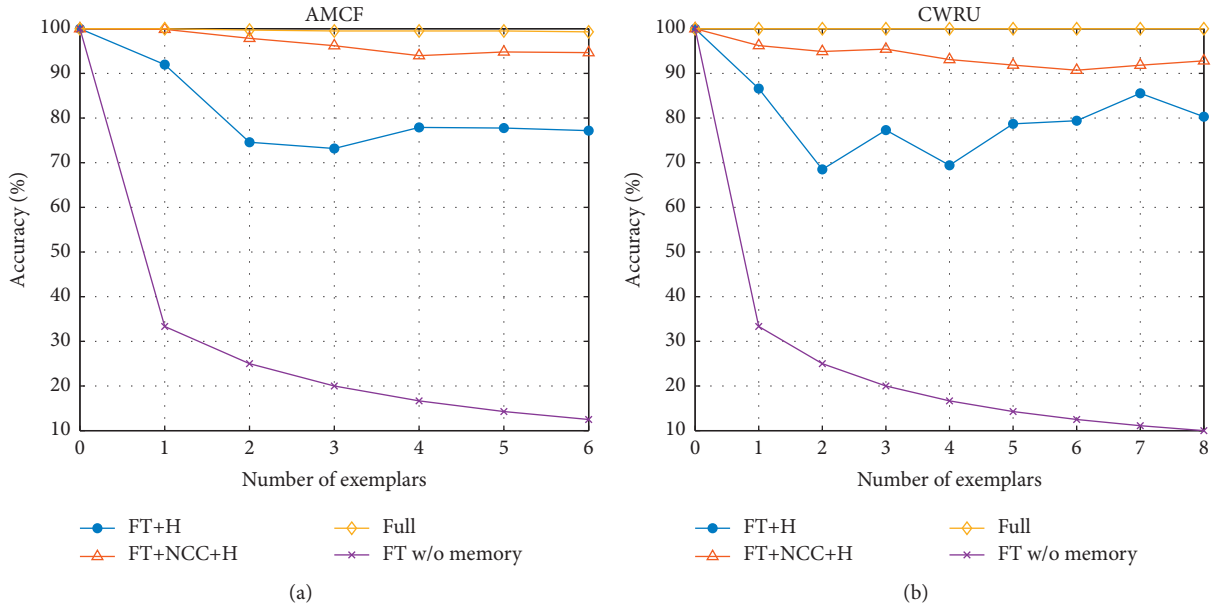

Figure 4: Impact of each component of FT + NCC + H on (a) AMCF and (b) CWRU across 6 and 8 incremental phases, retaining one exemplar per fault. Accuracy results of FT without (w/o) memory also were included.

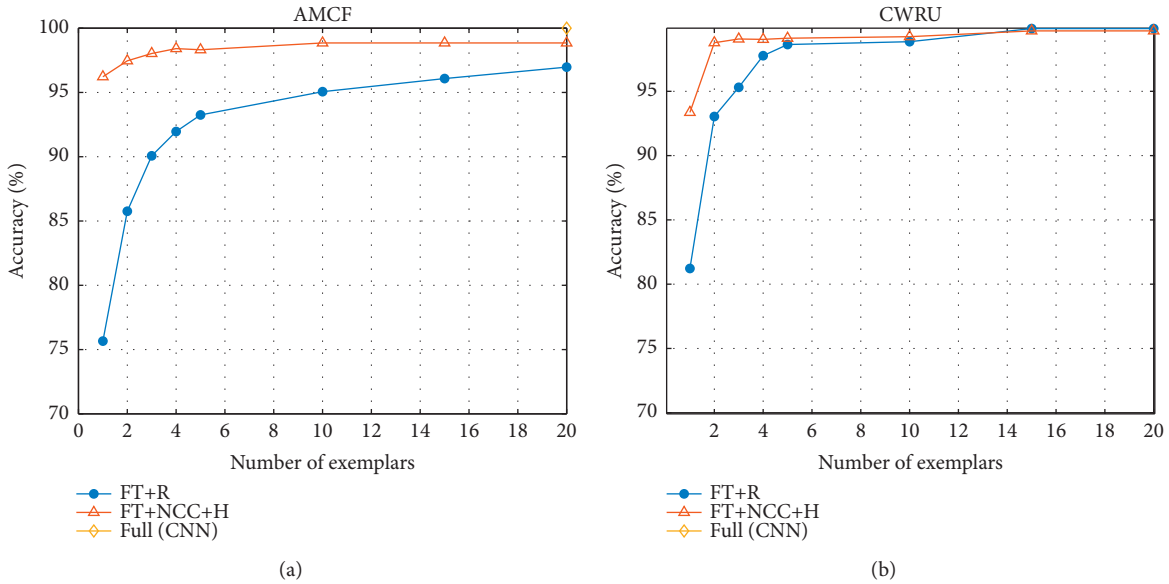

Figure 5: Impact of the number of exemplars stored in memory: (a) AMCF and (b) CWRU.

increased their accuracy performance starting from 2 samples per fault. FT + NCC + H obtained an average accuracy above 99%, storing at least 3 exemplars per fault, while FT + R achieved the same performance above 5 exemplars.

5.3.3. Effect of the Herding Method for Exemplar Selection. We studied the impact of the exemplar selection via Herding and a random selection over the accuracy performance on AMCF and CWRU. Figure 6 shows the accuracy performances on AMCF and CWRU across 6 and 8 incremental phases, while a different number of exemplars from past faults are retained. For AMCF, we observed that the Herding method (marked as + H) slightly improves the accuracy performance over random selection (marked as + R) when 1 to 10 exemplars are retained. For CWRU, only improvements can be seen when 2 to 5 exemplars are retained. We observed that random selection obtained a similar or even better performance than the herding method for the rest of the cases.

5.3.4. Effect of Noise over the Proposed Framework. In order to test the performance of the proposed framework under different noise conditions, we applied additive white Gaussian noise (AWGN) to the raw signals from the test set; 6 and 8 incremental phases were used on AMCF and CWRU, retaining 5 exemplars from past classes. Table 7 presents the classification results of FT + NCC + H under three different noise levels; accuracy results of FT + H (CNN trained incrementally) and the full model (CNN using all data) were included as reference. As expected, evaluated solutions reduced their average accuracy when a lower noise level is applied. However, we can see that FT + NCC + H obtained average accuracies beyond 92% and 94% when an SNR = 5 is applied on signals from AMCF and CWRU, respectively. For AMCF and CWRU, FT + NCC + H obtained the best average accuracies when SNR is 5 and 10, while it obtained a similar accuracy performance compared with the full model when SNR is 15.

5.3.5. Comparison of Classification Time. We analyzed the classification times of our proposed framework (FT + NCC + H) across different incremental phases; we included times of FT + H (CNN trained incrementally) as reference. For this experiment, 6 and 8 incremental phases were used for AMCF and CWRU, although 5 exemplars from each learned class were stored in memory. Table 8 shows the classification times for evaluated solutions. We can see that times increased when new classes are added to the 1D CNN classifier. Also, we observed that the times of FT + NCC + H did not significantly increase with respect to FT + H (CNN as classifier). From this, notice that NCC uses a reduced number of exemplars from past and current faults as training set.

6. Discussion

In experiments, we evaluated and validated the proposed MCIL framework on two different cases of study for motor fault detection in IMs. The evaluation was performed under scenarios where data from new faults are streamed in different time phases. From the results, we found that the MCIL framework allows the incorporation and detection of past and new motor faults from vibration signals with high accuracy across different incremental phases. Unlike previous works [14, 15], one or more faults can be added to the 1D CNN model in each incremental phase. Notice that computational requirements and memory should be bounded. In this sense, the proposed MCIL framework maintains a constant complexity while a few samples from past faults are retained. To the best of our knowledge, this is the first work that studies MCIL, based on a deep learning approach, for fault diagnosis in IMs from vibration signals.

From ablation studies, we observed that a neural network model tends to forget previously learned faults. This problem is known as catastrophic forgetting, which is produced by incorporating new faults into a pretrained model in a sequential way. In this direction, we found that the fine-tuning procedure with a memory of exemplars and the NCC classifier provides an effective solution to tackle the catastrophic forgetting problem [16] for fault diagnosis in IMs. As expected, the average accuracies of evaluated solutions significantly improved when the number of retained exemplars in memory increased. Notice that results on AMCF showed that at least 5 exemplars per fault are required across 6 incremental phases to achieve a competitive accuracy than training on full data. Also, we found that at least 3 exemplars were required across 8 incremental phases to obtain a similar performance using all data on CWRU. Notice that this amount of stored exemplars per fault represents approximately 1% of the size of the training set. Moreover, AMCF results showed that a greater number of incremental phases do not negatively impact the accuracy performance of the 1D CNN model; CWRU results showed that a greater number of incremental phases negatively impact the MCIL model's accuracy performance. Concerning to the exemplar selection, we found that the herding method slightly improved over the accuracy results than using a random selection when a few exemplars are retained, but similar or even worst results were obtained in other cases. Regarding noise conditions, we found that FT + NCC + H provides a robustness to disturbances in signals, outperforming to the full model in accuracy performance for SNRs with low values. In particular, we found that NCC helps to face such disturbances in signals. Finally, we found that NCC does not increase the classification time because a reduced number of samples are used as training set.

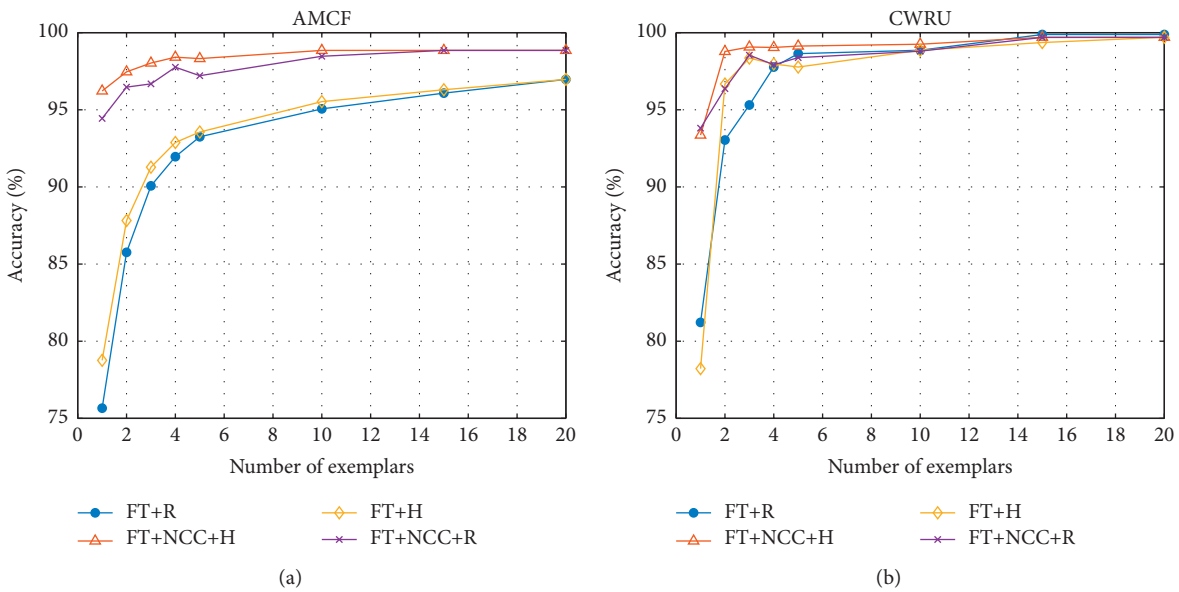

Figure 6: Impact of the herding method for exemplar selection on (a) AMCF and (b) CWRU. Herding method is marked as + H, whereas a random selection is marked as + R.

Table 7: Accuracy performances and standard deviations for evaluated solutions under different noise levels on AMCF and CWRU.

	SNR		
	5	10	15
AMCF			
Full	74.21 ± 00.91	94.41 ± 01.70	99.45 ± 00.21
FT + H	85.68 ± 03.37	93.55 ± 04.14	94.96 ± 03.32
FT + NCC + H	92.51 ± 03.22	98.15 ± 01.03	98.39 ± 00.89
CWRU			
Full	70.16 ± 06.18	96.20 ± 01.13	99.81 ± 00.07
FT + H	77.74 ± 07.08	93.25 ± 02.84	97.33 ± 01.62
FT + NCC + H	94.35 ± 04.49	98.77 ± 01.03	98.92 ± 00.89

Table 8: Classification time (seconds) across different incremental phases.

AMCF		
Incremental phases	FT + H	FT + NCC + H
Initial	0.1092	0.1084
1	0.1173	0.1386
2	0.1340	0.1443
3	0.1403	0.1588
4	0.1652	0.1704
5	0.1677	0.1862
6	0.1905	0.2034
CWRU		
Incremental phases	FT + H	FT + NCC + H
Initial	0.1087	0.1067
1	0.1129	0.1240
2	0.1308	0.1336
3	0.1462	0.1498
4	0.1555	0.1669
5	0.1590	0.1821
6	0.1836	0.2077
7	0.2011	0.2164
8	0.2093	0.2355

7. Conclusions

This study presents a MCIL framework based on fine-tuning with a memory of exemplars and the nearest centroid classifier (NCC) over an 1D convolutional neural network (CNN), to incorporate new motor faults from vibration signals to already known. Specifically, 1D CNN is fine-tuned over samples from new faults and exemplars from known (past) faults, whereas NCC is used during testing phase to classify samples from past and new faults. The proposed framework was evaluated over two datasets for motor fault diagnosis: AMCF and CWRU. Different experimental scenarios were considered, including different numbers of incremental phases and stored exemplars. Experiments showed that the proposed framework achieved an accuracy performance beyond 93% and 94% on AMCF and CWRU, retaining one exemplar per fault and varying the number of incremental phases. We found that 5 and 3 exemplars per fault across 6 and 8 phases on AMCF and CWRU are required to achieve competitive accuracy than training with full data (98.32% vs. 99.38% and 99% vs. 100.00%). These results suggest that the catastrophic forgetting problem can be reduced by the proposed framework over AMCF and CWRU. Another interesting finding is that NCC may help to obtain a robust classifier when noise is presented in data. Using this proposed framework, we showed that a classifier, based on a deep learning model, may be trained incrementally, achieving satisfactory diagnosis results for fault detection in IMs and maintaining a constant complexity of the model. As future work, we are interested in developing an end-to-end MCIL framework, where the feature extractor and the classifier can be trained jointly. Likewise, we are planning to extend our study for the diagnostic of incipient and electrical faults.

Data Availability

The data used to support the findings of this study are included within the article.

Conflicts of Interest

The authors declare no conflicts of interest with respect to the research, authorship, and/or publication of this article.

Acknowledgments

This research was financially supported by National Institute For Astrophysics, Optics, and Electronics.

References

[1] Y. Liang, B. Li, and B. Jiao, "A deep learning method for motor fault diagnosis based on a capsule network with gate-structure dilated convolutions," *Signal Processing*, vol. 17, no. 18, 2020.

[2] G. Adam, W. Glowacz, J. Kozik et al., "Detection of deterioration of three-phase induction motor using vibration signals," *Measurement Science Review*, vol. 19, no. 6, pp. 241–249, 2019.

[3] A. Omar, F. Alkahatni, M. Masadeh et al., "Sounds and acoustic emission-based early fault diagnosis of induction motor: a review study," *Advances in Mechanical Engineering*, vol. 13, no. 2, 2021.

[4] M. M. Rahman and M. N. Uddin, "Online unbalanced rotor fault detection of an im drive based on both time and frequency domain analyses," *IEEE Transactions on Industry Applications*, vol. 53, no. 4, pp. 4087–4096, 2017.

[5] A. Y. Khodja, N. Guersi, M. N. Saadi, and N. Boutasseta, "Rolling element bearing fault diagnosis for rotating machinery using vibration spectrum imaging and convolutional neural networks," *International Journal of Advanced Manufacturing Technology*, vol. 106, no. 5, pp. 1737–1751, 2020.

[6] F. Cipollini, L. Oneto, A. Coraddu, and S. Savio, "Unsupervised deep learning for induction motor bearings monitoring," *Data-Enabled Discovery and Applications*, vol. 3, no. 1, 2019.

[7] J. Wu, T. Tang, M. Chen, Yi Wang, and K. Wang, "A study on adaptation lightweight architecture based deep learning models for bearing fault diagnosis under varying working conditions," *Expert Systems with Applications*, vol. 160, Article ID 113710, 2020.

[8] J. R. R. Guillen, J. A. B. Hurtado, J. J. D. S. Perez, D. G. Lieberman, and J. P. A. Sanchez, "Convolutional neural network and motor current signature analysis during the transient state for detection of broken rotor bars in induction motors," *Sensors*, vol. 20, no. 13, 2020.

[9] F. B. Abid, M. Sallem, and A. Braham, "Robust interpretable deep learning for intelligent fault diagnosis of induction motors," *IEEE Transactions on Instrumentation and Measurement*, vol. 69, no. 6, pp. 3506–3515, 2020.

[10] X. Li, J. Li, C. Zhao, Y. Qu, and D. He, "Gear pitting fault diagnosis with mixed operating conditions based on adaptive 1d separable convolution with residual connection," *Mechanical Systems and Signal Processing*, vol. 142, Article ID 106740, 2020.

[11] C. Wu, P. Jiang, C. Ding, F. Feng, and T. Chen, "Intelligent fault diagnosis of rotating machinery based on one-dimensional convolutional neural network," *Computers in Industry*, vol. 108, pp. 53–61, 2019.

[12] Y. Wang, J. Zhou, L. Zheng, and C. Gogu, "An end-to-end fault diagnostics method based on convolutional neural network for rotating machinery with multiple case studies," *Journal of Intelligent Manufacturing*, vol. 32, pp. 1–22, 2020.

[13] Y. Liu and Y. Su, "An-an liu, bernt schiele and qianru sun. "Mnemonics training: multi-class incremental learning without forgetting"" in *Proceedings of the IEEE/CVF Conference on Computer Vision and Pattern Recognition*, pp. 12245–12254, IEEE, Seattle, WA, USA, June 2020.

[14] J. J. S. Dorantes, M. D. Prieto, R. A. O. Rios, and R. D. J. T. Romero, "Industrial data-driven monitoring based on incremental learning applied to the detection of novel faults," *IEEE Transactions on Industrial Informatics*, vol. 16, no. 9, pp. 5985–5995, 2020.

[15] X. Wang, X. Liu, and Y. Li, "An incremental model transfer method for complex process fault diagnosis," *IEEE/CAA Journal of Automatica Sinica*, vol. 6, no. 5, pp. 1268–1280, 2019.

[16] E. Belouadah, A. Popescu, and I. Kanellos, "A comprehensive study of class incremental learning algorithms for visual tasks," *Neural Networks: The Official Journal of the International Neural Network Society*, vol. 135, pp. 38–54, 2021.

[17] S. Rebuffi, A. Kolesnikov, G. Sperl, and C. H. Lampert, "icarl: incremental classifier and representation learning," in *Proceedings of the 2017 IEEE Conference on Computer Vision and Pattern Recognition (CVPR)*, pp. 5533–5542, IEEE, Honolulu, HI, USA, July 2017.

[18] I. Goodfellow, Y. Bengio, and A. Courville, *Deep Learning*, MIT Press, 2016.

[19] H. Zeng, Z. Wu, J. Zhang et al., "Eeg emotion classification using an improved sincnet-based deep learning model," *Brain Sciences*, vol. 9, no. 11, 2019.

[20] M. Ravanelli and Y. Bengio, "Speaker recognition from raw waveform with sincnet," in *Proceedings of the 2018 IEEE Spoken Language Technology Workshop (SLT)*, pp. 1021–1028, IEEE, Athens, Greece, December 2018.

[21] L. Rabiner and R. Schafer, *Theory and Applications of Digital Speech Processing*, Prentice Hall Press, NJ, USA, 2010.

[22] B. Zhou, A. Khosla, A. Lapedriza, A. Oliva, and A. Torralba, "Learning deep features for discriminative localization," in *Proceedings of the IEEE conference on computer vision and pattern recognition*, pp. 2921–2929, IEEE, Las Vegas, NV, USA, June 2016.

[23] S. Hou, X. Pan, C. C. Loy, Z. Wang, and D. Lin, "Learning a unified classifier incrementally via rebalancing," in *Proceedings of the IEEE Conference on Computer Vision and Pattern Recognition*, pp. 831–839, IEEE, Long Beach, CA, USA, June 2019.

[24] R. Tibshirani, T. Hastie, B. Narasimhan, and G. Chu, "Diagnosis of multiple cancer types by shrunken centroids of gene expression," *Proceedings of the National Academy of Sciences*, vol. 99, no. 10, pp. 6567–6572, 2002.

[25] W. A. Smith and R. B. Randall, "Rolling element bearing diagnostics using the case western reserve university data: a benchmark study," *Mechanical Systems and Signal Processing*, vol. 64, pp. 100–131, 2015.

[26] D. P. Kingma and B. Jimmy, "Adam: a method for stochastic optimization," in *Proceedings of the International Conference on Learning Representations*, Cornell University Press, San Diego, California, December 2014.

[27] G. Montavon, B. O Genevieve, and M. K. Robert, "Neural Networks: Tricks Of the Trade," *Lecture Notes In Computer Science*, Vol. 7700, Springer, Berlin/Heidelberg, Germany, Second edition, 2012.

Hindawi
Shock and Vibration
Volume 2021, Article ID 9958412, 12 pages
https://doi.org/10.1155/2021/9958412

Research Article

Failure Probability Modeling of Miniature DC Motors and Its Application in Fault Diagnosis

Zhiping Xie, Rongchen Zhao, Jiming Zheng, and Yancheng Lang

School of Mechanical & Electrical Engineering, Guizhou Normal University, Guiyang 550001, China

Correspondence should be addressed to Rongchen Zhao; zhaorongchen99@gmail.com

Received 28 March 2021; Accepted 18 May 2021; Published 8 October 2021

Academic Editor: Mickael Lallart

This paper proposes a fault diagnosis method for miniature DC motors (MDCMs) in the presence of the uncertainties caused by material and random factors of the production process. In this method, the probability models of fault multiple features are established based on the advantage criterion of the maximum overall average membership to determine the distribution of fault multiple features. The fault diagnosis algorithm is synthesized to obtain the threshold ranges of fault multiple features according to different confidence levels. Experimental test results are presented and analyzed to validate the efficiency and performance of the proposed fault diagnosis method.

1. Introduction

Due to their small size, lightweight, and easy control, miniature DC motors (MDCMs) are widely used in the industrial fields of home appliances, office automation, automotive parts, etc. [1]. In these applications, the efficient and reliable operation of MDCMs is increasingly important. However, the factory quality inspection of MDCMs mainly relies on the manual experience, which leads to low production efficiency, heavy workload, and missed inspection [2]. Therefore, the effective motor fault detection technology on the production line is crucial for the factory quality of MDCMs.

Generally, there are four main techniques for the motor fault diagnosis, which are classified into the signal-based, model-based, data-based, and indicator-based method classes [3, 4]. The signal-based method uses sensor equipment to measure the diagnostic signals of the motor, such as current [5], vibration [6], acoustic [7], and thermal [8], and the fault type is detected by comparing and analyzing the diagnostic signals. Measurements of the acoustic signal, vibration signal, and thermal signal are noninvasive. The motor current signature analysis (MCSA) has been successfully applied to the fault diagnosis of DC motors and induction motors, especially under steady-state conditions and rated load [9]. However, the signal-based method requires a large number of sensing devices.

The model-based method relies on the theoretical analysis of the motor, which key is to establish the motor model under the fault condition [3]. The motor fault can be detected by comparing the actual parameters with the estimated parameters of the properly functioning motor. Residual analysis and suitable signal processing are used to define the fault indicators [3]. Winding function approach [10], dynamic mesh reluctance approach [3], and finite element approach [11] were used to model. The available models are nice analytical tools predicting motor behavior, but their parameters are not easily determined. The least-squares (LS) method [11, 12], fully decoupled parity equation [13], and universal adaptive stabilizer [14] were used to estimate the motor parameters. Since the motor faults generally change multiple electromechanical parameters, it is difficult to establish a fault prediction model of the complex fault systems.

The data-based method is a powerful tool to improve the effectiveness and reliability of the diagnosis since it does not require any knowledge about motor parameters and models [3, 4]. Artificial intelligence techniques are widely used in the

data-based method, which need to use the healthy and faulty motor data for feature extraction and classification. Several artificial intelligence techniques, such as neural networks [15, 16], support vector machine [15], fuzzy logic [17], expert system networks [18], deep learning [19], and algorithms [20], have been developed to detect the motor faults. The combinations of the above techniques have been reported in the literature. The convolutional neural network (CNN) was used for extracting features, and then the support vector machine [21] and deep transfer learning [22] were used to diagnose faults. The application of artificial intelligence techniques in the motor fault diagnosis can promote the automation of the diagnostic process. However, these methods require a large set of training samples [23], and the generalization performance of artificial intelligence techniques has limitations.

The indicator-based method is to compare the measured value with the indicator threshold, which is a widely used fault diagnosis method. An and Li [24] proposed the permutation entropy of the reconstructed signal as the fault feature of piezoelectric ceramics. Jafari et al. [25] established four different indices and used the well-established Otsu thresholding technique to set the index thresholds for fault diagnosis. Ali and Liang [26] used d8 for the fault indicator, and the indicator threshold was determined using the universal threshold technique. Irfan et al. [27] designed an adaptive threshold scheme using the statistical decision theory. An accurate indicator threshold is essential for the indicator-based method. In addition, in the manufacturing process of MDCMs, various uncontrollable factors (material nonlinearity and random factors of the production process) lead to uncertainties of the MDCM output performance. Therefore, a fixed indicator threshold is difficult to apply to the fault diagnosis of the MDCM.

Fault diagnosis methods of the MDCM need to consider the uncertainty of the production process. Wang et al. [23] used a probability modeling approach for photovoltaic fault diagnosis to solve the problems of the nonlinearity and uncertainty of the PV array output interval. Liu et al. [28] proposed a failure probability calculation method for power equipment based on multicharacteristic parameters. Li et al. [29] proposed an adaptive dynamic update model of the equipment alarm threshold based on a similar proportion and state probability model. Wen and Gao [30] estimated the probability distribution of health indicator points, and the deterioration of the ball screw is evaluated by the probability distribution. The probability density function of fault indicators can be determined using the error comparison method [23] and kernel density estimation [29, 30].

However, the probabilistic fault diagnoses of DC motors have not been considered in the previous studies. This paper proposes a novel solution to apply a fault diagnosis method for the MDCM by incorporating the probability modeling and the advantage criterion of the maximum overall average membership.

The novelties and contributions of this paper are summarized as follows:

(1) Proposing the advantage criterion of the maximum overall average membership to determine the optimal fitting distribution, which cannot be handled by the traditional hypothesis test

(2) Designing a fault diagnosis algorithm based on probability modeling to deal with the uncertainties caused by material and random factors of the production process, improving the accuracy of MDCM fault diagnosis

(3) Designing the diagnostic test platform of MDCMs to validate the performance of the proposed fault diagnosis method

The rest of this paper is arranged as follows: in Section 2, the structure of the MDCM and data sources are described in detail. In Section 3, the probability models of fault multiple features are established using the advantage criterion of the maximum overall average membership, and the fault diagnosis method is discussed in detail, which is verified in Section 4. Section 5 summarizes this paper and outlines future research directions.

2. Data Acquisition

2.1. Structure of the MDCM. Figure 1 shows the schematic diagram of the MDCM discussed in this paper. The MDCM consists of a rotor and a stator (Figure 1(a)). The stator is equipped with a ring permanent magnet, and the rotor consists of three coil windings which are wounded on three teeth [31]. The motor windings are connected by a triangle connection (Figure 1(b)). The parameters of a healthy MDCM used for testing are listed in Table 1.

2.2. Data Sources. By analyzing and solving the mathematical model of the MDCM, the fault multiple features, namely, DC component (P_{dc}), frequency point (f_m), amplitude of frequency point (P_f), and spectrum area (A), were proposed to diagnose motor faults in [2]. Figure 2 shows the structure diagram of data acquisition of the MDCM with no load. After preamplification, low-pass filtering, analog-to-digital (A/D) converter, and fast Fourier transform (FFT) conversion, the frequency domain data of fault multiple features (P_{dc}, f_m, P_f, and A) can be obtained by the data statistics [2]. In this paper, the healthy motor (HM), the interturn short fault motor (ISFM), the open winding fault motor (OWFM), the winding desoldering fault motor (WDFM), and the abnormal magnet loop fault motor (AMFM) were studied. 110 healthy motors and 60 motors (Xiamen Dazhen Electric Co., Ltd.) with each fault type were randomly selected as experimental samples.

3. Fault Diagnosis Method

3.1. Maximum Overall Average Membership Advantage Criterion. The advantage criterion of the maximum overall average membership was used to determine the distribution of the fault multiple features [32, 33]. The key to the

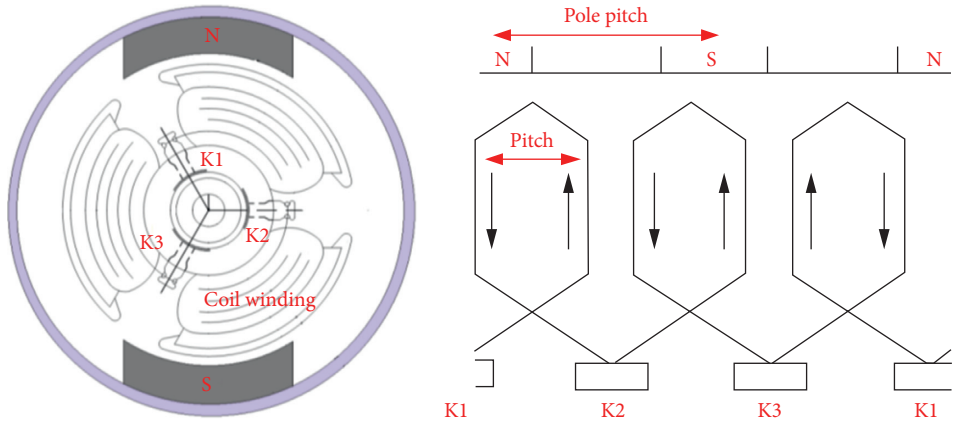

Figure 1: Schematic diagram of the MDCM: (a) structure of the MDCM; (b) coil winding diagram.

Table 1: Main parameters of a healthy MDCM.

Motor parameters	Values
Rated voltage	5.0 V DC
No load current	45 mA max
No load speed	5400–6700 r/min
Phase resistance of the winding	18 Ω
Moment of inertia	$2.668 \times 10\text{–}7\ \mathrm{kgm}^2$
Damping coefficient	4×10^{-7}
Number of poles	2

advantage criterion of the maximum overall average membership is to construct membership functions.

Step 1. Determine the membership function.

Let the domain of the fault multiple features' distribution model be U, and $\tilde{A}_1$, $\tilde{A}_2$, $\tilde{A}_3$, and $\tilde{A}_4$ denote the normal distribution, exponential distribution, Weibull distribution, and lognormal distribution, respectively. They are the fuzzy subset of $F(U)$. Y is a sample of U, $Y = \{y_1, y_2, \ldots, y_n\}^T$, where n is the number of motor samples. The membership function $\mu_{\tilde{A}_i}(y_j)$ $(i = 1, 2, 3, 4)$ represents the fuzzy membership degree of the y_jth index in the sample Y to the fuzzy subset $\tilde{A}_i$. The normalization of $\mu_{\tilde{A}_i}(y_j)$ is as follows:

$$\mu_{\tilde{A}_1}(y_j) + \mu_{\tilde{A}_2}(y_j) + \mu_{\tilde{A}_3}(y_j) + \mu_{\tilde{A}_4}(y_j) = 1, \quad j = 1, 2, \ldots, n. \tag{1}$$

Normal distribution membership function $\mu_{\tilde{A}_1}(y_j)$ is expressed as

$$\mu_{\tilde{A}_1}(y_j) = \frac{F_1(y_j)}{F_1(y_j) + F_2(y_j) + F_3(y_j) + F_4(y_j)}, \tag{2}$$

where

$$\begin{aligned}
F_1(y_j) &= 1 - \left| \varnothing\left(\frac{y_j - \mu}{\sigma}\right) - F(y_j) \right|, \\
\varnothing\left(\frac{y_j - \mu}{\sigma}\right) &= \int_{-\infty}^{y_j - \mu/\sigma} \frac{1}{\sqrt{2\pi}} e^{-t^2/2} \mathrm{d}t, \\
F_2(y_j) &= 1 - \left| 1 - e^{-y_j/\lambda} - F(y_j) \right|, \\
F_3(y_j) &= 1 - \left| 1 - e^{-(y_j/\eta)^{\beta}} - F(y_j) \right|, \\
F_4(y_j) &= 1 - \left| \varnothing\left(\frac{\ln y_j - \mu_l}{\sigma_l}\right) - F(y_j) \right|, \\
\varnothing\left(\frac{\ln y_j - \mu_l}{\sigma_l}\right) &= \int_{-\infty}^{\mathrm{n}y_j - \mu_l/\sigma_l} \frac{1}{\sqrt{2\pi}} e^{-t^2/2} \mathrm{d}t,
\end{aligned} \tag{3}$$

where $\varnothing(y_j - \mu/\sigma)$ and $F(y_j)$ are the distribution function of the normal distribution and the empirical cumulative distribution function of the sample data, respectively. Parameters σ and μ are estimated from the sample data. $1 - e^{-y_j/\lambda}$ is the distribution function of the exponential distribution, and the parameter λ is estimated from the sample data. $1 - e^{-(y_j/\eta)^m}$ is the distribution function of the Weibull distribution, and the parameters η and m are estimated from the sample data. $\varnothing(\ln y_j - \mu/\sigma)$ is the distribution function of the lognormal distribution, and the parameters σ_l and μ_l are estimated from the sample data.

Exponential distribution membership function $\mu_{\tilde{A}_2}(y_j)$ is expressed as

$$\mu_{\tilde{A}_2}(y_j) = \frac{F_2(y_j)}{F_1(y_j) + F_2(y_j) + F_3(y_j) + F_4(y_j)}. \tag{4}$$

Weibull distribution membership function $\mu_{\tilde{A}_3}(y_j)$ is expressed as

$$\mu_{\tilde{A}_3}(y_j) = \frac{F_3(y_j)}{F_1(y_j) + F_2(y_j) + F_3(y_j) + F_4(y_j)}. \tag{5}$$

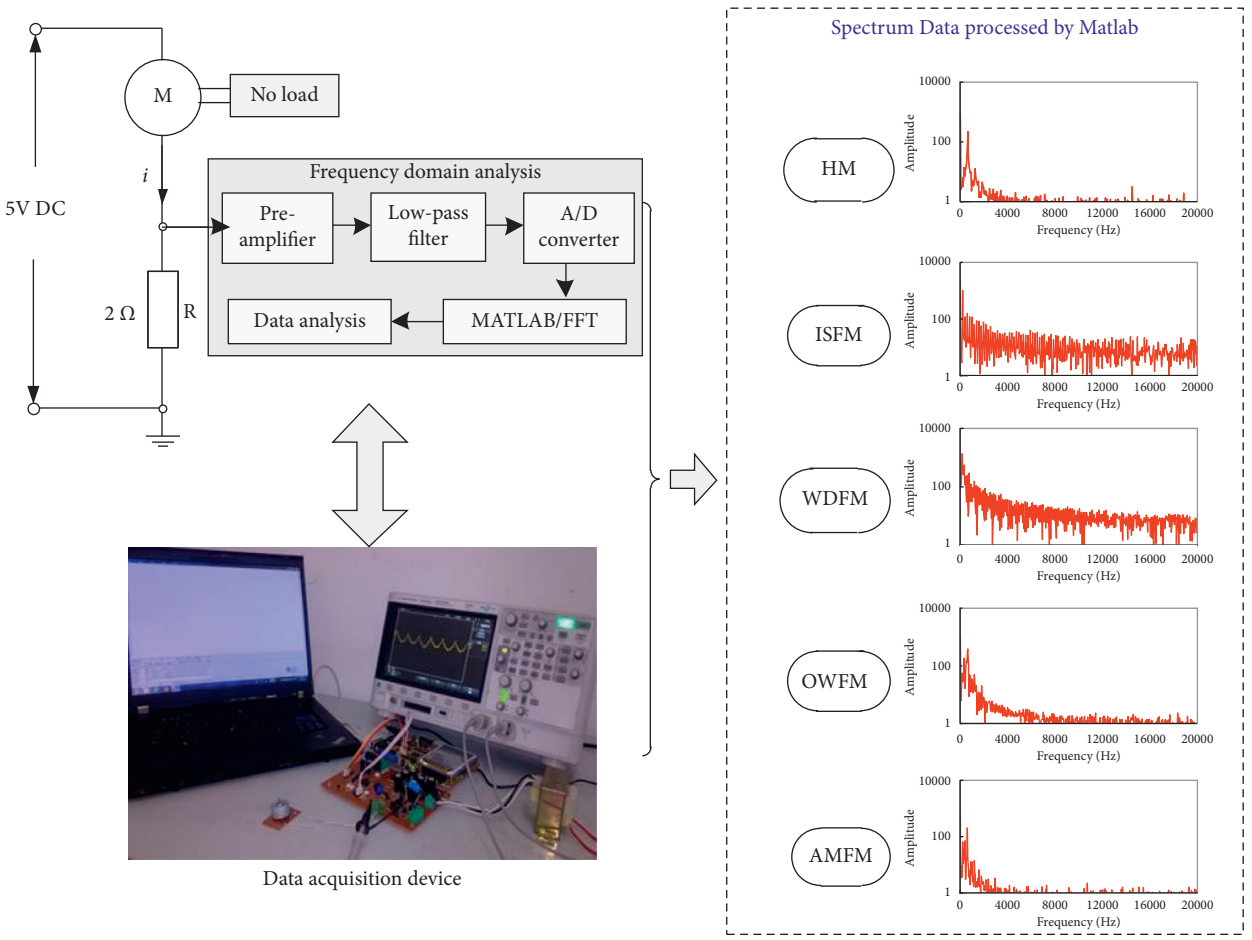

Figure 2: Data acquisition of the MDCM.

Logarithmic normal distribution membership function $\mu_{\tilde{A}_4}(y_j)$ is expressed as

$$\mu_{\tilde{A}_4}(y_j) = \frac{F_4(y_j)}{F_1(y_j) + F_2(y_j) + F_3(y_j) + F_4(y_j)}. \quad (6)$$

Step 2. Calculate the local membership advantage.

The local membership advantage $\Delta\mu_{\tilde{A}_i}(x_j)$ is defined as

$$\Delta\mu_{\tilde{A}_i}(x_j) = \mu^{(i)}_{\tilde{A}_k}(y_j) - \min\left\{\mu_{\tilde{A}_i}(y_j)\right\}, \quad i = 1, 2, 3, 4;\ j = 1, 2, \ldots, n, \quad (7)$$

where $\mu^{(i)}_{\tilde{A}_k}(y_j)$ represents the new sequence of $\mu_{\tilde{A}_i}(y_j)$ sorted from the largest to the smallest. k represents the sort of the new sequence, and i represents the sort of the original sequence.

Step 3. Calculate the overall average membership advantage.

The overall average membership advantage $\mu_{\tilde{A}_i}(Y)$ is defined as

$$\mu_{\tilde{A}_i}(Y) = \frac{1}{n}\sum_{j=1}^{n}\Delta\mu_{\tilde{A}_i}(y_j), \quad i = 1, 2, 3, 4. \quad (8)$$

Step 4. Calculate the maximum overall average membership advantage.

The maximum overall average membership advantage $\mu_{\tilde{A}}(Y)$ is defined as

$$\mu_{\tilde{A}}(Y) = \max\left\{\mu_{\tilde{A}_1}(Y), \mu_{\tilde{A}_2}(Y), \mu_{\tilde{A}_3}(Y), \mu_{\tilde{A}_4}(Y)\right\}. \quad (9)$$

3.2. Distribution Characteristics of Fault Multiple Features. Figure 3 shows the process of determining the distribution of fault multiple features. The maximum likelihood estimation method was used to estimate the parameters of the hypothetical distribution of fault multiple features. The advantage criterion of the maximum overall average membership was used to determine the distribution type of fault multiple features. The overall average membership advantage $\mu_{\tilde{A}_i}(Y)$ of fault multiple features was calculated based on the experimental data. The results of the hypothetical distribution of the fault multiple features are shown in Table 2. Because the resolution of the current spectrum is 40 Hz and the data interval of f_m is narrow, f_m does not meet any hypothetical distribution. Therefore, it is not necessary to confirm its distribution using the advantage criterion of the maximum overall average membership.

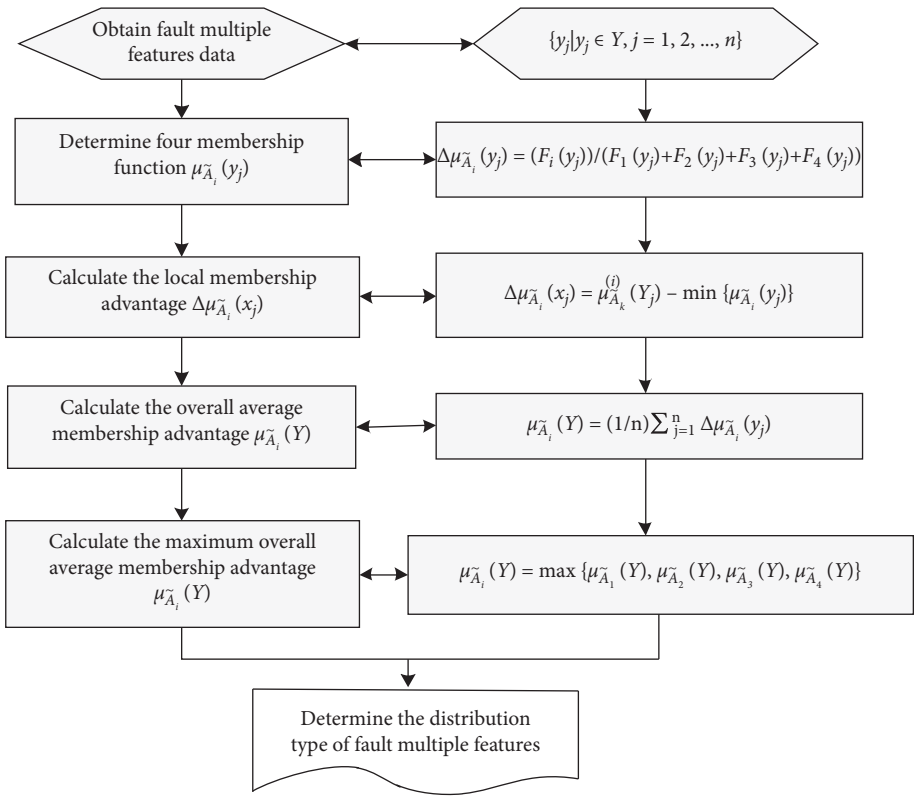

Figure 3: The flowchart of determining the distribution of fault multiple features.

Table 2: Results of the hypothetical distribution.

Type of fault	Indicators	Hypothetical distribution							
		Normal		Exponential		Weibull		Lognormal	
		μ, σ	$\mu_{\tilde{A}_1}(Y)$	λ	$\mu_{\tilde{A}_2}(Y)$	η, β	$\mu_{\tilde{A}_3}(Y)$	μ_l, σ_l	$\mu_{\tilde{A}_4}(Y)$
HM	P_{dc}	893.82, 59.98	0.0667	893.82	0.0009	922.32, 15.07	0.0607	6.79, 0.067	0.0673
	P_f	222.16, 35.44	0.0562	222.16	0.0010	237.08, 7.27	0.0580	5.39, 0.166	0.0531
	A	809.02, 200.36	0.0484	809.02	0.0011	887.39, 4.38	0.0472	6.67, 0.250	0.0487
ISFM	P_{dc}	2103.8, 84.30	0.0674	2103.8	0.0026	2144.8, 24.6	0.0609	7.65, 0.040	0.0679
	P_f	1050.22, 54.76	0.0669	1050.22	0.0005	1075.34, 21.94	0.0650	6.96, 0.053	0.065
	A	5632.8, 148.47	0.0709	5632.8	0.0011	688.19, 11.09	0.0643	8.64, 0.026	0.0622
OWFM	P_{dc}	661.78, 56.39	0.0631	659.58	0.0003	679.73, 16.19	0.0546	6.49, 0.084	**0.065**
	P_f	185.92, 23.38	0.0613	185.92	0.0003	196.12, 8.98	0.0589	5.22, 0.129	0.0599
	A	861.74, 53.19	0.0659	861.74	0.0017	887.19, 15.60	0.0580	6.76, 0.061	0.0647
WDFM	P_{dc}	915.66, 58.57	0.0657	915.66	0.0021	943.87, 14.56	0.0562	6.82, 0.063	0.0654
	P_f	1355.33, 70.9	0.0686	1355.33	0.0019	1389.57, 18.92	0.0618	7.21, 0.052	0.0696
	A	9780.93, 228.4	0.0701	9780.93	0.0022	9895.76, 39.81	0.0609	9.19, 0.023	0.0648
AMFM	P_{dc}	1072.4, 97.79	0.0627	1072.4	0.0005	1117, 11.8	0.0607	6.97, 0.092	0.0621
	P_f	380.54, 31.72	0.0629	380.54	0.0004	394.56, 14.60	0.0638	5.94, 0.085	0.0622
	A	2662.9, 139.8	0.0667	2662.9	0.0025	2730.83, 18.72	0.0604	7.89, 0.052	0.063

It can be seen from Table 2 that $\mu_{\tilde{A}_4}(Y)$ of P_{dc} is the largest among all of them for HM, and it obeys lognormal distribution according to the advantage criterion of the maximum overall average membership. P_f and A obey the Weibull distribution and lognormal distribution, respectively. For ISFM, OWFM, WDFM, and AMFM, the process of determining the distribution of fault multiple features is similar to that of HM.

3.3. Probability Density Function of Fault Multiple Features. The probability density functions of the fault multiple features for HM, ISFM, OWFM, WDFM, and AMFM are shown in Table 3. It can be seen from Table 3 that the fault multiple features obey normal distribution, lognormal distribution, and Weibull distribution, respectively.

The probability density function diagrams of the fault multiple features in different conditions are shown in

Table 3: Probability density function of the fault multiple features.

Type of fault	P_{dc}	P_f	A
HM	$1/\sqrt{2\pi}\times 0.067xe^{-(lnx-6.79)^2/2\times 0.067^2}$	$7.27/237.08\,(x/237.08)^{6.27}e^{-(x/237.08)^{7.27}}$	$1/\sqrt{2\pi}\times 0.025xe^{-(lnx-6.67)^2/2\times 0.025^2}$
ISFM	$1/\sqrt{2\pi}\times 0.04xe^{-(lnx-7.65)^2/2\times 0.04^2}$	$1/\sqrt{2\pi}\times 54.76e^{-(x-1050.22)^2/2\times 54.76^2}$	$1/\sqrt{2\pi}\times 148.47e^{-(x-5632.8)^2/2\times 148.47^2}$
OWFM	$1/\sqrt{2\pi}\times 0.084xe^{-(lnx-6.49)^2/2\times 0.084^2}$	$1/\sqrt{2\pi}\times 23.38e^{-(x-185.92)^2/2\times 23.38^2}$	$1/\sqrt{2\pi}\times 53.19e^{-(x-861.74)^2/2\times 53.19^2}$
WDFM	$1/\sqrt{2\pi}\times 58.57e^{-(x-915.66)^2/2\times 58.57^2}$	$1/\sqrt{2\pi}\times 0.052xe^{-(lnx-7.21)^2/2\times 0.052^2}$	$1/\sqrt{2\pi}\times 0228.4e^{-(x-9780.93)^2/2\times 0228.4^2}$
AMFM	$1/\sqrt{2\pi}\times 97.79e^{-(x-1072.4)^2/2\times 97.79^2}$	$14.6/394.56\,(x/394.56)^{13.6}e^{-(x/394.56)^{14.6}}$	$1/\sqrt{2\pi}\times 139.8e^{-(x-2662.9)^2/2\times 139.8^2}$

Figure 4. The characteristics of the probability density function are summarized as follows:

(1) The distribution of each fault multiple feature changes with the type of fault.

(2) There is no obvious regularity in the distribution of fault multiple features.

(3) It can clearly distinguish HM, ISFM, and WDFM using fault multiple features.

(4) The probability density curves of HM and OWFM have overlapping areas. Through the setting threshold range of P_{dc}, it is possible to distinguish between HM and OWFM.

3.4. Threshold of Fault Multiple Features. The probability distribution of fault multiple features with different fault types was determined using the probability statistics and the advantage criterion of the maximum overall average membership. The threshold range of fault multiple features with different fault types can be calculated by the following equation:

$$P\{t_l \le x \le t_u\} = \int_{t_l}^{t_u} f(x)\mathrm{d}x = 1-\alpha, \tag{10}$$

where t_l and t_u are the lower and upper bounds of the threshold range, $f(x)$ is the probability density function of each fault multiple feature, and $(1-\alpha)$ is the confidence level.

By comparing the threshold range of fault multiple features with different confidence levels, the optimal confidence level of fault multiple features was determined. The confidence levels of fault multiple features were set to 95%, 90%, 85%, and 80%, and the performance of different confidence levels was discussed. As shown in Figure 5, the threshold ranges of fault multiple features with different confidence levels were calculated. As can be seen from Figure 5, the larger the confidence level setting is, the larger the upper bound of the threshold range is and the smaller the lower bound of the threshold range is. It means that, as the confidence level increases, the threshold range becomes larger.

Table 4 shows the overbound rates for different confidence levels which can be used as a reference for the threshold range setting of the fault multiple features. It can be seen from Table 4 that the smaller the confidence level is, the larger the overbound rates' data and overbound rates are. In order to avoid a faulty motor being misjudged as a HM, the confidence level of fault diagnosis for the HM was set to 90%, and the confidence level of the faulty motor was set to 95% according to the results in Figure 4 and Table 4. The threshold ranges of the HM with a confidence level of 90% were calculated by equation (10) as shown in Figure 6.

By modeling the probability distribution of fault indicators in different fault conditions, the threshold ranges of fault multiple features with a confidence level of 90% were calculated by equation (10). Figure 7 shows the threshold ranges of the ISFM with a confidence level of 95%. The upper and lower bounds of the threshold ranges for each fault multiple feature are shown in Table 5, in which $f_m = kcpn/60$, where k, c, p, and n are the number of commutators, the coefficient determined by the number of commutators, the number of pole pairs, and the rotational speed, respectively. The speed range of the HM is 5400–6700 r/min, so the threshold range of f_m is [540, 670]. Similarly, the threshold ranges of f_m for other faulty motors are shown in Table 5. It can be seen from Table 5 that the threshold ranges of P_{DC} of the HM and P_{DC} of the OWFM do not overlap, and the HM and the OWFM can be diagnosed.

3.5. Fault Diagnosis Algorithm. The fault classification indicator $d_i(m)$ was defined to measure the membership degree of the tested motor (m) belonging to the ith motor type (HM, ISFM, OWFM, WDFM, and AMFM), and it can be calculated by the following equation:

$$d_i(m) = \prod_{j=1}^{j=4} u_{ij}\left(m_j\right), \quad (i = 1,2,3,4,5;\ j = 1,2,3,4), \tag{11}$$

where m_j is the jth fault multiple features of the tested motor m. $u_{ij}(m_j)$ reflects whether m_j is in the threshold range of the ith motor type, and it can be calculated by the following equation:

$$u_{ij}\left(m_j\right) = \begin{cases} 1, & t_{ij}^l \le m_j \le t_{ij}^u, \\ 0, & m_j \le t_{ij}^l \text{ or } m_j \ge t_{ij}^u, \end{cases} \tag{12}$$

where t_{ij}^l and t_{ij}^u are the lower and upper bound of the threshold range of the jth fault multiple features for the ith motor type (Table 4). According to equation (13), the tested motor was classified.

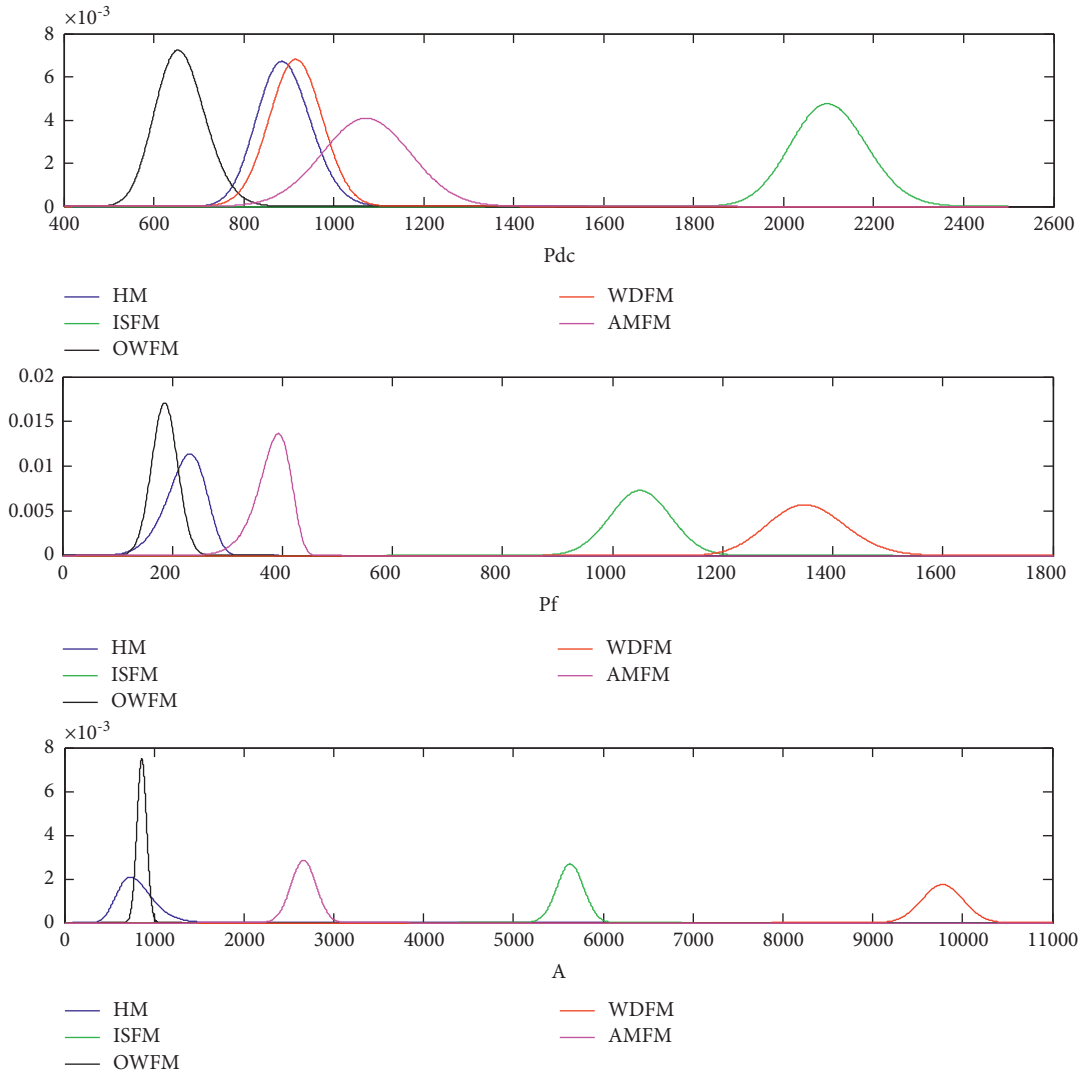

Figure 4: Probability density functions of the fault multiple features in different conditions.

$$\begin{cases} \text{If } d_1(m) = 1, \text{ then the tested motor is a } HM, \\ \text{if } d_2(m) = 1, \text{ then the tested motor is a } ISFM, \\ \text{if } d_3(m) = 1, \text{ then the tested motor is an } OWFM, \\ \text{if } d_4(m) = 1, \text{ then the tested motor is a } WDFM, \\ \text{if } d_5(m) = 1, \text{ then the tested motor is a } AMFM. \end{cases} \tag{13}$$

3.6. Steps of the Fault Diagnosis Method. Based on the above analysis, the MDCM fault diagnosis method is proposed and shown in Figure 8. The steps of the proposed fault diagnosis method can be summarized as follows.

Step 1. Data acquisition.

The armature currents are processed by a preamplifier, a low-pass filter, an A/D converter, and FFT transformation, and the values of fault multiple features are obtained.

Step 2. Confirm the probabilistic model.

Build the probability distribution model of fault multiple features, calculate the overall average membership advantage of each fault multiple feature, and then determine the probabilistic model of each fault multiple feature based on the advantage criterion of the maximum overall average membership.

Step 3. Calculate threshold ranges.

Calculate the threshold ranges of each fault multiple feature using the probability model.

Step 4. Fault diagnosis.

Calculate the fault classification indicator, and then give the fault diagnosis result of the tested motor based on the fault diagnosis algorithm.

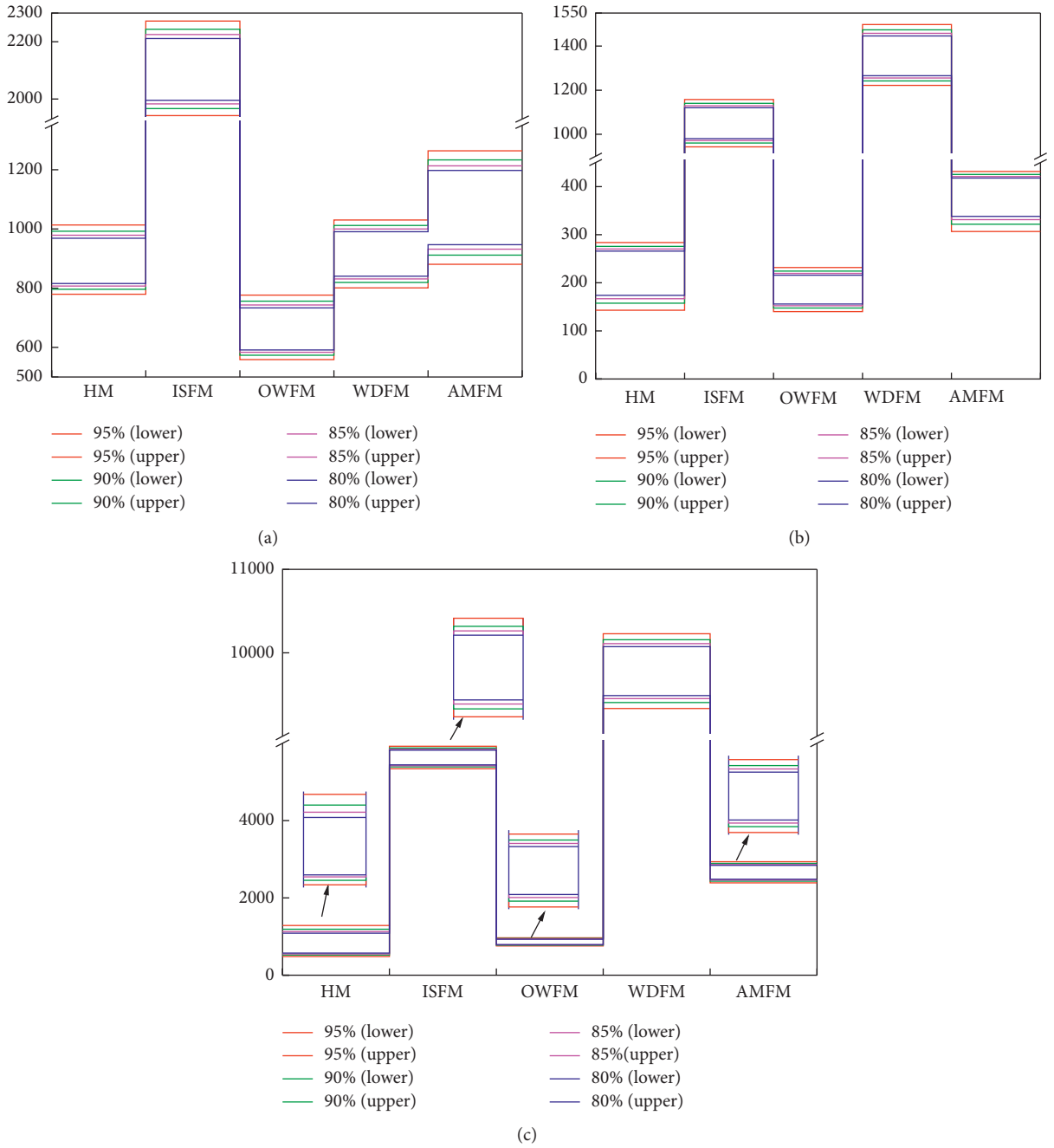

Figure 5: Threshold range of fault multiple features with different confidence levels: (a) P_{dc}, (b) P_f, and (c) A.

4. Performance Analysis of the Fault Diagnosis Method

4.1. Diagnostic Device. In order to verify the validity of the fault diagnosis method, the fault diagnosis experiments were performed. The diagnostic device of MDCMs is shown in Figure 9, which mainly includes the data collection and processing module, the microprocessing module, and the LCD display module. The function of the signal acquisition and processing module is to amplify the current signal and remove the high-frequency noise generated by the commutation. The STM32F107VCT chip is selected as the processor of the microprocessor module, which mainly plays the role of A/D sampling, FFT transformation, and fault diagnosis. The LCD display module mainly displays the fault multiple feature values and diagnosis results. 100 healthy motors and 30 motors (Xiamen Dazhen Electric Co., Ltd.) with each fault type were selected to test the proposed method.

4.2. Diagnostic Results. The fault diagnosis results of motors with different faults are shown in Table 6. Table 6 shows that one of the 100 HMs is misjudged as other faults, and the

Table 4: Overbound rates for different confidence levels.

Confidence level (%)	Fault multiple features	HM (%)	ISFM (%)	OWFM (%)	WDFM (%)	AMFM (%)
95	P_{dc}	2.73	5.00	3.33	6.67	3.33
	P_f	2.73	6.67	5.00	3.33	1.67
	A	0.91	6.67	6.67	6.67	3.33
90	P_{dc}	10.91	10.00	3.33	8.33	5.00
	P_f	7.27	11.67	10.00	8.33	11.67
	A	8.18	8.33	10.00	10.00	6.67
85	P_{dc}	16.36	11.67	6.67	10.00	13.33
	P_f	13.64	16.67	16.67	15.00	18.33
	A	17.27	10.00	13.33	11.67	16.67
80	P_{dc}	20.00	15.00	10.00	13.33	25.00
	P_f	24.55	21.67	23.33	20.00	26.67
	A	25.45	13.33	15.00	16.67	20.00

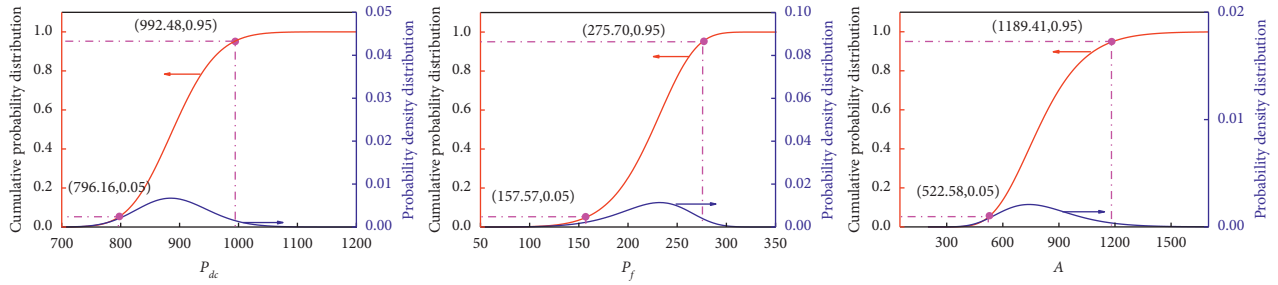

Figure 6: Threshold ranges of fault multiple features for the HM.

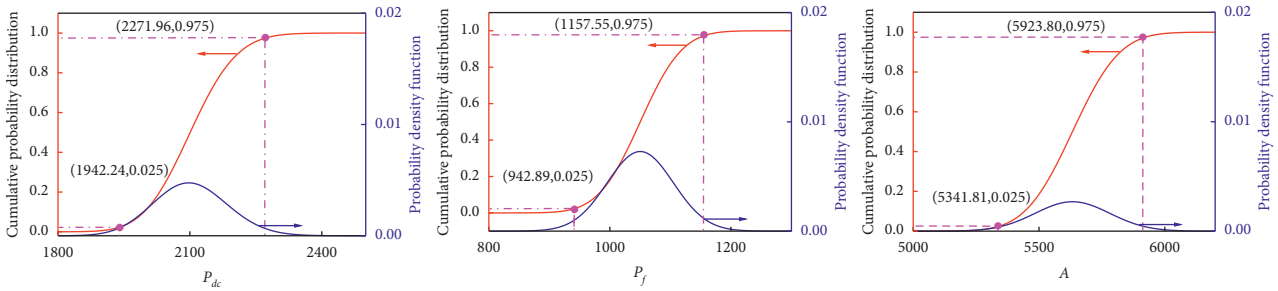

Figure 7: Threshold ranges of fault multiple features for the ISFM.

Table 5: Threshold of the fault multiple features in different conditions.

Type of fault	P_{dc}		f_m		P_f		A	
	t_1^l	t_1^u	t_2^l	t_2^u	t_3^l	t_3^u	t_4^l	t_4^u
HM	796.16	992.48	540.00	670.00	157.57	275.70	522.58	1189.41
ISFM	1942.24	2271.96	160.00	240.00	942.89	1157.55	5341.81	5923.80
OWFM	558.56	776.38	560.00	600.00	140.10	231.74	757.49	965.99
WDFM	800.86	1030.46	160.00	200.00	1221.80	1498.05	9333.27	1022.86
AMFM	880.73	1264.07	600.00	680.00	306.73	431.46	2388.89	2936.90

accuracy rate of HM is 99%. The reason is that the confidence level of HM was set to 90%, and the threshold ranges of fault multiple features were narrowed accordingly. From Table 6, the accuracy rate of ISFM, OWFM, WDFM, and AMFM is, respectively, 96.67%, 96.67%, 100%, and 93.33%, and the faulty motor has not been diagnosed as the healthy motor. The reason is that the confidence levels of ISFM, OWFM, WDFM, and AMFM were all set to 95%.

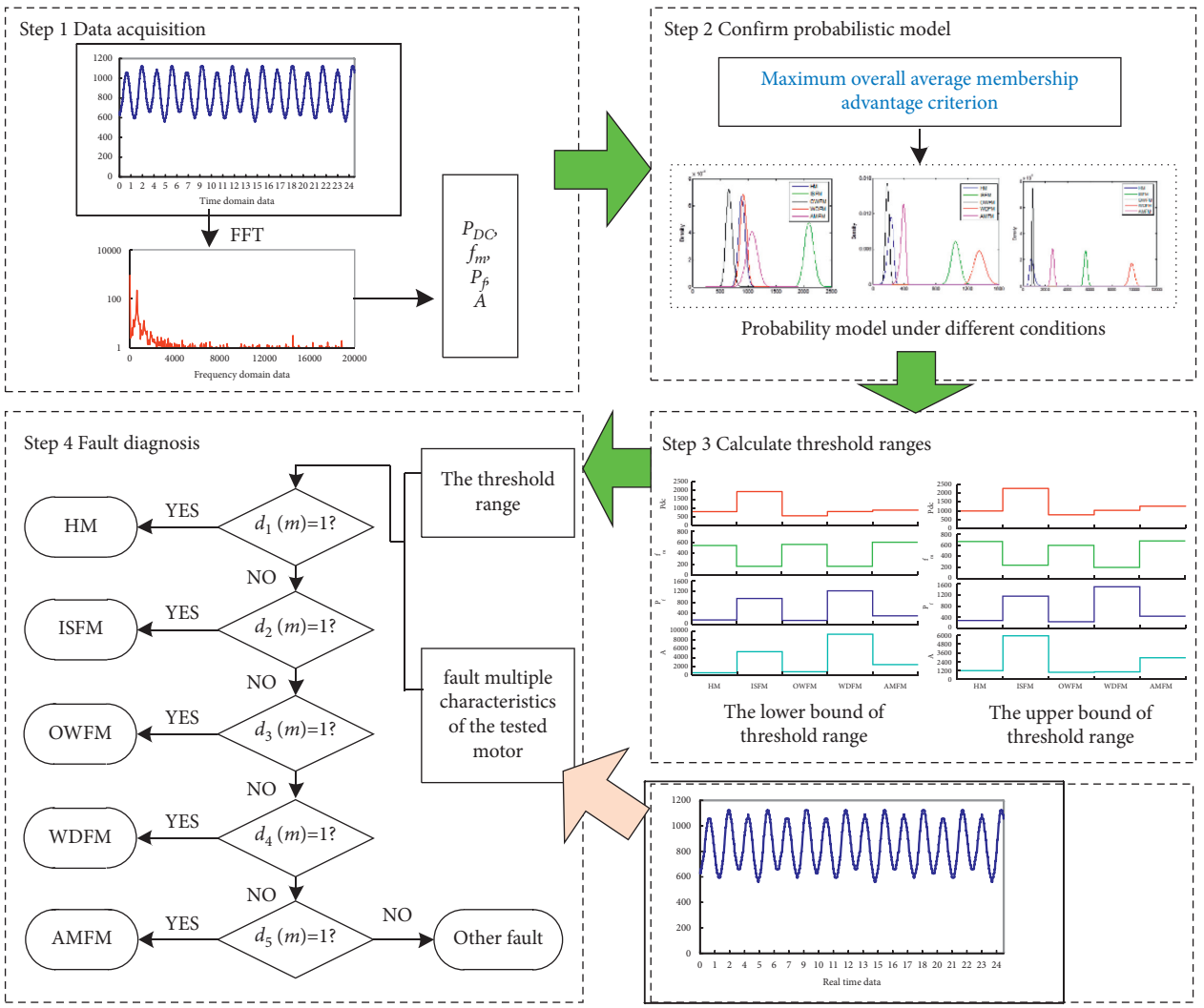

Figure 8: The flowchart of fault diagnosis.

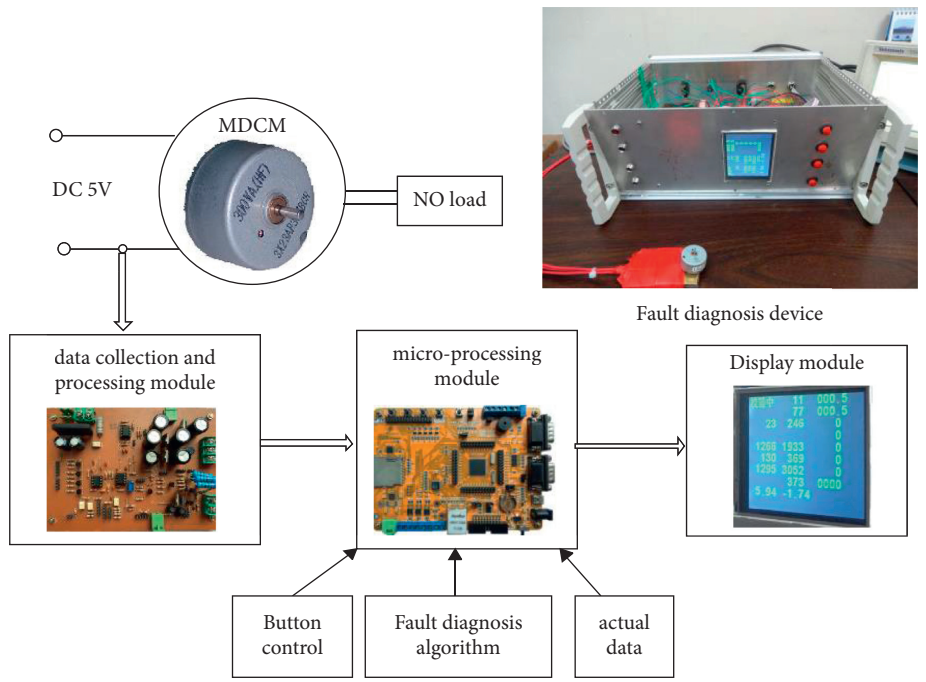

Figure 9: View of the fault diagnosis device.

Table 6: Diagnostic results of motors with different faults.

Type of fault	HM	ISFM	OWFM	WDFM	AMFM	Other faults	Accuracy rate (%)
HM	99	0	0	0	0	1	99
ISFM	0	29	0	0	0	1	96.67
OWFM	0	0	29	0	0	1	96.67
WDFM	0	0	0	30	0	0	100
AMFM	0	0	0	0	28	2	93.33

Table 7: Diagnostic results of motors on the production line.

Type of fault	Proposed method	Manual diagnosis
HM	2990	2990
Other faults	8	1 OWFM, 7 HMs
WDFM	2	2 WDFMs

To further calculate the diagnostic accuracy of the proposed method, 3000 motors were randomly selected from the production line, and the diagnostic accuracy of motors is calculated and shown in Table 7. It can be seen from Table 7 that the accuracy rate of HMs is 99.76%, and the faulty motor has not been diagnosed as the healthy motor. It means that the proposed method can be applied to the motor factory testing.

5. Conclusions

This paper proposes a probability modeling approach by the threshold ranges of each fault multiple feature. By calculating the overall average membership advantage of the four distribution functions, the probability density of fault multiple features can be determined; then, the threshold ranges of fault multiple features can be obtained. Finally, the validity of the fault diagnosis method is verified. In this paper, the main findings and the shortcomings can be summarized as follows:

(1) The membership functions of the normal distribution, exponential distribution, Weibull distribution, and lognormal distribution are established to calculate the maximum overall average membership advantage of the fault multiple features.

(2) The maximum overall average membership advantage criterion is used to determine the probability distribution model of fault multiple features, which solves the problem that the classical statistical analysis is difficult to determine the optimal probability distribution model.

(3) The threshold ranges of fault multiple features are calculated by setting the confidence of the probability density functions. The motor fault diagnosis algorithm is given based on the threshold range of fault multiple features.

(4) When the proposed method is applied to other types of motors, the probability model needs to be retrained.

Data Availability

The feature data of motor faults used to support the findings of this study are included within the article.

Conflicts of Interest

The authors declare no conflicts of interest.

Acknowledgments

The work described in this paper was supported by the Doctoral Research Project of Guizhou Normal University, Major Science and Technology Projects of Guizhou ([2019] 3003), Natural Science Foundation of Guizhou Province ([2019]1233), Technology Support Programme of Guizhou ([2018]2199), and Special Fund of Chinese Central Government Guidance for Local Science and Technology Development ([2016] 4006).

References

[1] S.-I. Moriyama, "Torque measurement method based on the lorentz force law for miniature dc motor," *IEEJ Transactions on Electrical and Electronic Engineering*, vol. 13, no. 2, pp. 322–329, 2018.

[2] Z. Xie, W. Wu, and J. Hong, "Study on properties of armature current for micro DC motors and multiple features of fault diagnosis," *Electric Machines and Control*, vol. 19, no. 8, pp. 107–114, 2015.

[3] A. Bellini, F. Filippetti, C. Tassoni, and G.-A. Capolino, "Advances in diagnostic techniques for induction machines," *IEEE Transactions on Industrial Electronics*, vol. 55, no. 12, pp. 4109–4126, 2008.

[4] H. Henao, G.-A. Capolino, M. Fernandez-Cabanas, F. Filippetti, C. Bruzzese, and E. Strangas, "Trends in fault diagnosis for electrical machines a review of diagnostic techniques," *Ieee Industrial Electronics Magazine*, vol. 8, no. 2, pp. 31–42, 2014.

[5] M. Heydarzadeh, M. Zafarani, M. Nourani, and B. Akin, "A wavelet-based fault diagnosis approach for permanent magnet synchronous motors," *IEEE Transactions on Energy Conversion*, vol. 34, no. 2, pp. 761–772, 2019.

[6] B. R Nayana and P. Geethanjali, "Analysis of statistical time-domain features effectiveness in identification of bearing faults from vibration signal," *IEEE Sensors Journal*, vol. 17, no. 17, pp. 5618–5625, 2017.

[7] A. Glowacz and Z. Glowacz, "Recognition of rotor damages in a dc motor using acoustic signals," *Bulletin of the Polish Academy of Sciences, Technical Sciences*, vol. 65, no. 2, pp. 187–194, 2017.

[8] G. Singh, T. C. Kumar, and V. N. Naikan, "Induction motor inter turn fault detection using infrared thermographic

analysis," *Infrared Physics & Technology*, vol. 77, pp. 277–282, 2016.

[9] M. Seera, C. P. Lim, D. Ishak, and H. Singh, "Fault detection and diagnosis of induction motors using motor current signature analysis and a hybrid FMM–CART model," *IEEE Transactions on Neural Networks*, vol. 23, no. 1, pp. 97–108, 2012.

[10] G. Joksimovic and J. Penman, "The detection of inter-turn short circuits in the stator windings of operating motors," *IEEE Transactions on Industrial Electronics*, vol. 47, no. 5, pp. 1078–1084, 2000.

[11] S. Moon, H. Jeong, H. Lee, and S. W. Kim, "Interturn short fault diagnosis in a pmsm by voltage and current residual analysis with the faulty winding model," *IEEE Transactions on Energy Conversion*, vol. 33, no. 1, pp. 190–198, 2018.

[12] O. Moseler and R. Isermann, "Application of model-based fault detection to a brushless dc motor," *IEEE Transactions on Industrial Electronics*, vol. 47, no. 5, pp. 1015–1020, 2000.

[13] C. Chan, S. Hua, and H. Zhang, "Application of fully decoupled parity equation in fault detection and identification of dc motors," *IEEE Transactions on Industrial Electronics*, vol. 5, no. 4, pp. 1277–1284, 2006.

[14] H. M. Usman, S. Mukhopadhyay, and H. Rehman, "Permanent magnet dc motor parameters estimation via universal adaptive stabilization," *Control Engineering Practice*, vol. 90, pp. 50–62, 2019.

[15] S. Munikoti S, L. Das, B. Natarajan, and B. Srinivasan, "Data-driven approaches for diagnosis of incipient faults in dc motors," *Ieee Transactions on Industrial Informatics*, vol. 15, no. 9, pp. 5299–5308, 2019.

[16] S. Lu, G. Qian, Q. He, F. Liu, Y. Liu, and Q. Wang, "In situ motor fault diagnosis using enhanced convolutional neural network in an embedded system," *IEEE Sensors Journal*, vol. 20, no. 15, pp. 8287–8296, 2020.

[17] X. Xu, X. Qiao, N. Zhang, J. Feng, and X. Wang, "Review of intelligent fault diagnosis for permanent magnet synchronous motors in electric vehicles," *Advances in Mechanical Engineering*, vol. 12, no. 7, Article ID 1687814020944323, 2020.

[18] J. Burriel-Valencia, R. Puche-Panadero, J. Martinez-Roman et al., "Automatic fault diagnostic system for induction motors under transient regime optimized with expert systems," *Electronics*, vol. 8, no. 1, p. 6, 2019.

[19] X. Li, W. Zhang, Q. Ding, and X. Li, "Diagnosing rotating machines with weakly supervised data using deep transfer learning," *Ieee Transactions on Industrial Informatics*, vol. 16, no. 3, pp. 1688–1697, 2020.

[20] Z. Guo, M. Liu, H. Qin, and B. Li, "Mechanical fault diagnosis of a dc motor utilizing united variational mode decomposition, sampen, and random forest-sprint algorithm classifiers," *Entropy*, vol. 21, no. 5, p. 470, 2019.

[21] W. Sun, R. Zhao, R. Yan, S. Shao, and X. Chen, "Convolutional discriminative feature learning for induction motor fault diagnosis," *Ieee Transactions on Industrial Informatics*, vol. 13, no. 3, pp. 1350–1359, 2017.

[22] D. Xiao, Y. Huang, L. Zhao, C. Qin, H. Shi, and C. Liu, "Domain adaptive motor fault diagnosis using deep transfer learning," *IEEE Access*, vol. 7, pp. 80937–80949, 2019.

[23] H. Wang, J. Zhao, Q. Sun, and H. Zhu, "Probability modeling for pv array output interval and its application in fault diagnosis," *Energy*, vol. 189, Article ID 116248, 2019.

[24] G. An and H. Li, "Degradation state identification of cracked ultrasonic motor by means of fault feature extraction method," *Shock and Vibration*, vol. 2019, Article ID 5180590, 13 pages, 2019.

[25] A. Jafari, J. Faiz, and M. A. Jarrahi, "A simple and efficient current-based method for interturn fault detection in BLDC motors," *Ieee Transactions on Industrial Informatics*, vol. 17, no. 4, pp. 2707–2715, 2021.

[26] M. Z. Ali and X. Liang, "Threshold-based induction motors single- and multifaults diagnosis using discrete wavelet transform and measured stator current signal," *Canadian Journal of Electrical and Computer Engineering-Revue Canadienne De Genie Electrique Et Informatique*, vol. 43, no. 3, pp. 136–145, 2020.

[27] M. Irfan, N. Saad, R. Ibrahim, V. Sagayan Asirvadam, and M. Magzoub, "An online fault diagnosis system for induction motors via instantaneous power analysis," *Tribology Transactions*, vol. 60, no. 4, pp. 592–604, 2017.

[28] H. Liu, Y. Wang, Y. Yang, R. Liao, Y. Geng, and L. Zhou, "A failure probability calculation method for power equipment based on multi-characteristic parameters," *Energies*, vol. 10, no. 5, p. 704, 2017.

[29] Y. Li, W. Dai, T. Huang, M. Shi, and W. Zhang, "Adaptive early warning method based on similar proportion and probability model," *Applied Sciences-Basel*, vol. 10, no. 12, p. 4278, 2020.

[30] J. Wen and H. Gao, "Degradation assessment for the ball screw with variational autoencoder and kernel density estimation," *Advances in Mechanical Engineering*, vol. 10, no. 9, Article ID 1687814018797261, 2018.

[31] Z. Xie, J. Zheng, and Y. Lang, "Modelling and simulation of interturn short fault in micro direct-current motors," *International Journal of Power and Energy Systems*, vol. 41, no. 2, pp. 122–129, 2021.

[32] J. Xie and C. Liu, *Method and Application of Fuzzy Mathematics*, Huazhong University of Science and Technology Press, Wuhan, China, 3rd edition, 2006.

[33] H. Zhang and Z. He, *Principles and Applications of Fuzzy Diagnosis*, Xi'an Jiaotong University Press, Xi'an, China, 1992.

Hindawi
Shock and Vibration
Volume 2021, Article ID 9590547, 11 pages
https://doi.org/10.1155/2021/9590547

Research Article

Spot Image Segmentation of Lifting Container Vibration Based on Improved Threshold Method and Mathematical Morphology

Tian-Bing Ma,[1,2] **Qiang Wu**,[2] **Fei Du**,[2] **Wei-Kang Hu**,[2] **and Yong-Jing Ding**[2]

[1]*State Key Laboratory of Mining Response and Disaster Prevention and Control in Deep Coal Mines, Anhui University of Science and Technology, Huainan 232001, China*
[2]*Department of Mechanical Engineering, Anhui University of Science and Technology, Huainan 232001, China*

Correspondence should be addressed to Tian-Bing Ma; dfmtb@163.com

Received 16 April 2021; Revised 14 July 2021; Accepted 20 July 2021; Published 28 July 2021

Academic Editor: Xian-Bo Wang

Because the mine is damp and dark, it is not easy to detect the rigid tank channel's structural failure directly. Therefore, we judged the tank channel's surface condition by detecting the magnitude of the vibration displacement of the lifting container. In our study, we used a laser vision system to measure the structural vibration displacement. In order to accurately segment the laser spot information from the vibration image, we proposed an approach that links the relationship between the gray value of the area adjacent to the threshold point and the background's gray value to the target in the image. We used MCE to evaluate the segmentation effect of threshold segmentation and verified the improved algorithm's accuracy by detecting the pixel centroid of laser spots. Results show that the improved algorithm in our study has the best threshold segmentation effect, the error classification can be close to 0.0003, and the minimum deviation of the obtained vibration displacement is close to 0.1 pixels, which can realize the accurate extraction of the vibration signal of the vertical shaft tank. The novelty of this method lies in the accurate threshold segmentation and noise reduction processing of the laser speck vibration image under various interference environments in the operation of the mine hoisting system and the accurate acquisition of vibration signals. The research work provides a basis for the accurate evaluation of mechanical faults of automation technology.

1. Introduction

China's coal resources are vibrant, and it is an essential part of the energy field [1]. The mine hoist system undertakes transportation tasks such as coal, equipment, and personnel, and its operation status will directly affect the safe and efficient production of the coal mine. When the lifting container is disturbed during operation, structural vibration will be generated. By analyzing its vibration characteristics, the health of the mine lifting system can be indirectly obtained. There are many existing vibration measurement methods, and the contact acceleration sensor method is generally used. However, such methods are prone to signal distortion, delay, and other consequences [2]. In contrast, the noncontact optical measurement technology of machine vision has received an increasing attention due to its advantages, such as high accuracy and intuitiveness [3]. The visual measurement method of laser spot vibration displacement refers to combining the laser and CCD camera, marking the laser spot on the vibration, using the CCD camera to collect the marking laser spot, and performing the corresponding image processing to obtain the vibration displacement of the measured position [4], as shown in Figure 1.

Image segmentation is the technique and process of dividing an image into several specific areas and proposing feature targets. The threshold segmentation method has attracted much attention for its simplicity and adaptability [5]. The more widely used threshold algorithm is the Otsu method based on the maximum variance between classes; it is an image binarization algorithm proposed by the Japanese scholar Otsu. However, the Otsu method has certain limitations. For some interfering images and grayscale histograms that do not have prominent bimodal characteristics, the segmentation accuracy cannot be guaranteed. Many

scholars have improved Otsu's method to adapt the algorithm to complex images in more situations. Ng has proposed an interclass variance method that emphasizes troughs, uses the probability of gray value as the threshold value as the weight, and adds it to the target formula of interclass variance, so that the optimal threshold of image segmentation tends to the gray level of the trough position value [6]. On this basis, Fan and Lei [7] proposed an interclass variance method emphasizing the trough neighborhood, considering the gray value distribution of the target and the background, and adding the distribution probability weights of all pixels in the neighborhood of the threshold point. Shen et al. [8] proposed a recursive method of multithreshold segmentation. Based on emphasizing the neighborhood of troughs, factors related to the relative relationship between channels and crests in the histogram were added, which effectively improved the segmentation results' boundary details. In order to consider the spatial relationship between the central pixel and its neighborhood, Yu proposed a new region-based active contour model, which effectively segments the image by measuring the similarity of local patches [9]. In the second year, a new level-set method for medical image segmentation based on adaptive perturbation was proposed, which can effectively segment medical images with intensity inhomogeneity [10].

The above algorithms have improved the Otsu method to a certain extent and have also been proved to be useful for similarly labeled target segmentation. However, the segmentation effect of such improved algorithms on non-uniformly illuminated images and noisy images is limited. The coal mine's underground environment is complex, and it is challenging to ensure that the image received by CCD is not affected by noise, dust, and intense light. Moreover, the underground mine environment is humid, and the laser is prone to produce abnormal transmission light during the transmission process, that is, stray light. Ghost imaging manifests stray light caused by reimaging a few reflected lights in the optical transmission system [11, 12]. In the visual system, the ghost images gathered on the image surface received by the CCD camera will increase the image's noise. The center of mass of the laser spot may be erroneously detected.

When the hardware measures cannot eliminate the noise, the image preprocessing can be optimized [13]. This research analyzes the related improved algorithm's problems in marking laser speckle segmentation under the interference of pulse noise, intense light, and ghost images. Considering the influence of different interference on image gray value distribution, an improved algorithm is proposed. Combined with the gray value pixel of the neighborhood of the threshold point, the difference between the gray value of the background and the target in the image histogram, the range size of the neighborhood and the ratio of the gray value of the threshold point to the background, and the gray value of the threshold point to the target area, the optimal threshold is selected to be closer to the ideal threshold of segmentation. Mathematical morphology algorithm has good robustness to noise, combined with mathematical morphology to process the segmented image, avoiding under- or oversegmentation generated during threshold segmentation, effectively solving the impact of environmental interference and improving segmentation target quality [14].

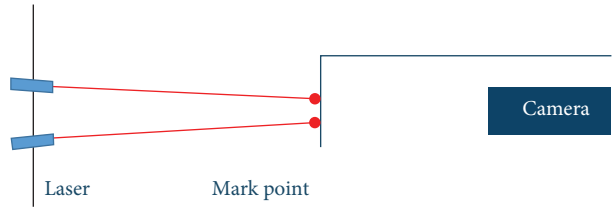

Figure 1: Structure diagram of the laser vision system.

2. Research Basis

To collect the fault vibration image of the vertical shaft hoisting tank, the vertical shaft hoisting system shown in Figure 2 was built. This experiment can simulate the three failure modes of step bump, joint misalignment, and joint gap, by acting different tank faults and collecting and hoisting the vibration image of the container. The lifting speed is 0.18 m/s, and the impact force caused by the high-frequency vibration caused by the impact step defect of the tank channel causes the displacement of the laser spot centroid pixel. The CCD camera sensor is attached to the top center of the lifting container. A fluorescent screen is placed H above the camera lens, and the fluorescent screen is relatively fixed to the CCD camera. Two laser transmitters are symmetrically installed in the same plane above the mine tank passage, and the direction of emission is downward. In this experiment, the laser spot vibration image of the vertical shaft hoisting system test bench was collected.

The experimental hardware conditions are Core i5-3470 CPU 3.20 GHZ, and the programming environment uses MATLAB R2015a. As shown in Figure 3, our research's images are collected by the DMK33G618 CCD industrial camera provided by the Imaging Source, with a resolution of 640×480 pixels, a maximum frame rate of 120fps, and a lens focal length of 16 mm. The two sets of laser emitters are ultrasmall red dots, emitting pure red lasers with a wavelength of 650 nm. The size of the red spot can be adjusted manually from 0.4 mm to several centimeters. It also adopts an anticorrosion DC plug cable, which is suitable for all-weather and all-environment use, as shown in Figure 4.

The laser vision vibration measurement system was built and completed, and the program design for the camera to collect vibration images was completed. Then, a series of algorithm processing is performed on the obtained vibration image, the laser spot in the vibration image is detected, the vibration displacement information of the centroid of the laser spot is extracted, and its pixel coordinates are obtained in real time. The basic idea is to do image preprocessing analysis and threshold segmentation on the vibration images collected by the camera and store the static centroid coordinate information of laser spots at the beginning. In the next frame image, the centroid coordinates of laser spots in real time are obtained, the initial centroid coordinates are calculated, and the relative vibration displacement information of laser spots is obtained; the process is shown in Figure 5.

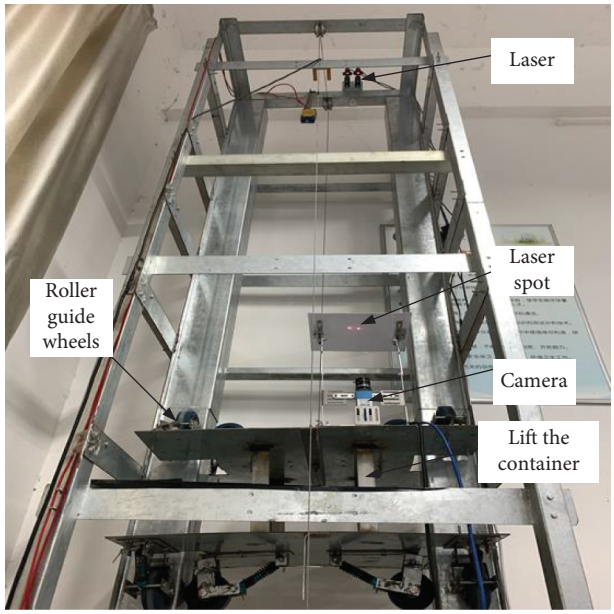

Figure 2: Vertical shaft rigid can way test bench based on the laser vision system.

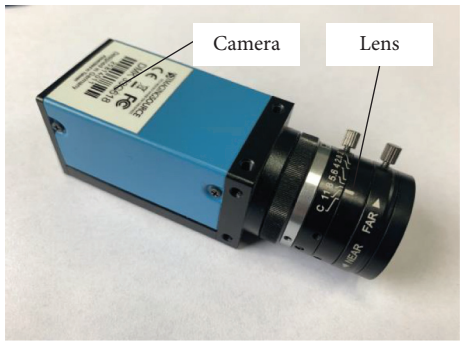

Figure 3: Camera and lens.

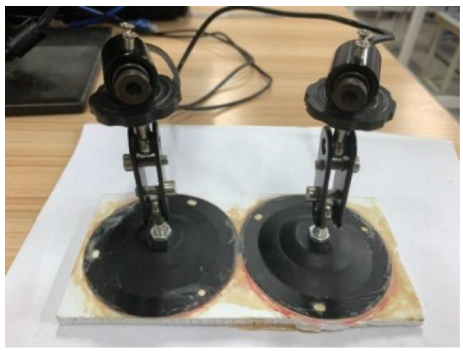

Figure 4: Laser transmitter in kind.

3. The Traditional Otsu Threshold Segmentation Algorithm

The Otsu method is an automatic threshold method to maximize the variance between classes. The algorithm is derived from the gray histogram using the principle of least squares. It has the characteristics of fast processing speed and simple operation. It is a commonly used method. It is characterized by fast processing speed and simple operation and is a commonly used threshold selection method [15]. The basic idea is as follows:

A digital image $F = [f(x, y)]_{M\times N}$ with a size of $M \times N$, $f(x, y)$ represents the gray value at the pixel point (x, y), in which there are L-level gray values, namely $f(x, y) \in H$, $H = \{0, 1, 2, \ldots, L-1\}$. The gray value l $(0 \le l \le L-1)$ is set as the abscissa and the number of pixels with the gray value of l in the image $h(l)$ as the ordinate and the gray histogram of the image is drawn. The pixels with the gray value of l appear in the image's probability is as follows:

$$p(l) = \frac{h(l)}{M \times N}, \tag{1}$$

where $l = 0, 1, \ldots, L-1$. Also,

$$\sum_{l=0}^{L-1} p(l) = 1. \tag{2}$$

The threshold T is set to divide the pixels in the image corresponding to the grayscale histogram into two types: background region C_0 and target region C_1, where C_0 is the total number of pixels $N_0 = \sum_{l=0}^{T} h(l)$ in the gray value $[0, T]$ and C_1 is the gray value in $[T+1, L-1]$ the total number of pixels $N_1 = \sum_{T+1}^{L-1} h(l)$; the proportion of the pixel area are as follows:

$$\begin{aligned} p_0(T) &= \frac{N_0}{M \times N}, \\ p_1(T) &= \frac{N_1}{M \times N} \\ &= 1 - p_0(T). \end{aligned} \tag{3}$$

The average values of C_0 and C_1 are as follows:

$$\begin{aligned} w_0 &= \frac{\mu_0(T)}{N_0}, \\ w_1 &= \frac{\mu_1(T)}{N_1}. \end{aligned} \tag{4}$$

From (4), we can see

$$w = w_0 N_0 + w_1 N_1, \tag{5}$$

where w_0 represents the mean value of background region C_0, w_1 represents the mean value of target region C_1, and w represents the global mean value of the image.

Then, the between-class variance is defined as follows:

$$\sigma_B^2 = p_0(T)(w_0 - w)^2 + p_1(T)(w_1 - w)^2. \tag{6}$$

Given that $T \in [0, L-1]$, the T value when reaches the maximum value is the optimal threshold which is

$$T = \operatorname{Arg} \max_{0 \le T \le L-1} \sigma_B^2. \tag{7}$$

To study the threshold segmentation effect of the traditional Otsu algorithm, a noninterference laser spot image was selected for verification.

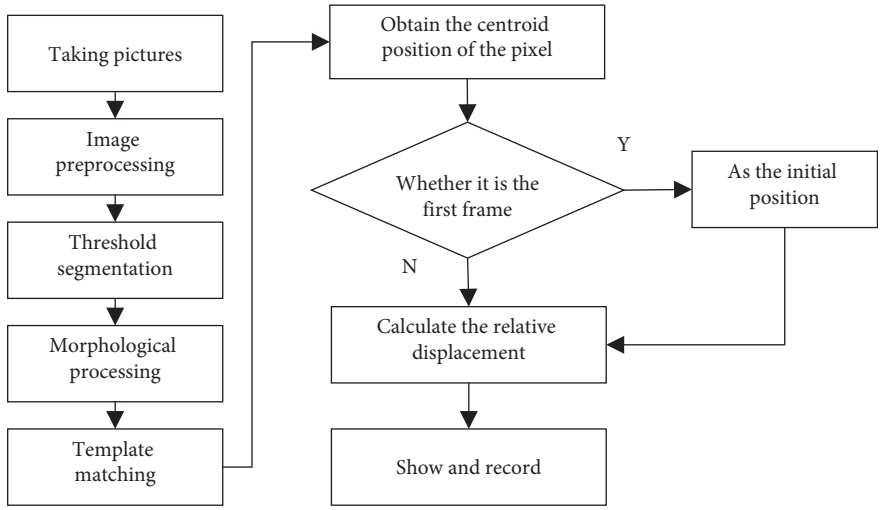

Figure 5: Flow chart of image processing and laser spot centroid detection.

As shown in Figure 6, it can be seen that the traditional Otsu method segmented the noninterference laser spot image. Although the target can be extracted, the segmented target part cannot be matched entirely with the original laser spot, leading to incorrect detection of the spot center. The black area is the background part less than the threshold gray value, and the white area is the target part greater than the threshold gray value. Because the traditional Otsu method does not entirely separate the target and the background from the interference-free laser spot image, it does not explore the image segmentation's effect under interference.

4. Other Improved Algorithms

In recent years, domestic and foreign scholars have made many optimization improvements based on Otsu method to make Otsu method widely and effectively perform threshold segmentation. Ng [6] proposed the probability of occurrence when the gray value is a threshold in the gray histogram as a weighting factor. The optimal threshold of image segmentation tends to be the gray value of the trough position. The improved specific expression is as follows:

$$\sigma_B^2 = [1 - h(T)]\left[p_0(T)(w_0 - w)^2 + p_1(T)(w_1 - w)^2\right]. \tag{8}$$

Fan et al. proposed a smooth histogram weighted Otsu method based on Ng [7]. This weighting includes the threshold point's gray value and considers the distribution of all pixels in the neighborhood of the threshold point. Probability information makes weighting more effective and threshold positioning more accurate. The improved specific expression is as follows:

$$\sigma_B^2 = [1 - \overline{h}(T)]\left[p_0(T)(w_0 - w)^2 + p_1(T)(w_1 - w)^2\right]. \tag{9}$$

Among them,

$$\overline{h}(T) = [h(T-k) + \cdots + h(T-1) + h(T) + h(T+1) + \cdots + h(T+k)], \tag{10}$$

where $\overline{h}(T)$ represents the sum of the gray value pixels' distribution probabilities in the threshold T neighborhood in the gray histogram with a range of $(2k+1)$, strengthening the likelihood of the valley's gray value in the histogram.

Based on the smooth histogram's weighting, Shen [8] further considered the probability of the trough's gray value in the histogram and the relative height of the gray value of the canal and the neighboring peaks. They used it as the weight item when selecting the threshold. The improved specific expression is as follows:

$$\sigma_B^2 = [1 - \nu(T)]\left[p_0(T)(w_0 - w)^2 + p_1(T)(w_1 - w)^2\right]. \tag{11}$$

Among them,

$$\nu(T) = \overline{h}(T)\frac{2h(T)}{h_L(T) + h_R(T)}, \tag{12}$$

where $h_L(T)$ and $h_R(T)$ are the probability of the nearest peaks' gray value pixels in the histogram. Combining the threshold neighborhood value pixels and the relative height of the threshold and the neighboring wave peaks, the influence of the target distribution ratio is reduced, and the optimal solution of the formula tends to be the valley gray value. If the gray value T is the adjacent left and right peaks, T is used to replace this peak's gray value.

To explore the improved Otsu algorithm's threshold segmentation effect, different specifications of noninterference laser speckle image i and laser speckle image in the case of high-intensity light ii, pulse noise iii, and ghost image iv are selected. These threshold segmentation algorithms are processed separately [12].

As can be seen from Figures 7–10, Ng, Fan, and Shen algorithms are all successful in segmenting the laser spot image without interference. Since the intense light's gray value is close to the target point's gray value, the Ng

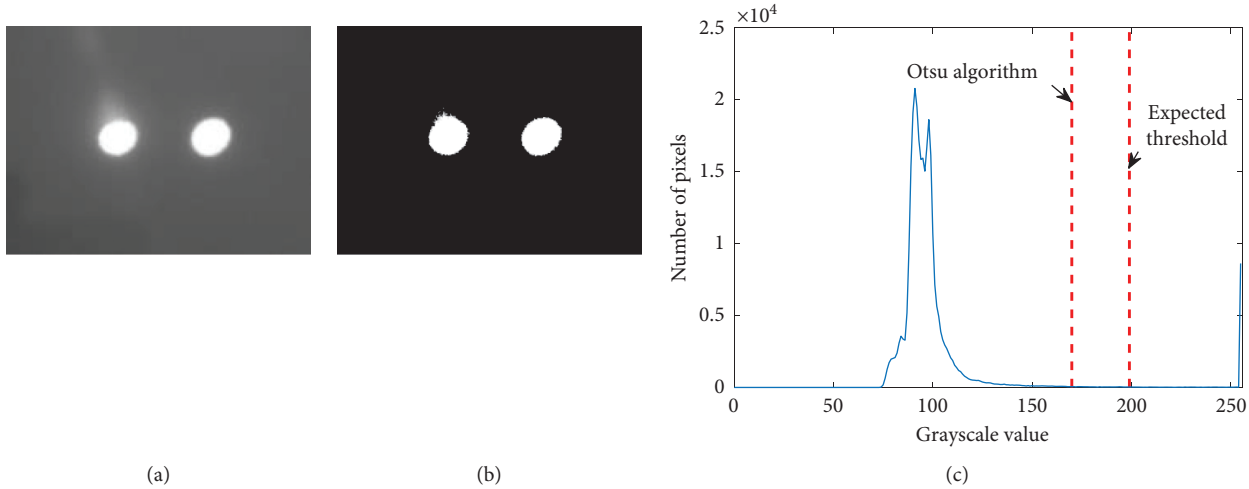

Figure 6: Otsu segmentation: (a) original image, (b) Otsu division, and (c) image histogram.

algorithm uses the gray neighborhood as the weight to increase the proportion of the trough. Under the interference of the intense light, the final threshold is almost entirely in the background area. Shen algorithm considers the relationship between the valley's gray value and its left and right peak gray values, making the threshold more towards the target. The final segmentation effect is improved compared with the Fan algorithm, but the segmentation fails. Ng algorithm only considers the gray value of the valley in the image; under the interference of intense light, the final segmentation effect is higher than the Fan and Shen algorithm, but the segmentation fails. Including the Otsu threshold and 70% and 80% of the pixel range, the laser spot cannot be wholly separated from the intense light background. Ghost imaging is also a kind of stray light. Ng, Fan, and Shen algorithms fail to segment, which cannot guarantee the target spot's integrity. It can be seen from the figure that the Ng, Fan, and Shen algorithms do not affect impulse noise.

5. Improved Algorithms

The specific improvement plan is: from the image histogram, filter out the gray value l_m at the background peak in the histogram and the gray value l_n at the target peak. The traversal range of the threshold T is $l_m < T < l_n$. The gray value at the background peak is l_m. The total pixel point at the gray value l_n at the target wave peak is N_A; the threshold value T in the histogram and the gray value T in the neighborhood are $(2k+1)$ the total number of pixels N_a of all gray values, occupying the background gray. The full pixel point ratio from the degree value to the gray target value is $P_l(T)$; the distances from the threshold to the background and the gray target value are X_m and X_n, respectively. The gray value T in the threshold neighborhood accounts for the threshold to the background, and the ratio of the target gray value difference is $P_X(T)$; the above parameters are introduced as weighting factors into the Otsu method, and the improved target formula for the between-class variance is as follows:

$$
\begin{aligned}
N_A &= \sum_{l=l_m}^{l_n} h(l),\\
N_a &= \sum_{l=T-k}^{T+k} h(l),\\
P_l(T) &= \frac{\sum_{l=T-k}^{T+k} h(l)}{\sum_{l=l_m}^{l_n} h(l)},\\
P_X(T) &= \frac{2k+1}{X_n - X_m},\\
\sigma_B^2 &= \left[1 - P_l(T)P_X(T)\right]\left[p_0(T)(w_0 - w)^2\right.\\
&\quad \left. + p_1(T)(w_1 - w)^2\right].
\end{aligned}
\tag{13}
$$

It can be seen from the improved interclass variance target formula that $P_l(T)$ and $P_X(T)$ are used as weighting coefficients, and the weighting factors of reference [6] are combined. The background target gray value and pixel information are added to make the target gray. The interclass variance of the degree value is relatively increased. The optimal threshold range is further approached to the target gray value, which reduces the influence on the optimal threshold when the background proportion is large.

Mathematical morphology is composed of a set of morphological algebraic operators, which can solve image processing problems such as noise suppression, feature extraction, threshold segmentation, and shape recognition [16]. In 2019, Yan proposed a novel early fault detection strategy based on enhanced scale morphological cap product filtering (ESMHPF), which realized the effects of noise suppression and feature enhancement [17]. At the same time, a multiscale morphological analysis algorithm based on a feature selection framework is proposed to build multidomain features, highlight fault symptoms, suppress noise, and improve fault detection ability [18].

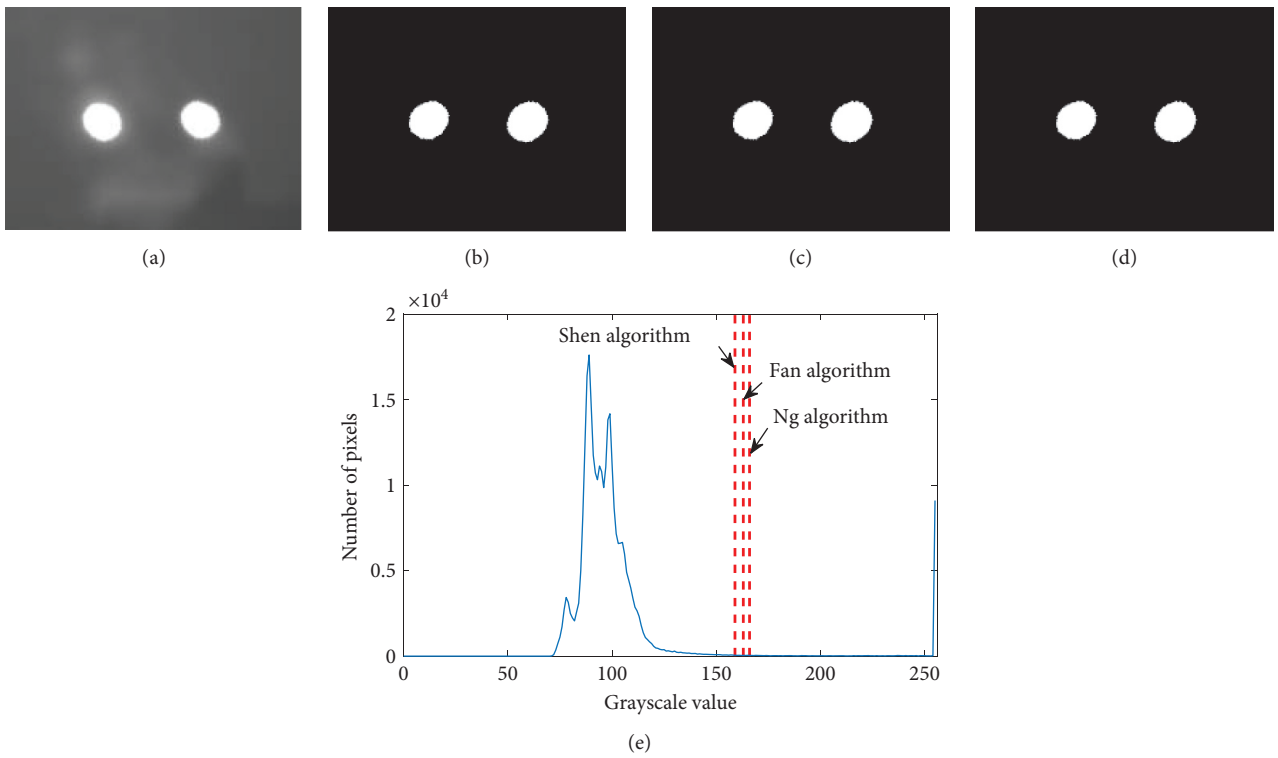

Figure 7: Laser spot segmentation effect without interference: (a) original image, (b) Ng algorithm, (c) Fan algorithm, (d) Shen algorithm, and (e) histogram and each segmentation threshold.

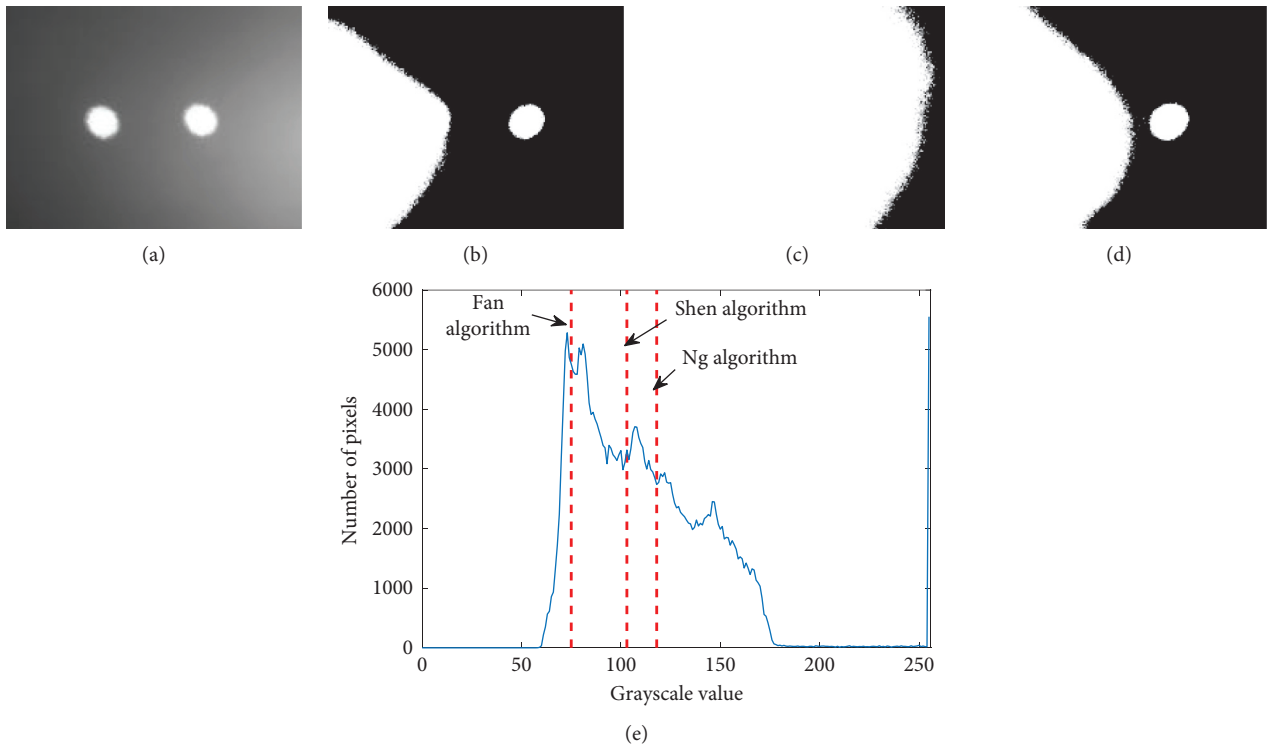

Figure 8: Laser spot segmentation effect under high-intensity light interference: (a) original image, (b) Ng algorithm, (c) Fan algorithm, (d) Shen algorithm, and (e) histogram and each segmentation threshold.

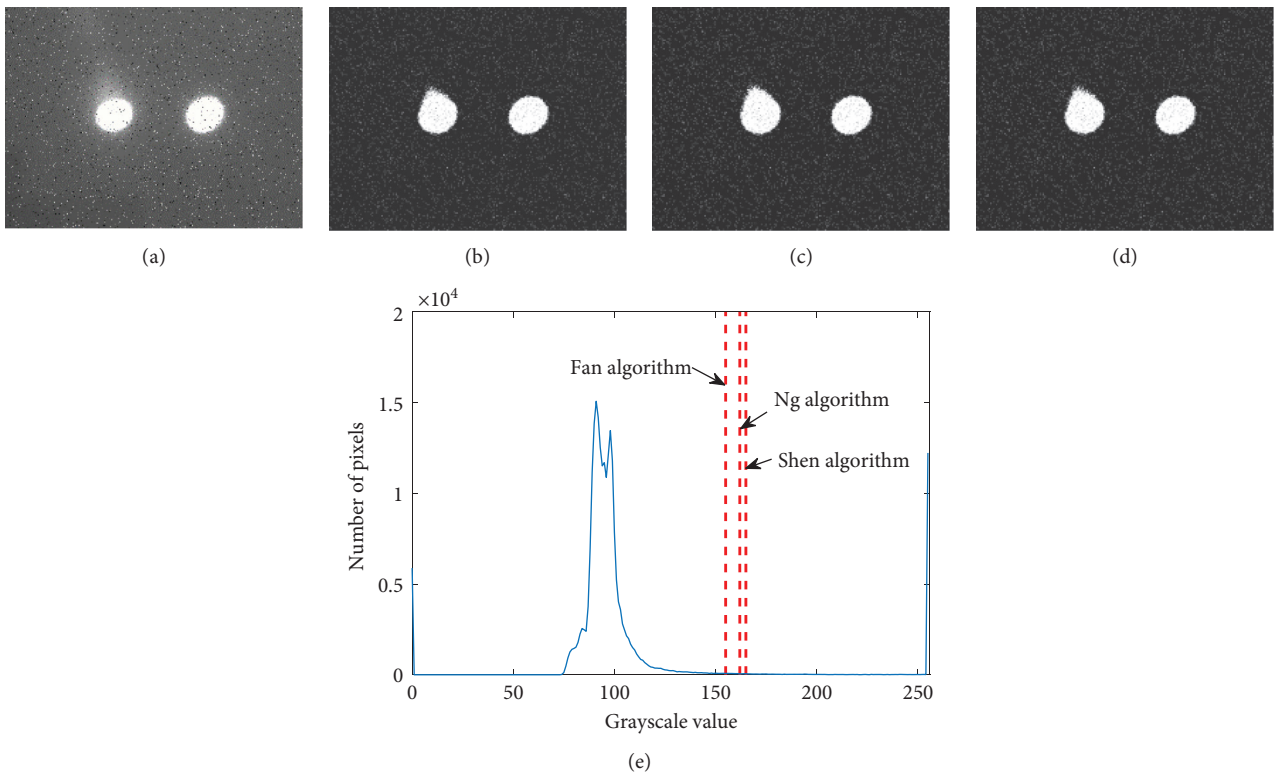

Figure 9: Laser speckle segmentation effect under the interference of pulse noise: (a) original image, (b) Ng algorithm, (c) Fan algorithm, (d) Shen algorithm, and (e) histogram and each segmentation threshold.

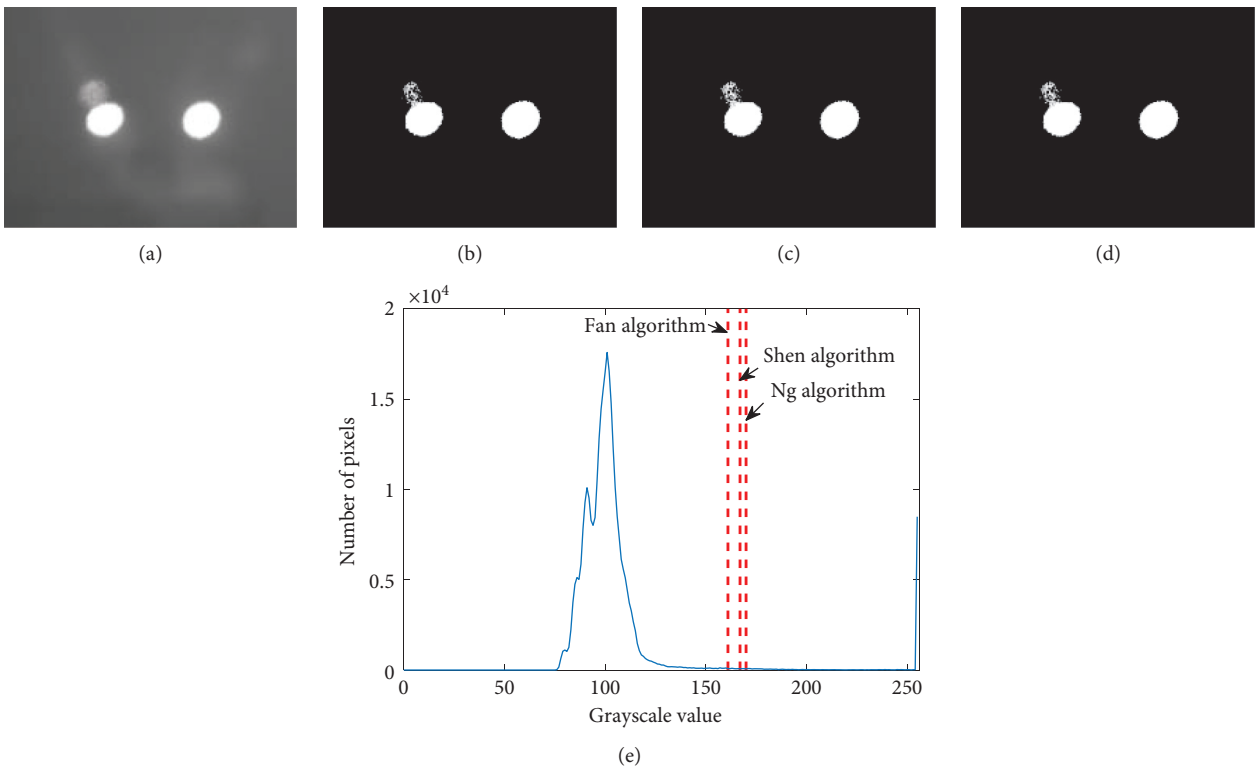

Figure 10: Laser speckle segmentation effect under ghost imaging interference: (a) original image, (b) Ng algorithm, (c) Fan algorithm, (d) Shen algorithm, and (e) histogram and segmentation threshold.

Table 1: MCE value of the vibration image under each threshold segmentation algorithm.

Image category	MCE value			
	Ng algorithm	Fan algorithm	Shen algorithm	Improved algorithm
i	0.0048	0.0053	0.0063	0.0032
ii	0.3517	0.8589	0.51	0.0003
iii	0.0031	0.0046	0.0025	0.0006
iv	0.0048	0.0071	0.0055	0.0006

After the laser spot's target segmentation is completed, a binary image containing the laser spot is obtained. However, there will still be a certain amount of noise, which still interferes with the subsequent detection. In this regard, the morphology is selected to filter impurity interference. Since the laser spots in the image are composed of several small laser spots, combined with the characteristics of environmental noise, the radius is defined as 2-pixel structural elements S, and S is used to perform open and close operations on the segmented image, which are defined as follows:

$$\begin{aligned} \overline{f} \circ S &= (\overline{f} \Theta S) \oplus S, \\ \overline{f} \cdot S &= (\overline{f} \oplus S) \Theta S, \end{aligned} \tag{14}$$

where $\oplus$ denotes the dilation operator, Θ denotes the erosion operator, $\cdot$ is the opening operator, and $\circ$ is the closing operator.

6. Discussion of Experimental Results

To test the segmentation effect of the improved threshold segmentation algorithm on the vertical shaft tank's vibration image, the segmentation performance is evaluated by two evaluation indicators: the misclassification error (MCE) and the pixel centroid deviation. MCE represents the result of threshold segmentation of a single image, which indicates the proportion of the wrongly divided background pixel to the target area when the image's target pixel is classified into the background area. The pixel centroid deviation value represents the result of a comprehensive evaluation of the machine vision vibration displacement detection in actual operation. It represents the deviation value of the laser spot pixel centroid's displacement in the segmented image and the cage's displacement running on the tank in the vertical shaft lifting system.

7. MCE Evaluation Threshold Segmentation Results

MCE is used to evaluate the effects of threshold segmentation [19]. MCE $\in$ [0, 1] represents the probability that the image is misclassified after threshold segmentation, where 0 represents no error classification of image pixels, 1 means complete error classification of image pixels, and the greater the MCE value, the more misclassified pixels. MCE is defined as follows:

$$\mathrm{MCE} = 1 - \frac{\left|B_o \cap B_T\right| + \left|A_o \cap A_T\right|}{\left|B_o\right| + \left|A_o\right|}, \tag{15}$$

where B_o and A_o, respectively, are the background area and target area pixels in the standard segmentation state (no standard segmentation image, manually adjusted to the best segmentation effect as the standard segmentation image) and B_T and A_T, respectively, are the background area and target area pixels in the test segmentation state. The number of points, $\|$, represents the number of pixels in the area.

As shown in Table 1, the segmentation effect of a single image can be seen through the MCE value. No matter if it is without interference or other interference, the improved algorithm's segmentation effect in this research is the best. In the visual inspection failure, the MCE value is not enough to bear the overall image segmentation effect's burden. The most important thing is whether the obtained vibration displacement is accurate and useful. Therefore, it is necessary to calculate the position deviation of the pixel centroid after segmentation.

8. Algorithm Validity Test

To test the segmentation algorithm in this research, under the same experimental environment, the improved algorithm is presented in this research using no interference image I, impulse noise under the strong light interference image II, and ghost imaging under impulse noise interference III image threshold segmentation, to explore its segmentation effect. The test images and the corresponding threshold segmentation results are shown in Figures 11–13.

As can be seen from the segmentation results in Figures 11–13, the threshold value determined by the algorithm in this research can effectively distinguish the target from the background edge region [20]. Although some noise processing is left, the target point's feature information in the test image can be retained under feature matching.

Centroid detection is carried out on the above segmentation images, and the standard mean square error is used to detect the original centroid coordinates and the actual centroid coordinates [21], which is defined as follows:

$$e = \sqrt{(x_1 - x_0)^2 + (y_1 - y_0)^2}, \tag{16}$$

where (x_1, y_1) is the actual centroid coordinate of the laser spots in the segmented image and $(x_0, y_0)$is the original centroid coordinate, and the unit is pixel.

As shown in Table 2, it can be seen from the deviation value of the laser spot centroid after segmentation of each algorithm that the method in this research is slightly higher than other ways for interference-free images. However, for intense light interference images under impulse noise and ghost imaging interference images under impulse noise, this algorithm's improved threshold is far better than the other three threshold segmentation algorithms. Therefore, according to the laser speckle characteristics, this research

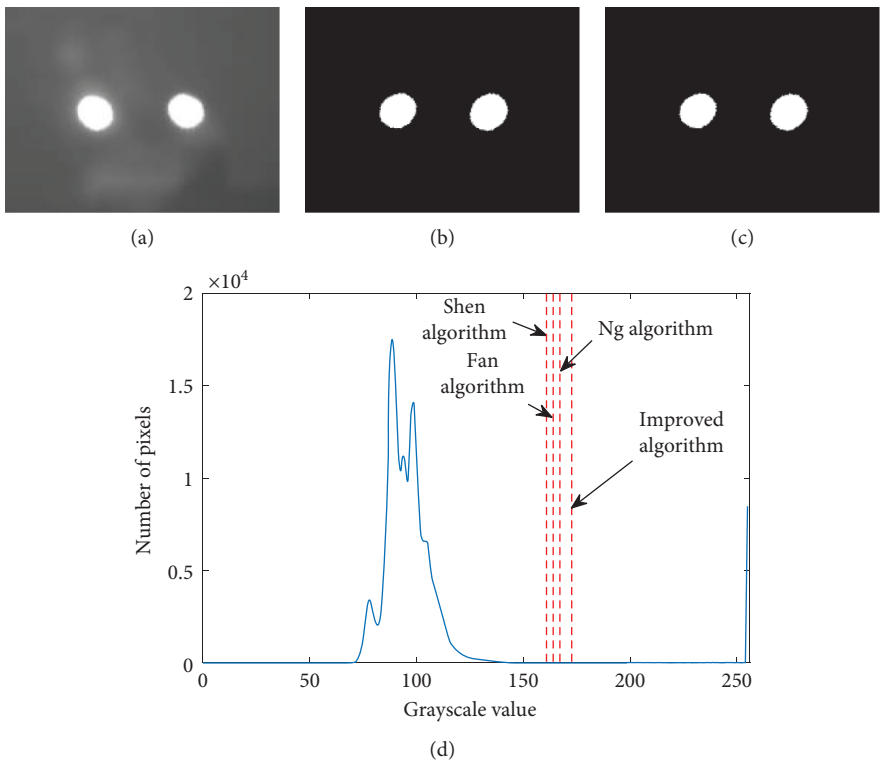

Figure 11: Laser spot segmentation effect without interference: (a) original image, (b) improved algorithm, (c) morphological processing, and (d) histogram and each segmentation threshold.

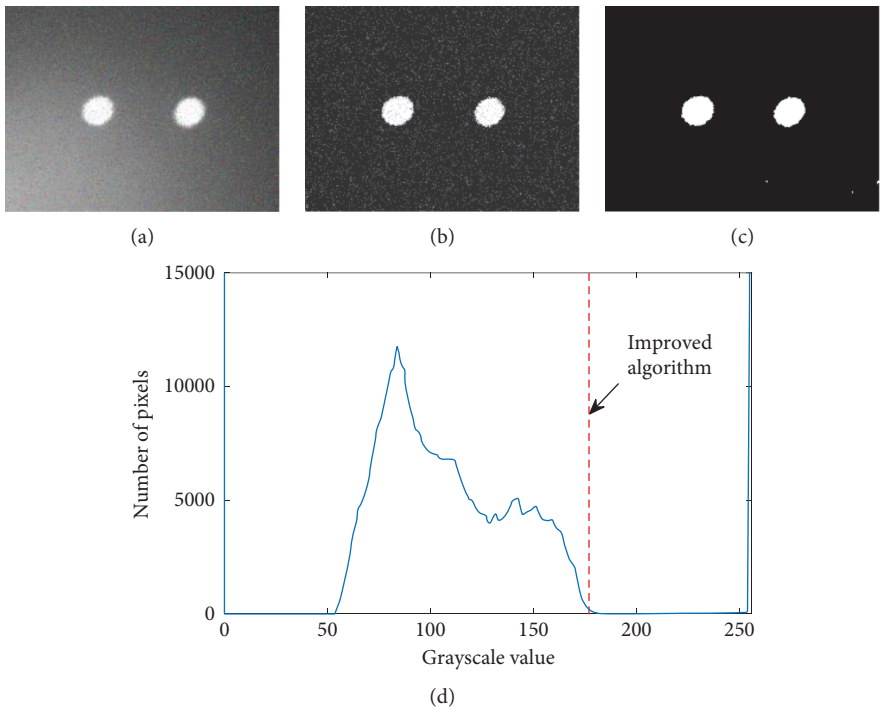

Figure 12: Laser speckle segmentation effect of intense light interference under pulse noise: (a) original image, (b) improved algorithm, (c) morphological processing, and (d) histogram and each segmentation threshold.

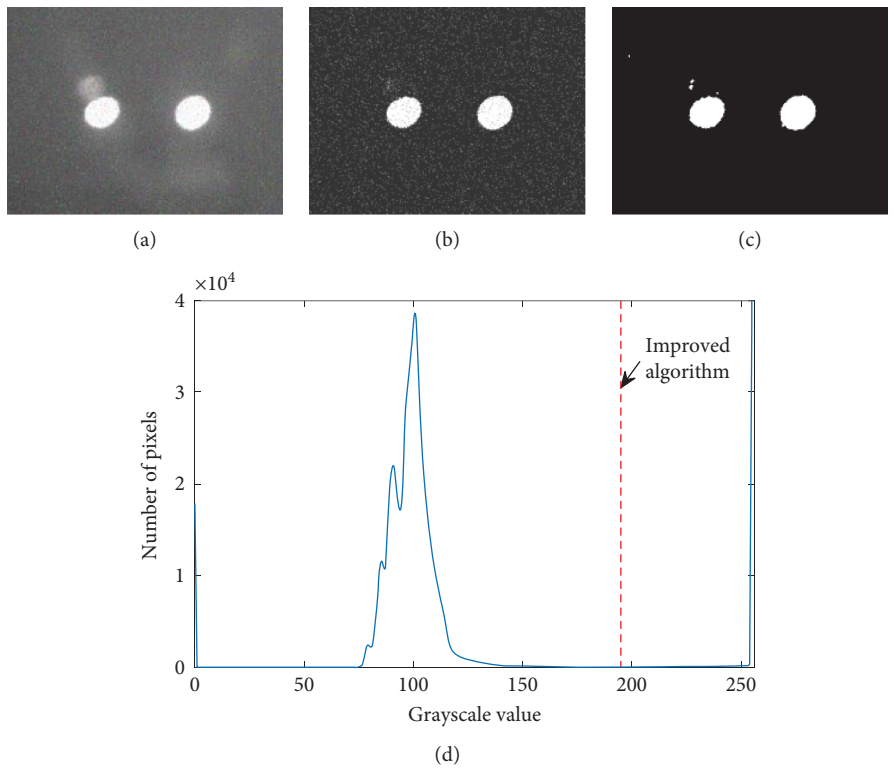

Figure 13: The effect of ghost imaging interference laser speckle segmentation under impulse noise: (a) original image, (b) improved algorithm, (c) morphological processing, and (d) histogram and each segmentation threshold.

Table 2: Position deviation value of each threshold segmentation algorithm.

Image category	Error value (pixel)			
	Ng algorithm	Fan algorithm	Shen algorithm	Improved algorithm
I	0.224	0.224	0.173	0.1
II	—	—	—	0.6
III	41.742	42.035	41.937	0.1

improves a threshold segmentation algorithm based on the Otsu method and combines the mathematical morphology to segment the laser speckle vibration image.

9. Conclusion

This research proposes a laser vision detection method for vertical shaft rigid tank road surface failure. Aiming at the obtained vibration spot image, an improved Otsu segmentation algorithm is proposed. Based on the relative height of the trough's gray value and the nearest peak in the histogram, the background is introduced. The relative relationship between the target gray value and the pixel information is used as the weight, combined with mathematical morphology processing, effectively segmenting the spot's shape and data under impulse noise, high-intensity light interference, and ghost imaging interference. Thus, the vibration displacement of the lifting vessel obtained is more accurate. Comparing the Ng algorithm, Fan algorithm, Shen algorithm, and the improved threshold algorithm in this research, the results show that the segmentation effect of the algorithm in this research is significantly enhanced compared with other algorithms, the error classification can be close to 0.0003, and the segmentation effect is the best. And the contrast experiment of the pixel centroid detection of the spot image and the deviation value was carried out. The minimum error value was close to 0.1 pixels, which verified the spot information's accuracy and completeness after the algorithm segmentation.

This research mainly uses a laser vision system, a fusion of mathematical morphology, and an improved Otsu threshold segmentation algorithm to detect the vertical shaft lifting container's vibration image. The follow-up will further discuss the intelligent fault diagnosis method to diagnose vertical shaft rigid tank channel fault accurately.

Data Availability

The video data used to support the findings of this study are available from the corresponding author upon request.

Conflicts of Interest

The authors declare that there are no conflicts of interest regarding the publication of this paper.

Acknowledgments

This work was supported by the Natural Science Research Foundation of Anhui Universities (Grant no. KJ2020A0281), the Natural Science Foundation of Anhui Province (Grant no. 2008085ME178), the State Key Laboratories (Grant no. SKLMRDPC20ZZ01), the Anhui University Top-Notch Talents Program (Grant no. gxbjZD202020063), the Collaborative Innovation Project of Anhui Universities (Grant no. GXXT-2019-048), and the Key Research and Development Program of Anhui Province (Grant no. 202104a07020005).

References

[1] X. D. Wang, "Study on high quality development index system and basic path of coal industry in China," *China Coal*, vol. 46, no. 2, pp. 22–27, 2020.

[2] X. Gang, X. Gui, and X. D. Niu, "Study of non-contact detection sensor based on fiber bragg grating," in *Proceedings 2011 International Conference On Transportation, Mechanical, and Electrical Engineering (TMEE)*, pp. 990–993, IEEE, Changchun, China, December 2011.

[3] J. Dang, R. Jia, H. Wu, X. Luo, and D. Chen, "Probabilistic entropy EMD thresholding for periodic fault signal enhancement in rotating machine," *Shock and Vibration*, vol. 2017, Article ID 1254310, 14 pages, 2017.

[4] Q. Zhang, J. Y. Gu, and J. M. Liu, "Research on coal and rock type recognition based on mechanical vision," *Shock and Vibration*, vol. 2021, Article ID 6617717, 10 pages, 2021.

[5] T. Yang, H. W. Tian, and X. M. Liu, "Otsu thresholding segmentation method based on two boundaries and its fast algorithm," *Application Research of Computers*, vol. 33, no. 12, pp. 3872–3875, 2016.

[6] H.-F. Ng, "Automatic thresholding for defect detection," *Pattern Recognition Letters*, vol. 27, no. 14, pp. 1644–1649, 2006.

[7] J. L. Fan and B. Lei, "A modified valley-emphasis method for automatic thresholding," *Pattern Recognition Letters*, vol. 33, no. 6, pp. 703–708, 2012.

[8] X. J. Shen, H. Zhang, and H. P. Chen, "Fast recursive multi-thresholding algorithm," *Journal of Jilin University (Engineering And Technology Edition)*, vol. 46, no. 2, pp. 528–534, 2016.

[9] H. Yu, F. He, and Y. Pan, "A novel region-based active contour model via local patch similarity measure for image segmentation," *Multimedia Tools and Applications*, vol. 77, no. 18, pp. 24097–24119, 2018.

[10] H. Yu, F. He, and Y. Pan, "A novel segmentation model for medical images with intensity inhomogeneity based on adaptive perturbation," *Multimedia Tools and Applications*, vol. 78, no. 9, pp. 11779–11798, 2019.

[11] Y. Tao, X. X. Wang, and F. B. Yang, "Edge detection based on high-pass filter ghost imaging," *Laser & Optoelectronics Progress*, vol. 57, no. 2, pp. 193–198, 2020.

[12] S. X. Zhou, W. Shen, and C. L. Luo, "Effect of defocus on lensless ghost diffraction and traditional imaging," *Optical Technique*, vol. 44, no. 5, pp. 536–541, 2018.

[13] T. Zafar, K. Kamal, and Z. Sheikh, "A neural network based approach for background noise reduction in airborne acoustic emission of a machining process," *Journal of Mechanical Science and Technology*, vol. 31, no. 7, pp. 3171–3182, 2017.

[14] G. J. Wang, Y. X. Huang, and Q. L. Zhao, "Study on the robustness of spot center based on adaptive region," *Laser Technology*, vol. 44, no. 5, pp. 616–622, 2020.

[15] Q. Y. Huang, Q. Li, M. X. Ran, X. Liu, and Y. Zhou, "Threshold-optimized swarm decomposition using grey wolf optimizer for the acoustic-based internal defect detection of arc magnets," *Shock and Vibration*, vol. 2021, Article ID 6636873, 21 pages, 2021.

[16] Z. W. Chen, N. Gao, W. Sun et al., "A signal based triangular structuring element for mathematical morphological analysis and its application in rolling element bearing fault diagnosis," *Shock and Vibration*, vol. 2014, Article ID 590875, 16 pages, 2014.

[17] X. Yan, Y. Liu, and M. Jia, "Research on an enhanced scale morphological-hat product filtering in incipient fault detection of rolling element bearings," *Measurement*, vol. 147, Article ID 106856, 2019.

[18] X. Yan, Y. Liu, and M. Jia, "A feature selection framework-based multiscale morphological analysis algorithm for fault diagnosis of rolling element bearing," *IEEE Access*, vol. 7, pp. 123436–123452, 2019.

[19] X.C. Yuan, L.-S. Wu, and H.-W. Chen, "Rail image segmentation based on Otsu threshold method," *Optics and Precision Engineering*, vol. 24, no. 7, pp. 1772–1781, 2016.

[20] S. L. Lu and J. W. Zhang, "Quantitative nondestructive testing of wire ropes based on features fusion of magnetic image and infrared image," *Shock and Vibration*, vol. 2019, Article ID 2041401, 15 pages, 2019.

[21] F. S. Gu, *Research on Neural Network Method for Recognizing Road Surface Roughness Based on Vehicle Response*, Jilin University, Changchan, China, 2018.

Hindawi
Shock and Vibration
Volume 2021, Article ID 5271785, 7 pages
https://doi.org/10.1155/2021/5271785

Research Article

Residual Life Prediction of Metro Traction Motor Bearing Based on Convolutional Neural Network

Yanwei Xu,[1,2] **Weiwei Cai**,[1] **Tancheng Xie**,[1,2] **and Pengfei Zhao**[1]

[1]*School of Mechatronics Engineering, Henan University of Science and Technology, Luoyang 471003, China*
[2]*Intelligent Numerical Control Equipment Engineering Laboratory of Henan Province, Luoyang 471003, China*

Correspondence should be addressed to Yanwei Xu; xuyanweiluoyang@163.com

Received 15 May 2021; Revised 1 July 2021; Accepted 19 July 2021; Published 26 July 2021

Academic Editor: Wenxian Yang

In order to solve the problem that a single type of sensor cannot fully reflect the bearing life information in the process of bearing residual life prediction of metro traction motor, a bearing residual life prediction method based on multi-information fusion and convolutional neural network is proposed. Firstly, the vibration sensor and acoustic emission sensor are used to collect the bearing life signals on the bearing fatigue life test bench. Secondly, wavelet packet decomposition is used to denoise the collected bearing life signal and extract multiple eigenvalues. On this basis, the multiple eigenvalues are normalized, and the bearing degradation trend is analyzed. Finally, the collected bearing life is divided into five stages, and the processed multiple eigenvalues are fused and input into convolutional neural network for training and recognition. The results show that the probability of predicting the stage of bearing life based on multiple eigenvalues and convolutional neural network is more than 98%.

1. Introduction

Rolling element bearings are one of the most critical components in rotating machinery to support rotating shafts. Any unexpected failure of bearings may result in several negative implications, such as downtime increase, productivity reduction, and even raise of safety risks [1–5].

In recent years, great achievements have been made in the research of algorithms in various fields. For example, Deng et al. [6] proposed an improved MSIQDE algorithm based on hybrid Multistrategy to solve the problem that quantum differential evolution (QDE) is easy to lead to premature convergence and low search ability and fall into local optimum. Aiming at the problems of slow convergence speed, poor global search ability, and difficulty in designing rotation angle of quantum heuristic evolutionary algorithm (QEA), Cai et al. [7] proposed an improved quantum cooperative coevolution algorithm with faster convergence speed and higher convergence accuracy based on coevolution strategy. Deng et al. [8] and others proposed an improved differential evolution algorithm (HMCFQDE) in order to overcome the shortcomings of differential evolution algorithm, such as low efficiency, insufficient search diversity, slow convergence speed, and high possibility of search stagnation, combined with the quantum computing characteristics of quantum evolutionary algorithm (QEA) and the idea of divide and rule of cooperative coevolutionary algorithm (CCEA). Based on the nonlinear Wiener process model, Wen et al. [9] and others proposed an improved method to predict the remaining service life of bearings. Chen [10] and others proposed a prediction model based on correlation features and multivariable support vector machine to solve the problem of using small samples to predict the residual life of rolling bearings due to the lack of sufficient condition monitoring data. Zhao et al. [11] proposed KELM (maximum power spectral density fitting curve differentiation) and weight applied to time to failure (WAFT) to solve the problem of different individual methods of rolling bearings and the different performance degradation curves caused by the difference of kernel extreme learning quality and working conditions and established a new RUL prediction model of rolling bearings. Yang and Court [12] conducted a study on the actual health status of test bearings with different types and severity of failures by

using four dimensionless status monitoring standards. These studies have achieved good results in the direction of bearing life prediction, but they all input a single eigenvalue into the model for training, the extracted bearing life information is limited, and the multieigenvalue information fusion technology is not considered. The multieigenvalue information fusion technology can improve the prediction accuracy. With the development of information fusion technology, more and more scholars join in the research. Wu and Zhang [13] proposed a new cascaded fusion convolutional long- and short-term memory network for orientation rule prediction because of the limited structure of current deep learning methods and the poor stability of prediction results due to the use of single sensory data. Wang et al. [14] used KPCA method to reduce the dimension of the extracted features and used kernel principal component to estimate the parameters of WPHM model and proposed a trend prediction method of rolling bearing residual service life based on Pchip-EEMD-GM(1, 1). These studies using information fusion technology in the direction of bearing residual life prediction have achieved good results and provide useful reference in information fusion technology, but, using a single type of sensor, the information collected cannot fully reflect the bearing life information, which will affect the prediction of bearing life.

In order to solve the problem that a single sensor cannot fully reflect the bearing life information, this paper uses wavelet packet decomposition [15] to denoise the collected original signal and extract multiple eigenvalues and studies the remaining life prediction of metro traction motor bearing based on information fusion and convolutional neural network.

2. Signal Preprocessing and Degradation Index Selection

2.1. Signal Acquisition and Preprocessing. The model of the bearing studied in this paper is Nu 216. As the bearing of metro traction motor, it plays an important role in the safe operation of the subway, so it is particularly important to predict the remaining service life of the bearing. In order to reduce the test cycle and simulate the early defects in the actual operation of the bearing, the Da Zu YLP-MDF-152 three-dimensional laser instrument was used to prefabricate the defects on the rolling element. During the process of defect prefabrication, 30% laser energy was used. The pitting diameter was 20 μm and the crack width was 15 μm. On this basis, the remaining life is explored and the remaining life test is carried out. The selected test bench is T40-120, which is located in Henan Engineering Laboratory of intelligent numerical control equipment. The test bench is composed of hydraulic system (providing loading, cooling, and lubrication), temperature measurement system, pressure measurement system, and data acquisition system. The data acquisition system includes acoustic emission sensor (model: R50S-TC, measurement range: 50 kHz–700 kHz, maximum sampling frequency: 10 m/sS) and vibration sensor (model: LC0151T, range: 33 g, sensitivity: 150 mv/g). The test bench is shown in Figure 1.

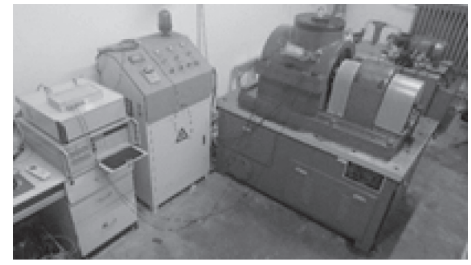

Figure 1: Bearing fatigue life test bench.

The test was carried out according to GB/T24607-2009 national test standard. The 120-hour fatigue life strengthening test was carried out under the working conditions of radial equivalent dynamic load of 40 kN and rotating speed of 2400 r/min. The bearing status data is collected every 10 minutes. After the test is completed, a total of 720 sets of bearing performance degradation test data are collected. There are a lot of noises in the collected original signals. In order to filter and denoise the original signals, they are decomposed by wavelet packet. Wavelet packet decomposition is a more detailed time-frequency analysis method. It decomposes the high frequency and low frequency of the original signal at the same time, which ensures that the signal has high resolution in different frequency bands and greatly improves the signal analysis ability [16].

Wavelet packet decomposition is used to decompose the signal N times, and each decomposition will decompose the high-frequency and low-frequency signals obtained from the previous decomposition. The decomposed signal retains the bearing life information without distortion. Suppose that the eigenvector extracted from a single sensor is Z_i ($i = 1,2, \ldots, k$), so the eigenvector obtained by multisensor synthesis is $W \times Z_i$. The expansion of Z_i is shown in the following formula:

$$Z_i = \begin{pmatrix} z_{11} & \cdots & z_{1k} \\ \vdots & \ddots & \vdots \\ z_{m1} & \cdots & z_{mk} \end{pmatrix}, \quad (1)$$

where W is the number of sensors, k is the number of extracted eigenvalues, and m is the number of samples. In this paper, db4 wavelet basis function is selected, and the original signal is decomposed by eight times wavelet packet, and the multiple eigenvalues of each frequency band are extracted.

2.2. Selection of Degradation Index of Bearing Residual Life. After performing wavelet packet decomposition on the original signal, it is necessary to extract the eigenvalues of the obtained high-frequency and low-frequency signals. In this paper, Fourier transform is used to analyze the original signal in frequency domain, and wavelet packet decomposition is used to process the original signal, so as to extract the characteristic value of time-domain signal. The time-domain features are divided into dimensional and dimensionless. Among them, dimensional time-domain features include standard deviation (SD) and root mean square

(RMS), and dimensionless time-domain features include kurtosis (Kr) and margin (C). Their formula is as follows:

$$\begin{aligned} \mathrm{SD} &= \sqrt{\frac{1}{N}\sum_{i=1}^{N}\left(x_i - \frac{1}{N}\sum_{i=1}^{N}x_i\right)^2}, \\ \mathrm{RMS} &= \sqrt{\frac{1}{N}\sum_{i=1}^{N}x_i^2}, \\ K_r &= \frac{1}{N}\sum_{i=1}^{N}x_i^4, \\ C &= \frac{\sqrt{(1/N)\sum_{i=1}^{N}x_i^2}}{(1/N)\sum_{i=1}^{n}x_i}. \end{aligned} \tag{2}$$

The standard deviation, root mean square value, kurtosis, and margin are calculated according to the above formula. Some calculation results are shown in Tables 1 and 2.

From Tables 1 and 2, we can see that the same sensor cannot be directly fused because of the different magnitude of the value between different eigenvalues. At the same time, the numerical unit of the same feature value is different between different sensors, and it cannot be directly fused. Therefore, we need to normalize them to map them to the same interval and perform fusion within the same interval.

3. Information Fusion and Model Building

3.1. Fusion of Eigenvalues. In engineering practice, the life decline process of rolling bearings is often reflected by vibration signals, so as to carry out life state identification and life assessment [17]. However, in order to cope with the shortcomings of single type of sensors, vibration and acoustic emission sensors are used to collect bearing life information in this test. After the preprocessed signal and the feature value are extracted, the simultaneous interpreting cannot be directly integrated, because the physical meaning of data collected by different sensors is different, and normalization is needed.

Normalization refers to mapping from one interval to another. Suppose that the original eigenvalue interval extracted is (X_1, X_2), and the normalized interval is (Y_1, Y_2). If the data before normalization is G and the normalized data is H, then the mapping relationship between G and H is as follows:

$$H = f(G). \tag{3}$$

The mapping relation is linear:

$$H = \frac{(G - X_1)(Y_2 - Y_1)}{X_2 - X_1} + c. \tag{4}$$

Information fusion technology is based on normalization and has the characteristics of complementary measurement results of multisensor. Information fusion can evaluate and decide the importance of its parameters [18]. Information fusion can be divided into data layer fusion, feature layer fusion, and decision level fusion according to the fusion mode. Data layer fusion belongs to the most original fusion [19], and the loss of information is the least. However, due to the difference of detection technology between acoustic emission sensor and vibration sensor, data layer fusion is not adopted; feature level fusion belongs to the fusion of extracted eigenvalues. Although some information is lost, the difference between sensors can be eliminated by normalization processing, and a lot of information will be lost in decision level fusion, so feature level fusion is used in this experiment.

Table 1: Characteristic values of bearing life collected by vibration sensor.

Vibration sensor			
SD	RMS	K_r	C
43.6529	1980.265	3.3203	1.0473
45.4865	1981.92	14.5511	1.263
52.9402	1981.651	79.2886	1.4892
53.5617	1979.754	90.9587	1.0493

Table 2: Characteristic values of bearing life collected by acoustic emission sensor.

Acoustic emission sensor			
SD	RMS	K_r	C
0.0176	0.0178	687.014	170.6823
0.1956	0.1961	134.212	497.5525
0.0454	0.0458	108.6922	111.4096
0.0653	0.0653	125.7846	183.2307

It can be seen from Table 2 that the extracted eigenvalues cannot be directly fused, and they need to be normalized and then fused. After 720 groups of data are fused, 120 groups are selected as the test group, and the remaining 600 groups are taken as the training group. The test group and training group are divided into five stages. The divided test group and training group are marked and input into the neural network for training.

3.2. Prediction Model of Bearing Residual Life Based on Multi-Information Fusion and CNN. Convolutional neural network is a feedforward neural network composed of multilayer networks. In view of the LeNet-5 structure, the convolutional neural network is improved. Initially determine the size of the convolution kernel to be 3×3; the activation function of convolutional neural network includes sigmoid, tan$h$, and ReLU, as well as initial selection of activation function ReLU. After the feature information is extracted in convolution layer and transmitted to pooling layer, the pooling layer performs feature selection and information filtering and preliminarily determines that the pooling matrix is 2×2. The full-connection layer needs to carry out nonlinear combination of the extracted features to get the output, and the output layer selects softmax classification function for classification. The structure of convolutional neural network is shown in Figure 2.

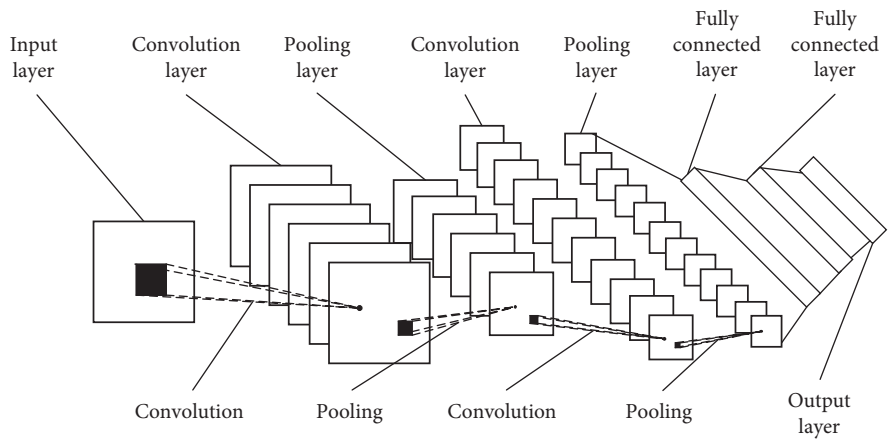

Figure 2: Convolutional neural network model.

After normalization, it is necessary to train convolutional neural network, input normalized data into neural network, and adjust the numbers of convolution layers and pooling layers in the convolutional neural network model. Finally, it is determined that the size of the convolution kernel of the first layer of the convolutional neural network is 3×3, the output dimension is 46×46, the sliding step is 1, the pooling matrix of the first layer is 2×2, and the moving step is 2. The size of the second layer of convolution kernel is 3×3, the output dimension is 21×21, the sliding step is 1, the pooling matrix of the second layer is 2×2, the moving step is 2, and the first layer is fully connected set to 100, the fully connected layer of the second layer is set to 64, and the output layer is set to 5. The activation function of the first layer is ReLU, and the activation function of the second layer is tan$h$. The optimal training times (Epochs) of the model are 100.

After the above work is completed, the normalized eigenvalues of each sensor are input into the adjusted neural network, and the recognition rate is shown in Table 3.

According to Table 3, the recognition rate of different eigenvalues is different. The root mean square value has the best recognition rate, which indicates that the root mean square can extract the most bearing life information, and standard deviation, kurtosis, and margin decrease in turn, which indicates that the bearing life information extracted by them decreases in turn. It can be seen from Table 3 that, for a single sensor, the fusion of different eigenvalues can improve the accuracy of remaining life prediction, which shows that there are similarities and differences between different eigenvalues in extracting bearing life information. Through fusion of feature values extracted by different sensors, it is seen that the accuracy of predicting the remaining life of bearing is also improved, and it is shown that different sensors can be complemented to improve the accuracy of bearing remaining life prediction.

4. Data Analysis

By analyzing the normalized eigenvalues, the bearing life trend is shown in Figures 3 and 4.

It can be seen from Figure 3 that, except for kurtosis, the trend of other indicators is upward, which indicates that kurtosis index can extract the least bearing life information, while the root mean square and standard deviation can extract more bearing life information than margin. Figure 4 shows the trend of bearing life collected by AE sensor, and the above conclusion can be verified from Figure 4.

It can be seen from Figures 3 and 4 that, with the increase of bearing running time, the bearing life index is getting larger and larger. Through the analysis, it can be concluded that dimensionless kurtosis and margin are not as good as dimensionless root mean square and standard deviation. From the two kinds of sensors, vibration sensor is better than acoustic emission sensor in root mean square and standard deviation, and acoustic emission sensor is better than vibration sensor in margin and kurtosis.

It can be seen from Figures 3 and 4 that they have the same bearing life index, and the upper and lower wave momentum are different. In order to explore the influence of the up and down wave momentum on the accuracy, taking root mean square as an example, the root mean square (RMS) obtained from the two sensors is input into the convolutional neural network to obtain the color scale diagram of the accuracy in each stage, as shown in Figure 5.

In the above figure, A, B, C, D, and E represent the five stages of bearing life: A represents the first stage, B represents the second stage, C represents the third stage, D represents the fourth stage, and E represents the fifth stage. This experiment is carried out after the discovery of bearing early defects. The first stage is the bearing early defects, and the fifth stage is the final stage of bearing life collection. A total of 720 groups of data were collected, and the collected data were divided into test set and training set, including 120 groups of test samples and 600 groups of training samples. In the training process, the neural network will output the probability values of these five stages for each group of test samples. The 120 groups of test samples will output 120×5 probability values. Taking an average value of each two groups of 120 groups as the new probability value, the new probability value will be made into a color scale diagram of Figure 5. In this grayscale image, the deeper the color is, the higher the probability is.

Table 3: Recognition rate of each normalized eigenvalue.

Eigenvalue	Acoustic emission sensor (%)	Vibration sensor (%)
RMS	94.17	95.83
K_r	70.83	66.67
C	70.00	61.67
SD	93.33	95.00
Recognition rate of multiple eigenvalues of a single sensor	95.83	96.67
Comprehensive recognition rate of two sensors	98.33	

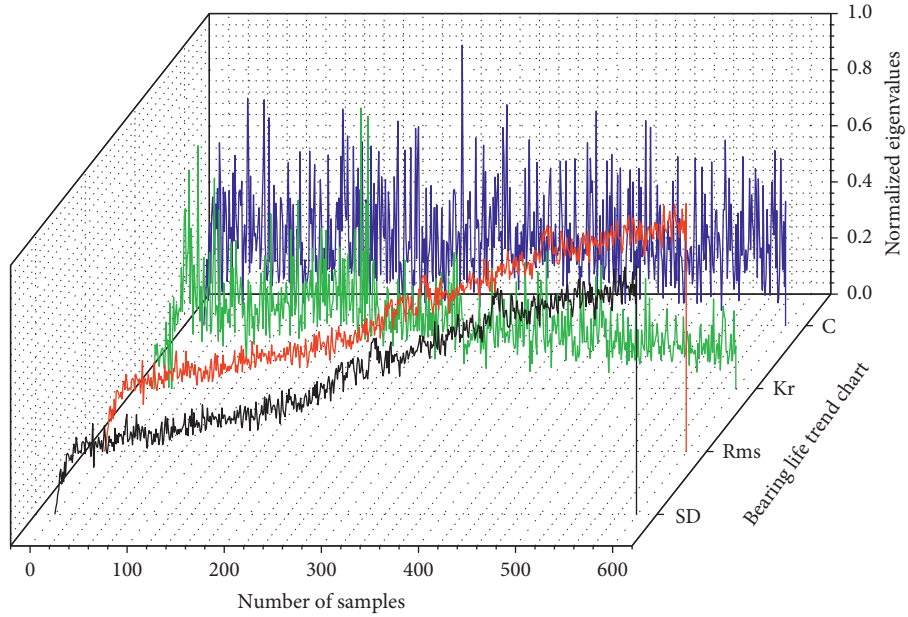

Figure 3: Bearing life curve collected by vibration sensor.

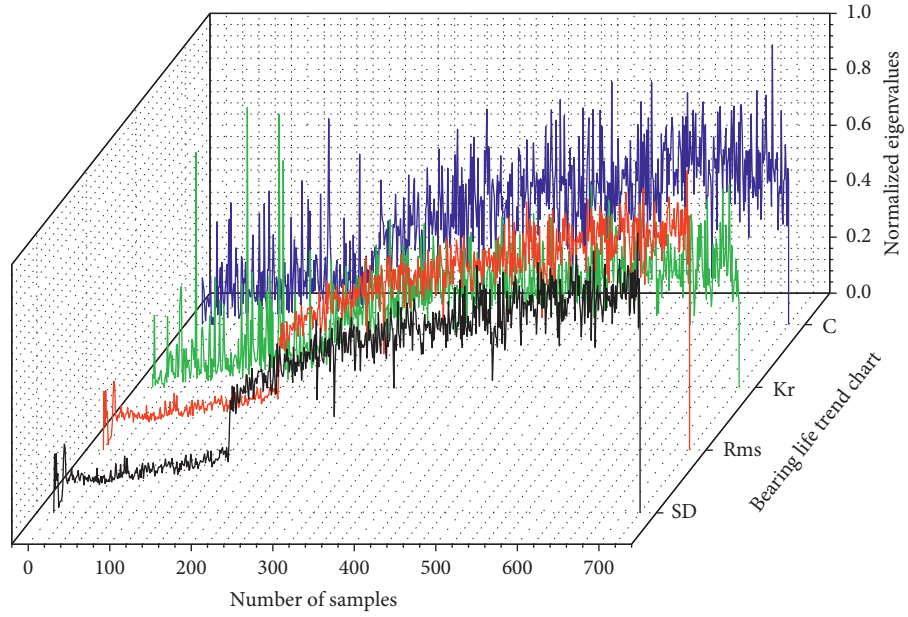

Figure 4: Bearing life curve collected by acoustic emission sensor.

From Figure 5, we can see that the vibration sensor is not as good as the acoustic emission sensor in the first stage and the second stage, but it is better than the acoustic emission sensor in other stages, which shows that the fusion of the information obtained by the two sensors is conducive to improving the accuracy of bearing residual life prediction.

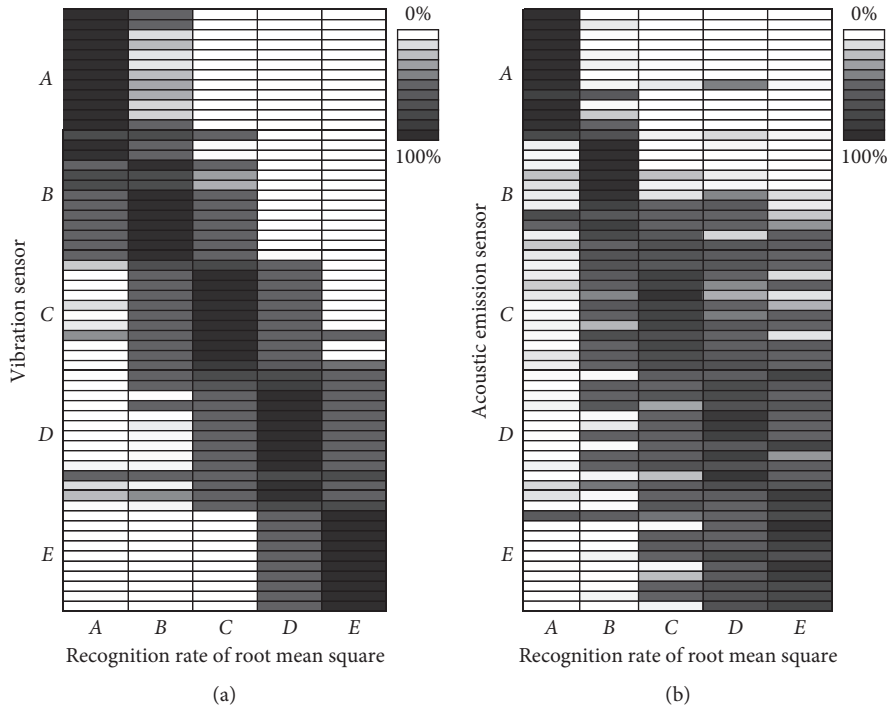

Figure 5: Color scale diagram of root mean square recognition rate.

At the same time, in Figure 5, we can see that the accuracy rate of the two adjacent stages is lower than that of the middle part of the stage.

Taking root mean square value as an example, it can be seen from Figures 3–5 that the fluctuation of life curve collected by acoustic emission sensor in the first stage is smaller than that of vibration sensor. At this time, we can see that the accuracy rate of acoustic emission sensor in the first stage is high. Compared with other stages, it can be found that the smaller the fluctuation of bearing life curve is, the higher the accuracy of bearing life stage is. On the whole, the fluctuation of bearing life curve collected by vibration sensor is smaller than that of acoustic emission sensor, so vibration sensor is better than acoustic emission sensor in bearing life prediction.

5. Conclusion

Aiming at the problem that a single sensor cannot reflect the bearing life information comprehensively, a bearing residual life prediction method based on multi-information fusion and convolutional neural network is proposed.

(1) This paper studies the prediction of the remaining life of subway traction motor bearings with deep learning and information fusion technology. First, use vibration sensor and acoustic emission sensor to collect bearing life signals on the bearing fatigue test bench; secondly, use wavelet packet decomposition to denoise the collected original signals and extract multiple eigenvalues. On this basis, multiple eigenvalues are extracted. The eigenvalues are normalized and the bearing degradation trend is analyzed. It is found that the vibration sensor performs better than the acoustic emission sensor in terms of dimension, and the acoustic emission sensor performs better than the vibration sensor in the dimensionless aspect. Finally, the processed multiple eigenvalues are fused and input into the convolutional neural network for training to predict the remaining service life of the bearing.

(2) The results show the following: ① The vibration sensor has less fluctuation on the bearing life curve compared to the acoustic emission sensor, and the recognition rate of using two types of sensors at the same time is higher than that of using a single type of sensor. ② The information fusion of different types of sensors is realized by using feature layer fusion, and the combination of convolutional neural network can effectively predict the remaining life of the bearing.

Data Availability

The data used to support the findings of this study are included within the article.

Conflicts of Interest

The authors declare that they have no conflicts of interest.

References

[1] Y. Lei, J. Lin, and M. J. Zuo, "Condition monitoring and fault diagnosis of planetary gearboxes: a review," *Measurement*, vol. 48, no. 1, pp. 292–305, 2014.

[2] A. Ghods and H. H. Lee, "Probabilistic frequency-domain discrete wavelet transform for better detection of bearing faults in induction motors," *Neurocomputing*, vol. 188, pp. 206–216, 2016.

[3] J. Liu, W. Wang, and F. Golnaraghi, "An enhanced diagnostic scheme for bearing condition monitoring," *IEEE Transactions on Instrumentation and Measurement*, vol. 59, pp. 309–321, 2010.

[4] Y. Wang, G. Xu, Q. Zhang, D. Liu, and K. Jianga, "Rotating speed isolation and its application to rolling element bearing fault diagnosis under large speed variation conditions," *Journal of Sound and Vibration*, vol. 348, pp. 381–396, 2015.

[5] F. Jia, Y. Lei, J. Lin, X. Zhou, and N. Lu, "Deep neural networks: a promising tool for fault characteristic mining and intelligent diagnosis of rotating machinery with massive data," *Mechanical Systems and Signal Processing*, vol. 72, pp. 303–315, 2016.

[6] W. Deng, J. Xu, X.-Z. Gao, and H. Zhao, "An enhanced MSIQDE algorithm with novel multiple strategies for global optimization problems," *IEEE Transactions on Systems, Man, and Cybernetics: Systems*, pp. 1–10, 2020.

[7] X. Cai, H. Zhao, S. Shang et al., "An improved quantum-inspired cooperative co-evolution algorithm with muli-strategy and its application," *Expert Systems with Applications*, vol. 171, Article ID 114629, 2021.

[8] W. Deng, S. Shang, X. Cai et al., "Quantum differential evolution with cooperative coevolution framework and hybrid mutation strategy for large scale optimization," *Knowledge-Based Systems*, vol. 224, Article ID 107080, 2021.

[9] J. Wen, H. Gao, and J. Zhang, "Bearing remaining useful life prediction based on a nonlinear wiener process Model," *Shock and Vibration*, vol. 2018, Article ID 4068431, 13 pages, 2018.

[10] X. Chen, Z. Shen, Z. He et al., "Remaining life prognostics of rolling bearing based on relative features and multivariable support vector machine," in *Proceedings of the Institution of Mechanical Engineers–Part C: Journal of Mechanical Engineering Science*, vol. 227, pp. 2849–2860, January 2013.

[11] H. Zhao, H. Liu, Y. Jin, X. Dang, and W. Deng, "Feature extraction for data-driven remaining useful life prediction of rolling bearings," *IEEE Transactions on Instrumentation and Measurement*, vol. 70, pp. 1–10, 2021.

[12] W Yang and R Court, "Experimental study on the optimum time for conducting bearing maintenance," *Measurement*, vol. 46, no. 8, pp. 2781–2791, 2013.

[13] Q. Wu and C. Zhang, "Cascade fusion convolutional long-short time memory network for remaining useful life prediction of rolling bearing," *IEEE Access*, vol. 8, pp. 32957–32965, 2020.

[14] F. Wang, X. Liu, C. Liu, H. Li, and Q. Han, "Remaining useful life prediction method of rolling bearings based on pchip-EEMD-GM(1, 1) model," *Shock and Vibration*, vol. 2018, Article ID 3013684, 10 pages, 2018.

[15] Y. Cekic, "Bearing fault detection by four-band wavelet packet decomposition," *Technology News Focus*, vol. 23, no. 1, pp. 91–98, 2019.

[16] S. Fei, "Fault diagnosis of bearing based on wavelet packet transform-phase space reconstruction-singular value decomposition and SVM classifier," *Arabian Journal for Science and Engineering*, vol. 42, pp. 1967–1975, 2017.

[17] L. Ren, Y. Sun, J. Cui, and L. Zhang, "Bearing remaining useful life prediction based on deep autoencoder and deep neural networks," *Journal of Manufacturing Systems*, vol. 48, pp. 71–77, 2018.

[18] X. Pang, D. Wang, L. Chen, and L. Ye, "Grey relation evaluation and truth value fusion of rolling bearing multisource residual stress," *Mathematical Problems in Engineering*, vol. 2020, Article ID 3401385, 15 pages, 2020.

[19] Y. Xu, W. Cai, and T. Xie, "Fault diagnosis of subway traction motor bearing based on information fusion under variable working conditions," *Shock and Vibration*, vol. 2021, Article ID 5522887, 12 pages, 2021.

Hindawi
Shock and Vibration
Volume 2021, Article ID 7610884, 10 pages
https://doi.org/10.1155/2021/7610884

Research Article

Intelligent Recognition Method of Turning Tool Wear State Based on Information Fusion Technology and BP Neural Network

Yanwei Xu,[1,2] **Lin Gui**,[1] **and Tancheng Xie**[1,2]

[1]*School of Mechatronics Engineering, Henan University of Science and Technology, Luoyang 471003, China*
[2]*Intelligent Numerical Control Equipment Engineering Laboratory of Henan Province, Luoyang 471003, China*

Correspondence should be addressed to Yanwei Xu; xuyanweiluoyang@163.com

Received 28 April 2021; Revised 11 June 2021; Accepted 10 July 2021; Published 20 July 2021

Academic Editor: Zi-Qiang Lang

The multi-information data acquisition system of tool wear condition of CNC lathe is built by acquiring the acoustic emission and vibration acceleration signals. The data of acoustic emission and vibration acceleration signals during the process of CNC machine tool processing under the conditions of different tool wear degrees and different cutting conditions are acquired and analyzed using the orthogonal experimental method. The optimum characteristic frequency band of acoustic emission and vibration acceleration signals was extracted by the wavelet envelope decomposition method so as to recognize tool wear condition as the characteristic parameters. The characteristic information of acoustic emission and vibration acceleration signals during the process of CNC machine tool processing was fused. In addition, the intelligent recognition of tool wear condition during the process of machine tool processing was researched.

1. Introduction

Tool wear and breakage will occur in the process of CNC machine tool cutting, which will directly affect the machining accuracy and surface quality of the workpiece. Tool wear and breakage will also directly affect the machining efficiency and cutting stability of the whole manufacturing equipment system. According to statistics, the failure shutdown rate caused by tool failure accounts for about 22.4% of the total failure shutdown rate of CNC machine tools. In the actual production process [1], there is a highly nonlinear relationship between the influencing factors and the tool wear [2], so it is difficult to judge the tool wear accurately by the manual method. In order to ensure the accuracy of machining, it is necessary to replace the tool before the tool is severely worn, so it is necessary to replace the tool frequently, but the frequent replacement of the tool reduces the efficiency of production and improves the cost of machining. If the serious situation of tool wear and damage is not found in time or the tool is not replaced in time, the processing process may be interrupted, and the workpiece may be scrapped. By monitoring and identifying the tool wear status, the tool can be replaced at the right time. Monitoring, identifying the tool wear status, and timely replacing the tool not only can ensure the machining accuracy but also can improve the tool utilization and reduce the production cost. Replacing the cutting tool at the right time can avoid the scrapping of the workpiece and the failure of the machine tool caused by the failure of the cutting tool.

In recent years, many experts and scholars have studied the methods to identify the tool wear state [3–9], and their research has promoted the development of tool wear state identification technology. However, many experts and scholars study the tool wear state identification method based on the information provided by a single sensor, and it is difficult to ensure that a single sensor provides correct and comprehensive information. Information fusion technology is a comprehensive decision-making process to accurately estimate the measurement results of multiple sensors, so as to comprehensively and timely evaluate the situation, threat, and importance. Therefore, information fusion technology has the advantages of high fault tolerance, complementarity, economy, and being real time [10–17]. In recent years, information fusion technology has been applied more and

more in the field of tool wear state recognition, but there is no unified standard [18–22].

At present, the common methods of multi-sensor data fusion can be summarized as random and artificial intelligence. Artificial intelligence includes fuzzy logic reasoning, neural network, and so on. The representation and processing of information by fuzzy logic reasoning is closer to the way of human thinking, but there are many subjective factors in the description of information, so the representation and processing of information by fuzzy logic reasoning lacks objectivity. Neural network has strong fault tolerance, self-learning, self-organization, and self-adaptive ability. It can simulate complex nonlinear mapping and meet the requirements of multi-sensor data fusion technology. In this paper, BP neural network technology is used to fuse the acoustic emission (AE) signal of tool wear and the characteristic information of vibration signal in the process of numerical control cutting, so as to study the intelligent recognition technology of tool wear state in the process of numerical control turning.

2. Acquisition System of Tool Wear Condition

2.1. The Structure of the System. The acquisition system of tool wear condition is composed of a CNC lathe, workpiece, turning tool, AE sensor, vibration sensor, amplifier, signal conditioner, data acquisition card, and computer (the structure diagram of the system is shown in Figure 1).

The AE sensor and vibration sensor are placed in the tool handle. The signal detected by the sensor is processed by the preamplifier and signal conditioner and then transmitted to the computer by data acquisition card for analysis and processing. Figure 2 shows the physical diagram of the multi-information data acquisition system of tool wear condition of the CNC lathe, which is composed of a CKJ6152 CNC lathe, PCI-8 acoustic emission instrument, WD/FM01 broadband differential AE sensor, LC0151T acceleration sensor, LC0201-5 signal conditioner matched with acceleration sensor, and PCI8510 data acquisition card. The signal-to-noise ratio of the acoustic emission instrument is 4.5, the frequency range is 1 kHz–3 MHz, and the maximum sampling frequency is 10 m/s. The AE sensor collects the voltage signal, the measurement range is 1 kHz –1 MHz, and the resonant frequency is 531.25 kHz. The sensitivity of the acceleration sensor is 150 mV/g, the measurement range is 33 g, the resolution is 40 kHz, the resonant frequency is 0.0002 g, and the frequency range is 0.7 Hz–13 kHz. And the 8-channel data acquisition card with the speed of 500 k/s is adopted is 500 k/s.

2.2. The Location of Sensors. The vibration sensor and AE sensor are fixed on the new turning tool of CNC lathe according to different directions and distances. The material of the turning tool is YT15. The turning test of 45# steel bar is carried out under the conditions of spindle speed $n = 800$ r/min, feed rate $f = 40$ mm/min, and back engagement ap = 0.5 mm. The signals of vibration sensor and AE sensor are collected and analyzed to determine the reasonable fixed position of the sensor.

As shown in Figure 3, the AE sensor is tested in five installation positions. Position 1 is 15 cm from the tip at the rear of the left side of the handle, position 2 is 4 cm from the tip at the front of the left side of the handle, position 3 is 2 cm from the tip at the right side of the handle, position 4 is 4 cm from the tip at the right side of the handle, and position 5 is 6 cm from the tip at the right side of the handle. We find the root-mean-square value of data collected by AE sensor and judge the strength of signal according to the value of root-mean-square value. The results show that the root-mean-square values of positions 3, 4, and 5 decrease in turn, while the root-mean-square values of positions 2 and 4 are basically the same, indicating that the signal strength is independent of direction, while position 1 has the smallest root-mean-square value. Therefore, the best installation position for the AE sensor is position 3.

As shown in Figure 4, the acceleration sensor is tested in three different positions: position 1 is 4 cm away from the tip, position 2 is 8 cm away from the tip, position 3 is 12 cm away from the tip, and the three spatial positions are shown in X, Y, and Z directions in Figure 4. The results show that position 1 and Z direction have the largest root-mean-square value, so position 1 and Z direction are selected as the best installation position for acceleration sensor.

2.3. Dividing the Degree of Tool Wear. One kind of indexable cemented carbide tool CNMG120404-PM and 45# steel bar are selected as test objects. And the parameters of the tool CNMG120404-PM are as follows: tool material YT15, tool rake angle $\gamma = 11^\circ$, clearance angle $\alpha = 10^\circ$, tool cutting edge angle $\mathrm{Kr}' = 95^\circ$, tool cutting edge inclination angle $\lambda = 0^\circ$. Cutting tests are carried out according to engagement ranging from 0.3 mm to 1.0 mm to obtain tool test samples of different wear degrees.

During the turning process, the wear of the flank surface has a great influence on the quality of the workpiece, cutting force, and cutting temperature. Since the wear of the flank surface is easy to observe and measure [23], according to the international standard ISO 3685-1977, the wear band width VB measured at the middle part of the flank surface is selected as the test standard, and the tool wear state is divided into 4 wear degrees as shown in Table 1.

2.4. Orthogonal Experimental Method. Taking the tool wear degrees, spindle speed, feed rate, and cutting depth as the main factors, four kinds of blade samples with different wear degrees were selected, and 16 groups of turning experiments were carried out by the orthogonal experimental method. The AE signal and vibration signal were collected in each group of tests, and the influence degree of different factors on AE signal and vibration signal was analyzed.

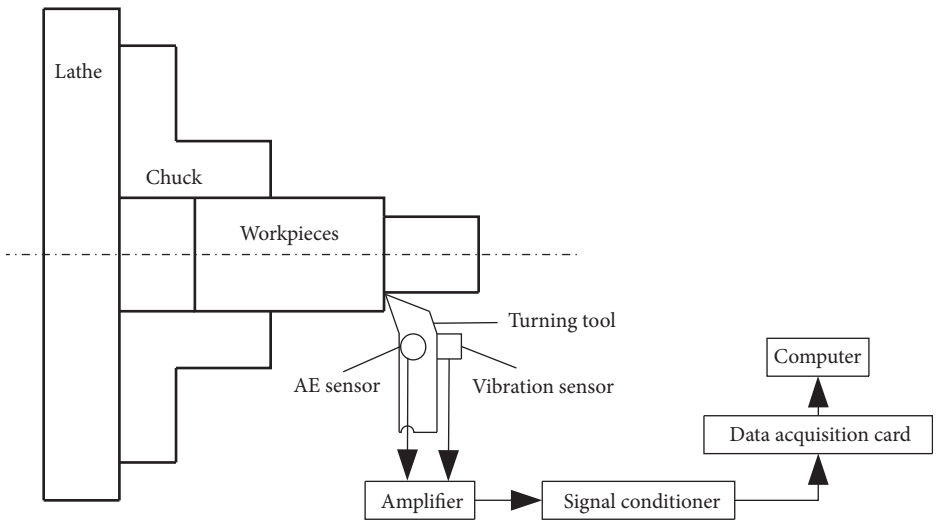

Figure 1: The structure diagram of the system.

Figure 2: The physical diagram of the multi-information data acquisition system of tool wear condition of CNC lathe.

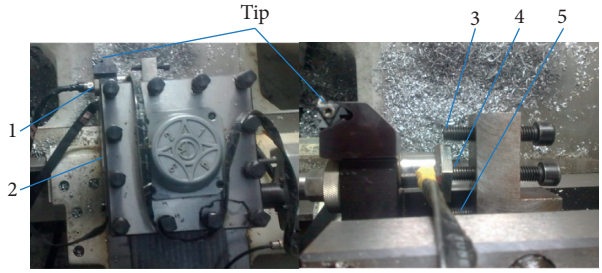

Figure 3: Installation position of AE sensor.

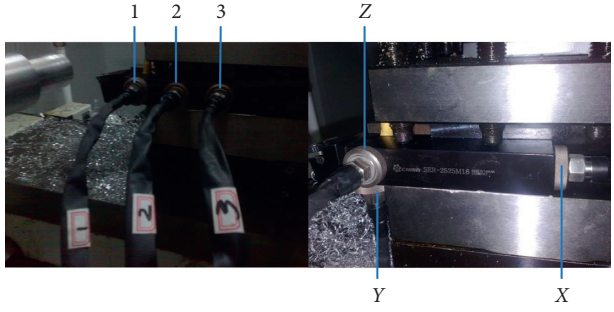

Figure 4: Installation position of acceleration sensor.

Table 1: Tool wear degrees.

Classification	Initial wear	Normal wear	Medium wear	Severe wear
Degrees	1	2	3	4
VB values (mm)	0~0.1	0.1~0.3	0.3~0.6	0.6~

The test conditions are cutting with cutting fluid. The material processed is 45# steel bar, and the experimental time of each group is 30 s.

Table 2 shows the experimental parameters and the data collected by the sensor, and Table 3 shows the analysis results of the experimental data using the mean method.

According to the analysis results in Table 3, for AE signal, the maximum range of wear degree is 1.9357, the maximum range of spindle speed is 2.5541, the maximum range of feed speed is 0.3083, and the maximum range of cutting depth is 0.5408. Therefore, the spindle speed has the most significant effect on AE signal, followed by wear degree and cutting depth, and the feed speed has the least effect on AE signal. For vibration signal, the maximum range of wear degree is 0.5346, the maximum range of spindle speed is 0.2944, the maximum range of feed speed is 0.2650, and the maximum range of cutting depth is 0.1615. Therefore, the influence of wear degree on vibration signal is the most significant, followed by spindle speed and feed speed, and the influence of cutting depth on vibration signal is the least.

3. Selection of Tool Wear Characteristics

Acoustic emission and vibration signals are nonstationary random signals whose frequency and statistical characteristics vary with time. Spectrum analysis can analyze the characteristics of nonstationary random signals in a certain period. Wavelet packet analysis is a kind of signal processing technology, which concentrates the information energy, finds the order in the details, and selects the rules, and it can divide the frequency band into multiple levels and can adaptively select the corresponding frequency band according to the

Table 2: Experimental parameters and collected data.

Serial numbers	Degrees of wear	Experimental parameters			Collected data	
		Spindle speed (r/min)	Feed rate (mm/min)	Cutting depth (mm)	AE sensor (V)	Vibration sensor (V)
1	1	560	20	0.4	0.7522	0.1542
2	1	800	30	0.6	1.4141	0.1732
3	1	1120	40	0.8	2.0434	0.2119
4	1	1600	50	1.0	3.1657	0.2183
5	2	560	30	0.8	1.1045	0.3117
6	2	800	20	1.0	1.9643	0.2944
7	2	1120	50	0.4	1.7929	0.2357
8	2	1600	40	0.6	3.9895	0.2698
9	3	560	40	1.0	2.3615	0.4471
10	3	800	50	0.8	3.3478	0.3960
11	3	1120	20	0.6	4.4762	0.1940
12	3	1600	30	0.4	4.9327	0.2112
13	4	560	50	0.6	2.0609	1.2597
14	4	800	40	0.4	2.2999	0.6498
15	4	1120	30	1.0	4.0951	0.3535
16	4	1600	20	0.8	4.4076	0.6331

Table 3: Analysis result of experiment data.

Signal classification		Influence factors			
		Degrees of wear	Spindle speed	Feed rate	Cutting depth
AE signal	Mean 1	1.8439	1.5698	2.9001	2.4444
	Mean 2	2.2128	2.2565	2.8866	2.9852
	Mean 3	3.7796	3.1019	2.6736	2.7258
	Mean 4	3.2159	4.1239	2.5918	2.8967
	Range	1.9357	2.5541	0.3083	0.5408
Vibration signal	Mean 1	0.1894	0.5432	0.3189	0.3127
	Mean 2	0.2779	0.3784	0.2624	0.4742
	Mean 3	0.3121	0.2488	0.3947	0.3882
	Mean 4	0.7240	0.3331	0.5274	0.3283
	Range	0.5346	0.2944	0.2650	0.1615

characteristics of the analyzed signal, so that it can match the signal spectrum and improve the resolution of time-frequency, and it is widely used in engineering practice. In this paper, the wavelet packet decomposition method is used to decompose the test data, and the energy value of each frequency band signal is obtained. Then, according to the mean and range of each frequency band energy under different conditions, the relevant characteristic frequency band of acoustic emission and vibration signal is selected.

3.1. Selection of Vibration Signal Characteristics. The vibration signal of tool wear is mainly in the low-frequency band (no more than 8 kHz) [24]. Considering the integrity of the collected signal, the sensor with the frequency range of 0.7–13 kHz and sampling speed of 250 k/s is selected to collect the signal, and the db8 is selected as the wavelet base to decompose the collected signal by 6-level wavelet packet, and then the frequency difference of each frequency band is reduced to 1.95 kHz. The 6-level wavelet packet decomposition of medium wear tool vibration signal in 13–16 frequency bands is shown in Figure 5.

Since the effective frequency of the signal is not more than 13 kHz, only the first 16 of 64 bands (0~31.2 kHz) are analyzed to avoid information redundancy. The energy changes of the first 16 frequency bands of vibration signals with different tool wear degrees are shown in Figure 6.

It can be seen from Figure 6 that the energy is mainly concentrated in P1, P2, P3, P4, P7, and P8 frequency bands. With the increase of tool wear degree, the energy increases significantly in P2, P4, P7, and P8 frequency bands. Since the effective frequency range of acceleration sensor is 0.7 Hz~13 kHz (±10%), the P8 band is omitted. The characteristic frequency bands of vibration signal are P2, P4, and P7.

Then, the mean and range of energy values in P2, P4, and P7 frequency bands under different conditions are calculated by orthogonal table to determine the characteristic frequency band which can best reflect the wear degree and is least affected by external factors. Table 4 shows the mean and range of energy values of vibration signals in P2, P4, and P7 frequency bands obtained by using orthogonal test table.

According to Table 4, the wear degree has the greatest influence on the energy changes of P2, P4, and P7 bands, which is consistent with the analysis results in Table 3.

In P2 band (1.95~3.9 kHz), the range of wear degree is 24.96, which is much larger than that of the other three

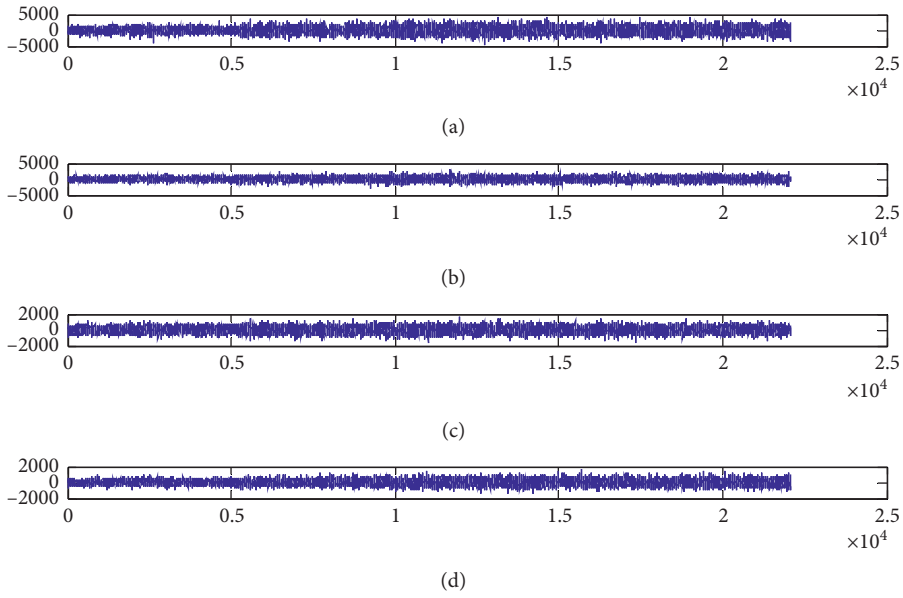

Figure 5: 6-level wavelet packet decomposition of medium wear tool vibration signal in 13–16 frequency bands. (a) P13. (b) P14. (c) P15. (d) P16.

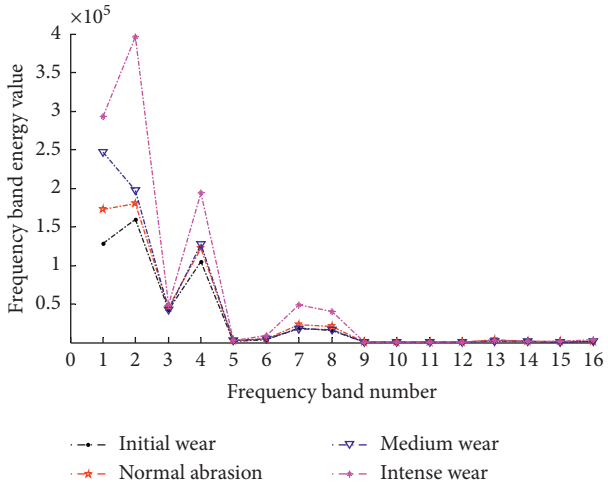

Figure 6: Energy value of vibration signal in different frequency bands.

factors, which are 3.35 times, 7.66 times, and 4.11 times that of spindle speed, feed speed, and cutting depth, respectively. The P2 frequency band is the most important one, and the three factors of cutting cannot be considered, so it is an ideal characteristic frequency band.

In P4 band (5.85~7.8 kHz), the range of wear degree is 41.88, which is 2.18 times, 3.23 times, and 3.70 times that of the range of spindle speed, feed speed, and cutting depth, respectively. In the P4 frequency band, the wear degree has the greatest influence on the energy change, but the influence of the three cutting factors on the energy change is relatively small, so P4 can be selected as the characteristic frequency band.

The range of wear degree in P7 band (11.7~13.65 kHz) is 18.59, which is 1.27 times, 1.44 times, and 2.02 times that of spindle speed, feed speed, and cutting depth, respectively. P7 band cannot be used as characteristic band.

Therefore, P2 is the best characteristic band of vibration signal, followed by P4.

3.2. Feature Selection of AE Signal. The acoustic emission signal of tool wear is an ultra-high frequency stress wave pulse signal with a frequency of more than 100 kHz released when dislocation, crack propagation, and plastic deformation occur in the molecular lattice during metal processing [25]. This paper selects 100 kHz~1 MHz sensor, with a sampling frequency of 2 m/s, adopts 5-stage wavelet packet decomposition, and selects dB8 as wavelet base to reduce the frequency difference of each frequency band to 31.25 kHz. The wavelet packet decomposition of AE signal shows that the energy mainly exists in P1~P16 bands (0~500 kHz), and there is almost no energy in P17~P32 bands, so only P1~P16 bands are analyzed. The energy changes of the first 16 bands of acoustic emission signals with different wear degree of the tool are shown in Figure 7.

It can be seen from Figure 7 that the energy is mainly concentrated in P1~P8 and P13 frequency bands. With the increase of tool wear degree, the energy increases significantly in P1, P2, P4, P7, and P13 frequency bands. Since the effective frequency band of AE signal is greater than 100 kHz, P1 and P2 frequency bands (0~62.5 kHz) are omitted. The characteristic frequency bands of AE signal are P4, P7, and P13.

Then, the mean and range of energy values in P4, P7, and P13 frequency bands under different conditions are calculated by orthogonal table to determine the characteristic

Table 4: Energy analysis results of P2, P4, and P7 frequency bands of vibration signal ($\times 10^5$).

Frequency band	Mean and range	Experimental factors			
		Degrees of wear	Spindle speed	Feed rate	Cutting depth
P2	Mean 1	6.97	21.07	14.97	12.47
	Mean 2	11.97	13.63	15.46	18.54
	Mean 3	12.09	13.84	14.64	16.45
	Mean 4	31.93	14.43	17.9	15.51
	Range	24.96	7.44	3.26	6.07
P4	Mean 1	7.66	33.08	18.14	20.67
	Mean 2	13.38	22.83	15.84	28.32
	Mean 3	16.33	13.84	24.12	20.92
	Mean 4	49.54	17.16	28.82	17.00
	Range	41.88	19.24	12.98	11.32
P7	Mean 1	6.46	22.54	10.29	10.15
	Mean 2	10.28	11.91	8.42	19.37
	Mean 3	11.36	7.92	13.15	12.07
	Mean 4	25.05	10.77	21.29	11.55
	Range	18.59	14.62	12.87	9.22

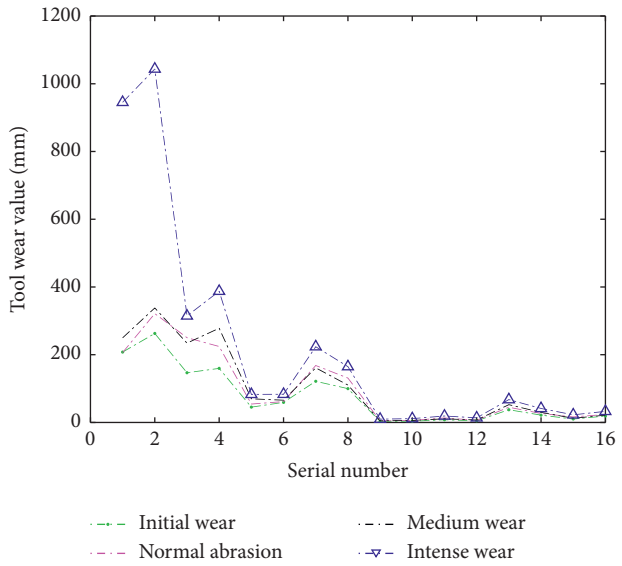

Figure 7: Energy value of AE signal in different frequency bands.

frequency band which can best reflect the wear degree and is least affected by external factors. Table 5 shows the mean value and range of energy value of vibration signal P4, P7, and P13 under different conditions.

It can be seen from Table 5 that the spindle speed has the greatest influence on the energy change of P4, P7, and P13 bands, which is consistent with the analysis results in Table 3.

In P4 frequency band (93.75~125 kHz), the range of spindle speed is 1432.7, the influence of tool wear degree is second only to spindle speed (range is 1116.6), and the influence of feed speed and cutting depth is relatively small (range is 568.6 and 692, respectively).

In P7 frequency band (187.5 ~ 218.75 kHz) and P13 frequency band (375~406.25 kHz), the influence of wear degree is the second, but the influence of wear degree is similar to that of feed speed and cutting depth, so it is not suitable to be used as characteristic frequency band.

Therefore, it is more suitable to select P4 band as the characteristic band of AE signal in tool wear detection. At the same time, considering that the acoustic emission signal characteristics in tool wear monitoring system are greatly affected by the spindle speed, in order to reduce the error rate of intelligent recognition, the spindle speed is also selected as the characteristic value of AE signal.

In view of the small influence of cutting depth and feed speed on vibration and acoustic emission signals, the short-term experimental processing was carried out on the obtained worn blade samples by keeping the cutting depth and feed speed at the constant value and selecting the spindle speed randomly according to the orthogonal test speed. The acoustic emission and vibration signals of each blade during processing were collected, and the energy values of P2 and P4 frequency bands of vibration signals, the energy values of P4 frequency band of acoustic emission signals, and the corresponding spindle speed are extracted as the required characteristic parameters for the training and verification of the intelligent recognition model of tool wear state. The test parameters of this short-term experimental processing are as follows: cutting depth ap is 0.6 mm, feed speed vf is 30 mm/min, spindle speed random, using cutting fluid, processing material 45# steel bar, and each blade test time is 30 s.

4. Information Fusion Model Based on BP Neural Network

The cutting process is a complex nonlinear stochastic process with many variables. The relationship between the tool wear state and the monitored signal is also highly nonlinear. Artificial intelligence algorithms such as support vector machine (SVM), fuzzy clustering analysis (FCA), and neural network (NN) are widely used in tool wear condition

Table 5: Energy analysis results of P4, P7, and P13 frequency bands of AE signal.

Frequency band	Mean and range	Experimental factors			
		Degrees of wear	Spindle speed	Feed rate	Cutting depth
P4	Mean 1	1051.9	732.2	1821.5	1281.7
	Mean 2	1182.8	1159.8	1607.2	1754.3
	Mean 3	2157.1	2007.4	1306.6	1062.3
	Mean 4	1116.6	2164.9	1252.9	1618.9
	Range	1105.2	1432.7	568.6	692
P7	Mean 1	372.3	138.6	439.5	376.7
	Mean 2	331.4	250.9	499	432.3
	Mean 3	484.3	493.7	397	434.1
	Mean 4	489.3	794.1	341.7	434.2
	Range	157.9	655.5	157.3	57.5
P13	Mean 1	309.1	117.7	383.4	316.3
	Mean 2	255.8	209.1	422.5	354.5
	Mean 3	404.1	417.1	325.7	382.1
	Mean 4	445.0	670	282.4	361.1
	Range	189.2	552.3	140.1	65.8

monitoring and recognition. Support vector machine (SVM) is a pattern recognition method based on statistical learning theory and structural risk minimization principle. It takes into account the training error and generalization ability. Support vector machine (SVM) is a pattern recognition method based on statistical learning theory and structural risk minimization principle and taking into account the training error and generalization ability. SVM is widely used in pattern recognition and feature extraction such as small sample, high dimension, nonlinear, and local minimum. Fuzzy clustering analysis is an analysis method that establishes the fuzzy similarity relationship according to the characteristics, intimacy, and similarity of objective things based on the fuzzy mathematics and then classifies and identifies the fuzzy state of samples according to a certain membership degree, so as to cluster objective things. Fuzzy clustering analysis method is widely used in meteorological forecast, geology, agriculture, forestry monitoring, and other aspects. It is widely used in meteorological forecast, geology, agriculture, forestry monitoring, and other aspects. Artificial neural network is a nonlinear and adaptive information processing system composed of a large number of interconnected processing units. It can imitate the information processing function of human brain neural system in different degrees and levels. Artificial neural network is a nonlinear and adaptive information processing system composed of a large number of interconnected processing units, which can imitate the information processing function of the human brain neural system in different degrees and levels and also can provide high accuracy automatic classification ability for signals with large amount of data and complex characteristics. Artificial neural network is mainly used in the field of information processing and pattern recognition. It is mainly used in the field of information processing and pattern recognition.

In the information fusion pattern recognition system, the information provided by each information source has certain uncertainty. Choosing the appropriate fusion algorithm is the core problem of the information fusion pattern recognition system. The process of fusion of information with uncertain features is essentially an uncertain reasoning process. Neural network has strong fault tolerance, self-learning, self-organization, and self-adaptive ability, can simulate complex nonlinear mapping, and can determine the classification standard according to the similarity of the samples accepted by the current system. The characteristics of neural network and its powerful nonlinear processing ability can meet the technical requirements of multi-sensor information fusion. In view of this, this paper uses BP neural network technology to study the intelligent recognition method of tool wear state.

4.1. Structure Parameter Design of BP Neural Network

4.1.1. Design of Input Layer and Output Layer. The energy values of P2 and P4 frequency bands of vibration signal, P4 frequency band of AE signal, and corresponding spindle speed are selected as the four main characteristic parameters of tool wear. Therefore, the input vector is determined to be 4, that is, the number of neurons in the input layer is 4. The output is the tool wear, so the number of neurons in the output layer is 1.

4.1.2. Hidden Layer Design. According to Kolmogorov theorem, a three-layer BP neural network can realize the nonlinear mapping from any n dimension to m dimension. In this paper, a single hidden layer structure is selected. The number of nodes in the hidden layer directly affects the performance of neural network. The number of nodes is too small, and the pattern space is rough, which leads to poor fault tolerance and low ability of identifying the samples without learning. Too many nodes and too fine division of pattern space lead to too long network training time, slow or even nonconvergence of the network, and storage of the irregular content in the sample, reducing the generalization ability of the system. The number of hidden layer nodes is [26]

$$l = \sqrt{n + m + a}, \tag{1}$$

where l is the number of hidden layer nodes, n is the number of input nodes, m is the number of output nodes, and a is the adjustment constant between 1 and 10.

The BP neural network model is established among 4–15 hidden layer neurons by the trial method, and the optimal number of hidden layer neurons is determined by network error. When the number of hidden layer neurons is 9, the network error is the smallest, and the number of hidden layer nodes is 9. Therefore, the 3-layer BP neural network structure based on the intelligent recognition of tool wear state based on information fusion is 4-9-1. According to the output of BP neural network, the wear degree of the tool can be directly determined.

4.2. Multi-Information Fusion Based on BP Neural Network. The physical quantities of vibration signal, acoustic emission signal, and spindle speed characteristic parameters have different meanings. Before neural network training, the characteristic data should be normalized. The normalization method was used.

$$x_i^0 = 1 - \frac{|x_i - \overline{x}|}{(x_{\max} - x_{\min})}. \quad (2)$$

Among them, $x_{\max} = \max\{x_i\}, x_{\min} = \{x_i\}, \overline{x} = \sum_{i=1}^{n} x_i/n$.

So, the values of the input vectors are all between 0 and 1.

The hyperbolic tangent function is chosen as the activation function [27]. The initial weight of the network is randomly selected between (0, 1). The learning rate is 0.01, the training error is 1×10^{-8}, and the maximum training period is 40000. From the test characteristic data, 16 groups of P2 and P4 band energy value of the vibration signal and P4 band energy value of the acoustic emission signal are selected randomly, and the corresponding spindle speed also is selected together as the training samples to train the BP neural network. The 3-layer BP neural network model with 4-9-1 network structure is trained, and the training target precision is achieved through 31 steps. The training error curve is shown in Figure 8.

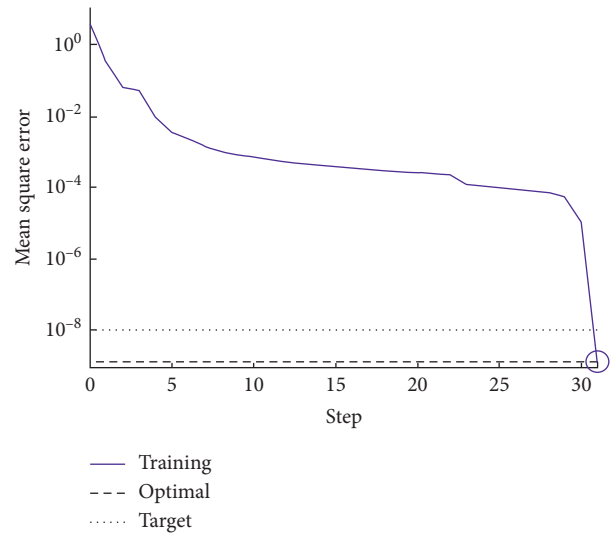

Figure 8: Training error curve.

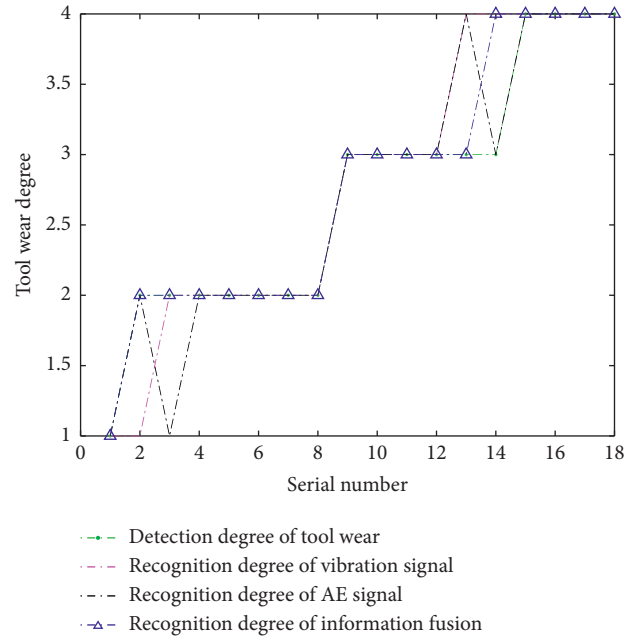

Figure 9: Tool wear detection and recognition degree.

5. Test Results and Analysis

18 groups of P2 and P4 band energy value of the vibration signal and P4 band energy value of the acoustic emission signal which are not the training samples are selected from the test characteristic data, and the corresponding spindle speed also is selected as the test samples together. These test samples are input into the BP neural network to verify the intelligent recognition method of tool wear state.

Firstly, the pattern recognition method of support vector machine is used to recognize the tool wear state based on single sensor information. Then, BP neural network technology is used to identify the tool wear state by fusing the vibration signal, acoustic emission signal, and spindle speed feature information. Finally, the above discrimination results were compared with the actual detection results of tool wear (18 samples, including 1 initial wear, 7 types of normal wear, 6 types of moderate wear, and 4 types of severe wear).

The 18 samples were sorted according to the actual value of tool wear. The actual detection degree of tool wear, the recognition degrees by single vibration signal or single acoustic emission signal, and the recognition degree by information fusion are shown in Figure 9.

The results of single vibration signal identification were as follows: one normal wear (No. 1) was misjudged as initial wear, and two kinds of moderate wear (Nos. 13 and 14) were misjudged as severe wear. The recognition accuracy of all samples was 83.33%. The results of single acoustic signal recognition were as follows: 1 normal wear (No. 3) was misjudged as initial wear, 1 medium wear (No. 13) was

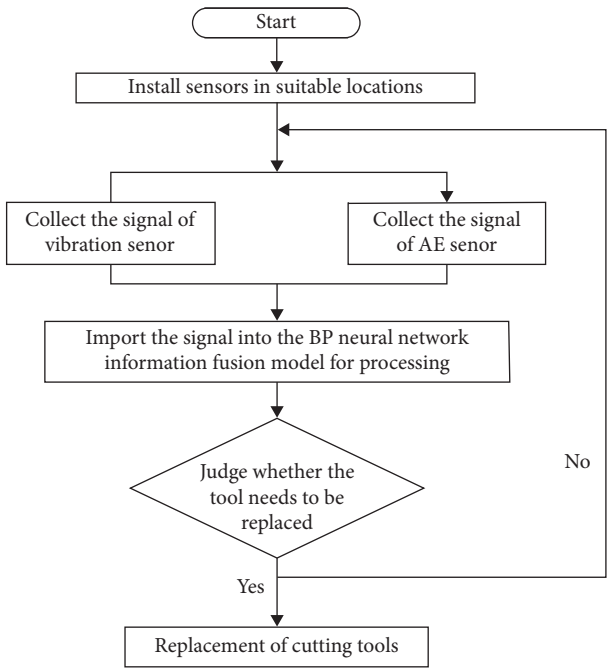

Figure 10: Diagnosis flowchart of tool wear status.

misjudged as severe wear, and the accuracy rate of identification for all samples was 88.89%. The result of information fusion identification was as follows: one medium wear (No. 14) was misjudged as severe wear, and the accuracy of all samples was 94.44%.

The accuracy of tool wear state recognition based on neural network multi-information fusion is 11.11% and 5.55% higher than that based on vibration signal and acoustic emission signal.

The diagnosis flowchart of the tool wear status is shown in Figure 10.

6. Concluding Remarks

Tool wear state directly affects the accuracy, efficiency, and cost of workpiece processing and the stability of the whole manufacturing equipment system.

(1) This paper studies the application of information fusion technology in tool wear state recognition. The multi-information data acquisition system of tool wear condition of CNC lathe is composed of a CNC lathe, workpiece, sensor, and signal amplifier and also includes a data acquisition, analysis, and processing device.

(2) In this paper, BP neural network is used to fuse the feature information of vibration signal and AE signal with high correlation with tool wear degree, a 3-layer BP neural network tool wear state intelligent recognition model with 4-9-1 structure is constructed, and the model is trained.

(3) The experimental results show that the recognition accuracy of the intelligent recognition system for tool wear state of CNC turning tool in all experimental samples is 94.44%, which is 11.11% higher than that of vibration sensor and 5.55% higher than that of AE sensor.

The accuracy of the tool wear state identified by the information fusion method is higher than that of the tool wear state identified by a single sensor, which effectively realizes the monitoring and automatic monitoring of the tool wear state and has a certain practical application value. However, the model established in this paper is only suitable for CNC lathe and has low universality.

Data Availability

The data used to support the findings of this study are included within the article.

Conflicts of Interest

The authors declare that they have no conflicts of interest.

Acknowledgments

The authors are grateful for the financial support provided by the National Natural Science Foundation of China under grant no. 51805151 and the Key Scientific Research Project of the University of Henan Province of China under grant no. 21B460004.

References

[1] Q. Zhou and K. Liu, "Fault diagnosis of CNC machine tools common," *Advanced Materials Research*, vol. 317-319, pp. 1882–1885, 2011.

[2] X. Liao, G. Zhou, Z. Zhang, J. Lu, and J. Ma, "Tool wear state recognition based on GWO–SVM with feature selection of genetic algorithm," *International Journal of Advanced Manufacturing Technology*, vol. 104, no. 1, pp. 1051–1063, 2019.

[3] H. Yuan, S. Shudong, and L. Jingyao, "Prediction of cutting tool life based on ACO-BP neural network," *Mechanical Science & Technology for Aerospace Engineering*, vol. 28, no. 11, pp. 1517–1521, 2009.

[4] Y. Hou, D. Zhang, B. Wu, and M. Luo, "Milling force modeling of worn tool and tool flank wear recognition in end milling," *IEEE*, vol. 20, no. 3, pp. 1024–1035, 2015.

[5] C. W. Xu, H. L. Chen, and Z. Liu, "State recognition technology and application on milling tool wear," *Applied Mechanics and Materials*, vol. 10-12, pp. 869–873, 2007.

[6] Z. Q. Li, P. Nie, and S. G. Zhao, "Identification method of tool wear based on locally linear embedding and support vector machine," *Applied Mechanics and Materials*, vol. 246-247, pp. 1289–1293, 2012.

[7] B. Ye, J. Liu, R. Peng, Y. Tang, and X. Zhao, "Study on fuzzy data fusion for real-time intelligent recognition of tool wear state," in *Advances in Machining & Manufacturing Technology IX* School of Mechanical Engineering, South China University of Technology, Guangdong, China, 2008.

[8] G. Wang and X. Feng, "Tool wear state recognition based on linear chain conditional random field model," *Engineering Applications of Artificial Intelligence*, vol. 26, no. 4, pp. 1421–1427, 2013.

[9] S. Guan, H. Pang, W. Song, and Z. Kang, "Cutting tool wear recognition based on MF-DFA feature and LS-SVM algorithm," *Nongye Gongcheng Xuebao/Transactions of the Chinese Society of Agricultural Engineering*, vol. 34, no. 14, pp. 61–68, 2018.

[10] K. Ge, L. Xu, X. Zhang et al., "Information fusion technology based on multi-sensor," *International Core Journal of Engineering*, vol. 6, no. 8, 2020.

[11] T. Yan and X. Liu, "Fault diagnosis method of ship main machinery based on information fusion technology," *Journal of Coastal Research*, vol. 103, no. 1, pp. 905–908, 2020.

[12] S. Zhu, "Multi-source information fusion technology and its engineering application," *Research in Health Science*, vol. 4, no. 4, p. 408, 2020.

[13] Y. Wang, "Information fusion technology based on multi-sensor," *International Journal of Educational Management*, vol. 4, no. 4, 2019.

[14] Z. Chen, "Multi-sensor information fusion technology and its application in target recognition," *International Journal of New Developments in Engineering and Society*, vol. 3, no. 5, 2019.

[15] M. Xiao, K. Li, W. Liu, and X. Xin, "Fast fault location method for power distribution systems based on multi-source information fusion technology," *IOP Conference Series: Materials Science and Engineering*, vol. 486, no. 1, Article ID 012070, 2019.

[16] T. Zhang, W. Ji, and Y. Qiu, "NC equipment fault diagnosis research in uncertain circumstance based on information fusion and bayesian networks integrated," *IOP Conference Series: Materials Science and Engineering*, vol. 493, no. 1, Article ID 012151, 2019.

[17] G. Li, Y. Wang, J. He, Q. Hao, H. Yang, and J. Wei, "Tool wear state recognition based on gradient boosting decision tree and hybrid classification RBM," *International Journal of Advanced Manufacturing Technology*, vol. 110, no. 1-2, 2020.

[18] Y. Du, G. Wu, Y. Tang, H. Cao, and S. Liu, "Reliability allocation method for remanufactured machine tools based on fuzzy evaluation importance and failure influence," *International Journal of Precision Engineering and Manufacturing-Green Technology*, 2020.

[19] A. Muzaffer, S. David, S. Max, A. Drik, and B. Thomas, "Kernel selection for support vector machines for system identification of a CNC machining center," *IFAC-PapersOnLine*, vol. 52, no. 29, pp. 192–198, 2019.

[20] G. Xu, H. Zhou, and J. Chen, "CNC internal data based incremental cost-sensitive support vector machine method for tool breakage monitoring in end milling," *Engineering Applications of Artificial Intelligence*, vol. 74, pp. 90–103, 2018.

[21] B. Jose, K. Nikita, T. Patil, S. Hemakumar, and P. Kuppan, "Online monitoring of tool wear and surface roughness by using acoustic and force sensors," *Materials Today: Proceedings*, vol. 5, no. 2, pp. 8299–8306, 2018.

[22] J. Herwan, S. Kano, O. Ryabov, H. Sawada, and M. Watanabe, "Comparing vibration sensor positions in CNC turning for a feasible application in smart manufacturing system," *International Journal of Automation Technology*, vol. 12, no. 3, pp. 282–289, 2018.

[23] T. Junge, H. Liborius, T. Mehner, A. Nestler, A. Schubert, and T. Lampke, "Measurement system based on the Seebeck effect for the determination of temperature and tool wear during turning of aluminum alloys," *Procedia CIRP*, vol. 93, pp. 1435–1441, 2020.

[24] R. Upase and N. Ambhore, "Experimental investigation of tool wear using vibration signals: an ANN approach," *Materials Today: Proceedings*, vol. 24, no. 2, pp. 1365–1375, 2020.

[25] Y. Liu, F. Wang, J. Lv, and X. Wang, "A novel method for tool identification and wear condition assessment based on multi-sensor data," *Applied Sciences*, vol. 10, no. 8, p. 2746, 2020.

[26] J. Michalkiewicz, "Modified Kolmogorov's neural network in the identification of Hammerstein and Wiener systems," *IEEE transactions on neural networks and learning systems*, vol. 23, no. 4, pp. 657–662, 2012.

[27] A. Ngaopitakkul and S. Bunjongjit, *Selection of Proper Activation Functions in Back-Propagation Neural Network Algorithm for Transformer and Transmission System Protection*, Springer, Berlin, Germany, 2015.

Hindawi
Shock and Vibration
Volume 2021, Article ID 5297043, 14 pages
https://doi.org/10.1155/2021/5297043

Research Article

Random Target Localization for an Upper Limb Prosthesis

Xinglei Zhang[1,2] **Binghui Fan**[3] **Chuanjiang Wang**[3] **Xiaolin Cheng**[4] **Hongguang Feng**[4] **and Zhaohui Tian**[4]

[1]*College of Mechanical and Electronic Engineering, Shandong University of Science and Technology, Qingdao 266590, China*
[2]*College of Mechanical and Electric Engineering, Zaozhuang University, Zaozhuang 277160, China*
[3]*College of Electrical and Automation Engineering, Shandong University of Science and Technology, Qingdao 266590, China*
[4]*College of Mechanical Engineering, Shandong University, Jinan 250100, China*

Correspondence should be addressed to Binghui Fan; fanbinghui@sdust.edu.cn

Received 5 April 2021; Accepted 31 May 2021; Published 21 June 2021

Academic Editor: Xian-Bo Wang

To achieve the purpose of accurately grasping a random target with the upper limb prosthesis, the acquisition of target localization information is especially important. For this reason, a novel type of random target localization algorithm is proposed. Firstly, an initial localization algorithm (ILA) that uses two 3D attitude sensors and a laser range sensor to detect the target attitude and distance is presented. Secondly, an error correction algorithm where a multipopulation genetic algorithm (MPGA) optimizes backpropagation neural network (BPNN) is utilized to improve the accuracy of ILA. Thirdly, a general regression neural network (GRNN) algorithm is proposed to calculate the joint angles, which are used to control the upper limb prosthetic gripper to move to the target position. Finally, the proposed algorithm is applied to the 5-DOF upper limb prosthesis, and the simulations and experiments are proved to demonstrate the validity of the proposed localization algorithm and inverse kinematics (IK) algorithm.

1. Introduction

According to the 2006 China National Disability Sample Survey, there were 2.26 million amputees, accounting for approximately 9.37% of the disabled [1]. From the information provided by the National Limb Loss Information Center, in 2005, there were 1.6 million who lost a limb in the United States, and this number is expected to reach 3.6 million by 2050 [2]. A large proportion of these amputees are upper limb amputees who do not have the means to perform some daily activities, such as drinking water, eating, and dressing. Upper limb prostheses that can capture and move objects according to the wearer's needs are wearable robots from the perspective of human–computer integration [3]. However, for upper limb prostheses, the pose (position and orientation) information of a random target is not fixed, and inverse kinematics (IK) solution cannot be determined. Unfortunately, research on random target localization algorithms is mostly seen in the fields of mobile robots and industrial robots and rare in the field of upper limb prostheses. Therefore, how to accurately obtain the pose information of a random target has become a difficult problem that researchers need to urgently address.

Cao et al. [4] studied a method of using machine vision and a neural network (NN) to decrease the absolute position error of the robot. However, the NN was easily trapped in a local solution, which led to instability in the localization accuracy. Jiang et al. [5] proposed an algorithm which combined particle swarm optimization algorithm with back propagation neural network (BPNN) to solve the IK solution of the UR3 robot. However, there was a lack of blindness in the selection of the step size, which affected the accuracy of the solution. Yi et al. [6] proposed a positioning system using optical flow sensor based on the sensor fusion technique, However, in low-light and slippery environments, the system generates large errors. Jung et al. [7] selected the pose of robot by extracting the initial state of the surrounding environment of the robot and determined the sample distribution according to the given area map. The positioning success was determined by calculating the similarity between

the robot sensor state and the estimated posture on a given map. But the positioning accuracy is greatly affected by the environment.

The research object of this paper is 5 degrees of freedom (DOF) upper limb prosthesis, as shown in Figure 1. It is not a commercial product, but a product developed by the research group and is an internal product of the laboratory. The remainder of this paper is structured as follows. In Section 2, the kinematic of the upper limb prosthesis is analyzed. The localization algorithm is introduced in Section 3. In Section 2.2, the IK algorithm is addressed. The proposed algorithm is validated through simulations and experiments in Section 4. Finally, Section 5 provides conclusions and future work.

2. Kinematic Analysis

2.1. Forward Kinematics. The relationship among the joint coordinate systems is illustrated in Figure 2, and the D-H parameters are shown in Table 1.

$$ {}^{i-1}_{i}T = \begin{bmatrix} c_i & -s_i c\alpha_i & s_i s\alpha_i & a_i c_i \\ s_i & c_i c\alpha_i & -c_i s\alpha_i & a_i s_i \\ 0 & s\alpha_i & c\alpha_i & d_i \\ 0 & 0 & 0 & 1 \end{bmatrix}, \tag{1} $$

where $s_i = \sin\theta_i$, $c_i = \cos\theta_i$, $s\alpha_i = \sin\alpha_i$, and $c\alpha_i = \cos\alpha_i$.

The pose of end-effector (EE) in the base coordinate system is described as ${}_0^nT$:

$$ {}^0_nT = {}^0_1T(\theta_1){}^1_2T(\theta_2)\ldots{}^{n-1}_nT(\theta_n). \tag{2} $$

When $(\theta_1, \theta_2 \ldots \theta_n)$ is known, solving the pose of the EE in the base coordinate system is called positive kinematics. Conversely, when the pose of the EE in the base coordinate system is known, solving the joint angle is called IK.

Drinking water is a common activity in real life. To avoid the overflow of water from the cup during the movement of the upper limb prosthesis, this paper uses an MPU6050 hand attitude sensor to control the gripper to always hold and move in the horizontal direction. Therefore, the EE coordinate system is described as in the coordinate system $o_3 - x_3y_3z_3$. Additionally, the EE coordinate system is described as ${}_5^0T$ in the base coordinate system.

$$ \begin{aligned} {}^0_5T &= T(\theta_0){}^0_1T(\theta_1){}^1_2T(\theta_2){}^2_3T(\theta_3)Q, \\ &= \begin{bmatrix} 1 & 0 & 0 & 295\sin_1 + 212\sin_1\cos_3 + 212\cos_1\cos_2\sin_3 \\ 0 & 1 & 0 & -212\sin_2\sin_3 \\ 0 & 0 & 1 & 212\cos_2\sin_1\sin_3 - 212\cos_1\cos_3 - 295\cos_1 \\ 0 & 0 & 0 & 1 \end{bmatrix}. \end{aligned} \tag{3} $$

Because the attitude information of the gripping object is simplified, the key problem of the IK solution becomes obtaining the exact position of a random target.

Figure 1: 5-DOF upper limb prosthesis.

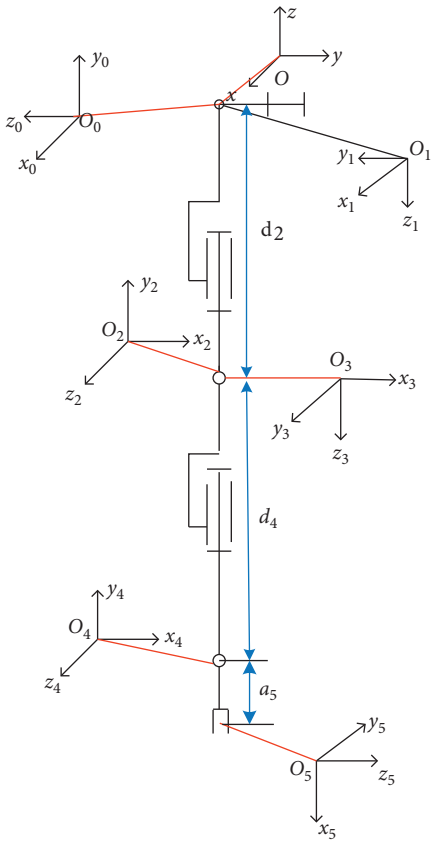

Figure 2: The coordinate systems of the upper limb prosthesis.

2.2. IK Algorithm. According to equation (3) and the output values of MPGA-BPNN, the following equations can be obtained:

Table 1: D-H parameters of the upper limb prosthesis.

Joint (i)	θ_i (rad)	d_i (mm)	a_i (mm)	α_i (rad)	Angle range (rad)
1	$\theta_1(0)$	0	0	$\pi/2$	$(-\pi/9, \pi/2)$
2	$\theta_2(-\pi/2)$	295	0	$-\pi/2$	$(-5\pi/6, 5\pi/18)$
3	$\theta_3(0)$	0	0	$\pi/2$	$(0, 5\pi/6)$
4	$\theta_4(0)$	212	0	$-\pi/2$	$(-5\pi/9, 5\pi/9)$
5	$\theta_5(-\pi/2)$	0	100	$\pi/2$	$(-5\pi/6, \pi/6)$

$$\begin{cases} 295\ \sin_1 + 212\ \sin_1 \cos_3 + 212\ \cos_1 \cos_2 \sin_3 = x_i^m, \\ -212\ \sin_2 \sin_3 = y_i^m, \\ 212\ \cos_2 \sin_1 \sin_3 - 212\ \cos_1 \cos_3 - 295\ \cos_1 = z_i^m. \end{cases} \tag{4}$$

Through equation (4), the angular values of the front three joints can be obtained. However, this is a complex set of nonlinear transcendental equations that has no analytical solution. Therefore, a method for solving transcendental equations by using the fast nonlinear approximation ability of a general regression neural network (GRNN) [9–11] is use d in this paper. Once the learning samples are determined, the connection weights between the corresponding network structure and neurons are also determined. When using a GRNN to solve the problem, we need to complete the following work. First, in view of the training time and accuracy requirements, $\theta_i\,(i = 1, 2, 3)$ are evenly dispersed into 100 copies in the range of the joint angle change, and then the prosthetic joint space $\theta_k = [\theta_{1k}, \theta_{2k}, \theta_{3k}]^T$ $(k = 1, 2 \ldots 100)$ is obtained and saved as the $\{Q\}$ matrix, which is used as the target sample of the GRNN. Then, the corresponding coordinates $[px, py, pz]^{\mathrm{T}}$ are obtained by substituting θ_k into the first three rows of the fourth column of equation (3) and saved as the $\{S\}$matrix, which is used as the input samples of GRNN. In this way, the IK solution model is established.

3. Localization Algorithm

3.1. Initial Localization Algorithm (ILA). The three-dimensional attitude sensor [12], which relies on geomagnetic localization, aggregates three-axis acceleration, a three-axis gyroscope, and a three-axis magnetometer. This attitude sensor can detect and describe three-dimensional pose changes with respect to Earth coordinates (roll direction, pitch direction, and yaw direction). To obtain a random target initial position, two attitude sensors (MPU9250) and a distance sensor (CY30) need to be installed on the wearer, as shown in Figure 3. Attitude sensor 1 is installed on the artificial limb shoulder to calibrate the attitude with the rotation of the body, and attitude sensor 2 is installed on the head of the wearer to detect head movement relative to attitude sensor 1. When the wearer's head is upright and looking straight ahead, the attitude data of sensor 1 and sensor 2 are consistent, and this moment is described as the preliminary state. When the wearer's head turns up and down or turns left and right, the upper limb prosthesis can

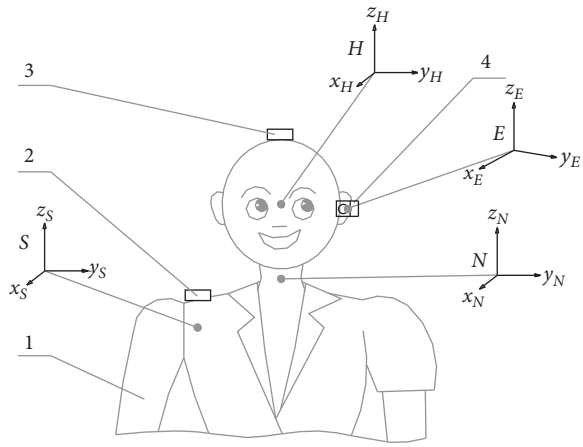

Figure 3: Schematic diagram of the installed sensors. 1: artificial limb; 2: attitude sensor 1; 3: attitude sensor 2; and 4: laser range sensor.

obtain the rotation or pitch angle of the head relative to the wearer's body by comparing the data of attitude sensor 1 and attitude sensor 2. To confirm the operation target distance, a laser range sensor is installed on the side of the head (left ear) and emits a laser projected onto the operation target by adjusting the head attitude.

The coordinate systems are shown in Figure 4. S is the prosthetic basic coordinate system, N is the coordinate system about the middle of the neck, H is the coordinate system about the middle of the head, and E is the laser range sensor coordinate system. When the user's head turns up and down, it is equivalent to N coordinates rotating by an angle β_s around the S coordinates of the $(0, 0, z_n)$ axis, and the origin of the N coordinate system is fixed at $(0, 0, z_n)$relative to the origin of the S coordinate system. When the user shakes his head left and right, it is equivalent to H coordinates rotating by an angle $(0, 0, z_n)$ around the N coordinates of the $(0, 0, z_n)$ axis, and the origin of the H coordinate system is fixed at $(0, 0, z_n)$ relative to the origin of the N coordinate system. When the head is in the preliminary state, the origin of the E coordinate system is set in the positive direction of the β_h axis about the H coordinate system, and the β_h axis of the E coordinate system coincides with the β_h axis of the H coordinate system. Furthermore, the β_h axis of the E coordinate system coincides with the direction of the laser beam, and the β_h axis of the E coordinate system and β_h axis of the H coordinate system form a fixed angle β_h, which is equivalent to the E coordinate system

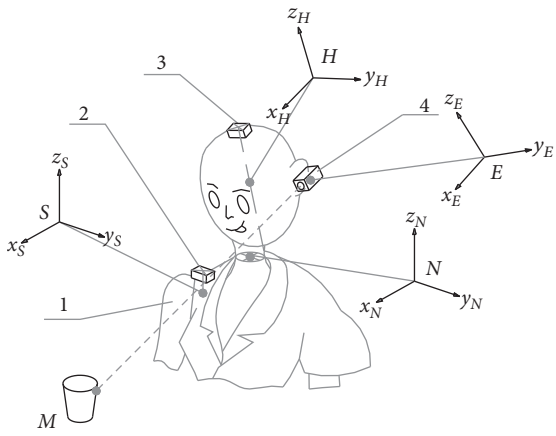

Figure 4: Schematic diagram of a random target M.

rotating around the ${}^{S}_{N}K$ axis of the H coordinate system. The origin of the E coordinate system is fixed at ${}^{S}_{N}K$ relative to the origin of the H coordinate system.

By comparing the relative attitude angle discrepancy between the two three-dimensional attitude sensors, the homogeneous transformation matrix of the N coordinate system to the S coordinate system ${}^{S}_{N}K$ can be derived as follows:

$$ {}^{S}_{N}K = \begin{bmatrix} \cos\beta_s & 0 & \sin\beta_s & x_s \\ 0 & 1 & 0 & y_s \\ -\sin\beta_s & 0 & \cos\beta_s & z_s \\ 0 & 0 & 0 & 1 \end{bmatrix}. \tag{5} $$

In the same way,

$$ {}^{N}_{H}K = \begin{bmatrix} \cos\gamma_n & \sin\gamma_n & 0 & 0 \\ \sin\gamma_n & \cos\gamma_n & 0 & 0 \\ 0 & 0 & 1 & z_n \\ 0 & 0 & 0 & 1 \end{bmatrix}, \tag{6} $$

$$ {}^{H}_{E}K = \begin{bmatrix} \cos\beta_h & \sin\beta_h & 0 & 0 \\ 0 & 1 & 0 & y_h \\ \sin\beta_h & 0 & \cos\beta_h & 0 \\ 0 & 0 & 0 & 1 \end{bmatrix}. \tag{7} $$

The target distance measured by the laser ranging sensor is d, and its homogeneous matrix D is

$$ D = \begin{bmatrix} d_x & d_y & d_z & 1 \end{bmatrix}^T = [d \ 0 \ 0 \ 1]^T. \tag{8} $$

An upper limb prosthesis controller for the wearer that has a random target coordinate calculation program is prepared. By adjusting the head attitude, the wearer projects the laser emitted onto the operation target. Through coordinate transformation, the position of the target M in the S coordinate system can be obtained.

$$ \begin{aligned} P &= {}^{S}_{N}K \cdot {}^{N}_{H}K \cdot {}^{H}_{E}K \cdot D \\ &= \begin{bmatrix} z_n \sin\beta_s - d(\sin\beta_h \sin\beta_s - \cos\beta_h \cos\beta_s \cos\gamma_n) - y_h \sin\gamma_n \cos\beta_s + x_s \\ y_h \cos\gamma_n + d \sin\gamma_n \cos\beta_h + y_s \\ z_s \cos\beta_s - d(\cos\beta_s \sin\beta_h + \cos\beta_h \cos\gamma_n \sin\beta_s) + y_h \sin\beta_s \sin\gamma_n + z_s \\ 1 \end{bmatrix}, \end{aligned} \tag{9} $$

where x_s, y_s, z_s, z_n, y_h are associated with the physical parameters of the wearer, and the rotation angles β_s and γ_n are found by comparing the data from the two attitude sensors. β_h depends on the installation position of the laser range sensor on the wearer's head.

3.2. Error Analysis. Although the ILA can locate a target in an unstructured environment, the attitude sensor used in the localization system is based on the principle of inertial attitude measurement. Drift accumulation error and the magnetic bias can produce positioning errors. In actual random localization experiments, we collected 100 deviation values from the three-dimensional attitude sensors relative to the roll, pitch, and yaw directions of the Earth. The detection accuracy of the two three-dimensional attitude sensors relative to the deviations in the roll and pitch directions of the Earth is relatively high (no more than 1°). However, the detection accuracy of the two three-dimensional attitude sensors relative to the deviation in the Earth's yaw direction is poor (approximately 10°). This is very unfavorable for the purpose of determining the localization of a random target. Through histogram analysis of 100 data points in the yaw direction, it is found that the distribution of this group of data basically conforms to a Gaussian distribution. Therefore, we set a fixed sampling period for the deviation values of the two attitude sensors in the yaw direction to collect and calculate 100 values of the deviation in the yaw direction each time and then to calculate their mathematical expectations. The distribution curves of the deviation values before and after processing by this method are shown in Figure 5. Although this method improves the

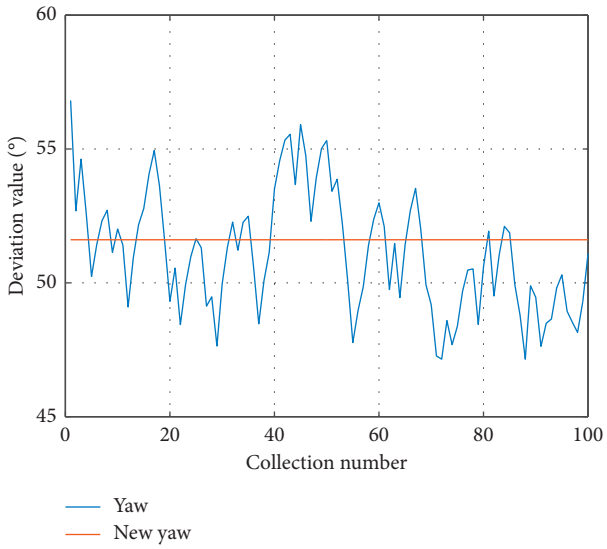

Figure 5: Distribution curves before and after numerical treatment of the deviation in the yaw direction.

stability of the random target location of the upper limb prosthesis, localization accuracy still needs to be improved.

In addition, structural clearance and installation angle errors will inevitably occur in the process of prosthetic limb assembly. There are many reasons for the errors that ultimately reduce the localization accuracy of the system. The red laser spot in Figure 6 represents the desired position. It is obvious that the actual position of the gripper center deviates from the desired position. Also, the errors between the initial positioning coordinates and the desired position coordinates are shown in Figure 7. It is found that the positioning error by ILA is approximately 28 mm, which cannot meet the wearer's requirements. Therefore, based on ILA, this paper further uses an error correction algorithm to improve the localization accuracy.

3.3. Error Correction Algorithm

3.3.1. BPNN Algorithm. NNs are currently popular in machine learning. Among them, BPNN is a multilayer feedforward NN whose characteristics are forward signal transmission and error back propagation. In the forward transmission process, the signal is processed layer by layer from the input layer through the hidden layer to the output layer. If the output layer cannot obtain the desired output, the signal is transmitted to back propagation, and the weight and threshold are adjusted according to the prediction error, so that the output of BPNN continues to be close to the expected output [13–15]. It is known that BPNN containing a hidden layer has sufficient accuracy to approximate any continuous function [16]. Figure 8 shows BPNN topology diagram, where (x_i^p, y_i^p, z_i^p) are the initial location

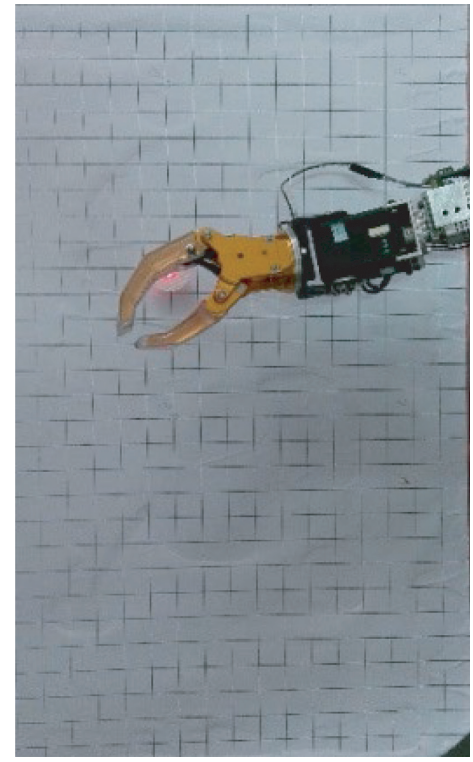

Figure 6: Difference between the desired position and the actual position of the gripper center.

coordinates of the target point and are obtained by the method described in Section 3.1. (x_i^t, y_i^t, z_i^t) are actual measured values of the target points corresponding to the aforementioned (x_i^p, y_i^p, z_i^p).

Because the initial weight and threshold are random, with the training of the BPNN, the weight and threshold will be constantly updated, and eventually the weight and threshold will converge to a certain value. However, the gradient descent training algorithm of the BPNN may produce local minima. Evolutionary algorithms (EAs) can be effectively used to find the optimal weight and threshold globally without calculating gradient information [17]. EAs include simulated annealing algorithm (SAA) [18, 19], particle swarm optimization (PSO) [20, 21], and genetic algorithm (GA). Compared with SAA and PSO, GA has the advantages of efficient heuristic search and parallel computing and has been widely used in function optimization and combination optimization. Therefore, this paper uses a GA combined with the BPNN (called GA-BPNN) to solve the problem that the BPNN falls into local minima solutions.

3.3.2. GA-BPNN Algorithm. A GA is an optimization method based on natural selection mechanism in the process of biological evolution [22–24]. This paper uses GA's global

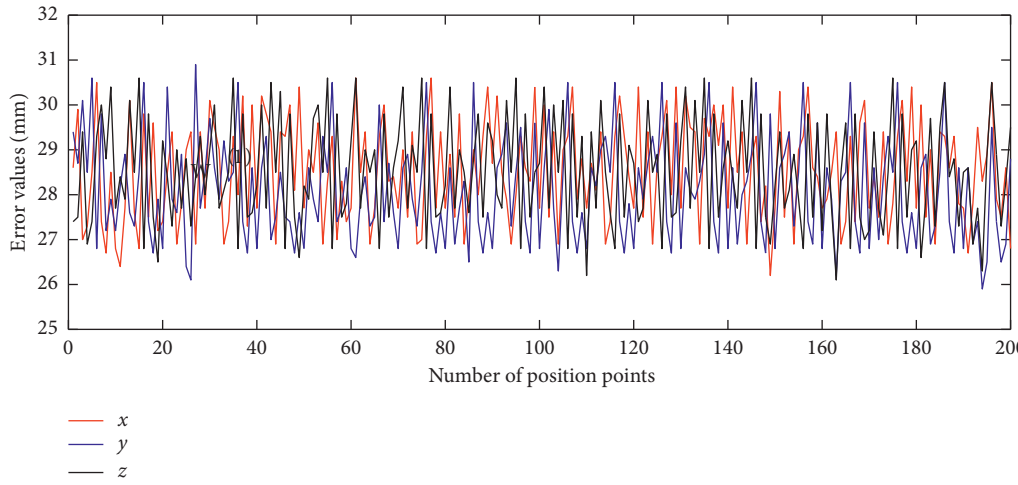

Figure 7: The error in the x-, y-, and z-directions between the initial positioning coordinates and the desired position coordinates.

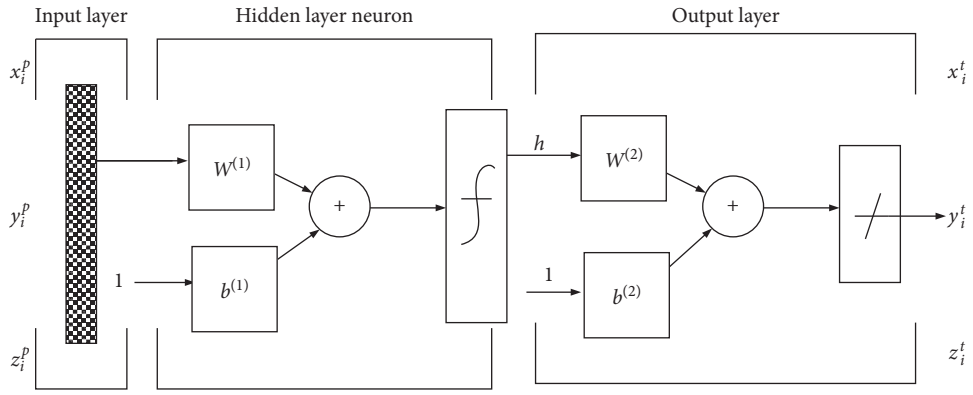

Figure 8: Architecture of BPNN.

search ability to search the optimal weights and thresholds of BPNN. Then, the prediction model with the optimal weight and threshold of BPNN is established, referred to as GA-BPNN. Figure 9 is a flowchart of GA-BPNN algorithm.

The deviation of the output values (x_i, y_i, z_i) of the BPNN and the actual measured values is taken as the objective function of the GA, defined as follows:

$$E_i = \sqrt{\left(x_i - x_i^t\right)^2 + \left(y_i - y_i^t\right)^2 + \left(z_i - z_i^t\right)^2}. \tag{10}$$

The goal of GA is to find the weight and threshold of BPNN with the least sum of squares in all evolutionary generations and to develop in the direction of increasing the value of the fitness function. It is constructed as follows:

$$\text{fitness} = \frac{1}{1 + E_i}. \tag{11}$$

GAs include single-population genetic algorithm (SPGA) and multiple-population genetic algorithm (MPGA). The early SPGA is popular, but there are some shortcomings, such as premature convergence, poor local search ability, and serious assimilation of the late population. For this reason, multipopulation genetic algorithm (MPGA) [25, 26] was proposed. Besides of solving the shortcomings of single-population genetic algorithm, the convergence speed and accuracy have been improved. This paper uses MPGA and SPGA to search the optimal weights and thresholds of BPNN (called MPGA-BPNN and SPGA-BPNN, resp.) and observes the changes of fitness values obtained by these two algorithms. The specific parameters of the SPGA and MPGA are as follows:

(a) SPGA: binary coding, roulette selection, and single-point crossover. The crossover probability is 0.85, and the mutation probability is 0.07. The evolutionary algebra is set to 200, and the total number of individuals is 1000.

(b) MPGA: binary coding, roulette selection, and multipoint crossover. The crossover probability and the mutation probability of various groups are randomly generated in [0.4, 0.9] and [0.005, 0.1], respectively,

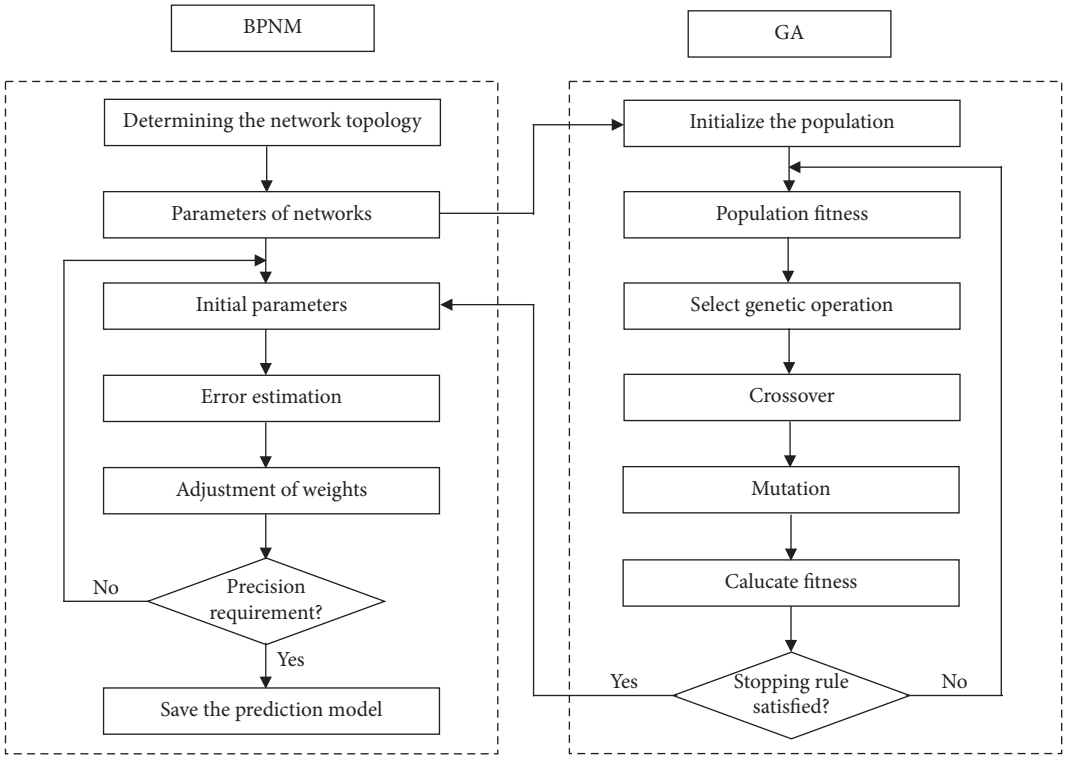

Figure 9: Framework of GA-BPNN.

and the immigration operator and artificial selection operator are introduced. The evolutionary algebra is set to 200, the number of populations is 10, and the number of individual populations is 100.

3.3.3. GA Evaluation. With the operation of SPGA-BPNN and MPGA-BPNN, the changes curve of fitness value is obtained, as shown in Figure 10. It is not difficult to find that the best fitness value obtained by MPGA is 0.996, which is much higher than the 0.56 obtained by SPGA. Therefore, this paper chooses MPGA-BPNN as error correction algorithm of ILA.

After the training, the E_i and the average absolute error (AAE) E_s of the output values of the MPGA-BPNN relative to the actual measurement value are obtained by (15) and (19). To evaluate the error correction ability of MPGA-BPNN, E_s of the ILA, BPNN, and SPGA-BPNN are introduced as follows:

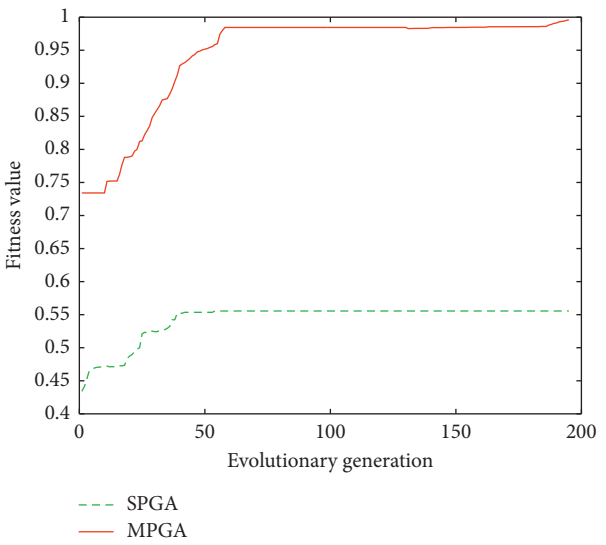

Figure 10: The changes of fitness value.

$$E_i^p = \sqrt{\left(x_i^p - x_i^t\right) + \left(y_i^p - y_i^t\right)^2 + \left(z_i^p - z_i^i\right)^2}, \quad (12)$$

$$E_i^b = \sqrt{\left(x_i^b - x_i^t\right) + \left(y_i^b - y_i^t\right)^2 + \left(z_i^b - z\right)^2}, \quad (13)$$

$$E_i^s = \sqrt{\left(x_i^s - x_i^t\right) + \left(y_i^s - y_i^t\right)^2 + \left(z_i^s - z_i^t\right)^2}, \quad (14)$$

$$E_i^m = \sqrt{\left(x_i^m - x_i^t\right) + \left(y_i^m - y_i^t\right)^2 + \left(z_i^m - z_i^t\right)^2}, \quad (15)$$

$$E_s^p = \frac{1}{N}\sum_{i=1}^{N}\sqrt{\left(x_i^p - x_i^t\right)^2 + \left(y_i^p - y_i^t\right)^2 + \left(z_i^p - z_i^t\right)^2}, \quad (16)$$

$$E_s^b = \frac{1}{N}\sum_{i=1}^{N}\sqrt{\left(x_i^b - x_i^t\right)^2 + \left(y_i^b - y_i^t\right)^2 + \left(z_i^b - z_i^t\right)^2}, \quad (17)$$

$$E_s^s = \frac{1}{N}\sum_{i=1}^{N}\sqrt{\left(x_i^s - x_i^t\right)^2 + \left(y_i^s - y_i^t\right)^2 + \left(z_i^s - z_i^t\right)^2}, \quad (18)$$

$$E_s^m = \frac{1}{N}\sum_{i=1}^{N}\sqrt{\left(x_i^m - x_i^t\right)^2 + \left(y_i^m - y_i^t\right)^2 + \left(z_i^m - z_i^t\right)^2}, \tag{19}$$

where, (x_i^b, y_i^b, z_i^b) are the output values of BPNN, (x_i^s, y_i^s, z_i^s) are the output values of SPGA-BPNN, (x_i^m, y_i^m, z_i^m) are the output values of MPGA-BPNN, and N is the number of test points.

4. Simulations and Experiments

In this section, simulations and experiments are constructed to prove the validity and practicability of the proposed algorithms. Simulations are implemented with the aid of the MATLAB R2015a tool and experiments are run using an Intel Core™ i5-2450M CPU @ 2.50 GHz and 2 GB RAM as the control platform.

4.1. Simulation Analysis of Localization Algorithm and IK Algorithm. To assess the accuracy of the proposed localization algorithm, 200 points were randomly selected from BPNN training samples as test points. The errors in the x-, y-, and z-directions between the actual position obtained by BPNN, SPGA-BPNN, and MPGA-BPNN and the desired position are obtained as shown in Figure 11. It is found that the average error by BPNN and SPGA-BPNN is 11 mm and 6.6 mm, respectively; however, the average error by our algorithm is 1 mm. In other words, compared with the initial positioning coordinates, BPNN and SPGA-BPNN error correction algorithm reduces position error by 57.1% and 78.6%, respectively; however, our algorithm reduces the error by 96.4%.

$(x_i^{\mathrm{m}}, y_i^{\mathrm{m}}, z_i^{\mathrm{m}})$ of the above 200 test points are selected to evaluate the accuracy of the IK algorithm. The corresponding joint angle values are obtained through the IK algorithm and brought into (3) to obtain corresponding position coordinates. Comparing with $(x_i^{\mathrm{m}}, y_i^{\mathrm{m}}, z_i^{\mathrm{m}})$ of the above 200 test points, the position errors in the x-, y-, and z-direction are obtained as shown in Figure 12. It is found that the average error is 0.035 mm.

The simulations show that the proposed localization algorithm and IK algorithm is valid. Furthermore, these proposed algorithms are applied to the developed 5-DOF upper limb prosthesis to verify the effectiveness.

4.2. Experiment Analysis of Localization Algorithm. The laser point was randomly hit 10 positions in the workspace by adjusting the head attitude, and the position coordinates of each test point were obtained by the ILA and used as input to the BPNN, SPGA-BPNN, and MPGA-BPNN. Then, the network output value by the BPNN, SPGA-BPNN, and MPGA-BPNN of each test point was obtained and compared with the corresponding actual measured values, as shown in Figure 13. It is easy to see that the output values of the MPGA-BPNN are closer to the actual measurement values.

Furthermore, through equation (15), E_i^p, E_i^b, E_i^s, and E_i^{m} of the test points are calculated, respectively, as shown in Table 2. The AAEs obtained by equation (19) are 48.71 mm, 18.92 mm, 11.18 mm, and 2.50 mm, respectively. Compared with the AAE of the initial position value, the AAE of the output values of the BPNN and SPGA-BPNN is reduced by 61.16% and 75.77%, respectively. However, the AAE of the output values of our algorithm is reduced by 94.87%. These results further illustrate that error correction algorithm of the MPGA-BPNN is more effective in the actual positioning of the upper limb prosthesis.

It is well known that classical visual location algorithms use point description to match features between the current view and the map. After consulting the related literature, we find that the visual positioning accuracy is approximately 5 mm. However, our positioning accuracy is 2.5 mm, which is higher than visual location algorithms. In addition, our method is an interactive localization method. In the case of multiple targets, visual localization algorithms cannot understand which random target the user is going to grasp, but our algorithm can aim the laser beam at a target and command the upper limb prosthesis to grasp it. Therefore, the proposed algorithm is more concise and accurate than visual localization algorithms.

4.3. Experiment Analysis of IK Algorithm. By inputting the output coordinates of MPGA-BPNN into GRNN solving model, the joint angles of the front three joints of the upper limb prosthesis were obtained, as shown in column 4 of Table 3. The upper limb prosthesis moves according to the obtained joint angles, and finally the gripper center accurately moves to the position of the laser point, as shown in Figure 14.

To verify the accuracy of the joint angle solution, the joint angles solved by GRNN are substituted into equation (3) to obtain the coordinates of the center of the gripper, as shown in column 5 of Table 3. At this time, $[px, py, pz]$ is regarded as the actual position, and $(x_i^{\mathrm{m}}, y_i^{\mathrm{m}}, z_i^{\mathrm{m}})$ is regarded as the desired position. The responses of the actual position and the desired position in the 3D coordinate system are obtained, as shown in Figure 15(a), and the projection results in the xy-, xz-, and yz-planes are illustrated in Figures 15(b)–15(d). It is easy to see that the IK algorithm can obtain a unique solution with high accuracy.

4.4. Practical Applications of Artificial Limbs. An experiment at which a cup is picked up from the table and moved to the mouth of the wearer is performed. First, the laser point is targeted to the center of the cup through wearer's head movement. Then, through the target localization algorithm and IK algorithm, the gripper moved to the center of the cup. Finally, the human–computer interaction system was used to complete the process of gripping the cup and moving it to the mouth, as shown in Figure 16. The effectiveness of the localization algorithm and IK algorithm is further verified.

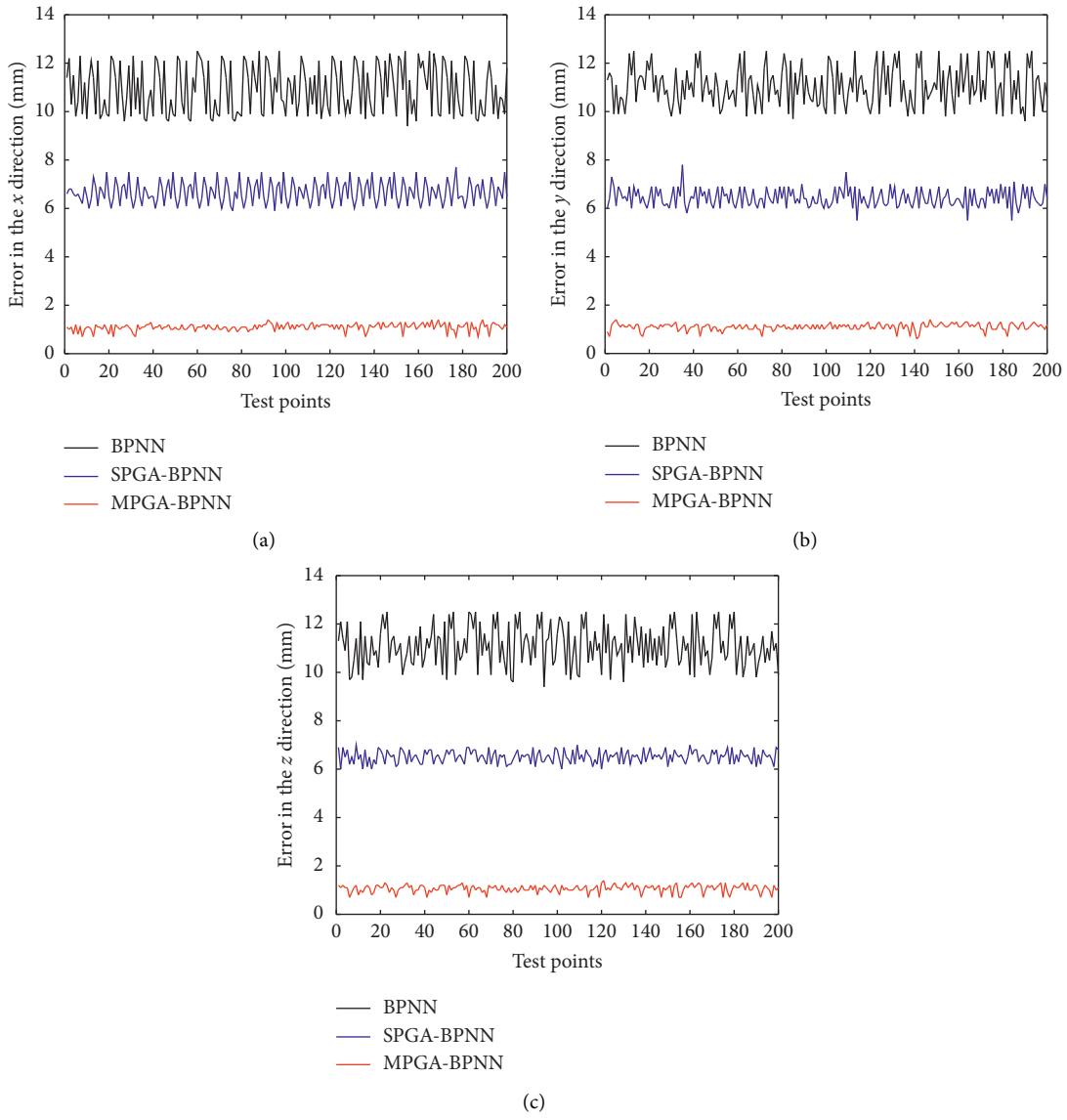

Figure 11: Error curve in the x-, y-, and z-directions of test points.

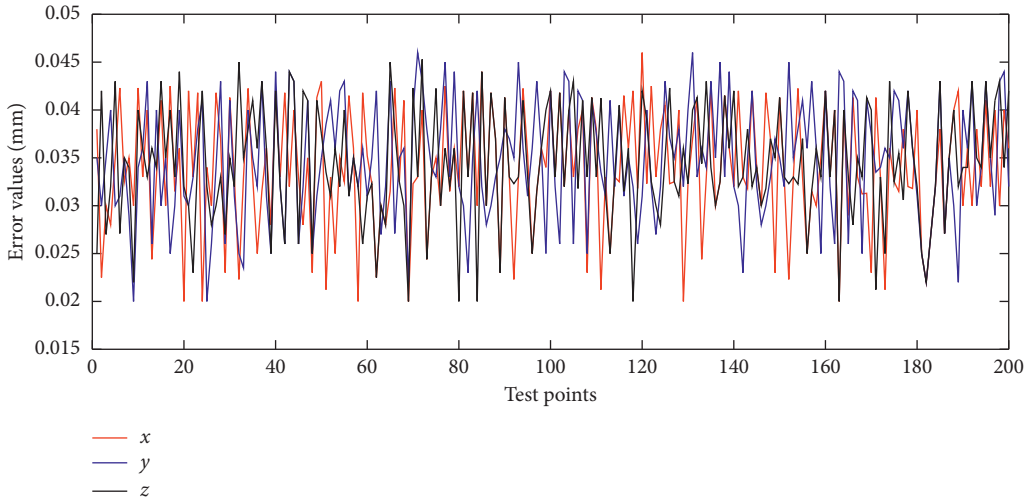

Figure 12: Error curve in the x-, y-, and z-directions of IK algorithm.

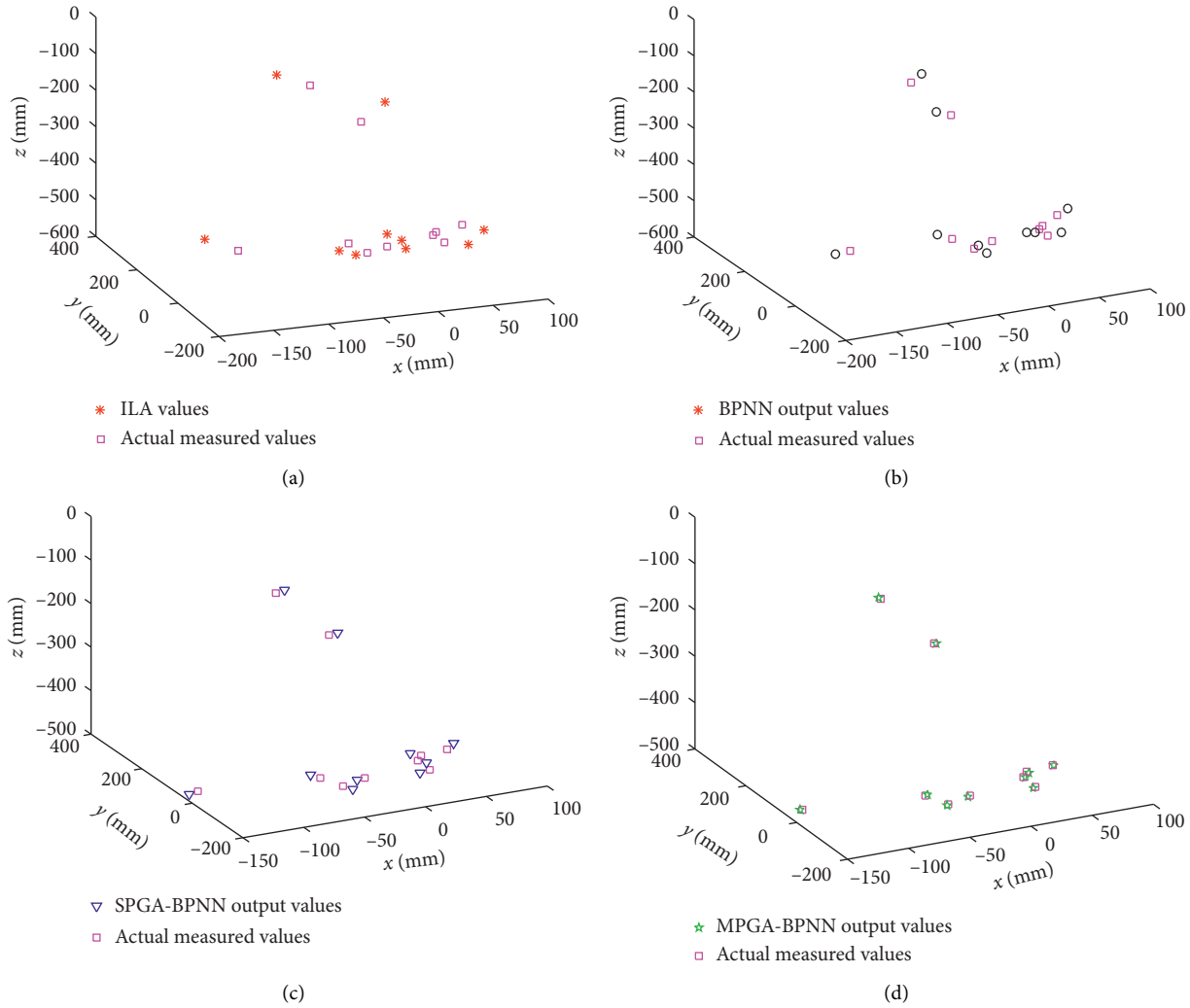

Figure 13: Tracking diagram between the actual values obtained by the test point through the ILA, BPNN, SPGA-BPNN, and MPGA-BPNN and the corresponding measured values.

Table 2: Deviations of test points.

Test point number deviations	1	2	3	4	5	6	7	8	9	10
E_i^p (mm)	56.50	44.58	49.10	46.65	49.67	50.07	51.23	44.86	48.43	46.05
E_i^b (mm)	20.86	21.44	19.80	17.85	19.24	17.74	18.92	17.56	18.89	16.86
E_i^s (mm)	11.28	10.52	11.13	10.45	11.36	11.38	11.05	10.30	12.36	12.00
E_i^m (mm)	2.33	2.56	2.45	2.20	2.94	2.72	2.72	2.14	2.37	2.52

Table 3: Inverse and positive solution results of testing points.

Test point	(x_i^t, y_i^t, z_i^t) (mm)			(x_i^m, y_i^m, z_i^m) (mm)			Joint angle (rad)				(x_i^f, y_i^f, z_i^f) (mm)	
1	−41	18	−500	−39.83	16.46	−498.82	−0.21	−0.26	0.32	−40.41	17.14	−498.77
2	−61	100	−98	−62.30	101.71	−96.63	−0.33	−1.84	2.62	−62.61	101.83	−96.09
3	−17	−42	−488	−18.66	−40.83	−489.37	−0.23	0.41	0.50	−18.91	−40.51	−489.63
4	−141	21	−486	−142.33	22.32	−484.84	−0.24	−2.37	0.15	−142.00	22.09	−484.76
5	23	−105	−463	21.50	−103.63	−465.08	−0.14	0.87	0.69	22.18	−103.14	−466.16
6	−39	−63	−489	−40.38	−64.44	−490.72	−0.20	0.84	0.42	−40.52	−64.37	−490.30
7	6	209	−270	7.69	210.57	−271.63	0.02	−1.56	1.68	7.71	210.72	−271.79
8	10	−121	−430	11.23	−122.21	−431.31	−0.27	0.77	0.98	11.64	−122.57	−431.84
9	62	15	−482	63.41	16.33	−483.36	−0.10	−0.15	0.56	63.41	16.83	−483.36
10	9	−141	−411	10.12	−142.53	−412.67	−0.27	0.87	1.08	10.86	−142.91	−412.77

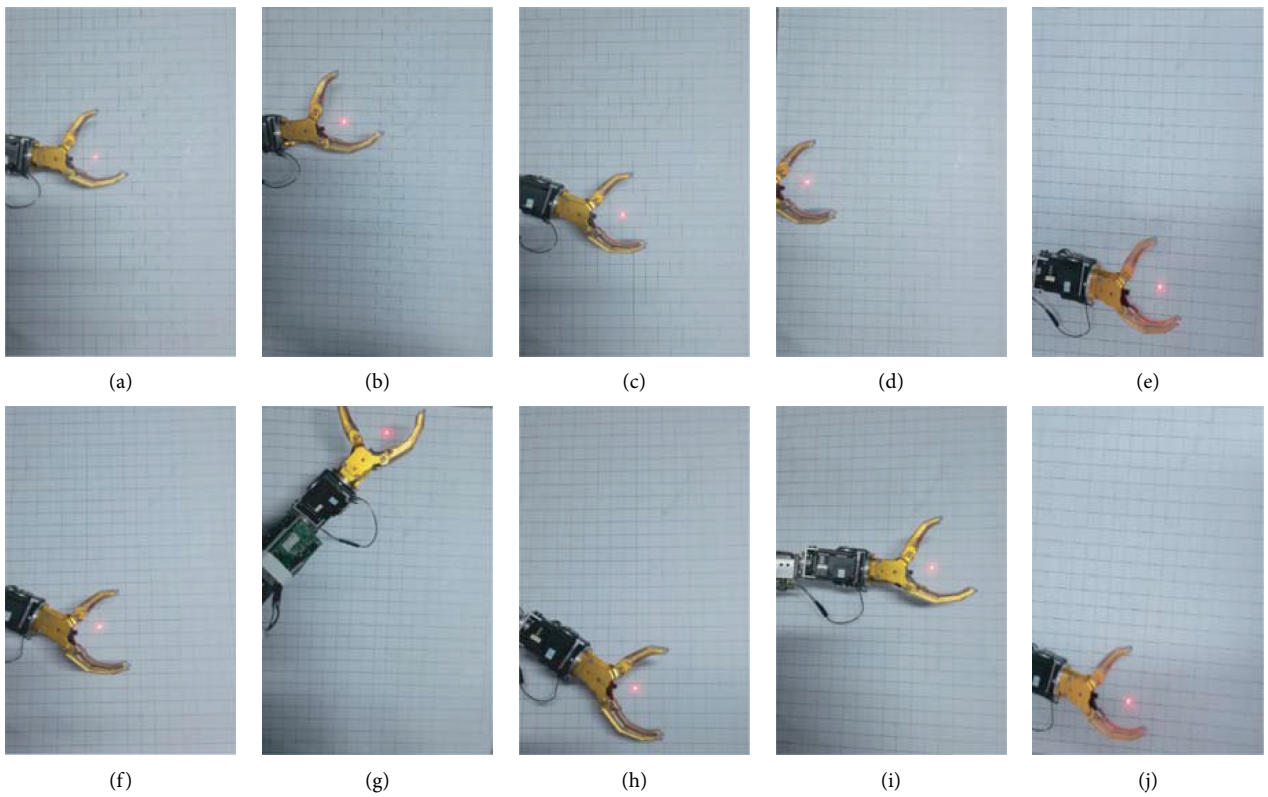

Figure 14: Artificial limb accurately moving to the target position. The numbers represent the laser test point at different positions.

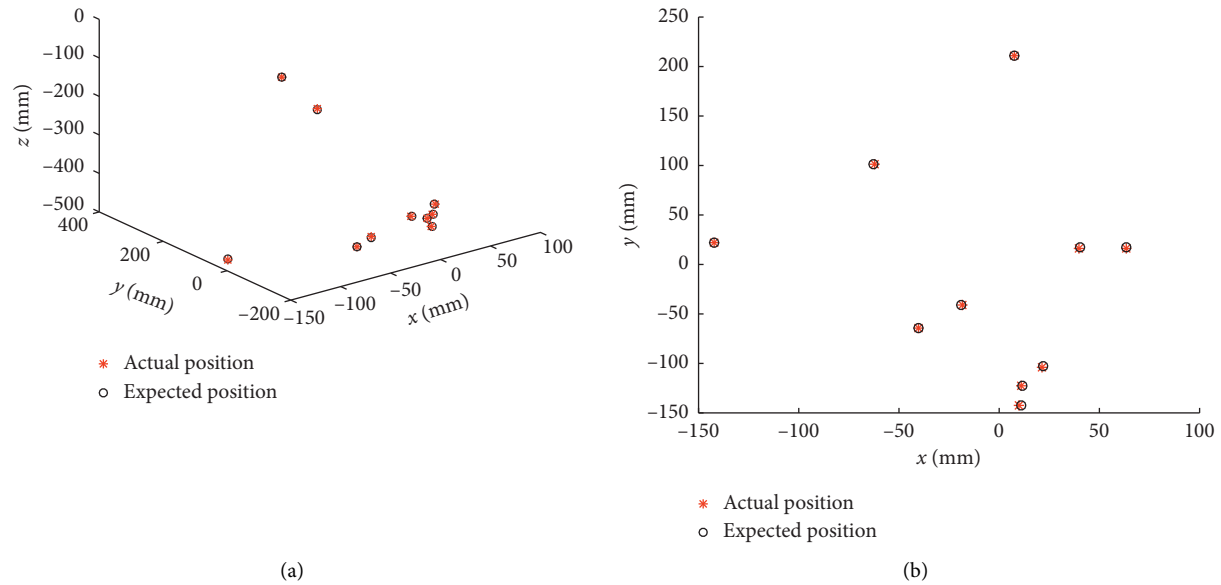

Figure 15: Continued.

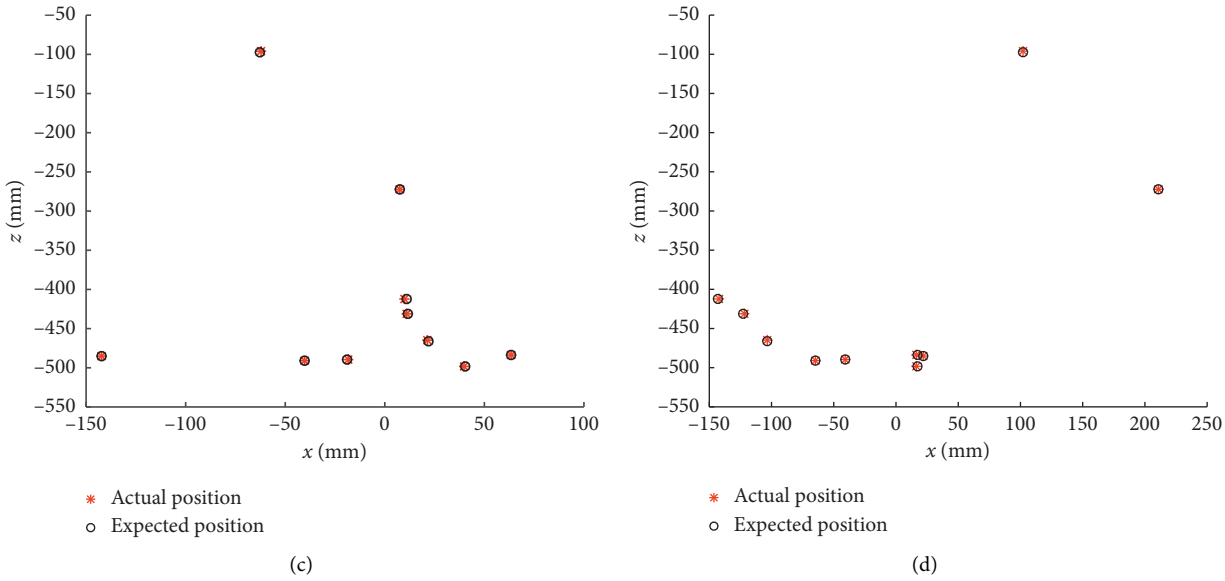

Figure 15: Response diagrams of the actual position and the desired position.

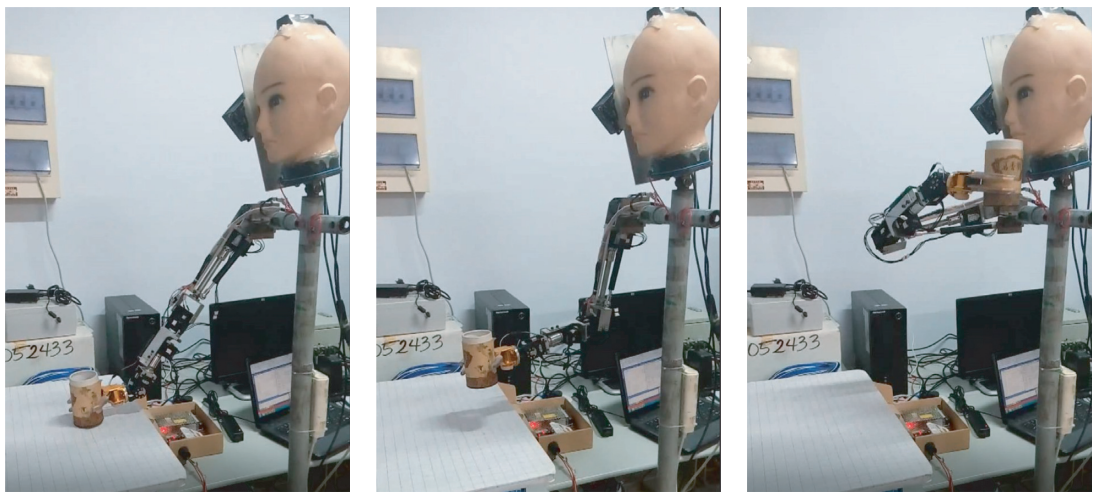

Figure 16: Motion process of the upper limb prosthesis. (a) Locating the position of the cup, (b) gripping the cup, and (c) moving the cup to the wearer's mouth.

5. Conclusions and Future Work

To achieve the purpose of accurately grasping a random target with the upper limb prosthesis, a novel type of random target localization algorithm is proposed. Firstly, an initial localization algorithm (ILA) that uses two 3D attitude sensors and a laser range sensor to detect the target attitude and distance is presented. Secondly, MPGA-BPNN error correction algorithm is proposed to improve the localization accuracy of the target based on the ILA is utilized. Thirdly, GRNN algorithm is presented to calculate the prosthetic joint angles. Finally, the proposed algorithm is applied to the 5-DOF upper limb prosthesis. The simulations show that the average positioning error by MPGA-BPNN error correction algorithm is 1 mm, and the average error of the IK algorithm is 0.035 mm. Compared with ILA, the accuracy by MPGA-BPNN error correction algorithm is greatly improved and better than BPNN error correction algorithm and SPGA-BPNN error correction algorithm.

The laser test point positioning experiment shows that the AAE between the output values after error correction by MPGA-BPNN and the actual values is 2.5 mm, and the proposed IK algorithm can accurately obtain a unique IK solution. The experiment of gripping a cup from a table and

moving it to the mouth of the wearer's further verifies that the positioning algorithm and the IK algorithm can meet the requirements of the wearer.

In our future work, we will try to eliminate the restriction of the upper limb prosthesis's DOF to meet the wearer's need for more use. We also aim to consider using voice or brain waves to control the movement of the upper limb prosthesis.

Data Availability

The data used to support the findings of this study are included within the article.

Conflicts of Interest

The authors declare that there are no conflicts of interest regarding the publication of this article.

Authors' Contributions

All the authors contributed to the study conception and design. Material preparation, data collection, and analysis were performed by all authors. The first draft of the manuscript was written by Xinglei Zhang, and all authors commented on the previous versions of the manuscript. All authors read and approved the final version of the manuscript.

Acknowledgments

This work was supported by the Major Science and Technology Innovation Projects of Shandong Province (2017CXGC0919), the National Natural Science Foundation of China (61803235), and Key Research Programs of Shandong Province (2016GSF201197).

References

[1] R. C. Wang, "The research and development of prosthetic technology of in China," *Chinese Journal of Rehabilitation Medicine*, vol. 27, pp. 1058–1060, 2012.

[2] K. Ziegler-Graham, E. J. MacKenzie, P. L. Ephraim, T. G. Travison, and R. Brookmeyer, "Estimating the prevalence of limb loss in the United States: 2005 to 2050," *Archives of Physical Medicine and Rehabilitation*, vol. 89, no. 3, pp. 422–429, 2008.

[3] J. L. Pons, *Wearable Robots: Biomechatronic Exoskeletons*, John Wiley and Sons Press, Hoboken, NY, USA, 2008.

[4] C. T. Cao, V. P. Do, and B. R. Lee, "A novel indirect calibration approach for robot location error compensation based on neural network and hand-eye vision," *Applied Sciences*, vol. 9, p. 1940, 2019.

[5] G. Jiang, M. Luo, K. Bai, and S. Chen, "A precise positioning method for a puncture robot based on a PSO-optimized BP neural network algorithm," *Applied Sciences*, vol. 7, p. 969, 2017.

[6] D. Yi, T. Lee, and D. Cho, "A new localization system for indoor service robots in low luminance and slippery indoor environment using afocal optical flow sensor based sensor fusion," *Sensors*, vol. 18, no. 2, p. 171, 2018.

[7] M. Jung and J.-B. Song, "Efficient autonomous global localization for service robots using dual laser scanners and rotational motion," *International Journal of Control, Automation and Systems*, vol. 15, no. 2, pp. 743–751, 2017.

[8] J. J. Craig, *Introduction to Robotics: Mechanics and Control*, Pearson Press, New York, NY, USA, 2004.

[9] J. D. Wu, J. Lu, H. L. Ren, Y. L. Qin, S. Q. Guo, and W. S. Hu, "Nonlinear equalizer based on general regression neural network in coherent optical OFDM system," *Acta Optica Sinica*, vol. 38, Article ID 0906002, 2018.

[10] W. Wang, S. Bei, L. Zhang, Z. Kai, Y. Wang, and W. Hang, "Vehicle sideslip angle estimation based on general regression neural network," *Mathematical Problems in Engineering*, vol. 2016, Article ID 3107910, 2016.

[11] B. H. Dana and M. Khasawneh, "A recursive general regression neural network (R-GRNN) oracle for classification problems," *Expert Systems with Applications*, vol. 135, pp. 273–286, 2019.

[12] H. Ahmed and M. Tahir, "Accurate attitude estimation of a moving land vehicle using low-cost MEMS IMU sensors," *IEEE Transactions on Intelligent Transportation Systems*, vol. 18, no. 7, pp. 1723–1739, 2017.

[13] Y. Gao, "Forecast model of perceived demand of museum tourists based on neural network integration," *Neural Computing and Applications*, vol. 33, no. 2, pp. 625–635, 2021.

[14] E. Rava and E. M. Chirwa, "Prediction of performance of the moving-bed biofilm pilot reactor using back-propagation artificial neural network (BP-ann)," *Chemical Engineering Transactions*, vol. 61, pp. 1189–1194, 2017.

[15] M. D. T. Mcdonnell, D. Arnaldo, E. Pelletier et al., "Machine learning for multi-dimensional optimisation and predictive visualisation of laser machining," *Journal of Intelligent Manufacturing*, vol. 32, no. 5, pp. 1471–1483, 2021.

[16] J. Di, "Investigation on the traffic flow based on wireless sensor network technologies combined with FA-BPNN models," *Journal of Intelligent Technology*, vol. 20, pp. 589–597, 2019.

[17] X. Xin Yao, "Evolving artificial neural networks," *Proceedings of the IEEE*, vol. 87, no. 9, pp. 1423–1447, 1999.

[18] F. Musharavati and A. S. M. Hamouda, "Enhanced simulated-annealing-based algorithms and their applications to process planning in reconfigurable manufacturing systems," *Advances in Engineering Software*, vol. 45, no. 1, pp. 80–90, 2012.

[19] M. Wang and P. Cao, "Calibrating the micromechanical parameters of the PFC2D(3D) models using the improved simulated annealing algorithm," *Mathematical Problems in Engineering*, vol. 2017, Article ID 6401835, 14 pages, 2017.

[20] A. A. Alnaqi, H. Moayedi, A. Shahsavar, and T. K. Nguyen, "Prediction of energetic performance of a building integrated photovoltaic/thermal system thorough artificial neural network and hybrid particle swarm optimization models," *Energy Conversion and Management*, vol. 183, pp. 137–148, 2019.

[21] S. Shao, Y. Peng, C. He, and Y. Du, "Efficient path planning for UAV formation via comprehensively improved particle swarm optimization," *ISA Transactions*, vol. 97, pp. 415–430, 2020.

[22] N. Chindapan, S. S. Sablani, N. Chiewchan, and S. Devahastin, "Modeling and optimization of electrodialytic desalination of fish sauce using artificial neural networks and genetic algorithm," *Food and Bioprocess Technology*, vol. 6, no. 10, pp. 2695–2707, 2013.

[23] M. F. Yan, G. Hu, B. Liu, Z. H. Liu, R. J. Wu, and S. Wang, "Optimization design of a fast neutron imaging collimator by genetic algorithm," *Journal of Instrumentation*, vol. 15, Article ID P12002, 2020.

[24] D. S. Deng, W. Long, Y. Y. Li, and X. Q. Shi, "Multipopulation genetic algorithms with different interaction structures to

solve flexible job-shop scheduling problems: a network science perspective," *Mathematical Problems in Engineering*, vol. 2020, Article ID 8503454, 12 pages, 2020.

[25] Y. Hou, N. Wu, M. Zhou, and Z. Li, "Pareto-optimization for scheduling of crude oil operations in refinery via genetic algorithm," *IEEE Transactions On Systems, Man, and Cybernetics: Systems*, vol. 47, no. 3, pp. 517–530, 2017.

[26] M. Alshraideh and L. Tahat, "Multiple-population genetic algorithm for solving min-max optimization problems," *International Review on Computers and Software (IRECOS)*, vol. 10, no. 1, pp. 9–19, 2015.

Hindawi
Shock and Vibration
Volume 2021, Article ID 9967278, 11 pages
https://doi.org/10.1155/2021/9967278

Research Article

An Experimental Study of the Influence of Hand-Arm Posture and Grip Force on the Mechanical Impedance of Hand-Arm System

Wenjie Zhang,[1,2] Qichao Wang,[1,2] Zheng Xu,[1,2] Hongmei Xu ,[1,2] Hang Li,[1,2] Jiajun Dong,[1,2] and Xinbo Ma[3]

[1]*College of Engineering, Huazhong Agricultural University, Wuhan 430070, China*
[2]*Key Laboratory of Agricultural Equipment in Mid-lower Reaches of the Yangtze River, Ministry of Agriculture and Rural Affairs, Huazhong Agricultural University, Wuhan 430070, China*
[3]*School of Intelligent Manufacturing, Nanyang Institute of Technology, Nanyang 473004, China*

Correspondence should be addressed to Hongmei Xu; xhm790912@163.com

Received 24 March 2021; Accepted 26 May 2021; Published 10 June 2021

Academic Editor: Pak Kin Wong

In order to investigate the effects of hand-arm posture, grip force, push force, and vibration excitation intensity on the mechanical impedance of human hand-arm system, a test system with a self-developed vibration handle has been prepared. Based on the testing system, the mechanical impedance of the hand-arm system of seven Chinese adult males were tested and calculated under the random vibration excitation with the frequency of 10–1000 Hz. The results reveal that when the frequency is lower (<40 Hz), the hand-arm system with an elbow angle of 180° produces a higher mechanical impedance; when the frequency ranges from 40 Hz to 100 Hz, the hand-arm system with an elbow angle of 90° generates a higher mechanical impedance; while when the frequency is higher (>100 Hz), the hand-arm posture seems to have no obvious effect on the mechanical impedance. Higher grip or push force would increase the frequency corresponding to the peak value of the mechanical impedance and often correspond to a higher mechanical impedance in a specific frequency range (30–200 Hz). When the frequency is lower (<140 Hz), vibration intensity has certain effects on the mechanical impedance of the hand-arm system. In conclusion, vibration intensity does not directly affect the mechanical impedance, but an increase in grip or push force often causes an increase in mechanical impedance and a higher frequency that corresponds to the peak of mechanical impedance.

1. Introduction

When the agricultural machinery and equipment are working in the field, strong vibrations are inevitably produced due to the low levelness of the farmland, large motion range of the working device, high running speed of the transmission system and its own structural characteristics, and the vibrations will be passed to the body of the operator through the seat, steering wheel, handrails, and pedals. According to different body parts that are influenced by the transmitted vibrations, the vibrations can be divided into whole body vibration and local vibration. Whole body vibration mainly refers to the vibration transmitted to the body through the supporting surface, such as the seat. Local vibration, also known as hand-transmitted vibration, is the mechanical vibration or shock acting on or transmitted to the hand-arm system through the hand or fingers from the steering wheel and operating armrest [1, 2]. Some vibrating tools and machines, such as crushers, rock drills, and grinders, are widely used in many industrial occasions. The workers who manipulate this kind of tools or machines for a long time may feel tingling and numbness in their hands, the severity of which usually increases with stronger vibration intensity of the tool. In severe cases, it may cause physical discomfort and loss of control of the tool [3]. These acute effects usually disappear shortly after stopping the use of the tool. However, prolonged exposure to such high-intensity hand-transmitted vibrations can cause a series of diseases in the blood vessels, sensory nerves, and musculoskeletal parts of the human hand-arm system. These diseases are

collectively referred to as "arm vibration syndrome," also known as Raynaud's disease. For legal occupational diseases, the main symptoms are vibration white fingers [4, 5]. Figure 1 shows the symptoms and signs of vibration white fingers. According to previous reports, vibration white fingers are difficult to treat and require a long recovery period. The symptoms of some patients continue to deteriorate even after the vibration operation is stopped. For example, a study revealed that some patients with Raynaud's disease could not recover from vibration exposure even after more than 20 years [6].

Hand-transmitted vibration will cause some damage to the health of the operators of vibrating machinery, especially under high vibration intensity and long exposure to vibration. Hence, the harm caused by hand-transmitted vibration is a particularly prominent problem. At present, there is an increasing demand for the protection of the health of vibration tool operators. Therefore, it is critical to effectively control the hand-transmitted vibration to minimize the harm to the human hand-arm system.

So far, relevant research has been mainly focused on the vibration source of the tool itself, aiming to optimize the structure of the tool, reduce the strength of hand-transmitted vibration, and alleviate the adverse effects of vibration on the human hand-arm system. However, there has been little research on the human hand-arm system under hand-transmitted vibrations, such as the absorption and transmission characteristics of vibration energy in the hand-arm system, the response of the system to hand-transmitted vibration, and its relationship with vibration excitation. To minimize the impact of hand-transmitted vibration on human health, it is also highly necessary to study the characteristics of vibration transmission in the human hand-arm system, as well as some physical factors of vibration such as hand-arm posture, vibration frequency and amplitude, and gripping force. Exploration of the transfer law of vibration energy in the hand-arm system can not only help to improve and optimize the structure of the vibration machinery but also provide important reference for monitoring the occupational health of workers and the early diagnosis and prevention of arm vibration disease.

Investigation of the biodynamic response of the human hand-arm system can facilitate a better understanding of the mechanism underlying the damage caused by vibration, as well as help to formulate frequency weighting factors for the evaluation of the risk caused by vibration exposure. Besides, it may also facilitate the development of methods or devices for the isolation of the hand-arm system from vibration. Some studies have been carried out on the biodynamic responses of the hand-arm system, including apparent mass, apparent stiffness, and mechanical impedance, and most studies are focused on mechanical impedance. The main research findings are as follows. Lundström et al. measured the mechanical impedance of the hand-arm system in the frequency range of 20–1500 Hz and found that the mechanical impedance is strongly dependent on the frequency

Figure 1: Symptoms and signs of vibrating white fingers.

of vibration [7]. Burström studied the mechanical impedance of the human hand-arm system with random vibration under different experimental conditions and statistically analyzed whether the conditions have an effect on the amplitude and phase of the mechanical impedance. The results were further compared with those from other studies using the sinusoidal excitation. The results showed that the vibration level and vibration stimulation frequency have a very significant effect on the mechanical impedance of the hand-arm system. The increase in grip or push force will cause the increases of impedance [8]. Hempstock and O'Connor evaluated the measurement accuracy of the mechanical impedance of the human hand-arm system and found that when the frequency is lower than 25 Hz, there were certain differences between the measured impedance values [9]. Gurram et al. employed the impedance testing technique of the driving point to study the biodynamic response of the human hand-arm system under sinusoidal and random excitation and found that, within a certain frequency range, the response characteristics of the hand-arm system caused by sinusoidal excitation and random excitation are significantly different, indicating the nonlinear characteristics of the hand-arm system [10]. Dong et al. proposed a method to measure the mechanical impedance of the finger and the palm and studied the distribution characteristics of mechanical impedance. The results showed that, at lower frequencies (≤40 Hz), the mechanical impedance of the palm was significantly higher than that of the finger; when the frequency was increased to 100 Hz, most of the mechanical impedance was still distributed in the palm; when the frequency was above 160 Hz, the mechanical impedance of the finger was close to or slightly higher than that of the palm. They also discussed the basic distribution characteristics of mechanical impedance in the finger and palm under vibration in three orthogonal directions [11, 12]. Based on a theoretical analysis of the three-degree-of-freedom and four-degree-of-freedom biomechanical models of the human arm, Li studied the effects of vibration frequency, vibration intensity, hand-arm posture, and gripping force level on the mechanical impedance of the hand-arm system and found very significant relationships among these factors [13]. Dai et al. described mechanical impedance from the

perspective of vibration mechanics and biomechanics and designed a quantitative detection system for the muscle rigidity symptoms of Parkinson's disease [14].

From the above literature, it can be seen that, in recent years, great progress has been made in research on the vibration transmission of the hand-arm system. However, in many studies, adult males in Europe and the United States were taken as the subjects, whose physical characteristics are very different from those of Chinese adult men. Hence, it remains unclear whether the previously reported biodynamic characteristics and vibration transmission characteristics of the hand-arm system can also be applied to Chinese adult males, and little is known about whether the relevant results and conclusions can be directly used to guide the optimization design for vibration reduction of machines in China.

The mechanical impedance of the human hand-arm system is closely related to the tension of soft tissues such as arm muscles. In the process of operating the machine and tools, hand-arm posture and hand force are the main factors that affect the muscle tension and should be two key factors in testing the mechanical impedance of the hand-arm system. Therefore, this study intends to test the effects of hand-arm posture and hand force on the mechanical impedance of the hand-arm system under different vibration intensities.

2. Materials and Methods

2.1. Research Subjects. The subjects of this experiment were the right arms of seven healthy right-handed adult males with no history of vibration exposure. The anthropometric parameters measured according to GB/T 5703-2010 [15] are shown in Table 1.

The volume of the hand was measured by the Archimedes drainage method, with the wrist just being immersed in water. The maximum grip diameter refers to the linear distance between the middle finger point (ph III) and the most protruding part of the thumb knuckle when the fingertip of the thumb touches the middle fingertip. The test results of anthropometric parameters in Table 1 show that the hand-related parameter values are significantly lower than those of western subjects in hand-transmitted vibration-related tests. At the same time, in this experiment, there were also some differences in anthropometric parameters among different subjects, which might be utilized to study the influence of hand size on the hand-transmitted vibration later.

2.2. Definition of Mechanical Impedance of the Hand-Arm System. Mechanical impedance refers to the obstruction of the mechanical structure on the vibration transmission and can be obtained by calculating the ratio of the force F acting on the system to the speed V generated due to the force at the action point. The human arm is a musculoskeletal system consisting of muscle and bone parts. The bone has a large inertia, and the muscle has rigidity, viscosity, and inertia. These mechanical characteristics are collectively called arm impedance or arm mechanical impedance [16]. According to the standard GB/T 19740-2005 [17], the free mechanical impedance $Z(\omega)$ of the driving point of the hand-arm system is defined as the complex ratio of the excitation force $F(\omega)$ applied at the frequency and the vibration velocity $V(\omega)$ caused at the same frequency, and ω is the vibration angular frequency. For all other connection points, the system is free, which means that the applied external force is zero, namely,

$$Z(\omega) = \frac{F(\omega)}{V(\omega)}. \tag{1}$$

It should be noted that the mechanical impedance value of a hand-arm system is generally a complex number, that is, it has a real part and an imaginary part. Hence, it can also be expressed by mode and phase, and the real part is the mechanical resistance that reflects the absorption and dissipation of vibration energy. In this study, the hand and arm are regarded as a system whose vibrations in the three axes are independent under the biodynamic coordinate system (see Figure 2), as specified in ISO 5349-1-2001 [18]. In this test, the mechanical impedance was measured along the Z_h direction (along the forearm) specified in the human biodynamic coordinate system, which is the main vibration exposure direction of many hand-held power tools during operation. Besides, in this direction, the mechanical impedance value of the entire arm is also the highest [11].

2.3. Calculation of the Mechanical Impedance of the Hand-Arm System. In the experiment, the vibration handle was tested first in the contactless state. The sensor signal on the finger side was used to represent the vibration characteristics of the vibration handle. Therefore, the force signal and acceleration signal on the finger side were measured when subjects did not hold the handle. The mechanical impedance of handle (Z_{handle}) was calculated by the integral of acceleration value, Fourier transform of force value and velocity value in time domain and the calculation of equation (1). Similarly, the force signal and acceleration signal on the finger side and the palm were, respectively, measured when the subjects held the handle. The mechanical impedance of the finger (Z_{finger}) and the palm (Z_{palm}) were calculated in the same way as the calculation of Z_{handle}. Finally, the mechanical impedance value of the entire hand-arm system was obtained by subtracting Z_{handle} from Z_{finger} plus Z_{palm}.

Assuming that the force values measured by the two force sensors on the finger side of the subject are F_1 and F_2 and the force values measured by the two force sensors on the palm side are P_1 and P_2, respectively, the finger force (F_{finger}) and palm force (F_{palm}) can be expressed as follows:

$$\begin{aligned} F_{\text{finger}} &= F_1 + F_2, \\ F_{\text{palm}} &= P_1 + P_2. \end{aligned} \tag{2}$$

The acceleration values measured on the finger side and palm side were integrated once to obtain the velocity value on the finger side (V_{finger}) and palm side (V_{palm}), respectively. Then, the force value $F(t)$ and velocity value $V(t)$ in time domain were converted into force value $F(\omega)$ and velocity value $V(\omega)$ in frequency domain by Fourier

Table 1: Anthropometric measurements of the subjects.

Subject number	Height (cm)	Weight (kg)	Length of the hand (cm)	Width of the hand (mm)	Thickness of the hand (mm)	Volume of the hand (ml)	Maximum grip diameter (mm)	Length of the upper Arm (cm)	Length of the forearm (cm)
1	183.0	100.0	20.1	89.4	39.8	400.0	96.5	37.7	47.1
2	170.0	60.0	20.0	85.5	24.5	350.0	97.2	34.5	45.2
3	171.0	61.0	16.7	80.2	24.7	300.0	85.7	31.7	40.5
4	169.0	58.0	17.4	83.5	29.7	320.0	91.4	32.1	42.2
5	173.0	70.0	17.1	83.3	25.6	310.0	90.7	33.3	43.9
6	176.0	78.0	19.8	88.5	31.7	380.0	97.7	35.4	46.1
7	165.0	62.0	15.2	78.4	23.1	270.0	81.6	30.6	39.6

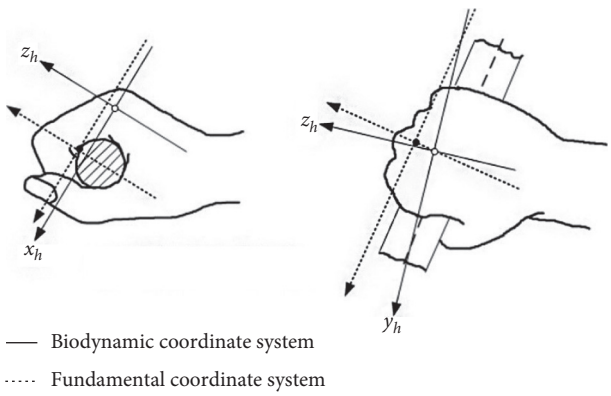

Figure 2: Hand grip coordinate system.

transform. In equations (3) and (4), the mechanical impedance value on the finger side (Z_{finger}) and the palm side (Z_{palm}) can be obtained as follows:

$$Z_{\text{finger}}(\omega) = \frac{F_{\text{finger}}(\omega)}{V_{\text{finger}}(\omega)}, \tag{3}$$

$$Z_{\text{palm}}(\omega) = \frac{F_{\text{palm}}(\omega)}{V_{\text{palm}}(\omega)}. \tag{4}$$

Finally, the mechanical impedance (Z) of the hand-arm system can be expressed by the following formula:

$$Z = Z_{\text{finger}} + Z_{\text{palm}} - Z_{\text{handle}}. \tag{5}$$

2.4. Mechanical Impedance Test of the Hand-Arm System

2.4.1. Test Equipment. In this study, a self-developed vibrating handle was used. The grip part of the test handle was 40 mm in diameter, 120 mm in length, and 2 mm in thickness. Figure 3 shows the structural schematic and physical diagram of the vibrating handle. In order to ensure its mechanical properties and avoid resonance within the analysis range, the vibrating handle was made of aluminum alloy, which has the characteristics of light weight and high rigidity. The handle was evenly divided into the upper and lower parts at the center line, which were connected by bolts. The middle of each part was equipped with a three-dimensional acceleration sensor, of which the upper half was used to measure the vibration response at the palm and the lower half was used to measure the vibration response at the fingers. Such installation method could provide the reliability of the vibration response test [19]. It is worth noting that the grip part of the vibrating handle was cylindrical and its inside was of a curved surface, which was not conducive to the installation of the acceleration sensor. Therefore, a small rectangle block was welded on the inner surface so that the acceleration sensor could be fixed on the surface of the block. The rectangular block had a flat surface and should be parallel to the middle bracket of the vibrating handle in the welding process and close to the center of the vibrating handle. Both ends of each part were, respectively, fixed with two three-dimensional force sensors on an aluminum alloy strip bracket, wherein the force sensor was fixed by bolts, and the acceleration sensor inside the vibrating handle was fixed with strong glue. All sensors were installed following the instructions. In addition, a clamp was designed to connect the vibrating handle to the vibrating table. The vibrating handle developed in this study can not only measure the vibration response of the finger side and palm side at the same time but also directly measure the grip and push force exerted by the hand-arm system. Therefore, a force plate device for measuring push force was not required.

The three-dimensional force sensor was used to measure the static and dynamic force at the driving points of the palm side and finger side at the same time. Through proper signal processing, the static and dynamic fractions in the force signal measured by each force sensor can be obtained. Figure 4 is a schematic diagram of the contact force, grip force, and push force of the hand, assuming that the static forces measured by the two force sensors on the palm side are P_1 and P_2 and those on the finger side are F_1 and F_2. According to ISO 10819-2013 [20], the static grip force (F_g) and push force (F_p) can be defined as

$$\begin{aligned} F_g &= F_1 + F_2, \\ F_p &= P_1 + P_2 - (F_1 + F_2). \end{aligned} \tag{6}$$

During the test, by rotating the shaker cylinder by 90°, the shaking table could be perpendicular to the horizontal plane so that the direction of the vibration excitation generated by the shaker could meet the Z_h direction of the test

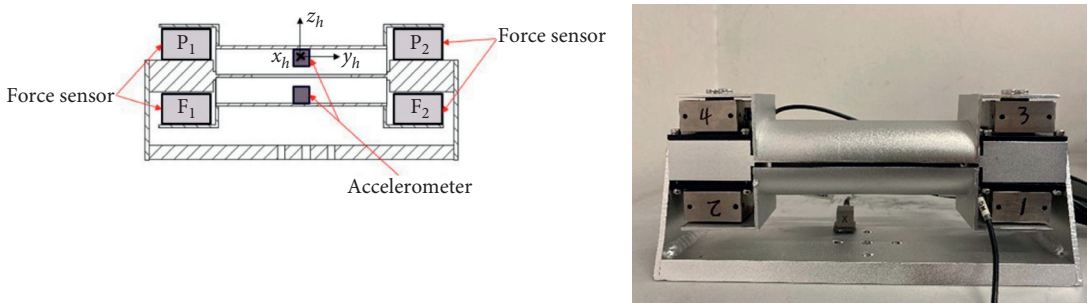

Figure 3: Vibration handle. (a) Structural sketch. (b) Physical map.

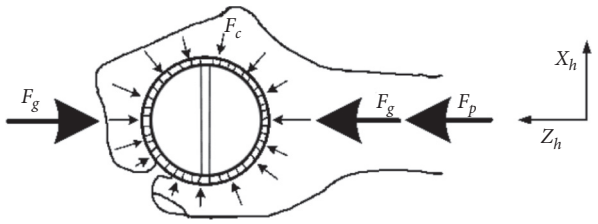

Figure 4: Sketch map of hand contact force (F_c), grip force (F_g), and push force (F_p).

(along the forearm). Figure 5 is the schematic diagram of the mechanical impedance test process (taking the subject's hand-arm posture at 90° as an example).

2.4.2. Test Design. According to the literature, the posture of the hand-arm system, grip force, push force, vibration intensity, and individual differences all have certain effects on the mechanical impedance of the human hand-arm system. Since individual differences are very complex, the research has been mainly focused on the influence of hand-arm posture, grip force, push force, and vibration intensity on the mechanical impedance of the human hand-arm system. In order to investigate the effect of hand-arm posture on the mechanical impedance, we tested and calculated the mechanical impedance of the subjects when the elbow angle of the hand arm was 90° and 180°, respectively. To investigate the effect of grip force on the mechanical impedance, we tested and calculated the mechanical impedance of the subjects when the grip force was 10, 30, and 50 N, respectively. Similarly, to assess the effect of push force on the mechanical impedance, we determined and calculated the mechanical impedance of the subjects when the push force was 10 and 30 N, respectively. Finally, because the usual research range of vibration intensity is 3.5–10 m/s^2, we tested and calculated the mechanical impedance of the subjects under the vibration intensity of 5 and 10 m/s^2, respectively. The test design is shown in Table 2.

Figure 6 shows the two hand-arm postures used in the mechanical impedance test of the hand-arm system.

2.4.3. Experimental Procedure. First, the parameters for the vibration table and data acquisition card were set. The excitation mode was set to broadband random vibration of 10–1000 Hz, and the vibration intensity was 5 m/s^2. In order to make the collected signal as close as possible to the real signal in the studied frequency range, the sampling frequency was set as 5000 Hz. After setting of the parameters, the vibrating handle was fixed on the vibrating table. It should be noted that the vibrating handle and the surface of the vibration table cannot be loosened. Then, the vibration characteristics of the empty handle were tested, so as to eliminate the influence of the mechanical impedance of the vibrating handle itself on the test results when calculating the mechanical impedance of the hand-arm system. At the same time, analysis of the vibration characteristics of the handle showed that there was no obvious resonance phenomenon in the handle in the frequency range studied. Therefore, the vibrating handle could meet the test requirements. All subjects were required to dress lightly and not to wear a coat or rings and watches to minimize the influence of clothing on the test results, and the subjects were tested in a random order. Subsequently, the subjects were required to take the postures according to the test requirements and hold the vibrating handle with appropriate force. Vibration exposure started after the correct postures and the required grip and push force were maintained. During the test, the subjects needed to observe the display screen of the force signal to maintain the grip and push force at levels required by the test (fluctuations within 3 N were allowed). If the subject could keep the grip and push force within the range required by the test, the vibration signal frequency of the hand-arm system would not change significantly in 20 s of vibration exposure. Furthermore, at higher hand force levels (grip force 50 N and push force 30 N), it would be difficult for the subjects to maintain hand force at this level for a long period of time. Therefore, the test of each combination of different test factors lasted for approximately 30 s. Each subject performed 12 trials under one vibration intensity. To avoid the possible impact of hand fatigue on the test results, after the end of each test, the subject would be allowed to take a three-minute rest before taking the next test. Then, the vibration

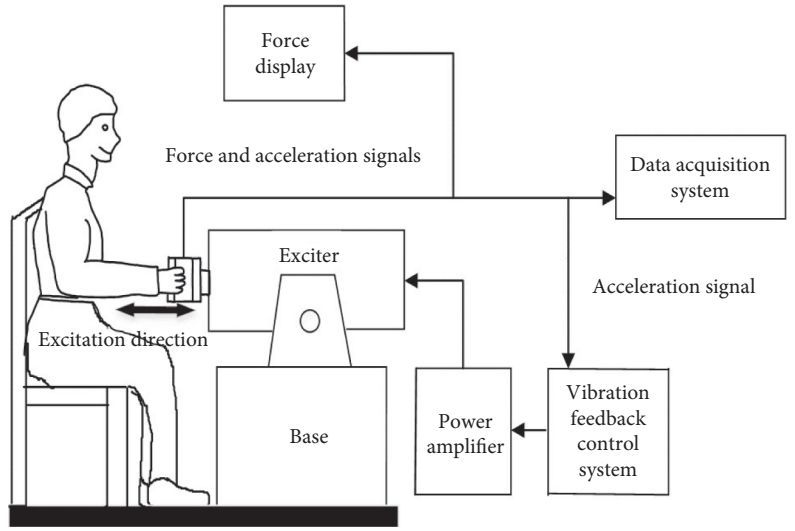

Figure 5: Schematic diagram of the mechanical impedance measurement process of the hand-arm system.

Table 2: Levels of different test factors.

Hand-arm posture	Vibration intensity (m/s^2)	Grip force (N)	Push force (N)
Elbow angle 90°	5	10 30	10
Elbow angle 180°	10	50	30

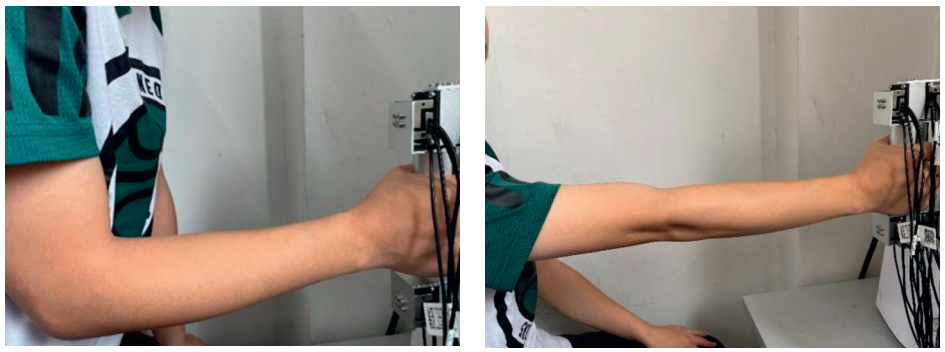

(a) (b)

Figure 6: Hand-arm posture in the mechanical impedance test. (a) 90° elbow angle. (b) 180° elbow angle.

excitation intensity of the vibration table was adjusted to 10 m/s^2, and other parameter settings were kept unchanged to repeat the above test.

3. Results and Discussion

Matlab software was used to calculate the mechanical impedance amplitude of the human hand-arm system, and the results were expressed at the center frequency point of 1/3 octave in the frequency range of 10–1000 Hz.

3.1. Influence of Individual Differences of Subjects on Mechanical Impedance. The hand-arm posture is the main factor affecting the mechanical impedance [21]. Therefore, we principally discussed the effect of individual differences on mechanical impedance under two different hand-arm postures. Furthermore, we set other test conditions to low strength state (vibration intensity was 5 m/s^2, the push force was 10 N, and the grip force was 30 N) to assure the accuracy of the results. The mechanical impedance amplitudes of seven subjects were calculated by the integral of acceleration value, Fourier transform of force value and velocity value in time domain and the calculation of equation (1). The results are shown in Figure 7.

Observations showed that, under two different hand-arm postures, the amplitude of mechanical impedance of the hand-arm system was only different among individual subjects at low vibration frequencies (<100 Hz), but when the frequency was above 100 Hz, the individual differences

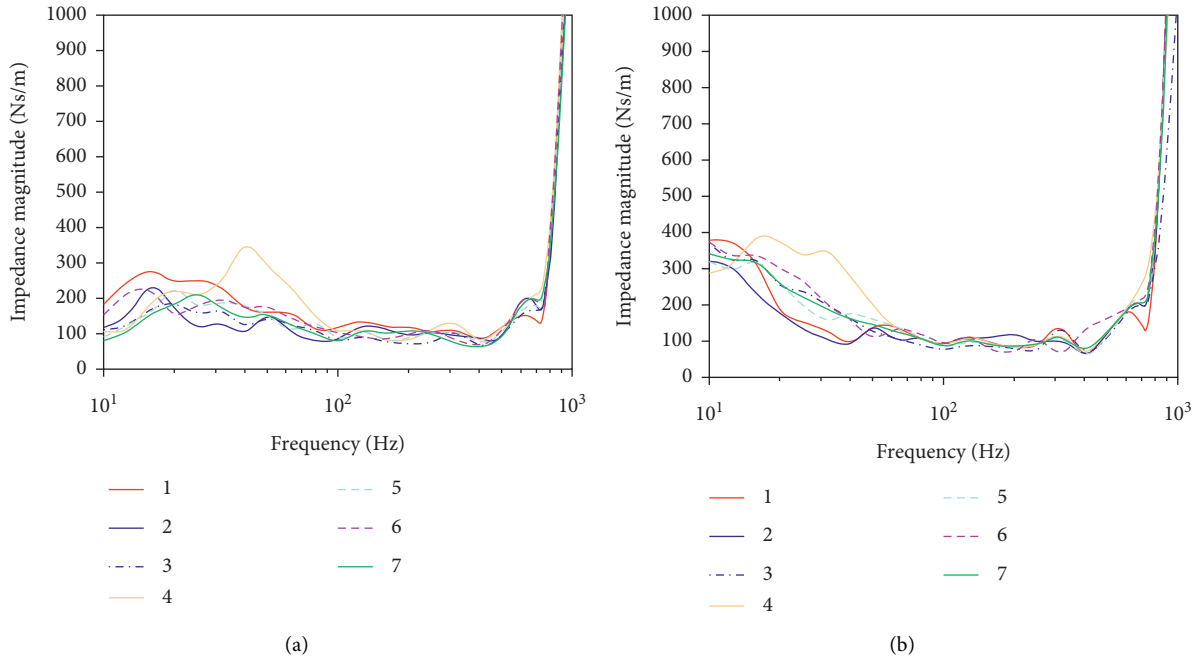

Figure 7: Amplitude of mechanical impedance of the hand-arm system for different subjects (5 m/s^2 vibration magnitude, 30 N grip force, and 10 N push force). (a) 90° elbow angle. (b) 180° elbow angle.

among the subjects showed no obvious effect on the mechanical impedance amplitude. Figure 7(a) shows that when the elbow angle was 90° and the frequency was lower than 14 Hz, the amplitude of mechanical impedance of the hand-arm system increased with increasing hand volume, hand length, hand width, and arm length. The large volume of hand means relatively large apparent mass of the arm system, which would result in a stronger coupling effect with the vibrating handle. In addition, it was observed that, in the frequency range of 30–100 Hz, a smaller hand volume usually corresponded to a higher mechanical impedance amplitude, with a peak value at around 40 Hz, possibly because resonance occurs in the hand-arm system at this frequency. Figure 7(b) shows that when the elbow angle was 180°, the individual differences of the subjects had no obvious effect on the mechanical impedance, but No. 4 subject had two peaks of mechanical impedance amplitude at around 16 Hz and 30 Hz. The second peak may be associated with the resonance frequency of the hand-arm system at this posture and hand force level. Although the differences among individual subjects had certain effects on the mechanical impedance of the hand-arm system in a specific frequency range, the change trend of mechanical impedance amplitude along with the vibration frequency was basically the same for all subjects. According to GB 10000-88 [22], the anthropometric values of the No. 4 subject were closer to the average of Chinese adult males, which were shown in Table 3. Consequently, the test and calculation results of the No. 4 subject were further discussed.

3.2. Effect of Hand-Arm Posture on Mechanical Impedance. Figure 8 shows the changes in the mechanical impedance amplitude of the human hand-arm system with the vibration frequency under different hand-arm postures. Other test conditions are as follows: vibration intensity is 5 m/s^2, grip force is 30 N, and push force is 30 N.

Figure 8 clearly shows that when the elbow angle was 180°, the hand-arm system would produce higher mechanical impedance amplitudes at lower frequencies (below 40 Hz), and when the frequency was extremely low, the hand-arm system exhibited similar characteristics to dampers. Under this combination of grip and push force levels, the peak value of the mechanical impedance amplitude occurred at a frequency of around 20 Hz. When the elbow angle was 90°, the peak value of mechanical impedance amplitude appeared at around 41 Hz. Aldien et al. have reported that the frequency corresponding to the peak value of the mechanical impedance amplitude is usually related to the main resonance frequency of the hand-arm system [21]. When the elbow angle was 90°, the frequency corresponding to the peak value of the mechanical impedance was in good agreement with the range of resonance frequency values of the hand-arm system reported in many studies [23]. When

Table 3: The average anthropometric values of Chinese adult males.

Main parameter	Weight (kg)	Height (cm)	Length of Hand (cm)	Width of Hand (mm)	Length of upper Arm (cm)	Length of Forearm (cm)
Average values	59.0	167.8	18.3	82.0	31.3	42.0

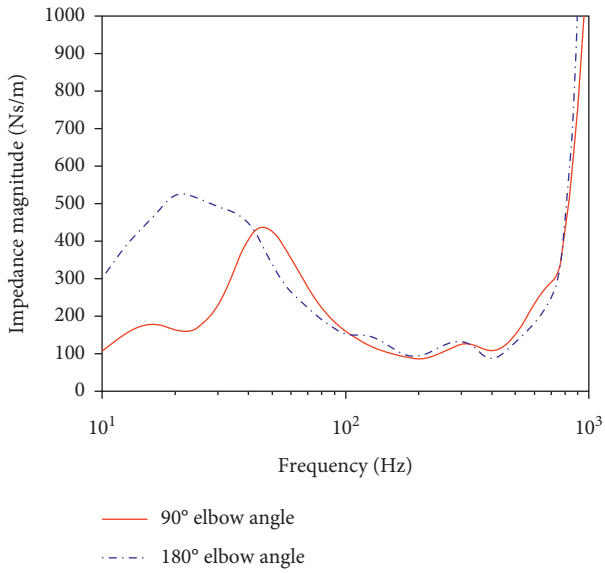

Figure 8: Amplitude of mechanical impedance of the hand-arm system under different postures (5 m/s^2 vibration magnitude, 30 N grip force, and 30 N push force).

the frequency ranged from 40 to 100 Hz and the elbow angle was 90°, the mechanical impedance amplitude of the hand-arm system was higher; when the frequency was higher than 100 Hz, the hand-arm posture had no obvious effect on the mechanical impedance.

When the frequency was low and the elbow angle was 180°, the system produced a significantly higher mechanical impedance amplitude, indicating a relatively high effective mass of the coupling of the hand-arm system with the vibrating handle, which would cause the flow of low-frequency vibration energy to the whole body through the hand-arm system. Compared with the resonance frequency of the hand-arm system with an elbow angle of 90°, a higher effective mass would bring a lower resonance frequency.

3.3. Effect of Grip Force on Mechanical Impedance. Figure 9 shows the effect of grip force on the mechanical impedance of the hand-arm system under different hand-arm postures when the vibration intensity was 5 m/s^2 and the push force was 30 N.

Figure 9 shows that, in two different hand-arm postures, an increase in grip force would increase the frequency corresponding to the peak value of mechanical impedance amplitude of the hand-arm system. When the elbow angle was 90° and the frequency was low (<34 Hz), grip force had no obvious effect on the mechanical impedance of the hand-arm system. When the frequency range was 34–400 Hz, the mechanical impedance amplitude of the hand-arm system increased with greater grip force; however, when the frequency was further increased, the effect of grip force was reduced. For the hand-arm posture with an elbow angle of 180°, when the frequency was low, the mechanical impedance amplitude was significantly higher, indicating that the hand-arm system was more strongly coupled to the vibrating handle. In almost the entire frequency range studied, a higher grip force usually corresponded to a higher mechanical impedance amplitude, but with the increases in frequency, the impact of grip force on the mechanical impedance of the hand-arm system would be gradually weakened. These findings are in good agreement with those of Aldien et al. [21].

3.4. Effect of Push Force on Mechanical Impedance. Figure 10 shows the effect of changes in push force on the mechanical impedance under the two hand-arm postures when the vibration intensity was 5 m/s^2 and the grip force was 30 N.

It can be seen that, similar to the effect of grip force, an increase in push force would also increase the frequency corresponding to the peak value of mechanical impedance amplitude of the hand-arm system under both hand-arm postures. When the elbow angle was 90° and the frequency ranged from 30 Hz to 200 Hz, an increase in push force also increased the mechanical impedance amplitude of the hand-arm system, but when the frequency was below 30 Hz or above 200 Hz, the effect of push force on the mechanical impedance of the hand-arm system was weakened. When the elbow angle was 180°, an increase in push force would elevate the mechanical impedance amplitude of the hand-arm system in almost the entire frequency range, particularly at lower frequencies (<100 Hz).

3.5. Effect of Vibration Intensity on Mechanical Impedance. Figure 11 shows the effects of different vibration intensities on the mechanical impedance of the hand-arm system under two hand-arm postures when the grip force was 30 N and the push force was 30 N.

For different vibration intensities, the variations of the mechanical impedance amplitude of the hand-arm system were basically consistent under the two hand-arm postures. When the frequency was lower (<140 Hz), vibration intensity had a greater impact on the mechanical impedance under the hand-arm posture with an elbow angle of 180°, which is consistent with the results of Aldien et al. [21]. In addition, under this posture, the mechanical impedance amplitude decreased with increasing vibration intensity. Lundström et al. also found that when the frequency was below 100 Hz, the mechanical impedance amplitude of the hand-arm system decreased with increasing vibration intensity, indicating the reliability of the measurement in this study [7].

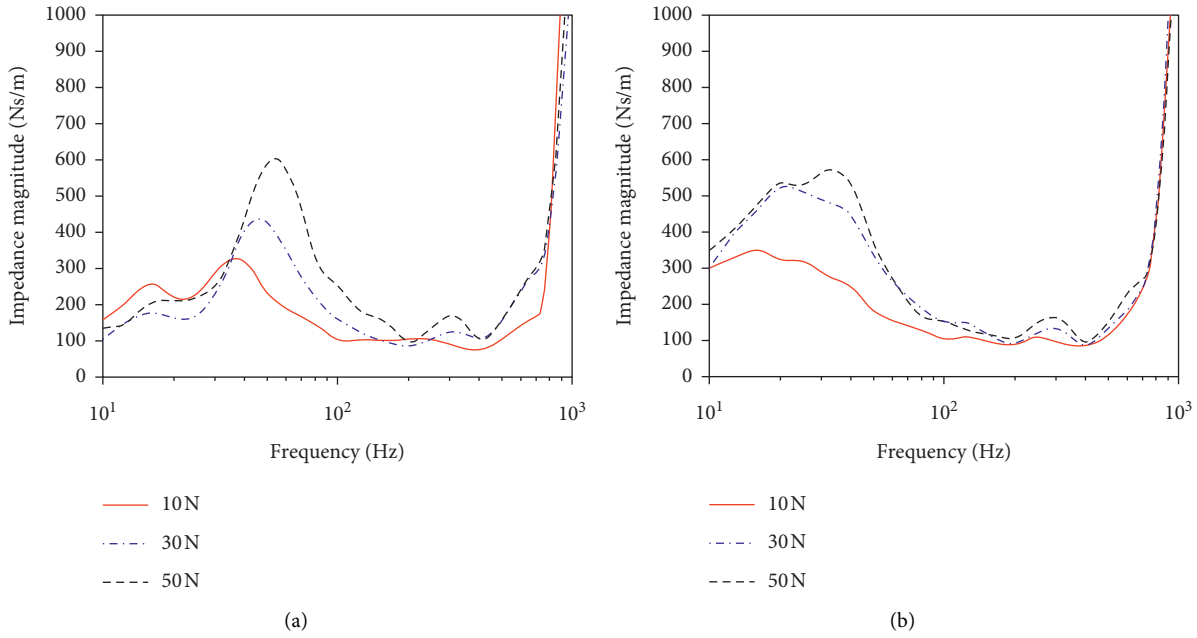

Figure 9: Amplitude of mechanical impedance of the hand-arm system under different grip forces (5 m/s^2 vibration magnitude and 30 N push force). (a) 90° elbow angle. (b) 180° elbow angle.

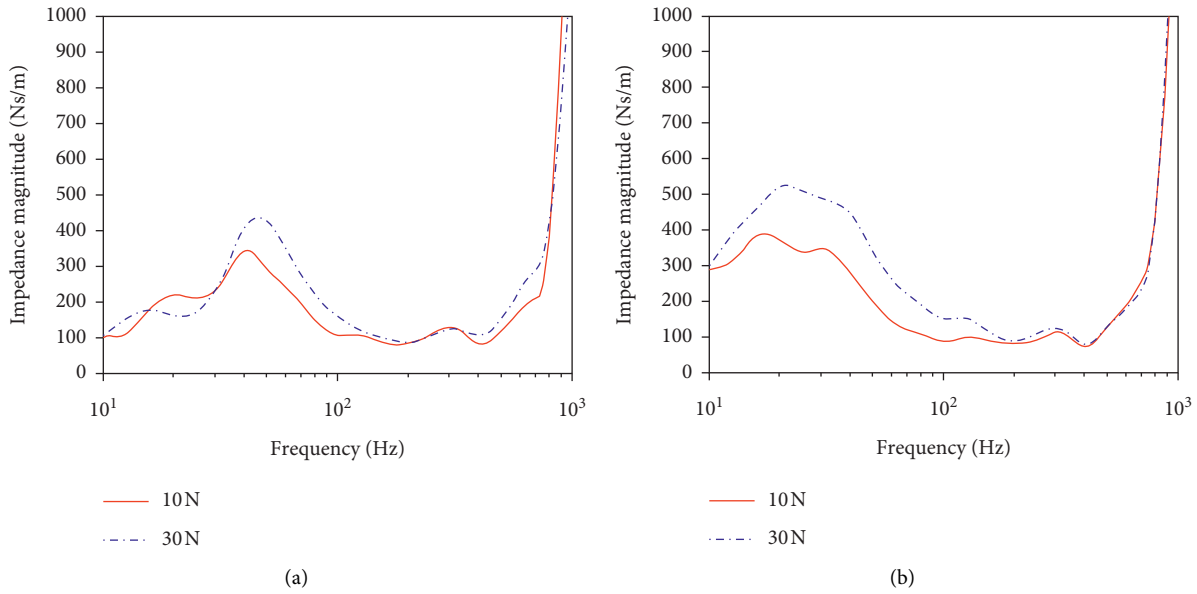

Figure 10: Amplitude of mechanical impedance of the hand-arm system under different push forces (5 m/s^2 vibration magnitude and 30 N grip force). (a) 90° elbow angle. (b) 180° elbow angle.

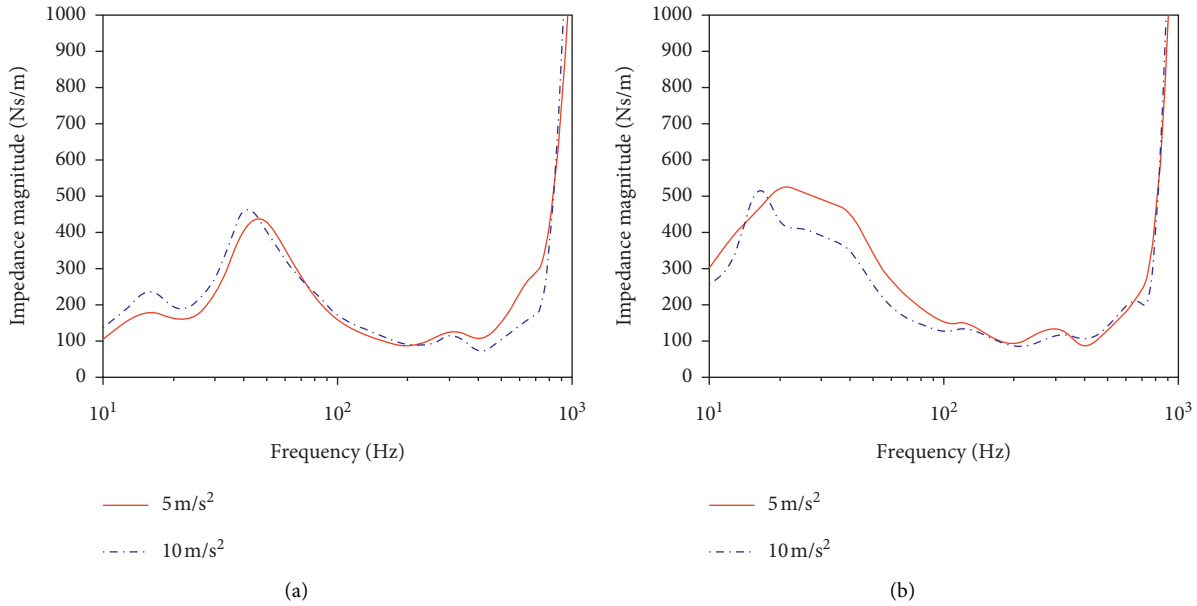

Figure 11: Amplitude of mechanical impedance of the hand-arm system under different vibration magnitude (30 N grip force and 30 N push force). (a) 90° elbow angle. (b) 180° elbow angle.

4. Conclusion

To investigate the effects of hand-arm posture, grip force, push force, and vibration excitation intensity on the mechanical impedance of human hand-arm system, a test system with a self-developed vibration handle has been established. On the basis of the testing system, the mechanical impedance of the right-hand-arm system of seven healthy adult males were tested and calculated under different hand-arm postures, vibration intensities, grip forces, and push forces. At the same time, taking the No. 4 subject as the research object, the influence of different test factors on the mechanical impedance of the human hand-arm system was discussed.

In conclusion, increases in grip or push force contribute to higher mechanical impedance amplitudes and frequencies corresponding to the peak value of the mechanical impedance. Vibration intensity greatly affects the mechanical impedance amplitude in a lower frequency range when the elbow angle is 180°. The investigation of the mechanical impedance of the hand-arm system will help to optimize and develop the biomechanical model of the human hand-arm system. In addition, since the influence of different factors on the mechanical impedance of the hand-arm system was analyzed within a certain frequency range, the injury of the human arm can be more accurately targeted, which is beneficial to the development of vibration isolators.

Data Availability

The data used to support the findings of this study are included within the article.

Conflicts of Interest

The authors declare that they have no conflicts of interest.

Acknowledgments

This study was supported by National Natural Science Foundation of China (Grant nos. 51875230 and 51405178).

References

[1] T. Y. Jin and G. F. Sun, *Occupational Health and Occupational Medicine*, People's Medical Publishing House, Beijing, China, 2007.

[2] The Ministry of Health of the People's Republic of China, *GBZ/T224-2010: Terms of Occupational Health*, The Ministry of Health of the People's Republic of China, Beijing, China, 2010.

[3] R. G. Dong, T. W. Mcdowell, and D. E. Welcome, "Biodynamic response at the palm of the human hand subjected to a random vibration," *Industrial Health*, vol. 43, no. 1, pp. 241–255, 2005.

[4] Q. L. Zheng, A. C. Yang, and J. B. Chen, "Clinical analysis of 84 patients with occupational arm vibration disease with peripheral circulatory disorders in the hands," *Chinese Vocational Medicine*, vol. 37, no. 4, pp. 311–313, 2010.

[5] Y. M. Liu, *Theory and Practice of Occupational Disease Prevention*, Chemical Industry Press, Beijing, China, 2010.

[6] L. Wang, K. Zhang, L. Lin, and J. C. Lie, "Research progress of hand-arm vibration syndrome abroad—introduction to the literatures of the 8th international conference on Hand-Arm vibration," *Chinese Journal of Industrial Hygiene and Occupational Diseases*, vol. 17, no. 5, pp. 315–317, 1999.

[7] R. Lundström and L. Burström, "Mechanical impedance of the human hand-arm system," *International Journal of Industrial Ergonomics*, vol. 3, no. 3, pp. 235–242, 1989.

[8] L. Burström, "The influence of biodynamic factors on the mechanical impedance of the hand and arm," *International Archives of Occupational and Environmental Health*, vol. 69, no. 6, pp. 437–446, 1997.

[9] T. I. Hempstock and D. E. O'Connor, "Accuracy of measuring impedance in the hand-arm system," *Scandinavian Journal of Work, Environment & Health*, vol. 12, no. 4, pp. 355–358, 1986.

[10] R. Gurram, S. Rakheja, and G. J. Gouw, "Mechanical impedance of the human hand-arm system subject to sinusoidal and stochastic excitations," *International Journal of Industrial Ergonomics*, vol. 16, no. 2, pp. 135–145, 1995.

[11] R. G. Dong, J. Z. Wu, T. W. Mcdowell, and D. E. Welcome, "Distribution of mechanical impedance at the fingers and the palm of the human hand," *Journal of Biomechanics*, vol. 38, no. 5, pp. 1165–1175, 2005.

[12] R. G. Dong, D. E. Welcome, X. Y. Xu et al., "Mechanical impedances distributed at the fingers and palm of the human hand in three orthogonal directions," *Journal of Sound and Vibration*, vol. 331, no. 5, pp. 1191–1206, 2011.

[13] J. Li, *Effect of Lcal Vibration on Human Qrm*, Changchun University of Technology, Changchun, China, 2010.

[14] H. D. Dai, Y. S. Xiong, G. E. Cai, X. K. Xia, and Z. R. Lin, "A mechanical impedance-based measurement system for quantifying Parkinsonian rigidity," *Journal of Biomedical Engineering*, vol. 35, no. 3, pp. 421–428, 2017.

[15] Standardization Administration of the People's Republic of China, *GB/T 5703-2010, Basic Human Body Measurements for Technological Design*, Beijing, China, 2010.

[16] I. E. Brown, S. H. Scott, and G. E. Loeb, "Mechanics of feline soleus: II. Design and validation of a mathematical model," *Journal of Muscle Research and Cell Motility*, vol. 17, no. 2, pp. 221–233, 1996.

[17] Standardization Administration of the People's Republic of China, *GB/T 19740-2005, Mechanical Vibration and Shock-Free, Mechanical Impedance of Human Hand-Arm System at the Driving Point*, Standardization Administration of the People's Republic of China, Beijing, China, 2005.

[18] International Organization for Standardization, *ISO 5349-1-2001, Mechanical Vibration—Measurement and Evaluation of Human Exposure to Hand-Transmitted Vibration—Part 1: General Requirements*, International Organization for Standardization, Geneva, Switzerland, 2001.

[19] S. A. Adewusi, *Distributed biodynamic Characteristics of the human hand-arm System Coupled with vibrating handles and Power Tools*, PhD thesis, The Department of Mechanical & Industrial Engineering, Concordia University, Canada, 2009.

[20] International Organization for Standardization, *ISO 10819-2013, Mechanical Vibration and Shock—Hand-Arm Vibration—Measurement and Evaluation of the Vibration Transmissibility of Gloves at the Palm of the Hand*, International Organization for Standardization, Geneva, Switzerland, 2013.

[21] Y. Aldien, P. Marcotte, S. Rakheja, and P. E. Boileau, "Influence of hand–arm posture on biodynamic response of the human hand–arm exposed to z_h-axis vibration," *International Journal of Industrial Ergonomics*, vol. 36, no. 1, pp. 45–59, 2006.

[22] The State Bureau of Quality and Technical Supervision, *GB 10000-88, Human Dimensions of Chinese Adults*, The State Bureau of Quality and Technical Supervision, Beijing, China, 1988.

[23] R. G. Dong, D. E. Welcome, T. W. Mcdowell, and J. Z. Wu, "Measurement of biodynamic response of human hand–arm system," *Journal of Sound and Vibration*, vol. 294, no. 4-5, pp. 807–827, 2006.